

# **Transient Permeability in Porous and Fractured Sandstones mediated by Fluid-rock Interactions**

**Chaojie Cheng**

Kumulative Univ.-Diss.

zur Erlangung des akademischen Grades

"doctor rerum naturalium"

(Dr. rer. nat.)

in der Wissenschaftsdisziplin "Hydrogeologie"

eingereicht an der

Mathematisch-Naturwissenschaftlichen Fakultät

Institut für Geowissenschaften

der Universität Potsdam



Ort und Tag der Disputation:

Potsdam, 03.05.2021

Hauptbetreuer: Prof. Dr. Michael Kühn

Universität Potsdam / GFZ Potsdam

Betreuer: Prof. Dr. Christoph Hilgers

Karlsruher Institut für Technologie

weitere Gutachter: Prof. Dr. Jörg Renner

Ruhr-Universität Bochum

Published online on the

Publication Server of the University of Potsdam:

<https://doi.org/10.25932/publishup-51012>

<https://nbn-resolving.org/urn:nbn:de:kobv:517-opus4-510124>

# Eidesstattliche Erklärung

Hiermit versichere ich an Eides statt, dass

- die eingereichte Arbeit oder wesentliche Teile derselben in keinem anderen Verfahren zur Erlangung eines akademischen Grades vorgelegt worden sind;
- bei der Anfertigung der Dissertation die Grundsätze zur Sicherung guter wissenschaftlicher Praxis der DFG eingehalten wurden, die Dissertation selbständig und ohne fremde Hilfe verfasst wurde, andere als die von mir angegebenen Quellen und Hilfsmittel nicht benutzt worden sind und die den benutzten Werken wörtlich oder sinngemäß entnommenen Stellen als solche kenntlich gemacht wurden.

Ort/Datum

Unterschrift

# Abstract

Understanding the fluid transport properties of subsurface rocks is essential for a large number of geotechnical applications, such as hydrocarbon (oil/gas) exploitation, geological storage (CO<sub>2</sub>/fluids), and geothermal reservoir utilization. To date, the hydromechanically-dependent fluid flow patterns in porous media and single macroscopic rock fractures have received numerous investigations and are relatively well understood. In contrast, fluid-rock interactions, which may permanently affect rock permeability by reshaping the structure and changing connectivity of pore throats or fracture apertures, need to be further elaborated. This is of significant importance for improving the knowledge of the long-term evolution of rock transport properties and evaluating a reservoir' sustainability. The thesis focuses on geothermal energy utilization, e.g., seasonal heat storage in aquifers and enhanced geothermal systems, where single fluid flow in porous rocks and rock fracture networks under various pressure and temperature conditions dominates.

In this experimental study, outcrop samples (i.e., Flechtinger sandstone, an illite-bearing Lower Permian rock, and Fontainebleau sandstone, consisting of pure quartz) were used for flow-through experiments under simulated hydrothermal conditions. The themes of the thesis are (1) the investigation of clay particle migration in intact Flechtinger sandstone and the coincident permeability damage upon cyclic temperature and fluid salinity variations; (2) the determination of hydro-mechanical properties of self-propping fractures in Flechtinger and Fontainebleau sandstones with different fracture features and contrasting mechanical properties; and (3) the investigation of the time-dependent fracture aperture evolution of Fontainebleau sandstone induced by fluid-rock interactions (i.e., predominantly pressure solution). Overall, the thesis aims to unravel the mechanisms of the instantaneous reduction (i.e., direct responses to thermo-hydro-mechanical-chemical (THMC) conditions) and progressively-cumulative changes (i.e., time-dependence) of rock transport properties.

Permeability of intact Flechtinger sandstone samples was measured under each constant condition, where temperature (room temperature up to 145 °C) and fluid salinity (NaCl: 0 ~ 2 mol/l) were stepwise changed. Mercury intrusion porosimetry (MIP), electron microprobe analysis (EMPA), and scanning electron microscopy (SEM) were performed to investigate the changes of local porosity, microstructures, and clay element contents before and after the experiments. The



results indicate that the permeability of illite-bearing Flechtinger sandstones will be impaired by heating and exposure to low salinity pore fluids. The chemically induced permeability variations prove to be path-dependent concerning the applied succession of fluid salinity changes. The permeability decay induced by a temperature increase and a fluid salinity reduction operates by relatively independent mechanisms, i.e., thermo-mechanical and thermo-chemical effects.

Further, the hydro-mechanical investigations of single macroscopic fractures (aligned, mismatched tensile fractures, and smooth saw-cut fractures) illustrate that a relative fracture wall offset could significantly increase fracture aperture and permeability, but the degree of increase depends on fracture surface roughness. X-ray computed tomography (CT) demonstrates that the contact area ratio after the pressure cycles is inversely correlated to the fracture offset. Moreover, rock mechanical properties, determining the strength of contact asperities, are crucial so that relatively harder rock (i.e., Fontainebleau sandstone) would have a higher self-propping potential for sustainable permeability during pressurization. This implies that self-propping rough fractures with a sufficient displacement are efficient pathways for fluid flow if the rock matrix is mechanically strong.

Finally, two long-term flow-through experiments with Fontainebleau sandstone samples containing single fractures were conducted with an intermittent flow (~140 days) and continuous flow (~120 days), respectively. Permeability and fluid element concentrations were measured throughout the experiments. Permeability reduction occurred at the beginning stage when the stress was applied, while it converged at later stages, even under stressed conditions. Fluid chemistry and microstructure observations demonstrate that pressure solution governs the long-term fracture aperture deformation, with remarkable effects of the pore fluid (Si) concentration and the structure of contact grain boundaries. The retardation and the cessation of rock fracture deformation are mainly induced by the contact stress decrease due to contact area enlargement and a dissolved mass accumulation within the contact boundaries. This work implies that fracture closure under constant (pressure/stress and temperature) conditions is likely a spontaneous process, especially at the beginning stage after pressurization when the contact area is relatively small. In contrast, a contact area growth yields changes of fracture closure behavior due to the evolution of contact boundaries and concurrent changes in their diffusive properties. Fracture aperture and thus permeability will likely be sustainable in the long term if no other processes (e.g., mineral precipitations in the open void space) occur.

# Zusammenfassung

Die Kenntnis von Gesteinstransporteigenschaften und das Verständnis ihrer zeitlichen Veränderungen sind für eine Vielzahl von geotechnischen Anwendungen von herausragender Bedeutung. Als Beispiele seien genannt: die Gewinnung von Kohlenwasserstoffen (Öl/Gas), die stoffliche geologische Speicherung (CO<sub>2</sub>/Fluide) und die geothermische Energiegewinnung. Die hydromechanischen Strömungseigenschaften von Fluiden in porösen Gesteinen und solchen mit einzelnen, makroskopischen Rissen sind mittlerweile vergleichsweise gut verstanden. Im Gegensatz dazu besteht im Hinblick auf Fluid-Gesteins-Wechselwirkungen, welche durch eine Veränderung der Struktur und Verbundenheit des Porenraums bzw. der Rissöffnungsweiten die Gesteinspermeabilität permanent beeinflussen können, entscheidender Forschungsbedarf. Dies ist insbesondere für eine verbesserte Kenntnis der langzeitlichen Entwicklung der (hydraulischen) Gesteinstransporteigenschaften sowie eine Evaluierung der Nachhaltigkeit einer Nutzung geologischer Reservoirs von großer Bedeutung und Gegenstand der vorliegenden Dissertation. Anwendungsaspekt dieser Arbeit ist insbesondere die geothermische Technologieentwicklung, d.h. die saisonale Wärmespeicherung in Aquiferen sowie sogenannte „Enhanced Geothermal Systems“, in der die Nutzung einphasiger Fluide in porösen Gesteinen bzw. Rissnetzwerken im Vordergrund steht.

In dieser experimentellen Arbeit wurden mit Gesteinsproben aus Aufschlüssen (unterpermischer, illitreicher Flechtinger Sandstein sowie quarzreicher Fontainebleau Sandstein) Durchflusseexperimente bei simulierten hydrothermalen Reservoirbedingungen durchgeführt. Themenschwerpunkte der Dissertation sind hierbei (1) die Untersuchung einer Tonpartikelmigration in intakten Proben des Flechtinger Sandsteins und eine damit verbundene Permeabilitätsschädigung durch zyklische Temperaturveränderungen sowie Variationen der Fluidsalinität, (2) die Bestimmung der hydromechanischen Eigenschaften selbststützender Risse in Flechtinger und Fontainebleau Sandsteinen mit unterschiedlichen Rissmorphologien und mechanischen Kennwerten und (3) die Untersuchung einer zeitlichen Veränderung der Rissöffnungsweiten in Fontainebleau Sandstein, welche durch Fluid-Gesteins-Wechselwirkungen (insbesondere Drucklösung) induziert wird. Zusammenfassend hat diese Dissertation zum Ziel, die Mechanismen sowohl unmittelbarer als auch zeitabhängiger, durch veränderte thermisch-hydraulisch-mechanisch-chemische Bedingungen hervorgerufene, Veränderungen von

Gesteinstransporteigenschaften herauszuarbeiten.

Die Permeabilität intakter Proben Flechtinger Sandsteins wurde systematisch bei stufenweise veränderten Temperaturen (von Raumtemperatur bis 145 °C) und Fluidsalinitäten (NaCl: 0 ~ 2 mol/l) gemessen. Quecksilberporosimetrie, Elektronenstrahlmikroanalyse und Rasterelektronenmikroskopie wurden angewandt, um Veränderungen der lokalen Porosität, der Gesteinsmikrostruktur sowie des Tongehalts nach Abschluss des Experiments im Vergleich zum Ausgangszustand zu bestimmen. Es zeigte sich, dass die Permeabilität des illitreichen Flechtinger Sandsteins durch eine Temperaturerhöhung sowie eine Verringerung der Salinität des Porenfluids geschädigt wird. Die chemisch induzierten Permeabilitätsveränderungen sind pfadabhängig von der Abfolge der Salinitätsveränderungen. Die Mechanismen einer durch Temperaturerhöhung oder Salinitätsreduktion induzierten Permeabilitätsschädigung arbeiten hierbei weitestgehend unabhängig voneinander, als thermo-mechanische bzw. thermo-chemische Prozesse.

Die hydromechanischen Untersuchungen an makroskopischen Einzelrissen (Scherrisse ohne und mit Versatz sowie gesägte Proben) zeigen, dass ein relativer Versatz der beiden Rissflächen eine erhebliche Erhöhung der Rissöffnungsweite und damit der Gesteinspermeabilität bewirken kann, deren Grad aber stark von der Oberflächenrauigkeit abhängt. Computertomographische Aufnahmen des Gesteins zeigen, dass das Kontaktflächenverhältnis nach den erfolgten Druckzyklen invers mit dem Scherversatz korreliert. Darüber hinaus haben die mechanischen Eigenschaften des jeweiligen Gesteins, welche die Festigkeit der Kontaktpunkte innerhalb des Risses bestimmen, einen entscheidenden Einfluss auf die Selbststützungsfähigkeit des Risses bei einer Druckerhöhung. Diese ist damit (höhere Festigkeit) bei Fontainebleau Sandstein gegenüber Flechtinger Sandstein verbessert. Insgesamt stellen selbststützende raue Risse mit ausreichendem Scherversatz in einem Gestein hoher Festigkeit effiziente Fließwege für Geofluidе dar.

Die zwei Langzeitexperimente an geklüftetem Fontainebleau Sandstein wurden mit intermittierender (~140 Tage) bzw. kontinuierlicher (~120 Tage) Durchströmung durchgeführt und die Permeabilität des Gesteins sowie der Fluidchemismus über die Dauer des jeweiligen Experiments bestimmt. Eine Permeabilitätsreduktion war insbesondere am Anfang der Messung zu beobachten, nachdem die Spannung erstmalig auf das Gestein aufgebracht wurde, und nahm dann im weiteren Verlauf des Experiments progressiv ab. Fluidchemische und mikrostrukturelle Beobachtungen zeigen, dass Drucklösung die langzeitliche Deformation des Risses kontrolliert, wobei die Porenfluidkonzentration (Si) und die Mikrostruktur der Kontaktpunkte eine herausragende Rolle spielen. Die Verlangsamung bzw. das Abklingen der Rissdeformation werden insbesondere durch die Verringerung der Kontaktspannung aufgrund einer Kontaktflächenvergrößerung sowie die Anreicherung gelöster Spezies in den Kontakten bestimmt. Ergebnis dieser Arbeit ist auch die Erkenntnis, dass eine Riss-schließung bei konstanten

Druck/Spannungs- und Temperaturbedingungen sehr wahrscheinlich ein spontan ablaufender Prozess ist, insbesondere zu Beginn einer Druckbeaufschlagung, wenn die Kontaktfläche noch relativ klein ist. Eine Vergrößerung der Kontaktfläche führt zu einem veränderten Riss-schließungsverhalten, da die Kontaktpunkte einer strukturellen Entwicklung unterworfen sind und sich damit ihre diffusiven Eigenschaften ändern. Über längere Zeiträume werden die Rissöffnungsweite und damit die Gesteinspermeabilität in einem geologischen Reservoir insbesondere dann nachhaltig sein, wenn keine zusätzlichen, entgegenwirkenden Prozesse (z.B. Mineralfällung innerhalb des Risses) in dem Gestein ablaufen.

## Statement of contribution

This cumulative thesis consists of four manuscripts, which are listed in the following.

**Cheng, C.**, and Milsch, H. (2020). Permeability variations in illite-bearing sandstone: effects of temperature and NaCl fluid salinity. **Journal of Geophysical Research: Solid Earth**. 125(9) e2020JB020122. <https://doi.org/10.1029/2020JB020122>

**Cheng, C.**, and Milsch, H. (2021). Hydromechanical investigations on the self-propping potential of fractures in tight sandstones. **Rock Mechanics and Rock Engineering**. <https://doi.org/10.1007/s00603-021-02500-4>

**Cheng, C.**, and Milsch, H. (2020). Evolution of fracture aperture in quartz sandstone under hydrothermal conditions: mechanical and chemical effects. **Minerals**, 10(8), 657. <https://doi.org/10.3390/min10080657>

**Cheng, C.**, Lu, R., Shao, H., Kolditz, O., and Milsch, H. (2020). Pressure solution-induced fracture closure in quartz sandstone at moderate temperature: the importance of contact boundary and diffusive properties. **Earth and Planetary Science Letters**. (Accepted for peer review)

**Contributions:** For the four experimental studies listed above, the PhD candidate designed and conducted the laboratory experiments, obtained and analyzed the results, prepared all figures, and wrote the manuscripts. The co-authors advised on the experiments, discussed the results, revised and improved the manuscripts. An additional publication during the author's PhD studies is not integrated into the thesis but is listed here for the readers' interest.

**Cheng, C.**, Hale, S., Milsch, H., and Blum, P. (2020). Measuring hydraulic fracture apertures: a comparison of methods. **Solid Earth**. 11, 2411–2423. <https://doi.org/10.5194/se-11-2411-2020>

Date

Signature

**The correctness of this statement is hereby confirmed:**

Date

Signature Principal Supervisor (Prof. Dr. Michael Kühn)

# Declaration

I, Chaojie Cheng, declare that the thesis titled "Transient permeability in porous and fractured sandstones mediated by fluid-rock interactions" is my own work. The present study, including experimental work, data analyses, and interpretations, was done by myself jointly with support from others at the "Deutsches GeoForschungZentrum (GFZ)" in Potsdam, Germany.

The collaborative researchers are listed as co-authors in each manuscript separately. Additional work, e.g., sample preparation and analytical investigations, done by others, is indicated and acknowledged in the corresponding manuscripts in the published versions.

The use of high-pressure, high-temperature flow-through apparatuses, was supervised by Harald Milsch (GFZ). X-ray diffraction (XRD) measurements were carried out by Anja Schleicher (GFZ). Franziska Wike (GFZ) provided the electron microprobe analysis (EMPA). I performed the mercury intrusion porosimetry (MIP) measurements with the assistance of Christian Cunow (GFZ). The scanning electron microscopy (SEM) measurements were performed by Ilona Schäpan (GFZ). The inductively coupled plasma optical emission spectroscopy (ICP-OES) measurements were conducted by Sabine Tonn (GFZ) and Iris Pieper (Technische Universität Berlin). X-ray computed tomography (CT) was performed by myself under the supervision of Erik Rybacki (GFZ).

Date

Signature

# Acknowledgements

Firstly, I want to express my heartfelt gratitude to my PhD advisor, Dr. Harald Milsch, for the great guidance and support for my research. I gained extensive experience in laboratory studies of rock and fluid physics from his group. His top professionalism, ethics, and approach to supervision set a bar for where I should achieve in my future career. I truly thank our collaboration. I sincerely thank Prof. Dr. Ernst Huenges, who provided me with an opportunity to conduct my PhD study in section 4.8 "Geoenergy" at GFZ. In addition, I am deeply grateful to my supervisor Prof. Dr. Michael Kühn (GFZ and the University of Potsdam), for providing thoughtful comments, support, and fruitful discussions on my PhD work. I would also like to express my sincere gratitude to my mentor Prof. Dr. Christoph Hilgers (KIT, Karlsruhe Institute of Technology). The short-term visiting studies in his group in KIT and discussions with Dr. Benjamin Busch and Alexander Monsees greatly promoted my view on reservoir geology and mineralogy.

I thank my colleagues, Dr. Guido Blöcher, Dr. Simona Regenspurg, Dr. Erik Rybacki, Dr. Hannes Hofmann, Dr. Martin Peter Lipus, Dr. Wenxia Wang, Christian Kluge, and Ulrike Hoffert for the help and scientific discussions during my PhD study. I also sincerely thank Jasper Florian Zimmermann, Tanja Ballerstedt, Christian Cunow, Michael Naumann, Ronny Giese, Stefan Gehrman, and Thomas Ziegenhagen for the technical support of laboratory experiments. In addition, I thank my intern Matt Gill for assistance with the laboratory work.

Furthermore, I want to thank the China Scholarship Council for providing me with a fellowship to conduct my PhD at GFZ. Financial support from section 4.8 "Geoenergy" covering the experimental consumptions, testing fees, and business travels, is highly acknowledged. The past four years at GFZ have been and will be a great fortune in my life. My lovely colleagues, who may not directly assist my PhD work but bring much fun to our daily life, are deeply grateful.

Last but not least, I am deeply indebted to my parents and family. Without their unconditional support, encouragement, and endless love, I cannot imagine how difficult it would be to complete my PhD. I especially want to tell my dear wife, Yuting Huang, that meeting you is the greatest fortune and the most romantic moment in my life. I am willing to be with you for the rest of my life and love you forever.

# Table of contents

<b>Eidesstattliche Erklärung</b> .....	<b>I</b>
<b>Abstract</b> .....	<b>II</b>
<b>Zusammenfassung</b> .....	<b>IV</b>
<b>Statement of contribution</b> .....	<b>VII</b>
<b>Declaration</b> .....	<b>VIII</b>
<b>Acknowledgements</b> .....	<b>IX</b>
<b>Table of contents</b> .....	<b>X</b>
<b>Chapter 1</b>	
<b>Introduction</b> .....	<b>1</b>
1.1 Background .....	1
1.2 Objective .....	3
1.2.1 Scientific questions .....	3
1.2.2 Aims of the present study .....	6
1.3 Thesis organization .....	7
<b>Chapter 2</b>	
<b>Permeability variations of illite-bearing sandstone</b> .....	<b>9</b>
2.1 Introduction .....	10
2.2 Experimental and analytical methodologies .....	11
2.2.1 Sample material .....	11
2.2.2 Flow-through apparatus and sample assembly .....	12
2.2.3 Flow-through experiments .....	13
2.2.4 Microstructural analyses .....	15
2.2.5 Initial rock microstructure .....	16
2.3 Results .....	18
2.3.1 Flow-through experiments and permeability .....	18
2.3.2 Microstructural evolution .....	20
2.4 Discussion .....	25
2.4.1 Hydraulic sample behavior at the start .....	25
2.4.2 Effects of temperature changes .....	26
2.4.3 Effects of NaCl salinity changes .....	28



2.5 Conclusions .....	31
<b>Chapter 3</b>	
<b>Hydro-mechanical investigations on self-propping fractures .....</b>	<b>33</b>
3.1 Introduction .....	34
3.2 Rock samples and methodology.....	36
3.2.1 Sample preparation and experimental apparatus .....	36
3.2.2 Experimental procedures .....	39
3.2.3 Fracture surface topography .....	42
3.2.4 Determination of fracture morphology using X-ray $\mu$ CT scans .....	45
3.3 Results .....	46
3.3.1 Hydraulic and mechanical aperture changes during loading-unloading cycles .....	46
3.3.2 Surface roughness .....	48
3.3.3 Numerical fracture apertures.....	51
3.3.4 Evolution of fracture aperture and contact area ratio based on X-ray $\mu$ CT .....	54
3.4 Discussion .....	57
3.4.1 Correlation between hydraulic aperture and mechanical aperture.....	57
3.4.2 Fracture roughness and displacement-related fracture aperture.....	61
3.4.3 Aperture changes with effective stress .....	61
3.4.4 Implications .....	63
3.5 Conclusions .....	63
<b>Chapter 4</b>	
<b>Mechano-chemical effects on fracture aperture evolution: intermittent flow.....</b>	<b>65</b>
4.1 Introduction .....	66
4.2 Sample material and experimental methods.....	68
4.2.1 Sample preparation and experimental apparatus .....	68
4.2.2 Experimental procedures .....	70
4.2.3 Sampling and chemical fluid analysis.....	71
4.2.4 Determination of fracture aperture.....	72
4.2.5 X-ray micro computed tomography ( $\mu$ CT).....	73
4.3 Results .....	73
4.3.1 Effects of pressure and temperature on fracture aperture .....	73
4.3.2 Time-dependent evolution of fracture aperture .....	74
4.3.3 Evolution of effluent Si concentration .....	75
4.3.4 Microstructure variations .....	78
4.4 Discussion .....	79
4.4.1 Mechanical and thermal effects on fracture aperture.....	79

4.4.2 Chemical effects on fracture aperture in the long term.....	80
4.4.3 Effects of stress corrosion-induced subcritical cracking.....	84
4.4.4 Implications.....	85
4.5 Conclusions .....	85
<b>Chapter 5</b>	
<b>Evolution of fracture aperture induced by fluid-rock interactions: continuous flow .....</b>	<b>87</b>
5.1 Introduction .....	88
5.2 Experimental methodology .....	90
5.2.1 Sample preparation and experimental setup.....	90
5.2.2 Experimental procedures.....	91
5.2.3 Preparation of the silica solution.....	93
5.2.4 Microstructural observations.....	94
5.3 Experimental results .....	94
5.3.1 Evolution of fracture permeability .....	94
5.3.2 Evolution of effluent Si concentration .....	96
5.3.3 Surface topography analysis .....	98
5.3.4 $\mu$ CT-based image analysis .....	99
5.3.5 SEM analysis.....	100
5.4 Discussion .....	101
5.4.1 Determination of the contact boundary and water film thickness.....	101
5.4.2 Effects of contact-boundary morphology on mass transfer and aperture closure ....	103
5.4.3 Stress-dependent diffusion .....	104
5.4.4 Equilibrium of pressure solution-induced compaction .....	106
5.5 Conclusions .....	107
<b>Chapter 6</b>	
<b>General conclusions, implications and suggestions .....</b>	<b>109</b>
6.1 Summary and remarks.....	109
6.2 Implications for natural rock systems and engineering applications.....	111
6.2.1 Seasonal heat storage in aquifers .....	111
6.2.2 Permeability of deep geothermal reservoirs.....	112
6.2.3 Long-term sustainability of fractures in the Earth's upper crust.....	113
6.3 Suggestions for further research .....	113
<b>Appendices .....</b>	<b>116</b>
Appendix A: Calculation of the particle interaction energy by DLVO theory (Chapter 2) ....	116
Appendix B: Experimental data of the permeability measurements (Chapter 2).....	119
Table B1 Sample FS1. ....	119

Table B2 Sample FS3. ....	120
Table B3 Sample FS4. ....	121
Appendix C: Images of the fracture microstructures (Chapter 3) .....	122
Appendix D: Changes of mechanical aperture during the loading-unloading sequences (Chapter 5) .....	124
Appendix E: Supplementary materials (Chapter 5) .....	125
<b>References .....</b>	<b>128</b>
<b>List of figures .....</b>	<b>144</b>
<b>List of tables.....</b>	<b>147</b>
<b>Curriculum Vitae .....</b>	<b>148</b>



# Chapter 1

## Introduction

### 1.1 Background

The fluid transport properties of rock masses such as porous sediments as well as crystalline and igneous rocks are of significant importance for a variety of geotechnical applications, including the extraction of hydrocarbons and geothermal energy utilization (e.g., Schembre et al., 2006; Huenges, 2010). In these cases, sufficient amounts of fluid need to be circulated through porous media (i.e., with a high-permeable rock matrix, such as in sandstones) or rock fracture networks (i.e., with a low- /non-permeable rock matrix, such as in shale and granite), and consequently high hydraulic conductivity is essential for saving costs and maintaining the potential reservoirs' economic production. Therefore, a thorough understanding of rock permeability changes may help better operate reservoir formations and minimize potential risks for permeability damage.

Numerous studies have been carried out since decades to understand the mechanisms of fluid transport properties of rock media under various conditions (e.g., changing effective stress, changing fluid salinity/composition, changing temperature), including porous media (e.g., Mungan, 1968; Khilar & Fogler, 1987; Mohan et al., 1993; Ochi & Vernoux, 1998; Blöcher et al., 2009; Bedrikovetsky et al., 2012; Rosenbrand et al., 2015a; Rosenbrand et al., 2015b; Meng et al., 2020), and rock fractures (e.g., Raven & Gale, 1985; Zimmerman et al., 1992; Ge, 1997; Min et al., 2009; Hofmann et al., 2016; Vogler et al., 2016). In porous media, apart from effective stress-related permeability variations, a fluid salinity/composition-induced permeability decline has received particular attention because various sedimentary rocks contain clay phases (Wilson et al., 2014), which are sensitive to fluid chemistry and flow dynamics due to their morphology and a net surface charge. The permeability may decrease by several orders of magnitude resulting from fine particle migration blocking pore connections (e.g., Mungan, 1968; Khilar & Fogler, 1987; Schembre & Kavscek, 2005; You et al., 2016; Russell et al., 2018). For rock fractures, hydro-mechanical

investigations in conjunction with quantifying spatial fracture configurations have been widely performed and these relations are fairly well understood (e.g., Rutqvist, 2015; Hofmann et al., 2016; Crawford et al., 2017; Zambrano et al., 2019).

What remains to be further elaborated in this regard are (i) the effects of elevated temperature on particle migration in porous media and the permeability, and (ii) the long-term evolution of fracture transport properties upon fluid-rock interactions. To the author's knowledge, there is a very limited amount of studies on porous rocks taking both the particle migration and the temperature effects into account, and mostly kaolinite was considered as the clay phase in previous studies (e.g., Schembre & Kovscek, 2005; You et al., 2015). For fracture permeability decline over large periods of time, previous studies, including a limited number of long-term investigations, showed that pressure solution plays a dominant role, leading to a permanent reduction of permeability (e.g., Polak et al., 2003; Yasuhara et al., 2003; Yasuhara et al., 2006; Gratier et al., 2013; Gratier et al., 2014; Yasuhara et al., 2015; Van den Ende et al., 2019).

The aforementioned issues are particularly interesting for geothermal energy utilization, such as seasonal heat storage in geological aquifers and enhanced geothermal systems (EGS) for electricity production (Huenges, 2010). Figure 1.1 shows a schematic diagram of fluid flow through porous media and rock fractures in the subsurface from shallow to deep layers for different purposes. At relatively shallow depth, heat is stored or extracted into/from porous aquifers by pumping fluids, which leads to changes in temperature and fluid salinity/composition. How the aquifer rock permeability reacts under changing the temperature and fluid conditions would affect utilization success. In EGS, at relatively deep formations (e.g., the Groß Schönebeck geothermal research site in the North German Basin with the borehole depth down to ~4km (Blöcher et al., 2016) and the hot dry rock geothermal site located inside the Rhine graben (Soultz-sous-Forêts, France) (Genter & Traineau, 1996; Dezayes et al., 2010)), fractures dominate fluid flow, and thus, the time-dependent fracture deformation would determine the lifespan and the economic use of the reservoirs.

Large-scale studies such as in-situ hydraulic tests and numerical simulations firstly need a better understanding of small-scale representatives. The properties of core samples at the laboratory scale under controlled and known conditions is the starting point to understand the fundamental mechanisms and, later on, more complex systems. Therefore, in the present study, laboratory experiments at the sample-scale and the micro-scale (Figure 1.1) were performed systematically on clay-bearing porous rocks and dense rocks containing predefined fractures to investigate how fluid-rock interactions (i.e., particle migration in porous media and pressure solution in rock fractures) govern permeability variations under hydrothermal conditions.

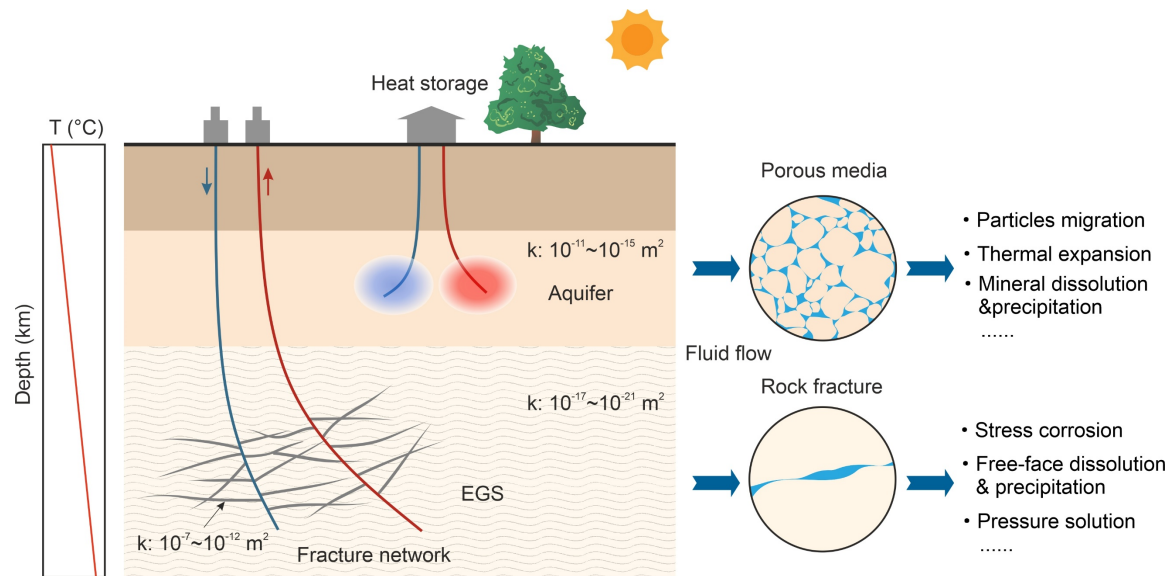


**Figure 1.1** Schematic diagram of fluid transport through porous media and rock fractures in the subsurface and how key factors, acting at the micro-scale, may affect the transport properties.

## 1.2 Objective

### 1.2.1 Scientific questions

Permeability decline, either instantaneous or time-dependent, of reservoir rocks, is a potential risk that needs to be eliminated or minimized in various geotechnical applications. As mentioned above, the present study mainly focuses on geothermal reservoir applications, where single fluid flow in reservoir rocks under hydrothermal conditions is the key matter.

The salinity reduction-induced permeability damage of sedimentary rocks containing clay minerals has been widely investigated experimentally and theoretically, since the middle of the last century, especially in the petroleum industry (e.g., Baptist & Sweeney, 1954; Mungan, 1968; Gabriel & Inamdar, 1983; Khilar & Fogler, 1983; Khilar & Fogler, 1987; Kia et al., 1987; Himes et al., 1989; Mohan et al., 1993; Ochi & Vernoux, 1998; Kwon et al., 2004a; Kwon et al., 2004b; Bedrikovetsky, 2008; Bedrikovetsky et al., 2011; Habibi et al., 2012; Wilson et al., 2014; Civan, 2015; Rosenbrand et al., 2015b). As shown in Figure 1.2, clay particle migration, which causes instantaneous formation permeability damage by blocking the effective pore connections, is well understood. The mechanism of the fluid-clay interaction and its effect on permeability have been established by combining the Derjaguin-Landau-Verwey-Overbeek (DLVO) theory with the fluid's dynamics (Bedrikovetsky et al., 2011; Bedrikovetsky et al., 2012). However, previous studies were done at room temperature without considering temperature effects. What remains

unclear is how elevated temperature affects this process. In geothermal reservoirs, the temperature would be an important factor that affects rock permeability, both thermo-mechanically and thermo-chemically. Limited studies showed that the temperature and fluid salinity/composition have a coupled effect on clay (kaolinite) detachment and migration (Schembre & Kavscek, 2005; Rosenbrand & Kj oller, 2014; Rosenbrand et al., 2015b), and thus, fine particle migration has a greater influence in geothermal reservoirs than in conventional fields (You et al., 2015). In contrast, experimental results are still not conclusive of whether temperature-related kaolinite-type particle migration is applicable in all clay-bearing sediments (Rosenbrand et al., 2015b). For instance, a reservoir sandstone in the North German Basin, a Lower Permian (Upper Rotliegend) sedimentary rock, contains mainly illite as the clay phase. Hence, potential heat storage aquifers in such formations need a better understanding of the thermo-chemical effects on the rock transport properties.

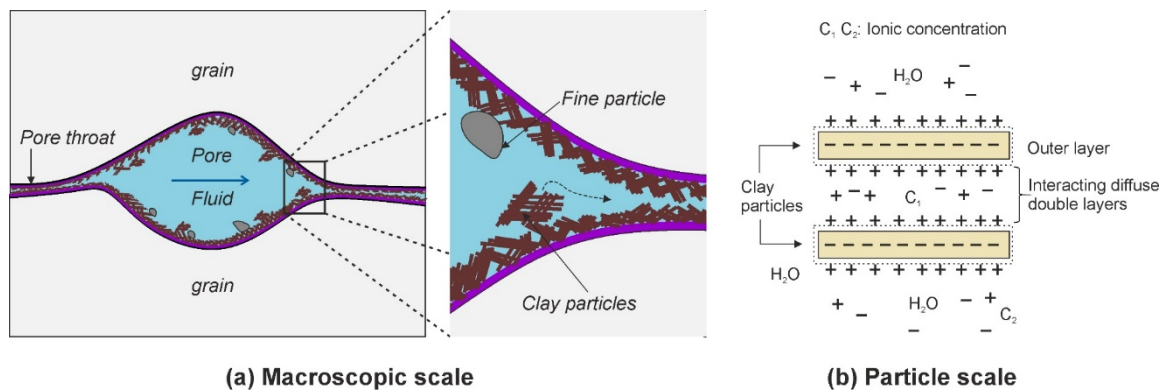


**Figure 1.2** Schematic diagram of (a) a representative pore and pore throat structure with clay mineral coating and (b) charged particles under aqueous conditions, where electrical double layers are established.

The second fundamental question is time-dependent fracture aperture deformation. Unlike consolidated porous media, whose frame structure is relatively stable after a long period of diagenesis. Fractures, particularly hydraulic fracturing generated ones, bear large effective stress on the contact asperities, which prop and maintain apertures open, as shown in Figure 1.3. They undergo not only mechanical deformation but also chemical deformation (e.g., pressure solution and stress corrosion) induced by the enhanced effective stress. Time-dependent fracture closure accompanied by a hydraulic conductivity decline was observed in laboratory experiments (Polak et al., 2003; Yasuhara et al., 2006; Yasuhara et al., 2011; Yasuhara et al., 2015; Hofmann et al., 2016) and after hydraulic stimulations in the field (Bl ocher et al., 2016). Insights into the



dominating process, i.e., pressure solution, have been obtained being a sequential rate-limiting process, that includes dissolution of the solid phase in the contact interface, mass diffusion from the contact interface to the pore fluid, and precipitation onto the pore walls, ultimately controlling overall deformation (Paterson, 1973; Rutter, 1976; Yasuhara et al., 2003). The driving force, i.e., the chemical potential difference between non-hydrostatically and hydrostatically stressed solid phases, that maintains the reaction active is known and theoretically well described from a thermodynamic perspective. However, there is still a significant inconsistency between theory and the experimental observations. The current understanding of pressure solution fails to predict the later stages of pressure solution creep that ultimately tends to retard and cease even under high stress conditions (Niemeijer et al., 2002). Whether there is a threshold energy (i.e., stress) barrier, below which pressure solution would cease, is still under debate (Yasuhara et al., 2003; Gratier et al., 2013; Neretnieks, 2014). In addition, the role of other fluid-rock interactions (e.g., dissolution/precipitation at the free fracture walls, subcritical cracking due to stress corrosion, and surface energy-driven healing of micro-cracks) also need to be further investigated.

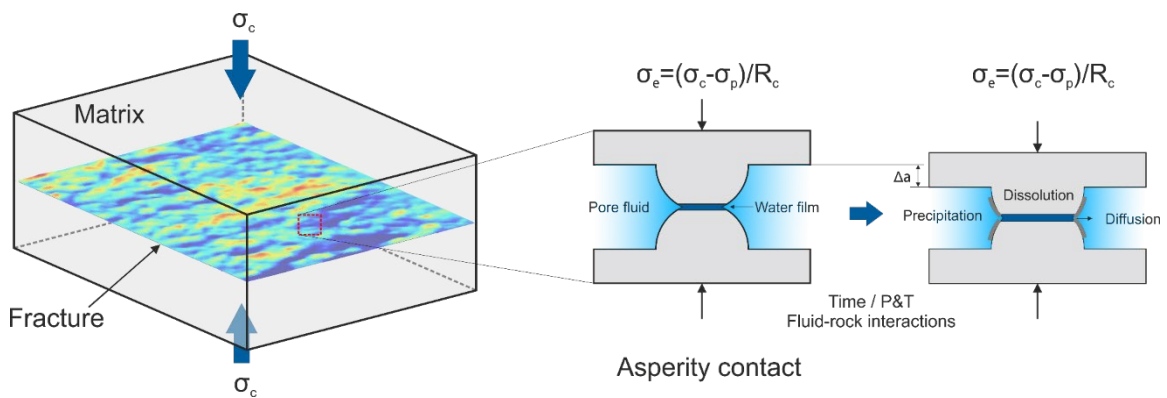


**Figure 1.3** Schematic diagram of asperity contacts in a macroscopic fracture and time-dependent deformation induced by fluid-rock interactions under aqueous fluid conditions.

In order to improve the understanding of the second question, i.e., time-dependent fracture closure under hydrothermal conditions, it is necessary to perform additional hydro-mechanical investigations on particular rocks of interest. This is because both mechanical deformation and fluid-enhanced deformation (e.g., pressure solution) are stress-dependent (Elias & Hajash, 1992; Gratier et al., 1999; Yasuhara et al., 2004; Yasuhara et al., 2006; Hofmann et al., 2016), but the two mechanisms operate at different time scales, i.e., faster for mechanical deformation, slower for chemical deformation. Thus, understanding the short-term variations of fracture aperture upon stress changes is essential to distinguish between the two. Therefore, a third point is to obtain fundamental knowledge of the correlation between the fracture transmissivity and other parameters,

e.g., fracture surface roughness, fracture wall offset, and matrix mechanical properties under varying stress conditions. Overall, the principal questions addressed in this thesis can be summarized as follows:

- 1) How will the permeability of clay-bearing porous rocks evolve with variations of temperature and fluid element concentrations?
- 2) How do specific factors (i.e., surface roughness, fracture wall displacement, rock mechanical properties) affect the stress dependence of rock fracture permeability?
- 3) How do rock fracture aperture and hydraulic conductivity evolve over a longer period of time under hydrothermal conditions?

### 1.2.2 Aims of the present study

This study's motivation is to gain insights into the permeability variations of clay-bearing porous rocks as well as fractured dense rocks induced by fluid-rock interactions under hydrothermal conditions. Flow-through experiments were conducted on rock cores under various conditions in the laboratory. A lower Permian (Upper Rotliegend) sedimentary rock, quarried from an outcrop near Flechtingen, Germany, was selected. It is an analogue rock for a geothermal reservoir formation near Groß Schönebeck, 50 km north of Berlin within the North German Basin, where a geothermal research platform has been established with two (injection and production) boreholes down to ~4 km (Milsch et al., 2008a). Flechtinger sandstone has a complex composition that comprises of quartz, K-feldspar, albite, calcite, hematite, and illite (Schepers & Milsch, 2013). In addition, a pure quartz sandstone of Oligocene age quarried from the Ile de France region at Fontainebleau near Paris, France, was used for comparison. Fontainebleau sandstone is an almost monomineralic sandstone (>99.5 wt% quartz), which is a reference material to simplify any effects of the interaction between different minerals to better reveal specific mechanisms of fluid-rock interactions.

Both rocks have received intensive investigations previously, and their geology, petrophysics, and mechanical properties are well known (Fischer et al., 2012; Hassanzadegan et al., 2012; Hassanzadegan et al., 2013; Schepers & Milsch, 2013; Saadi et al., 2017). Figure 1.4 shows the scope of this study, where Flechtinger sandstones with a permeability on the order of mD were used to study porous flow and both rocks with permeability on the order of  $\mu$ D were used for the study of fracture flow. Macroscopic fractures were artificially generated in the low-permeable rock samples.

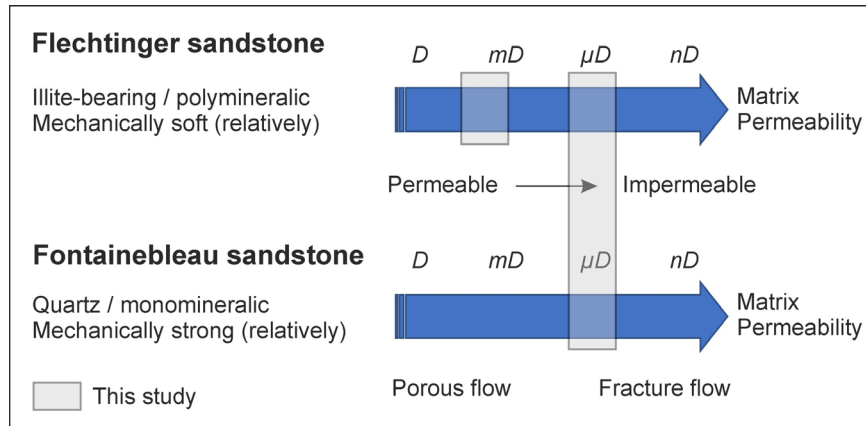


**Figure 1.4** Schematic of the scope of this study.

With the specific focus on the aforementioned sedimentary rocks and in the framework of geothermal energy utilization, the aims of this study can be specified as follows:

- 1) To determine the effects of temperature and fluid salinity variations on permeability decline of illite-bearing sandstones (Flechtinger sandstone) and to reveal whether temperature and fluid salinity play a coupled role in the changes of transport properties.
- 2) To compare the hydro-mechanical properties of fractures in dense sedimentary rocks with contrasting mechanical properties (Flechtinger and Fontainebleau sandstones) and to reveal the effects of fracture surface roughness and fracture wall offset.
- 3) To investigate the mechanisms of long-term deformation and permeability evolution of rock fractures due to fluid-rock interactions under hydrothermal conditions.

Overall, this study aims to strengthen the understanding of both an instantaneous damage (i.e., immediate responses to imposed thermal-hydraulic-mechanical-chemical (THMC) conditions) and a progressive-and/or cumulative decay (i.e., time-dependence) of rock permeability. Insights into the mechanisms governing the permeability decline may improve our knowledge for a better reservoir utilization and the minimization of operational risks.

### 1.3 Thesis organization

This thesis is publications-based and comprises four key manuscripts, which concern the above-mentioned scientific questions (Section 1.2.1). The four manuscripts, as listed in the Declaration above are separately and consecutively presented in the following chapters 2 – 5. Permeability of

porous rocks and rock fractures is the key parameter that is investigated in all four experimental studies.

Chapter 2 provides the study of clay-bearing porous media subjected to temperature and fluid salinity changes. Three long-term flow-through experiments with Flechtinger sandstone samples were performed under conditions of temperature cycling between room temperature and up to 145 °C and fluid salinities (i.e., NaCl solutions) between 0 and 2.0 mol/l. It will be experimentally evidenced under which conditions illite particles will start to migrate, causing permeability changes. It will also be revealed how temperature and fluid salinity essentially influence the permeability of this anisotropic illite-bearing type of sandstone. This chapter corresponds to question 1.

Chapter 3 presents hydro-mechanical investigations on self-propping rock fractures with contrasting mechanical properties (i.e., Flechtinger and Fontainebleau sandstones) under hydrostatic stress conditions. Eight flow-through experiments with aligned tensile fractures, mismatched tensile fractures, and saw-cut fractures were carried out, accompanied by quantification of fracture surface topographies and fracture aperture configurations. The factors, e.g., fracture surface roughness, fracture wall offset, and mechanical matrix properties that may govern the fracture transport properties under stressed conditions, have received particular attention. This chapter aims to answer question 2, which is also a prerequisite for designing the subsequent long-term flow-through experiments on rock fractures to observe any chemically-induced deformation of the fractures.

Chapter 4 describes a long-term flow-through experiment (~140 days) with a fractured Fontainebleau sandstone sample with intermittent flow. The fracture evolution correlated to mechanical effects and fluid-rock interactions was systematically investigated by measuring hydraulic aperture and fluid element concentrations. It is illustrated that pressure solution remains active during fracture deformation but is impacted by the cumulatively evolving pore fluid salinity due to solid phase dissolution and the predominant stagnant flow.

Chapter 5 presents a similar experiment to the one in chapter 4, but with continuous flow for about 120 days. This chapter mainly focuses on the effects of effective stress and fluid Si concentrations on the time-dependent fracture closure behavior. Here, particular emphasis is placed on the evolution of the grain contact (asperity) structure and the slowdown mechanisms of the fracture closure process. Finally, the general conclusions of the thesis are provided in chapter 6, with its implications as well as suggestions for further work.

# Chapter 2

## Permeability variations of illite-bearing sandstone

Temperature changes and variations in pore fluid salinity may negatively affect the permeability of clay-bearing sandstones with implications for natural fluid flow and geotechnical applications alike. These factors are investigated for Flechtinger sandstone dominated by illite as the clay phase. Systematic long-term flow-through experiments were conducted and complemented with comprehensive microstructural investigations and the application of Derjaguin-Landau-Verwey-Overbeek (DLVO) theory to explain the observed permeability changes mechanistically. Initially, sample permeability was not affected by low pore fluid salinity, indicating strong attraction of the illite particles to the pore walls as supported by electron microprobe analysis (EMPA). Increasing temperature up to 145 °C resulted in an irreversible permeability decrease by 1.5 orders of magnitude regardless of the pore fluid composition (i.e., deionized water and 2 M NaCl solution). Subsequently, diluting the high salinity pore fluid below 0.5 M yielded an additional permeability decline by 1.5 orders of magnitude, both at 145 °C and after cooling to room temperature. By applying scanning electron microscopy (SEM) and mercury intrusion porosimetry (MIP), thermo-mechanical pore throat closure and illite particle migration were identified as independently operating mechanisms responsible for observed permeability changes during heating and dilution, respectively. These observations indicate that the permeability of illite-bearing sandstones will be impaired by heating and exposure to low salinity pore fluids. In addition, chemically induced permeability variations proved to be path-dependent with respect to the applied succession of fluid salinity changes.

## **2.1 Introduction**

When the thermal and/or chemical equilibrium in geological formations is disturbed by variations in environmental conditions, permeability changes may occur. Understanding the mechanistic origin of these changes in geological porous media is crucial to reconstructions and predictions of natural fluid flow within the Earth's crust, as well as hydraulic properties in geotechnical applications, hydrocarbon (petroleum and gas) exploitation, CO<sub>2</sub> sequestration, nuclear waste disposal, and geothermal reservoir utilization (e.g., Juanes et al., 2006; Sundberg et al., 2009; Huenges, 2010). As an example, seasonal heat storage in geothermal aquifers and exploitation of geothermal reservoirs affect the temperature gradient within the formation. Fluid composition may also significantly change in the course of producing and/or injecting fluids from/into a reservoir.

Thermally-induced permeability variations were previously investigated in various sedimentary rocks. Contrary to intuition, it is commonly observed that a thermal expansion of the solid matrix leads to a pore volume decrease and, consequently, a permeability reduction in intact rocks (Casse & Ramey, 1979; Somerton, 1980; Somerton et al., 1981; Somerton, 1992; Gräf et al., 2013), given that the microstructure of a polycrystalline rock is heterogeneous in nature. In contrast, the anisotropic thermal expansion might result in thermal cracks (Wong & Brace, 1979), which may enhance permeability. A number of experimental studies performed on Berea, Vosges, Upper Coal, and Fontainebleau sandstones indicate that increasing temperature causes a permeability decrease that in most cases is fully or at least partially recovered after cooling (e.g., McKay & Brigham, 1984; Jing, 1990; Rosenbrand et al., 2015b; Sun et al., 2016). In some cases, recovered permeability can be slightly higher than the initial one (Baudracco & Aoubouazza, 1995). In contrast, the permeability of some low-permeable sandstones was observed to be independent of temperature (Potter et al., 1980; Wei et al., 1986; Gobran et al., 1987). The permeability of Berea sandstone to oil increased slightly with temperature in contrast to its permeability to water, which decreases, and to gas, which is independent of temperature (Casse & Ramey, 1979).

Chemically-induced permeability changes in clay-bearing sandstones related to low-salinity fluids are well-known (e.g., Mungan, 1968; Khilar & Fogler, 1984; Sharma et al., 1985; Kia et al., 1987; Azari & Leimkuhler, 1990; Omar, 1990; Mohan et al., 1993; Rahman et al., 1995; Mohan & Fogler, 1997; Yu et al., 2018). Generally, permeability is not reduced unless the salinity is lower than a critical salt concentration (CSC). In this case, the release and dispersion of clay aggregates are triggered, clogging pore throats. The CSC depends strongly on the cation type within the aqueous solution. K<sup>+</sup>-saturated clay-bearing sandstones show a significantly lower CSC as compared to that of Na<sup>+</sup>-saturated sandstones (e.g., Azari & Leimkuhler, 1990). Bivalent cations

like  $\text{Ca}^{2+}$  and  $\text{Mg}^{2+}$  stabilize permeability down to very low salt concentrations (Gray, 1966; Mungan, 1968; Khilar & Fogler, 1984; Mohan et al., 1993). Derjaguin-Landau-Verwey-Overbeek (DLVO) theory (Deraguin & Landau, 1941; Verwey, 1947, **Appendix A**) is often applied to account for clay particle release (e.g., Bhattacharjee et al., 1998; Tchistiakov, 2000), but other types of theoretical models, incorporating hydrodynamic interactions, were also derived in this regard (e.g., Bedrikovetsky et al., 2011; Bedrikovetsky et al., 2012; Russell et al., 2018). Overall, clay particle release will occur when hydrodynamic forces and physico-chemical repulsion dominate over any process yielding attraction of the particles towards the pore walls (e.g., Tchistiakov, 2000).

Whether or not a clay-bearing sandstone shows permeability variations upon changes in thermo-chemical conditions is strongly dependent on clay type (Wilson et al., 2014). In previous theoretical and experimental studies, sandstones containing predominantly kaolinite received particular attention in this regard (e.g., Khilar & Fogler, 1983; Schembre & Kovscek, 2005; Musharova et al., 2012; Rosenbrand et al., 2015b; You et al., 2016). Here, for experiments, Berea sandstone has become a reference material. In contrast, experimental investigations on sandstones containing illite as the dominant clay phase are scarce in this context. This particularly concerns studies that were conducted at multiple temperatures and in combination with salinity changes.

In this study, we conducted comprehensive long-term experiments to systematically investigate changes in rock permeability upon thermo-chemical forcing. Flow-through experiments on illite-bearing sandstone samples were complemented with extensive comparative microstructural investigations to explain the observations mechanistically. In Section 2.2, details of the experimental and analytical methodologies are given. Section 2.3 reports the permeability and microstructural results which are integrated and discussed in Section 2.4.

## 2.2 Experimental and analytical methodologies

### 2.2.1 Sample material

Flechtinger sandstone, a Lower Permian (Upper Rotliegend) sedimentary rock outcropping and commercially mined at the Sventesius quarry near Flechtingen, Germany, was selected for the experiments. Table 2.1 lists the mineralogical composition of the material measured by X-ray powder diffraction (XRD), indicating that illite is the dominant clay phase in this rock, having a content of approximately 10 % by weight. Other clay types, e.g., mixed-layer clays, were only found in trace amounts.

Four cylindrical cores were drilled from a larger block. The sample material is homogenous in macroscopic appearance but shows bedding as a result of sedimentation. All samples were cored perpendicular to the bedding to reduce any effect of texture and anisotropy on the flow-through experiments. Subsequently, samples were prepared with polished and plane-parallel end faces having a diameter of 30 mm and a length of 40 mm. The four samples were labeled S2, FS1, FS3, and FS4, respectively. Sample S2 was later used as the reference (starting) material to compare microstructural changes that had occurred during the flow-through experiments conducted with samples FS1, FS3, and FS4.

**Table 2.1** Mineral composition of Flechtinger sandstone from X-ray powder diffraction.

Minerals	Content (wt%)
Quartz	60.6
Calcite	3.0
K-feldspar	12.8
Albite	13.3
Illite	9.9
Hematite	0.4

Samples FS1, FS3, and FS4 were vacuum-dried in an oven at 60 °C for 24 hours. They were then set under vacuum in a desiccator chamber for 10 hours and saturated with deionized water for another 24 hours. Dry mass and saturated mass were measured to calculate the initial (connected) porosities yielding 9.2 % for sample S2, 9.0 % for FS1, 9.7 % for FS3, and 10.9 % for FS4, respectively. After the experiments, the samples were vacuum-dried again in order to detect any potential dry mass loss.

### **2.2.2 Flow-through apparatus and sample assembly**

All experiments were performed with two flow-through apparatuses with details described in Milsch et al. (2008b). Wetted parts in one of the devices are made of Hastelloy C-276 for experiments with saline fluids. Oil-medium-based confining pressure is generated with one ISCO 65D syringe pump. The pore fluid system consists of two ISCO 260D syringe pumps, one upstream and one downstream, to apply pore pressure and to realize flow. The flow rate can be as low as 0.001 ml/min.



Heating of the oil inside the pressure vessel is performed with a hollow-cylindrical resistance heater capable of 200 °C. Two Pt100-type Resistance Temperature Detectors (RTD) within the pressure vessel are closely attached to the rock sample to monitor the temperature. All pumps and their controllers are connected to a computer program that permits data acquisition.

The saturated sample is jacketed with a Fluorinated Ethylene Propylene (FEP) heat shrink tubing and is then mounted in the vessel. Afterwards, the two-sample ends are connected to the upstream and downstream pumps, respectively. Generally, the flow direction is from the bottom to the top side of the sample but can be reversed for return permeability measurements. The upstream capillary forms a spiral around the sample within the oil bath of the pressure vessel, permitting the injecting fluid to heat up before entering the sample.

### 2.2.3 Flow-through experiments

Intermittent flow-through experiments were carried out at a constant temperature and pressure conditions. Permeability  $k$  was measured applying steady-state flow and was calculated using Darcy's law (Darcy, 1856; Brown, 2002) directly.  $Q$  is the volumetric flow rate through the sample,  $A$  is the cross-sectional area,  $\Delta p$  is the differential pressure over the sample length  $L$ , and  $\mu$  the dynamic fluid viscosity is adjusted depending on the fluid type, salinity, temperature, and pore pressure,

$$k = \frac{Q\mu L}{\Delta p A} \quad (2.1)$$

Due to the temperature difference in the pump cylinders and the pressure vessel, the flow rate  $Q$  through the sample was corrected in accordance with the pump flow rate  $Q_p$  and the fluid densities  $\rho_p$  at room temperature and  $\rho_v$  at vessel temperature, respectively,

$$Q = \frac{Q_p \rho_p}{\rho_v} \quad (2.2)$$

Pore pressure was maintained constant at 1 MPa and thus was high enough to prevent fluid boiling at the maximum experimental temperature, i.e., 145 °C (Guildner et al., 1976). During the permeability measurements, the downstream pump was operated in constant pressure mode at 1 MPa, and the upstream pump was maintained in constant flow rate mode. In dependence on sample permeability, the flow rate was varied to keep the pressure difference between the sample ends below 0.5 MPa to minimize the distortion of the effective stress state. As was observed, a permeability decrease could occur rapidly. Hence, the flow rate had to be adjusted timely to ensure

that the upstream pressure would be limited to 1.5 MPa at steady state. Confining pressure was held constant at 10 MPa throughout the experiments.

Temperature was increased and decreased stepwise by intervals of approximately 20 °C between room temperature and 145 °C. An (active) temperature increase by 20 °C took about 4 hours, and (passive) cooling by 20 °C required up to 24 hours to ensure that the respective target temperature was homogeneously distributed throughout the sample.

In addition to deionized water, three different NaCl solutions were used as the pore fluid with concentrations of 0.5, 1.0, and 2.0 M, respectively, exchanging pore fluid. Densities and dynamic viscosities of the fluids were adjusted for the respective temperatures and pressures (Joseph et al., 1981; Cooper, 2008). At the initiation of experiments and during initial sample saturation (Section 2.2.1), the pump cylinders and capillaries were filled with deionized water. Fluid exchanges were performed by emptying the upstream pump cylinder and refilling it with the next fluid of choice. The volume of the upstream capillary connected to the sample is approximately 3 ml. Therefore, care had to be taken that the total fluid volume that flowed through the sample was always large enough to ensure that the previous pore fluid was exchanged completely by the new fluid. For all experiments, the final fluid that was flushed through a sample, again, was deionized water to ensure that no salt precipitation would occur upon drying the samples in preparation for the microstructural analyses. The total duration of the experiments with samples FS1, FS3, and FS4 was 54 d, 44 d, and 40 d, respectively.

It should be noted at this point that for none of the experiments, there was an indication of oil intrusion from the confining pressure into the pore fluid system. Any related experimental artifact yielding (apparent) changes in permeability, therefore, can be excluded.

Table 2.2 shows the order of the permeating fluids used, the temperature steps, as well as the flow rate range of each experiment. Sample FS4 underwent further experimental steps after those shown in Table 2.2, which are beyond the scope of the present study. This likely overprinted the microstructure of this sample. For this reason, our evaluations of microstructural changes associated with experimental measurements are made for samples FS1 and FS3 as outlined in Section 2.2.4.

Overall, the purpose of the experimental strategy was to investigate (A) the effect of a temperature increase for isochemical fluid conditions in terms of permeability changes and their potential reversibility as a result of a temperature decrease and return flow, respectively (sample FS1), (B) the potential hydrodynamic mobilization of fines (sample FS3), and (C) the effect of a decrease in NaCl pore fluid salinity at two different temperatures (samples FS3 and FS4).

**Table 2.2** Summary of experimental conditions.

Sample	Permeating fluids	Temperature steps (°C)	Flow rate range (ml/min)
FS1	H <sub>2</sub> O	25↔40↔60↔80↔ 100↔120↔141	0.05 - 2.00
FS3	H <sub>2</sub> O→2M Na→1M Na→0.5M Na→H <sub>2</sub> O	25↔40↔60↔80↔ 100↔120↔145	0.02 - 2.00
FS4	H <sub>2</sub> O→2M Na→1M Na→0.5M Na→H <sub>2</sub> O	27↔40↔60↔81↔ 100↔122↔145	0.005 - 2.00

Notes: H<sub>2</sub>O, 2M Na, 1M Na, and 0.5M Na are deionized water, 2.0 M NaCl, 1.0 M NaCl, and 0.5 M NaCl solutions, respectively. The electrical conductivity of deionized water was approximately 20 μS/cm at 25 °C.

### 2.2.4 Microstructural analyses

Samples S2, FS1, and FS3 were examined to evidence and compare microstructural changes in the course of the flow-through experiments. Figure 2.1 shows the individual parts of the samples as used for the different analyses. For each sample, polished thin sections and saw-cut thick sections, taken parallel and perpendicular to the flow direction, were prepared and carbon-coated. Scanning electron microscopy (SEM) was used for qualitative imaging of illite and pore space microstructure in SE and BSE modes, respectively. Electron microprobe analysis (EMPA) was applied on the thin sections to quantitatively detect element content variations in illite. Two sub-samples along the flow direction were prepared for mercury intrusion porosimetry (MIP) to investigate porosity differences and changes in pore-size distribution. In MIP, the pore diameter  $D$  is related to the capillary pressure  $P_c$  based on the Washburn equation (Washburn, 1921),

$$D = -\frac{4\gamma \cos(\theta)}{P_c} \quad (2.3)$$

where  $\gamma = 0.48$  N/m is the surface tension, and  $\theta = 140^\circ$  is the contact angle of mercury. The fraction of sample porosity for each pressure step during a measurement is expressed as  $\phi_{\text{Hg},i} = dV_{\text{Hg}}/V_s$ , where  $dV_{\text{Hg}}$  is the incremental volume of the injected mercury and  $V_s$  is the sample bulk volume. Finally, the cumulative (total connected) porosity is calculated as,

$$\phi_{\text{MIP}} = \sum \phi_{\text{Hg},i} \quad (2.4)$$

The resulting porosity of sample S2 was 9.4 %, which is in reasonable agreement with the value obtained from saturation and weighing (Section 2.2.1).

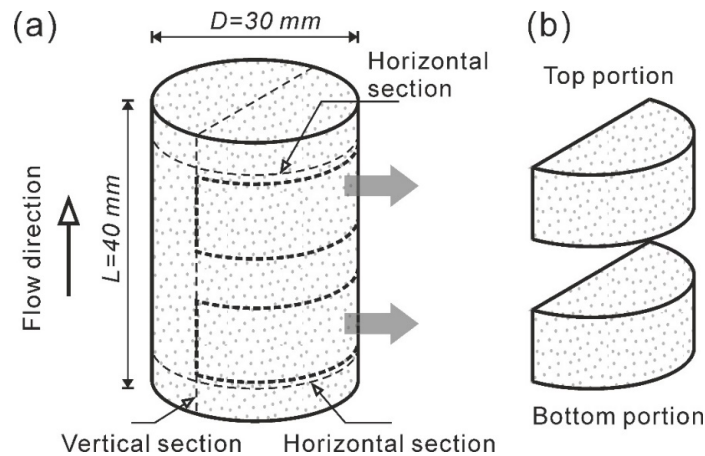


**Figure 2.1** Schematic sketch of sample preparation for the different microstructural analyses. **(a)** Cylindrical core sample and locations of thin and thick sections prepared for scanning electron microscopy (SEM) and electron microprobe analysis (EMPA); **(b)** top and bottom portions of the samples used for mercury intrusion porosimetry (MIP).

### 2.2.5 Initial rock microstructure

Figure 2.2 shows micrographs of the starting material (sample S2) at different magnifications. Figures 2.2a and b were taken on the polished thin sections in BSE mode. Pores and pore throats, as shown in Figure 2.2a, represent the typical flow paths. Pores and pore throats are partially filled with illite and, occasionally, some fines. The widths of pore throats are significantly smaller than those of the pores. Figure 2.2b shows that illite can occur as aggregates with both open and compact appearance. Within the pores and pore throats, illite develops three structural types: tangential illite, pore-lining illite, and pore-filling illite, respectively (Wilson et al., 2014; Desbois et al., 2016). The compact tangential illite has a variable thickness and is directly attached to the grain walls. The pore-lining illite is either connected to the tangential illite or directly to the grain walls. The pore-filling illite, with both fibrous and platy morphologies, appears to be mostly unconnected but can link to other illite types or the grain walls. Overall, these three types of illite are not uniformly distributed within the pores and pore throats. Moreover, they play a dominant role in defining the rock's transport properties.

Figures 2.2c-f, taken on saw-cut thick sections in SE mode, display images of the different illite types within the pore space. The pore-lining illite shown in Figure 2.2c is located in a pore throat and stretches towards the pore space while its other end is tightly bound to tangential illite. Figure 2.2d presents an example of pore-filling illite in a pore throat. In this case, the platy illite crystals form aggregates and partially clog the pore throat. Flocculent fibrous illite, as shown in Figure 2.2e, is found occasionally within the pore space and is classified here as pore-lining illite.

All grain walls were found to be coated with tangential and/or pore-lining illite (Figure 2.2f), and both illite types are authigenic (Wilkinson & Haszeldine, 2002; Wilson et al., 2014; Desbois et al., 2016).

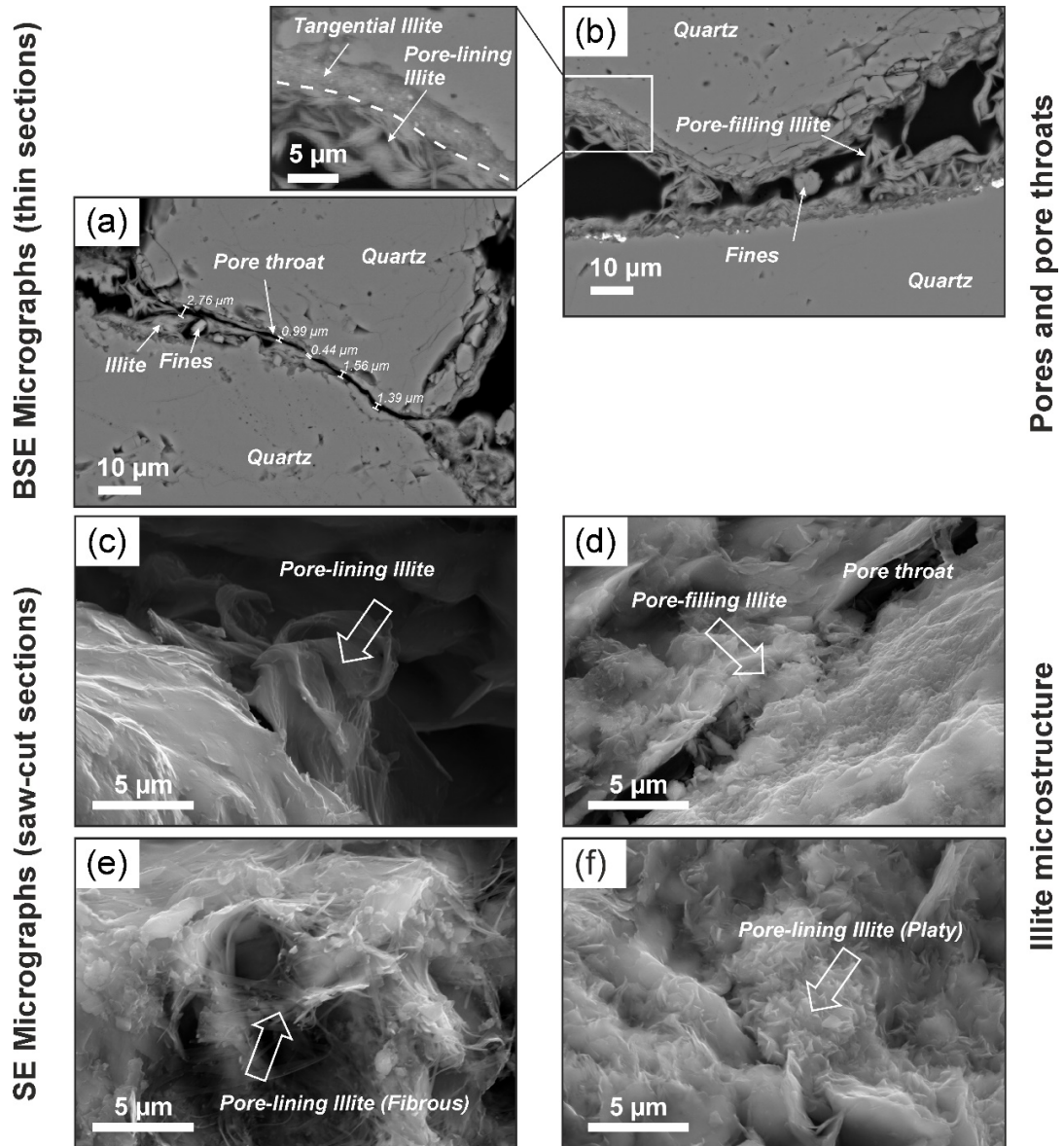


**Figure 2.2** Scanning electron micrographs in BSE and SE modes of the starting material (sample S2) at different magnifications. (a) Representative microstructure of pores and pore throats in Flechtinger sandstone; (b) structural types of illite found in the pore space (tangential, pore-lining and pore-filling); (c) pore-lining illite bound to tangential illite; (d) platy pore-filling illite within a pore throat; (e) fibrous pore-lining illite within a pore; (f) tangential and platy pore-lining illite covering the pore walls.

## 2.3 Results

### 2.3.1 Flow-through experiments and permeability

Figure 2.3 displays the permeability evolution of each sample (FS1 in (a), FS3 in (b), and FS4 in (c)) as a function of temperature during the total progress of each experiment. All individual permeability values (dots) and details of other experimental parameters are provided in **Appendix B**. To recall, all experiments started with deionized water as the pore fluid. In detail:

For sample FS1 (Figure 2.3a), when heating the sample from 25 °C to 80 °C, permeability decreased by approximately 1.5 orders of magnitude from 5.0 to 0.2 mD ( $1 \text{ mD} = 0.987 \times 10^{-15} \text{ m}^2$ ) with no further significant changes up to 141 °C. Subsequent cooling to 41 °C did not yield permeability recovery. A subsequent (second) heating-cooling cycle had a negligible effect on permeability. Finally, reversing the flow direction did not affect permeability which thus did not recover as a result of return flow. In summary, once temperature increases beyond approximately 80 °C, the permeability of this rock decreases significantly and irreversibly when deionized water is used as the pore fluid with (almost) no more changes observed afterwards.

For sample FS3 (Figure 2.3b), to investigate a possible effect of fine particle migration on permeability due to hydrodynamic interactions and before any temperature or salinity changes, more than 1100 ml of deionized water was injected into the sample at a flow rate of 2.0 or 1.0 ml/min. Permeability first decreased from 25.2 to 17.0 mD and then remained constant until the end of this experimental stage. Subsequently, the pore fluid was exchanged by a 2.0 M NaCl solution, after which permeability recovered to 19.0 mD. The following temperature increase from 25 °C to 145 °C caused permeability to decrease log-linearly, again by approximately 1.5 orders of magnitude, from 19.0 to 0.6 mD. At 145 °C, pore fluid salinity was reduced stepwise to 1.0 M NaCl and 0.5 M NaCl with only a marginal effect on permeability (0.6 mD to 0.5 mD). In contrast, when deionized water was reintroduced, permeability decreased significantly from 0.5 to 0.02 mD. Cooling to room temperature only yielded a negligible permeability increase from 0.02 to 0.04 mD. Total permeability reduction thus spanned over three orders of magnitude. In summary, hydrodynamically induced fine particle migration in this rock is negligible for the present flow rate range and as long as no thermo-chemical alteration of the illite and pore space microstructure has been induced. Permeability is reduced at temperature increases also for high NaCl salinity pore fluids. A further decrease in permeability is observed when deionized water is reintroduced at a high temperature. The permeability is reduced after a successive temperature increase-salinity decrease sequence is (nearly) irreversible when the temperature is decreased again.

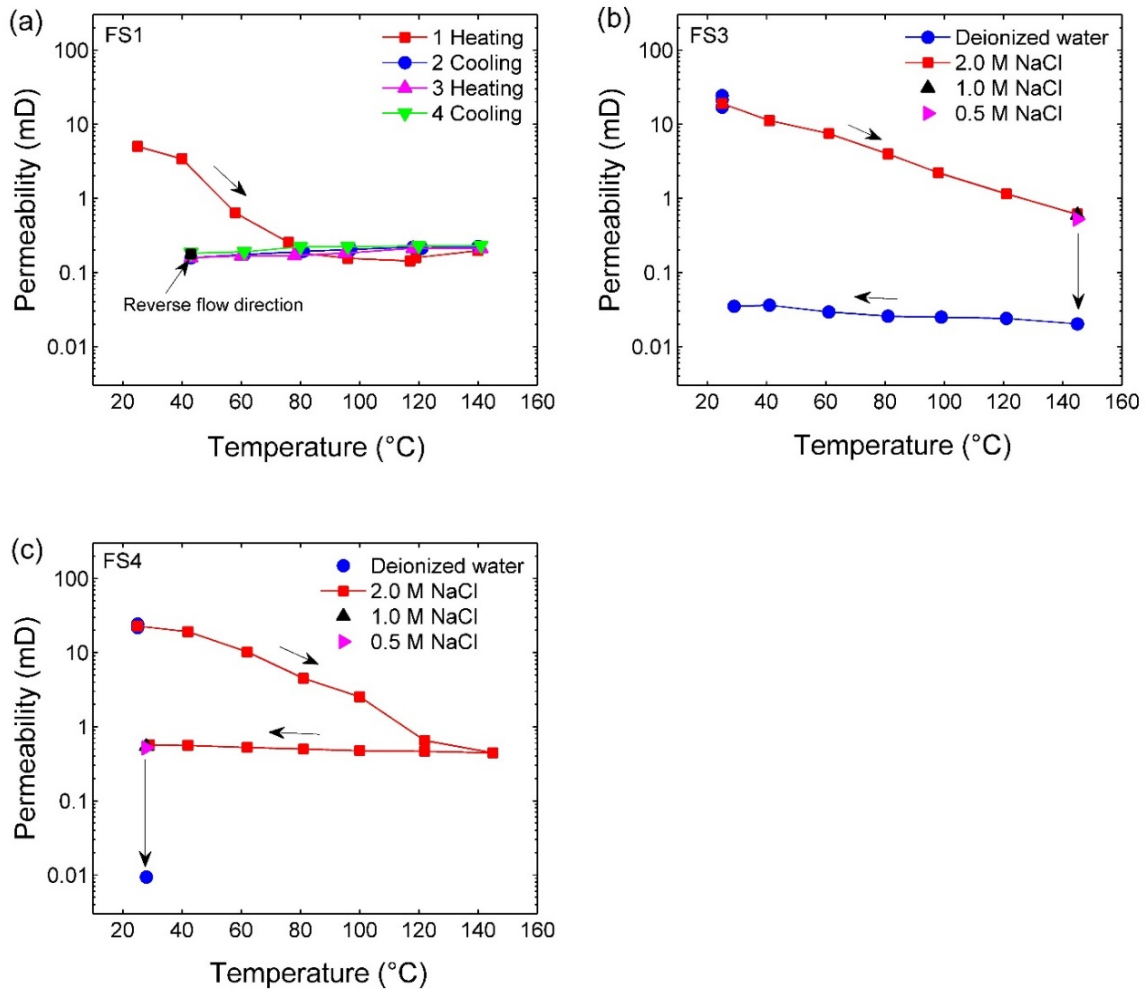


**Figure 2.3** Permeability as a function of temperature for samples FS1 (a), FS3 (b), and FS4 (c). Each dot is a steady-state permeability measurement at some constant temperature level and at constant confining and pore pressures, respectively. Systematic successions of temperature and salinity changes were implemented with implications for permeability summarized in this figure and detailed in Section 2.3.1.

Sample FS4 (Figure 2.3c) experienced a similar series of steps as imposed on sample FS3. The key difference is that temperature was decreased before the salinity decrease, which then was performed at room temperature. Firstly, after a flow of 32 ml of deionized water, permeability had decreased slightly from 24.3 to 21.8 mD. The pore fluid was then replaced by a 2.0 M NaCl solution, after which permeability had slightly recovered to 22.8 mD. Subsequent heating from 27 °C to 145 °C led to a permeability decrease from 22.8 to 0.5 mD, after which cooling to 28 °C, again, yielded virtually no permeability recovery. At 28 °C, salinity was decreased by successive fluid exchanges (1.0 M NaCl, 0.5 M NaCl, and deionized water) with the same effects as those observed for sample FS3. The final permeability of sample FS4 was 0.01 mD. In summary, the observations

reported before for sample FS3 are reproducible for identical procedural steps and possess excellent quantitative comparability. The previously observed permeability decreases as the temperature increases for high NaCl salinity pore fluid conditions are also irreversible when the temperature is directly decreased. Finally, a severe and further permeability reduction is observed upon a salinity decrease at low temperatures.

### 2.3.2 Microstructural evolution

The SEM micrographs in Figure 2.4 of both the starting material (sample S2) and the samples after the flow-through experiments (FS1 and FS3) show changes in pore throat and illite microstructures. For imaging of the pore throats (Figures 2.4a-c), the micrographs were taken in BSE mode on the polished thin sections. The walls of pore throats, like the one shown in Figure 2.4a (sample S2), are completely lined with illite, significantly reducing the original grain-to-grain distance and resulting in narrow but open flow channels. In contrast, the pore throat in Figure 2.4b (sample FS1) is virtually closed after the applied heating and cooling cycles. The same is true for the pore throat in Figure 2.4c (sample FS3) after the succession of temperature cycling and fluid exchanges. In comparison to sample FS1, the appearance of the pore throat filling in sample FS3 suggests that the illite particles not only were compacted but also experienced some amount of displacement, yielding illite particle pile-ups. Nominally closed pore throats were also found in sample S2. However, they appear at a significantly larger number in samples FS1 and FS3.

For imaging of the illite microstructure (Figures 2.4d-f), the micrographs were taken in SE mode on the saw-cut thick sections. Overall, at the  $\mu\text{m}$ -scale, morphological changes were hard to detect, and possibilities of definite statements are very limited. However, the wider surface of the platy pore-lining illite aggregates in the starting material (sample S2; Figure 2.4d) appears slightly smoother than observed in Figure 2.4e (sample FS1) or Figure 2.4f (sample FS3). Here, the images suggest some small degree of surface roughening and clay platelet loosening that might have resulted from heating (sample FS1) and, additionally, from the fluid exchanges (sample FS3).

Figure 2.5 shows the pore-size distribution in samples FS1 (Figure 2.5a) and FS3 (Figure 2.5b) after the flow-through experiments compared to the starting material (sample S2) as obtained from mercury intrusion porosimetry (MIP) and evaluated according to Eqs. 2.3 and 2.4. Weight measurements (Section 2.2.1) indicate that the dry mass loss of the samples associated with fluid flow is very small, in the range of 30 mg (FS1) to 100 mg (FS3). This indicates that nearly all material that could potentially be mobilized (i.e., approximately 6.7 g of illite) is still contained within the respective sample.



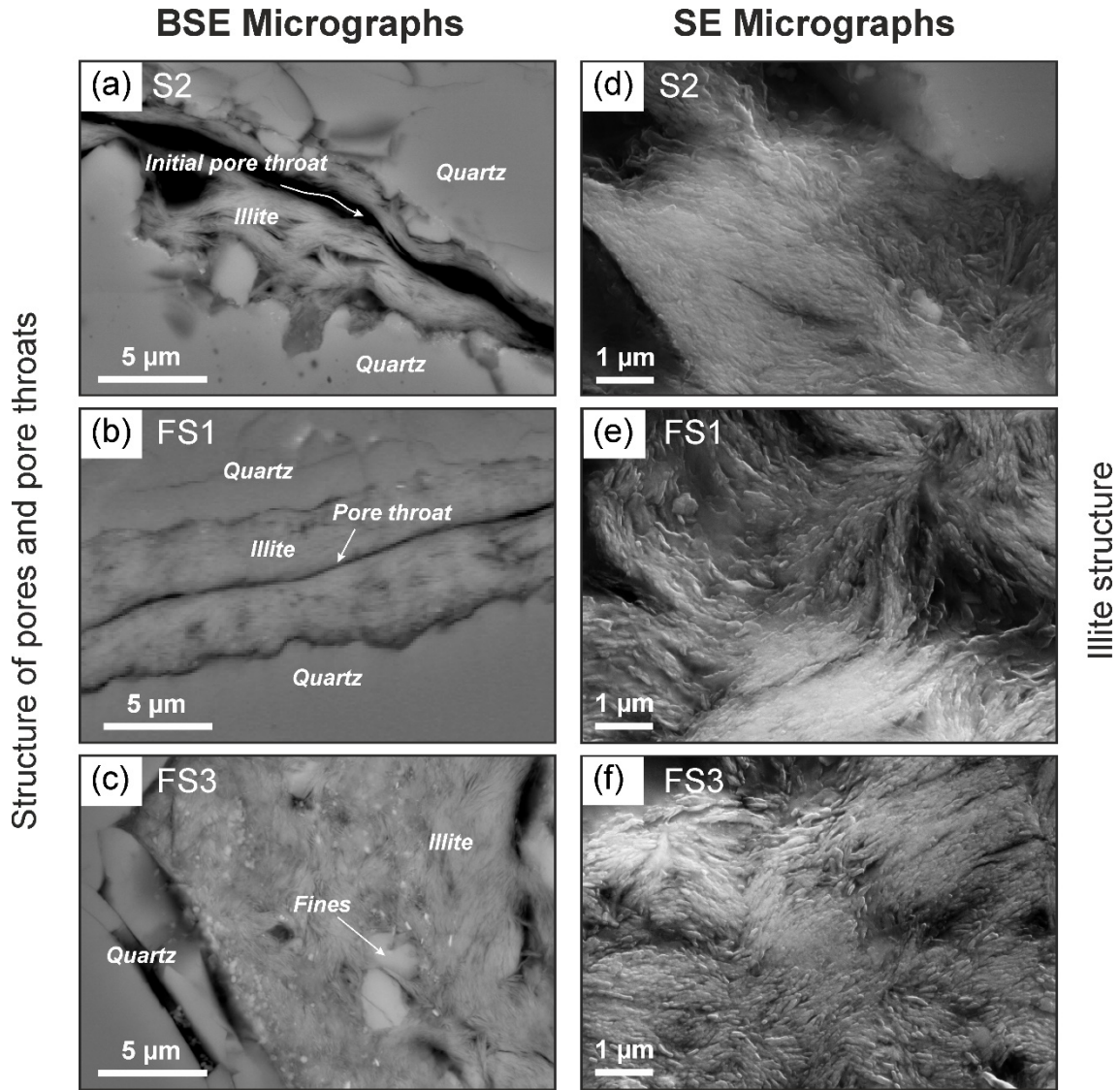


**Figure 2.4** Comparison of the microstructure of the samples before and after the flow-through experiments. Scanning electron microscope (SEM) images of the vertical polished thin and saw-cut thick sections, respectively (Figure 2.1). BSE mode images taken of the thin sections show: (a) open pore throats in the starting material (sample S2); (b) closed pore throat after temperature cycling only (sample FS1); (c) closed pore throat after the temperature cycle and the fluid exchanges (sample FS3). SE mode images taken of the thick sections might indicate changes in illite morphology, comparing images of (d) starting material (sample S2) and flow-through experimental samples (e) FS1 and (f) FS3 (see Section 2.3.2).

For sample FS1 (Figure 2.5a), the cumulative (total connected) porosity curves of the bottom and the top portions (Figure 2.1) are virtually identical, indicating a very similar pore-size distribution after the experiment. However, compared to the starting material (sample S2), the cumulative porosity of both sub-samples decreased slightly in the course of the experiment, i.e., by

approximately 0.4 % porosity. In connection with the evolution of permeability (Section 2.3.1), these observations strongly suggest that (1) the hydraulic properties of the starting material are governed by pores and pore throat sizes of 0.2  $\mu\text{m}$  and below, (2) temperature cycling resulted in partial and irreversible pore throat closure predominantly in this pore-size range, and (3) there was no displacement of solid material from the bottom to the top of the sample as fluid flow.

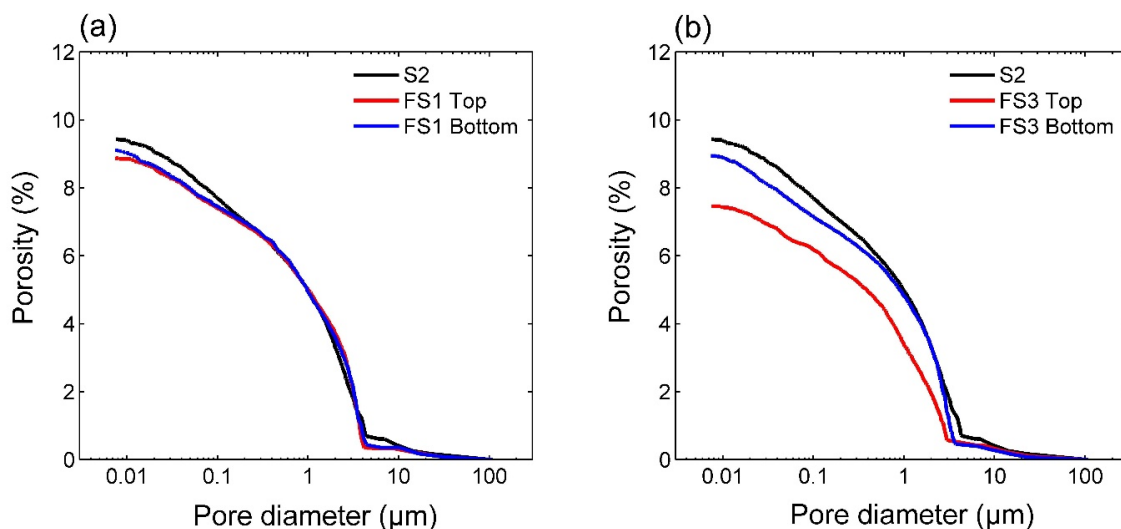


**Figure 2.5** Cumulative porosity as a function of pore diameter measured by mercury intrusion porosimetry (MIP). (a) Sample FS1 compared to the starting material (sample S2) with results for the bottom and top portions (Figure 2.1) indicated in blue and red, respectively. (b) Sample FS3 in comparison to sample S2. Overall, contrasting changes in pore-size distribution are evident that relate to the effects of temperature cycles (FS1) and the additional fluid exchanges (FS3) as outlined in Section 2.3.2.

For sample FS3 (Figure 2.5b), there is a significant mismatch in the pore-size distributions of the top and bottom portions of the sample. The overall decrease in cumulative porosity is large, particularly in the top portion, where porosity is reduced by 1.9 %. The fraction of pores affected most by the microstructural changes has increased to pore sizes of approximately 1  $\mu\text{m}$  in the bottom portion and 3  $\mu\text{m}$  in the top portion of the samples. The additional decrease in sample permeability as a result of the fluid exchanges is mirrored by these structural alterations of the pore space. Moreover, the mismatch in the pore-size distributions of the two sub-samples suggests the displacement of material in the direction of flow that progressively piles up, yielding additional pore throat closure over an extended pore size range.

It should be noted that the use of sample S2 as the starting material reference may yield a small uncertainty in the comparison of total porosities on the order of 0.2 %. This, however, does only

marginally affect the reasoning that a reduction in the contribution of the smaller pore size fractions to total porosity yields the observed permeability changes in FS1 and FS3. This is supported by the fact that both the S2 and FS1 porosity-pore size curves are, otherwise, absolutely identical in their characteristics up to the inflection point at around 4  $\mu\text{m}$  (Figure 2.5a).

Pore-filling illite was further investigated using electron microprobe analysis (EMPA; at 8kV and 1.2 nA with 5  $\mu\text{m}$  probe size) on polished thin sections of samples S2, FS1, and FS3. Element concentrations of Na, K, Si, Al, Ca, and Mg were measured. Fe was not detected. In the following, we focus attention on concentrations of  $\text{Na}^+$ ,  $\text{K}^+$ ,  $\text{Ca}^{2+}$ , and  $\text{Mg}^{2+}$ , given that these are the exchangeable cations of illite. Table 2.3 lists the measured (median) concentrations of the respective oxides within the different samples. For each thin section, measurements were performed at 14 to 17 locations.

**Table 2.3** Median concentrations of Na, K, Ca, and Mg oxides in pore-filling illite before and after the flow-through experiments.

Sample/Section	Na <sub>2</sub> O (wt%)	K <sub>2</sub> O (wt%)	CaO (wt%)	MgO (wt%)	No. of Locations
S2	0.03	7.65	0.28	1.25	16
FS1	0.06	7.91	0.35	0.98	16
FS3_1	0.19	7.24	0.35	1.09	17
FS3_2	0.14	8.12	0.43	1.03	14

Note: The values for S2 and FS1 relate to the respective vertical thin sections (Figure 2.1). The designations FS3\_1 and FS3\_2 denote measurements taken on the vertical and the bottom thin sections of this sample, respectively.

Figure 2.6 presents box plots of Na (a), K (b), Ca (c), and Mg (d) oxide concentrations in pore-filling illite for the different samples (S2, FS1, and FS3), respectively. In all samples,  $\text{K}^+$  is evidently the most abundant exchangeable cation in this illite. Conversion of the median concentrations from wt% to mol/g was then performed by applying  $2\omega/(Mz)$ , where  $\omega$  and  $M$  are the weight percent concentration and molecular weight of the respective oxide, and  $z$  is the valence of the corresponding cation, respectively. This yields that the pore-filling illite within the starting material (sample S2) contains 0.01 mmol/g  $\text{Na}^+$ , 1.62 mmol/g  $\text{K}^+$ , 0.05 mmol/g  $\text{Ca}^{2+}$ , and 0.31 mmol/g  $\text{Mg}^{2+}$ , respectively. It should be noted that  $\text{Mg}^{2+}$ , in addition to the exchangeable sites in the interlayer, can also be located in the octahedral layer (Anderson et al., 2010). Compared to the starting material, the relative changes of  $\text{K}^+$ ,  $\text{Ca}^{2+}$ , and  $\text{Mg}^{2+}$  in both samples FS1 and FS3 are negligible. This is also true for  $\text{Na}^+$  in FS1. In sample FS3, however, there is a substantial increase

in  $\text{Na}^+$  content that corresponds to the long-term exposure of the illite contained in this sample to  $\text{NaCl}$  solutions of high salinity during the experiment. Overall, the EMPA analyses yield for FS3 and yield the maximum  $\text{Na}^+$  content in pore-filling illite after the experiment was 0.11 mmol/g with a median of 0.05 mmol/g. From this result, one can infer that the cation exchange capacity (*CEC*) of this illite is no more than approximately 0.11 mmol/g. Both maximum and median  $\text{Na}^+$  concentrations will later be used in Section 2.4 in connection with Derjaguin-Landau-Verwey-Overbeek (DLVO) theory.

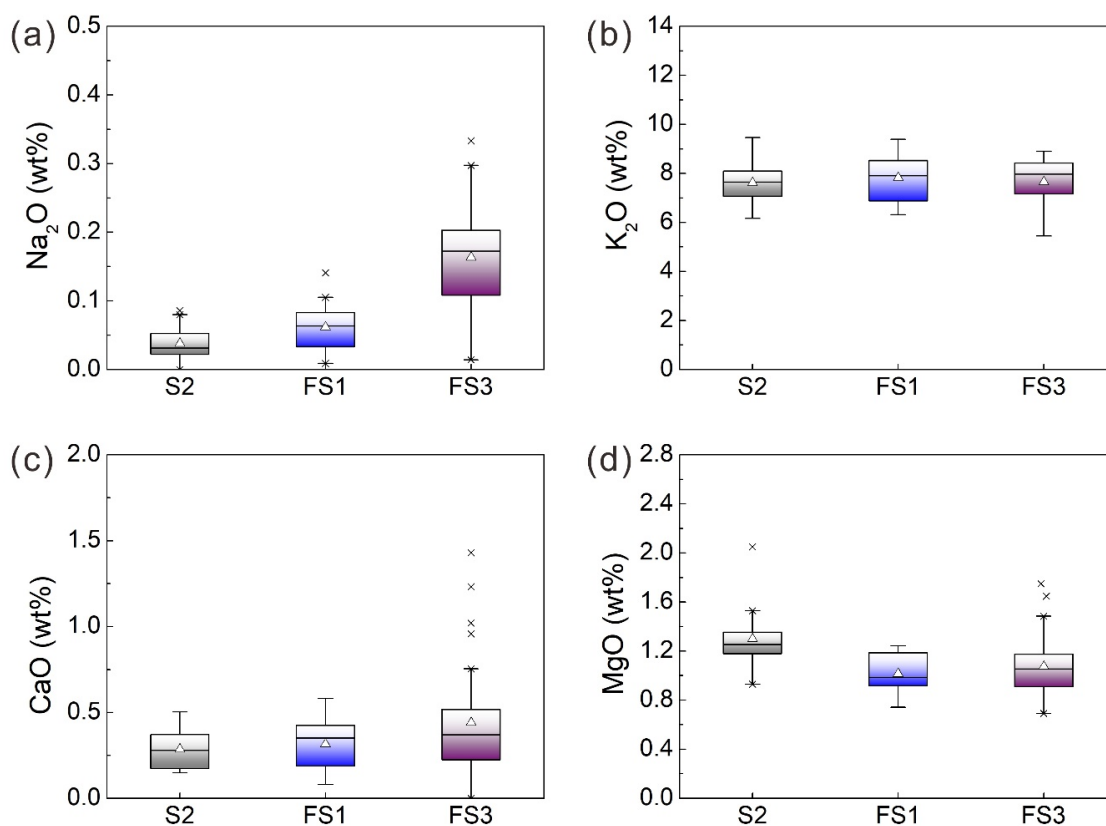


**Figure 2.6** Concentrations of Na (a), K (b), Ca (c), and Mg (d) oxides in pore-filling illite before (sample S2) and after (samples FS1 and FS3) the flow-through experiments as measured by electron microprobe analysis (EMPA) on polished thin sections. The solid line and the open triangle in the respective box indicate the median and mean of each dataset, respectively. Individual symbols (x) above and below the error bars are measured data but statistical outliers. In the box plots, the boxes signify the lower and upper quartiles, Q1 and Q3, of the datasets, respectively. The upper and lower horizontal error bar lines indicate the largest and smallest data values for  $Q3 + 1.5 \text{ IQR}$  and  $Q1 - 1.5 \text{ IQR}$ , respectively, where IQR is the interquartile range equal to  $Q3 - Q1$ . Overall, significant changes in ionic elemental concentration are only evident for  $\text{Na}^+$  in sample FS3, as outlined in Section 2.3.2.

## 2.4 Discussion

Any decrease in permeability implies a decrease in the effective cross-sectional area of the pore space that permits flow. In the present case, this may occur by thermomechanical compaction of the rock, yielding pore throat closure, or unfavorable migration of clay particles within the pore space stimulated hydrodynamically, thermally, or chemically. The key observations of this study that require discussion are:

(1) Initially, all samples were saturated with deionized water, but upon flow, permeability at room temperature remained high and only changed slightly (Section 2.4.1).

(2) Increasing temperature stepwise to 145 °C yielded a progressive and irreversible permeability decrease by 1.5 orders of magnitude in all samples regardless of the pore fluid composition investigated (Section 2.4.2).

(3) Sample permeability decreased further when progressively diluting a previously introduced 2 M NaCl pore fluid below approximately 0.5 M. This observation was made both at room temperature and 145 °C (Section 2.4.3).

### 2.4.1 Hydraulic sample behavior at the start

The application of DLVO theory for deionized water pore fluid conditions to our results suggests that repulsions between illite particles and between illite and the grain walls are strong (Section 2.4.3). The fact that permeability remained high upon first saturation with deionized water implies that the clay fraction in this sandstone, initially, is strongly attached to the pore walls. Therefore, any permeability decrease observed later upon dilution of a saline NaCl pore fluid requires some kind of weakening mechanism by the subsequent fluid exchange that permits particle release upon flow.

Path-dependent permeability changes have been described before (Mohan et al., 1993; Kwon et al., 2004a), indicating that high  $K^+$  contents within the interlayer and the presence of divalent cations like  $Ca^{2+}$  or  $Mg^{2+}$  on the exchangeable sites of the crystal lattice have a stabilizing effect on the clay fraction in the pore space of sandstones (Mungan, 1968). The EMPA results presented in Section 2.3.2 suggest that this is also the case for the illite clay in Flechtinger sandstone, at least initially and at room temperature. Consequently, when sample FS3 was initially flushed at room temperature with a substantial amount of deionized water (Section 2.3.1), permeability only changed slightly. This observation was also made for sample FS4, although the respective fluid

volume was small. This implies that an effect of purely hydrodynamic fines migration on permeability in the pristine rock is negligible at the applied flow rates. This conclusion is supported by the small mass loss measured for both samples FS1 and FS3 as well as the absence of fines migration evidenced by MIP for sample FS1 (Section 2.3.2).

For samples FS3 and FS4, it was observed that an exchange of the preexisting deionized water pore fluid by a 2 M NaCl solution at room temperature resulted in a slight permeability increase (Section 2.3.1). As was shown by Moore et al. (1982) for a swelling type of clay (montmorillonite), salinity-induced changes in electrical double layer (EDL) thickness result in variations of the size of clay particles that are exposed to the pore space and, consequently, of the effective cross-sectional area available for the flow of the free pore fluid. When increasing the salinity of the fluid, the thickness of the EDL decreases, yielding an increase in permeability. Whether this mechanism, in fact, also operates in (non-swelling) illite needs to be investigated further but might yield hints to explain the present observations.

However, for longer time periods and enhanced by elevated temperatures, when deionized water in the pore space is exchanged for the highly concentrated NaCl solution, the partial replacement of the divalent cations of illite grains by  $\text{Na}^+$  may occur, allowing more hydrodynamic dispersion of illite particles (Mungan, 1968; Rahman et al., 1995). Increased  $\text{Na}^+$  content in sample FS3, as measured by EMPA (Section 2.3.2), suggests that this weakening mechanism is important. At this stage, the rock continues to behave in agreement with DLVO theory, as will be shown below in Section 2.4.3.

### 2.4.2 Effects of temperature changes

All samples in this study, FS1, FS3, and FS4, experienced substantial permeability reductions as the temperature was increased from room temperature to 145 °C regardless of the pore fluid composition, i.e., deionized water or 2 M NaCl solution. Furthermore, this permeability damage was not recovered when the temperature was decreased. This irreversible decrease was also not changed by reversing the direction of fluid flow.

The thermal strain of a rock resulting from heating generally contains elastic and inelastic components related to its microstructure and mineral composition (Wong & Brace, 1979; Gräf et al., 2013; Pei et al., 2016). Hence, any thermally induced permeability decline should be partially reversible when decreasing temperature. Evidently, this is in disagreement with the present observations suggesting that the pore throats were closed, at least partially, by compressive stresses resulting from thermal expansion of the rock matrix under confinement (Weinbrandt et al., 1975;

Somerton, 1980; Somerton et al., 1981; McKay & Brigham, 1984). The degree of thermal strain that was attained at 80 °C (FS1) or ultimately at 145 °C (FS3 and FS4) reflects purely inelastic and thus irreversible deformation. Mechanistically this relates to the comparatively low mechanical strength of fine-grained illite (e.g., Cebell & Chilingarian, 1972; Vaidya et al., 1973; Tanaka et al., 1997), the high illite content within the rock (i.e., 10 wt%), the illite microstructure in the pore space, and the fact that illite completely covers the pore walls (Figure 2.2). Overall, this reduces the load-bearing capacity of the rock at the pore scale, yielding some degree of inelastic compaction sufficient to reduce the effective cross-sectional area of the pore throats that, in combination, define the hydraulic properties of this sandstone (Section 2.3.2; Figure 2.5).

Mineral dissolution reactions may also result in permanent changes of permeability (e.g., Yasuhara et al., 2015), particularly at elevated temperatures, since the dissolution rates will increase when heating a fluid-rock system that is in chemical disequilibrium. In contrast, cooling would potentially lead to oversaturation of some species in the pore fluid and thus mineral precipitation, consequently affecting permeability as well. However, in this study, after the temperature was increased to the next level and had stabilized after a few hours (Section 2.2.3), permeability was immediately measured and always showed to be less or equal to its value at the former (lower) temperature (Figure 2.3). This implies that the change (if any) likely had occurred concurrently to heating or shortly afterwards. Moreover, a longer duration of stagnant flow (about one day) at elevated (maximum) temperature yielded no or only a marginal change in permeability (**Appendix B**) for both samples FS1 (deionized water; 141 °C) and FS3 (2 M NaCl; 145 °C). Not least, there is no indication of any substantial hydraulic effect of mineral precipitation upon cooling as permeability remained more or less constant as the temperature was decreased to ambient conditions (Figure 2.3). Consequently, in this study, a significant effect of dissolution-precipitation reactions on the permeability of the sandstone samples during the temperature cycles is neither obvious nor likely as the respective rates of change differ significantly.

The SEM image of sample FS1 (Figure 2.4b) in comparison to sample S2 (Figure 2.4a) provides further evidence of compaction and irreversible pore throat closure after the experiment. This is supported by the MIP measurements in Figure 2.5a, where the overall porosity of sample FS1 has decreased by partial disappearance of the smallest pore throat-size fraction (i.e., 0.2 μm and below). Qualitatively sample FS3 has inherited the same microstructural changes during heating as sample FS1 but some features (Figures 2.4c and 2.5b) have evolved further as fluids were exchanged (Section 2.4.3). The same should apply to sample FS4 that showed reproducible changes in absolute and relative permeability during heating.

In contrast to the similar reductions in permeability by magnitude, a minimum permeability

threshold was only apparent for sample FS1 by 80 °C (Figure 2.3a). For samples FS3 and FS4, up to 145 °C, this was not obvious (Figures 2.3b and c). Whether this relates to the differences in pore fluid composition or subtle variations in sample microstructure is yet unclear and will require further investigations.

Our microstructural evidence demonstrates that permeability reductions with temperature measured in this study are thermo-mechanically induced. However, in other cases and particularly in kaolinite bearing sandstones, elevated temperatures may favor clay detachment and migration as a result of amplified repulsive forces (e.g., Schembre & Kavscek, 2005; García-García et al., 2006; Schembre et al., 2006; You et al., 2015; You et al., 2016). The results of the MIP measurements for sample FS1 (Figure 2.5a) and negligible mass loss for both samples FS1 and FS3 (Section 2.3.2) demonstrate that migration of fine particles is very limited in our heated samples before fluids are exchanged. This is different from the behavior of sandstones dominated by kaolinite as the clay fraction (e.g., Schembre & Kavscek, 2005; Rosenbrand et al., 2015b). In the present sandstones, fine particle migration becomes important when pore fluids are diluted from 2 M to below 0.5 M NaCl at room temperature and 145 °C (Section 2.4.3).

### 2.4.3 Effects of NaCl salinity changes

Permeability damage in clay-bearing sandstone following a decrease in pore fluid salinity has been observed and investigated in numerous prior studies (e.g., Gabriel & Inamdar, 1983; Khilar & Fogler, 1984; McDowell-Boyer et al., 1986; Mohan et al., 1993; Mohan & Fogler, 1997). DLVO theory has often been applied to explain these observations (e.g., Sharma et al., 1985; Schembre & Kavscek, 2005). In the following, this will be performed for a model sandstone of high quartz content with secondary illite that closely resembles Flechtinger sandstone. A sphere-plate model is used to express both illite particle-to-tangential illite interactions and illite particle-to-quartz grain surface interactions (Kia et al., 1987) (Section 2.2.5; Figure 2.2). The general theory is summarized in **Appendix A**, and the parameterization specific to illite is outlined in the following.

The net surface charge of illite is approximately 1.60 mmol/g, while its cation exchange capacity (*CEC*) is typically in the range of 0.10 - 0.40 mmol/g (Smith, 1967), resulting from some amount of non-exchangeable  $K^+$  ions in the interlayer. The net surface charge density of illite  $\sigma_{\text{illite}}$  is related to the ratio between the *CEC* and the illite specific surface area  $S_a$ ,

$$\sigma_{\text{illite}} = \frac{N_A \cdot e \cdot \text{CEC}}{S_a} \quad (2.5)$$



where  $N_A$  is the Avogadro constant and  $e$  is the elementary charge. The *CEC* depends on the net charge of the clay faces and is variable with pH. The charge of clay edges is generally negative in alkaline solutions and positive in acidic ones while the charge of the crystal surfaces is negative in both cases (Al-Ani & Sarapää, 2008). Here, a pH-neutral environment is considered, and the specific surface area of illite  $S_a$  is taken as 156 m<sup>2</sup>/g (Kahr & Madsen, 1995). Based on the EMPA analysis (Section 2.3.2), the *CEC* of illite is chosen to be either 0.11 mmol/g or 0.05 mmol/g as maximum and median values, respectively, associated with the Na<sup>+</sup> content in illite of sample FS3. Finally, a salinity- and temperature-independent net surface charge density of illite is assumed and all other temperature-dependent parameters are taken from literature as outlined in **Appendix A**.

The calculated total interaction free energy (Figure 2.7) may be attractive (negative) or repulsive (positive) at a given separation distance, depending on fluid salinity and temperature. For a NaCl salinity reduction from 2.0 to 0.5 M, illite-to-illite interactions continue to be attractive at either *CEC* (Figures 2.7a and b), and illite-quartz interactions are attractive at low *CEC* (0.05 mmol/g; Figure 2.7d). Repulsive forces and increases in the separation distance between the illite particles and the quartz surfaces are predicted by DLVO theory only for high *CEC* (0.11 mmol/g, Figure 2.7c). Furthermore, temperature variations at temperatures between 28 °C and 145 °C have a minor effect on the respective energy-separation dependence at high salinity conditions (i.e., 0.5 to 2.0 M), particularly when a low *CEC* (0.05 mmol/g; Figures 2.7b and d) is assumed.

Below NaCl concentrations of approximately 0.5 M, the energy-separation dependences in Figure 2.7 become repulsive for all types of interactions and both *CEC*. To exemplify the trend for deionized water conditions, calculations were performed for an NaCl concentration of 0.1 M, as shown in Figures 2.7a to d. In this case, a temperature dependence of the respective interaction energy can be observed, particularly for illite-to-quartz interactions, and repulsion is realized at higher temperatures (Figures 2.7c and d).

In both experiments with samples FS3 (Figure 2.3b) and FS4 (Figure 2.3c), a further decrease in permeability was observed when a 0.5 M NaCl solution in the pore space was exchanged to deionized water, irrespective of the temperature (i.e., 28 °C or 145 °C) at which this exchange was conducted. The SEM (Figure 2.4c) and MIP (Figure 2.5b) observations outlined in Section 2.3.2 supported by the outcome of the DLVO calculations (Figure 2.7) above demonstrate that this decrease was due to clay particle mobilization and subsequent clogging of pores and pore throats with overall very minor mass loss towards the outside of the samples.

Virtually all pore walls are covered with illite (Figure 2.2); thus, it can be assumed that the pore fluid is mostly in contact with illite rather than quartz (or some other mineral constituent of the rock; Table 2.1). Mobilized particles thus would be predominantly pore lining and pore filling

illite types (Section 2.2.5; Figure 2.2). From Figure 2.7a and b (0.1 M NaCl lines), it can be inferred that the amount of released clay particles and the release rate at a given fluid flow rate should only marginally depend on temperature. Moreover, a higher *CEC* favors and amplifies clay mobilization.

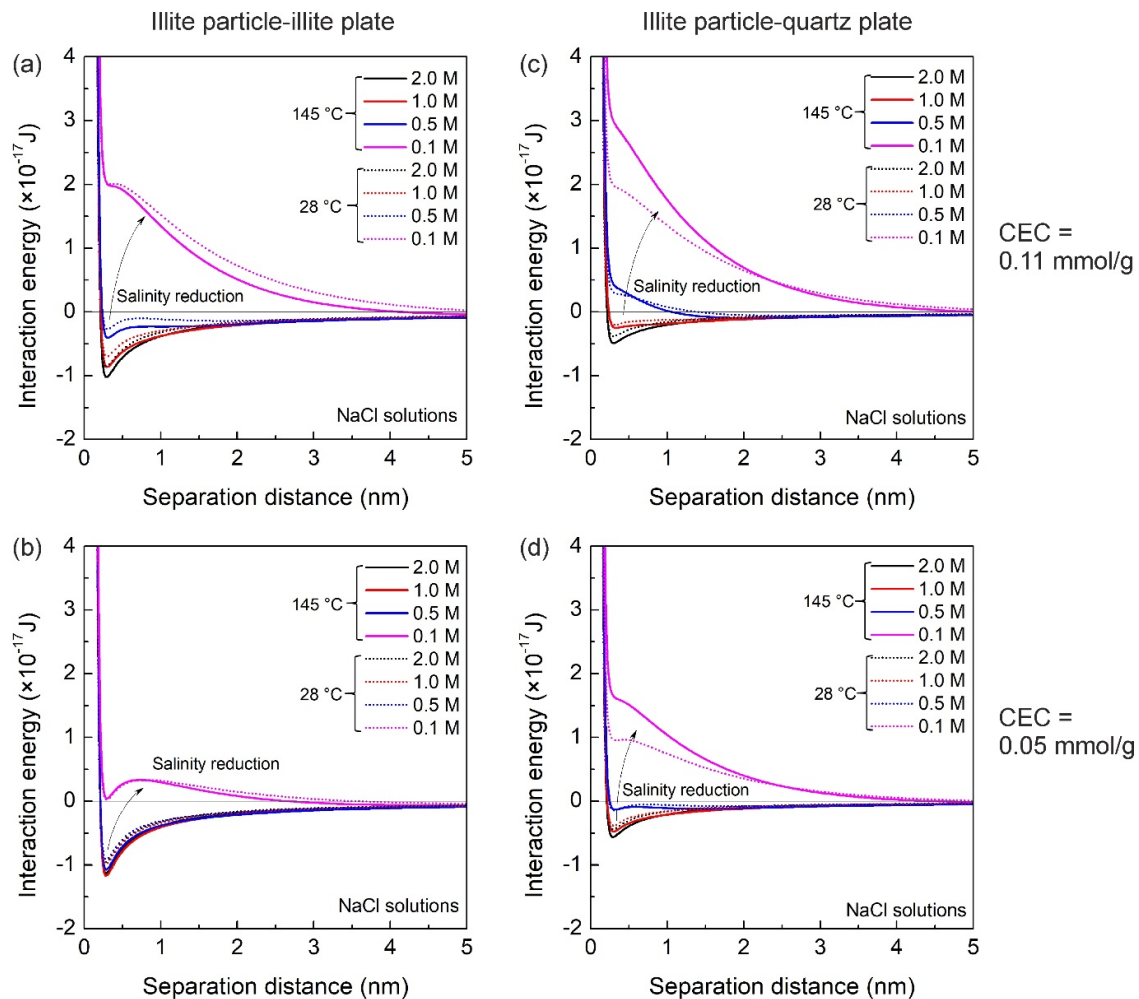


**Figure 2.7** Total interaction free energy between illite particle and illite plate (a and b) and between illite particle and quartz plate (c and d) as a function of separation distance at 28 °C (dashed lines), 145 °C (solid lines), and at different NaCl salinities. A 0.1 M NaCl solution was used to illustrate the pore fluid exchange from 0.5 M NaCl to deionized water during the experiments with samples FS3 and FS4. The cation exchange capacity (*CEC*) is assumed to be 0.11 mmol/g in (a and c) and 0.05 mmol/g in (b and d), respectively.

Once mobilized, illite particles may form a suspension with the pore fluid and migrate downstream as fluid flows through the rock until they are deposited in some pore constriction (Figure 2.4c). This behavior, now, is similar to that of kaolinite-bearing sandstones (e.g.,

Rosenbrand et al., 2015b). From the upstream towards the downstream side of sample FS3, a progressive increase in the accumulation of particles reduces the effective sample porosity systematically and shifts the interval of the affected pore size fraction towards larger pore radii (Figure 2.5b).

## 2.5 Conclusions

Comprehensive flow-through experiments on permeability changes in illite-bearing (Rotliegend) sandstone were performed at multiple and systematically varied temperature and NaCl fluid salinity conditions. The experiments were complemented with an application of Derjaguin-Landau-Verwey-Overbeek (DLVO) theory and comparative microstructural investigations performed by scanning electron microscopy (SEM), electron microprobe analysis (EMPA), and mercury intrusion porosimetry (MIP) on both the starting material and the tested samples. The experimental and analytical observations were mechanistically interpreted, yielding the following conclusions:

Permeability of sandstones containing illite as the dominant clay phase, even at substantial amounts, may be insensitive to changes in pore fluid salinity. This departure from DLVO theory predictions may be due to high  $K^+$  and  $Ca^{2+}$  or  $Mg^{2+}$  contents within the illite crystal lattices. As a result, illite particles are strongly attached to the pore walls and resist hydrodynamic mobilization.

Permeability of illite-bearing sandstones with narrow pore throats dominating the rock's hydraulic properties may be very sensitive to heating, yielding (nearly) irreversible and thermo-mechanically induced pore throat closure. This effect is observed both for low (deionized water) and high (2 M NaCl solution) pore fluid salinity.

When an initially present low salinity fluid (i.e., deionized water in the case) is exchanged by a high salinity NaCl solution (e.g., 2 M) before heating, a partial replacement of the divalent ions in the illite crystal lattices by  $Na^+$  may occur, as detected by EMPA. This yields an additional reduction in permeability as NaCl pore fluid salinity is subsequently decreased to below 0.5 M. This permeability reduction is observed at high temperature (i.e., 145 °C) and room temperature and is in agreement with predictions from DLVO theory. Mechanistically, this permeability decrease is chemically induced and results from clay particle mobilization, transport, and subsequent deposition in pores and pore throats.

Illite-bearing sandstones may show substantial and largely irreversible permeability variations following temperature and fluid salinity changes. The respective underlying thermo-mechanical and chemical processes identified operate independently but are path-dependent with respect to the

## **Chapter 2. Permeability variations of illite-bearing sandstone**

---

applied fluid salinity sequence. Any such natural or geotechnically used rock system may thus be susceptible to permeability reduction with consequences for the evolution of fluid flow when changes in the here investigated parameters occur or are induced.

# Chapter 3

## Hydro-mechanical investigations on self-propping fractures

The hydro-mechanical properties of self-propping fractures are of fundamental interest for fractured-rock hydrology and a large number of geotechnical applications. This experimental study investigates fracture closure and hydraulic aperture changes of displaced tensile fractures, aligned tensile fractures, and saw-cut fractures for two types of sandstone (i.e., Flechtinger and Fontainebleau) with contrasting mechanical properties, cycling confining pressure between 5 and 30 MPa. Emphasis is placed on how surface roughness, fracture wall offset, and the mechanical properties of the contact asperities affect the self-propping potential of these fractures under normal stress. A relative fracture wall displacement can significantly increase fracture aperture and hydraulic conductivity, but the degree of increase strongly depends on the fracture surface roughness. The surface roughness of saw-cut fractures remains scale-independent as long as the fracture area is larger than a roll-off wavelength, and thus any further displacement does not affect fracture aperture. Tensile fracture surfaces are self-affine over a larger scale, so an incremental fracture wall offset likely leads to an increase in fracture aperture. X-ray microtomography of the fractures after the confining pressure cycle indicates that the contact area ratio of the tensile fractures inversely correlates with the fracture wall offset, yielding values in the range of about 3% ~ 25%. Relatively larger contact areas occur in the more compressible rock due to the compression/damage of contact asperities. Moreover, the contact asperities mainly occur isolated and tend to be preferentially oriented in the direction perpendicular to the fracture wall displacement, which may induce flow anisotropy. These observations imply that self-propping fractures in sedimentary rocks are sustainable for fluid flow if sufficient displacement is applied to the scale-dependent fracture surfaces.

### **3.1 Introduction**

Sufficient amounts of fluid need to be extracted/injected within rock masses in the upper crust at depths as deep as 4~5 km for economic utilization of reservoirs, e.g., enhanced geothermal systems (Blöcher et al., 2016; Kushnir et al., 2018) or unconventional oil and gas extraction. Fractures, predominantly controlling fluid flow in rocks, are crucial in this regard. Consequently, the hydro-mechanical properties of rock fractures have received attention in numerous studies in the past (e.g., Bandis et al., 1983; Raven & Gale, 1985; Zimmerman & Bodvarsson, 1996; Sausse, 2002; Konzuk & Kueper, 2004; Rutqvist, 2015). The property of single self-propping fractures under normal stresses is one of the most fundamental problems in fractured-rock hydrology and is the starting point to understand more complex systems, e.g., shear fractures or fracture networks. To quantitatively characterize fluid flow through a single rock fracture, which is deformable under normal stresses, the notions of mechanical and hydraulic aperture are commonly considered (Witherspoon et al., 1980; Barton et al., 1985; Zimmerman et al., 1992). The mechanical aperture is the arithmetic mean of the separation distance between the opposing fracture surfaces, while the hydraulic aperture represents the equivalent flow through a fracture idealized as two smooth, parallel plates applying the so-called "cubic law" (Zimmerman & Bodvarsson, 1996).

Numerous experimental studies on the hydro-mechanical properties of single fractures have previously been performed, generally considering a lithostatic load equivalent to 1 to 3 km crustal depth (23 MPa/km) (Bandis et al., 1983; Hofmann et al., 2016; Milsch et al., 2016; Vogler et al., 2016; Crawford et al., 2017) but in some cases down to 7 km depth (Kranzz et al., 1979; Durham & Bonner, 1994). Experimental results showed that a mismatched joint in granitic rocks remains hydraulically conductive under normal stresses up to 160 MPa (Durham & Bonner, 1994). Moreover, fractures in granite and granodiorite are hard to completely close, either mechanically or hydraulically, under purely normal stresses (Hofmann et al., 2016; Vogler et al., 2016) unless the fracture surfaces are mated and/or subjected to extremely high loads (Kranzz et al., 1979; Durham & Bonner, 1994). In addition, studies on fractures in other rock types, such as slate, sandstone, dolerite, and limestone, essentially yielded similar results (Bandis et al., 1983; Crawford et al., 2017), which permits to conclude that the permeability of mismatched fractures is more sustainable in comparison to aligned fractures at the same normal stress conditions.

The main factors that control fracture deformation and fluid flow are the surface roughness (Bandis et al., 1983), fracture wall offset or shear displacement (Plouraboué et al., 1995; Vogler et al., 2016; Fang et al., 2018; Kluge et al., 2021), number of loading-unloading cycles

(Brown & Scholz, 1985; Hofmann et al., 2016; Milsch et al., 2016), fracture size (Raven & Gale, 1985), the direction of fluid flow relative to the fracture wall displacement (Thompson & Brown, 1991; Auradou et al., 2005; Watanabe et al., 2008; Nemoto et al., 2009; Lang et al., 2018), and fracture types, i.e., either natural or artificially generated (Kling et al., 2016; Vogler et al., 2016). The main conclusions drawn from these previous studies can be summarized as follows: 1) the irreversible deformation (permeability decline) after each loading-unloading cycle reduces with the number of cycles. Generally, 3~4 full cycles can efficiently eliminate any inelastic deformation component. 2) The degree of fracture closure strongly depends on the fracture surface topography as well as on the elastic properties of the material. 3) Artificially displaced fractures show shear dilation due to the mismatch between the surfaces. 4) The larger the relative fracture wall displacement, the less is stress-dependent permeability reduction and anisotropy. 5) A shear fracture under normal stress shows shear dilation with gouge production and permeability variations depending on fracture surface properties. 6) A permeability reduction is more pronounced when the flow direction is oriented parallel to the fracture wall displacement. 7) Flow channeling and tortuosity increase with increasing normal stress. 8) The contact area ratio, defined as the ratio between the contact area of the asperities and the nominal fracture area non-linearly varies with aperture closure. Overall, the intrinsic rock properties, e.g., the fracture surface roughness and mechanical behavior, fundamentally determine the properties mentioned before.

Previously, most experimental studies were performed on igneous rocks. However, for enhanced geothermal systems (Blöcher et al., 2016) or unconventional oil and gas exploitation, the fracture behavior in low permeability formations consisting of sedimentary rock such as tight sandstones, siltstones, and shales is of paramount interest. In this context, hydraulic fracturing is crucial for increasing the transmissivity of the formations (Blöcher et al., 2016; Zimmermann et al., 2018; Hofmann et al., 2019). Here, the generated fractures are tensile or shear fractures, depending on the stress field. Hydraulic fractures generally propagate in the direction perpendicular to the minimum principal stress (Zhuang et al., 2020). However, for sedimentary formations containing bedding layers or other anisotropic structural features, the fracture plane orientation will be strongly affected by the present structure-stress correlation encountered in situ (Cosgrove, 1995; Huang & Liu, 2017). In addition, fracture surfaces generated in sedimentary rocks show different spatial correlations (e.g., the Hurst exponent  $H$  is about 0.5 for tensile fractures in sandstone) compared to the ones in igneous rocks (e.g.,  $H \approx 0.8$  for fractures in granite and basalt) (Boffa & Allain, 1998; Ponson et al., 2007; Schmittbuhl et al., 2008). Other features (e.g., bedding layers, grain sizes) in sedimentary rocks may also affect fracture surface roughness. Consequently, it is necessary to investigate the self-propping potential of sedimentary rock

fractures with different features to conclude whether these fractures are sustainable, thus allowing for sufficient fluid flow under stress. This information will then help to decide whether proppants should be used in such reservoirs or not.

In this study, sedimentary rocks, i.e., two types of sandstone, are investigated regarding the mechanical and hydraulic response of different fracture configurations on effective pressure cycles. A more compressible rock is compared to a stronger one, as are tensile fractures with different degrees of displacement and saw-cut fractures. This study emphasizes how the fracture surface roughness, the degree of geometric matching of the opposing fracture surfaces, and the mechanical properties affect fracture aperture, both mechanically and hydraulically, when the normal stress on the fracture plane is varied and, moreover, how the aperture distribution, the fracture wall offset, and the contact area ratio correlate. Flow-through experiments and drained compression tests were conducted and complemented with microstructural investigations by fracture surface scans and X-ray micro tomography ( $\mu$ CT).

### **3.2 Rock samples and methodology**

#### **3.2.1 Sample preparation and experimental apparatus**

In this study, two types of sandstone were selected for hydro-mechanical experiments to examine the characteristics of single fracture flow subject to normal stress cycles. The two rock types were Flechtinger sandstone, quarried from an outcrop of the Lower Permian (Upper Rotliegend) near Flechtingen, Germany and Fontainebleau sandstone, quarried near Fontainebleau, France. The geology, petrophysics, and mechanical properties of both rocks are well known (Fischer et al., 2012; Saadi et al., 2017) and have been intensively investigated (Zang et al., 1996; Hassanzadegan et al., 2012; Hassanzadegan et al., 2013; Schepers & Milsch, 2013). Fontainebleau sandstone is an almost monomineralic sandstone (>99.5 wt% quartz), while Flechtinger sandstone is composed of quartz (63 wt%), K-feldspar (14 wt%), albite (12 wt%), illite (7 wt%), calcite (2 wt%), and hematite (1 wt%) as determined by X-ray diffraction (XRD). Figure 3.1 shows optical micrographs of the two rock types, where the Fontainebleau sandstone possesses a relatively uniform grain size in comparison to Flechtinger sandstone. The average grain size of both rocks is in the same order of magnitude, i.e., 200  $\mu$ m for Fontainebleau sandstone and 125  $\mu$ m for Flechtinger sandstone as derived from 2-D image analyses.



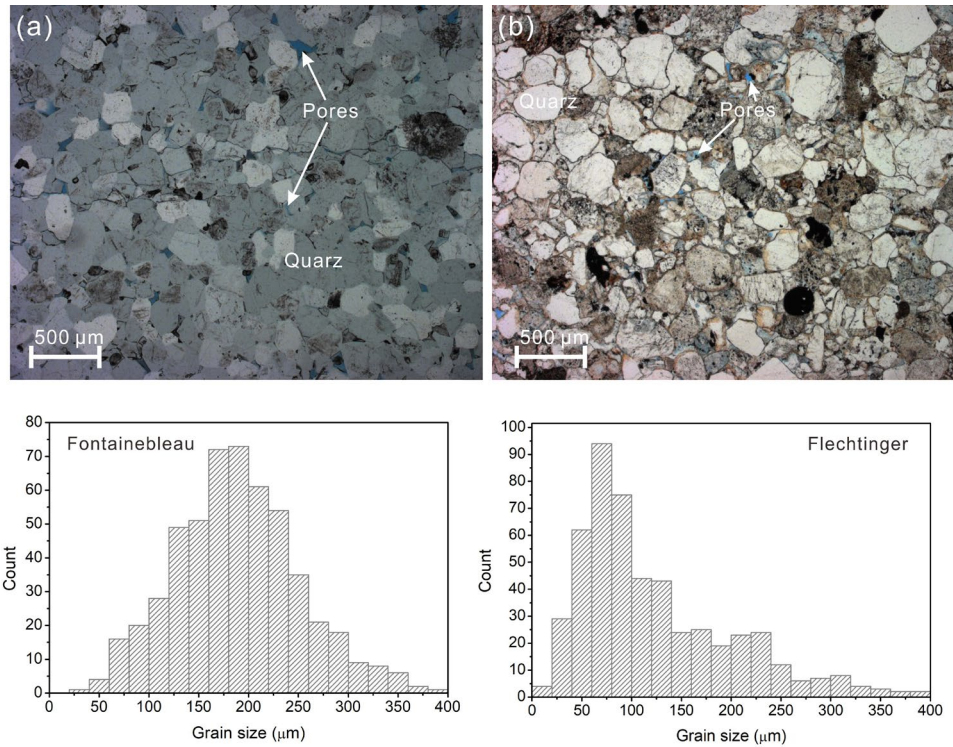


**Figure 3.1** Optical micrographs and grain size distributions derived from 2-D image analyses using ImageJ (Schneider et al., 2012). (a) Fontainebleau sandstone and (b) Flechtinger sandstone.

**Table 3.1** Basic physical parameters of the two rock types.

Rock type	$\phi$ (%)	$\rho$ (g/cm <sup>3</sup> )	$k$ (m <sup>2</sup> )	$UCS$ (MPa)	$K_b$ (GPa)
Flechtinger	8.1	2.40	$10^{-17} \sim 10^{-18}$	56.7~100	15.9
Fontainebleau	2.5	2.56	$10^{-18}$	122.3	33.0

The porosity  $\phi$  is measured by saturation and weighing, and  $\rho$  is the bulk density. The uniaxial compressive strength ( $UCS$ ) and the drained bulk modulus ( $K_b$ ) of Flechtinger sandstone were taken from previous investigations (Hassanzadegan et al., 2012). Flechtinger sandstone is anisotropic, where the  $UCS$  parallel and perpendicular to the bedding layers shows different values of up to 100 MPa (Zang et al., 1996). The permeability  $k$  of Flechtinger sandstone was measured with the flow direction oriented perpendicular to the bedding.  $UCS$  and  $K_b$  of Fontainebleau sandstone with a porosity of ~4% are reported in Baud et al. (2014) and Arns et al. (2002), respectively. One can infer that the present Fontainebleau sandstone with a porosity lower than 4% is mechanically stronger, implying that the values reported in the table for  $UCS$  and  $K_b$  should be considered lower bounds.

The basic physical parameters of the two rock types display significant differences, as shown in Table 3.1. These sandstones represent relatively "soft" (Flechtinger sandstone) and "hard" rock

(Fontainebleau sandstone), respectively. However, both sandstone types used in this study are of low matrix permeability on the order of  $10^{-18}$  m<sup>2</sup>, as determined with a gas permeameter.

The Fontainebleau sandstone used in this study appears isotropic and homogeneous. The Flechtinger sandstone is relatively homogeneous but microscopically shows bedding layers. The mechanical properties, consequently, vary in dependence of the stress orientation relative to bedding (Zang et al., 1996). In addition, generated fractures along the bedding layers may significantly differ in roughness depending on whether the layers consist of finer or coarser grains. To minimize any influence of bedding on the fracture roughness and the permeability measurements, all sample cores were drilled from larger blocks perpendicular to bedding. Three cylindrical samples of each rock type (Flechtinger sandstone: FF1, FF2, and FF3; Fontainebleau sandstone: FOF1, FOF2, and FOF3) with a diameter of 30 mm and a length of 40 mm were prepared. The six samples were split into two halves using a Brazilian test setup (Figure 3.2a) at a displacement rate of  $2 \times 10^{-6}$  m/s, yielding negligible edge damage. In addition, a rock block was cut by using a saw, and the obtained halves were then tightly attached. Subsequently, cylindrical core samples were drilled along the fracture located in the core center. Thin section images (Figure C1) of the generated fractures indicate that sawing results in intragranular fracturing while tensile fractures mainly form along the grain boundaries in Flechtinger sandstone as well as both across grains and along grain boundaries in Fontainebleau sandstone.

Examples of separated sample halves are displayed in Figure 3.2b. The respective subsamples were labeled A and B. The sample halves were subsequently assembled with or without PEEK spacers on the top, and the bottom ends to create a fixed displacement with offsets of 0.2 mm (FF2 and FOF2) (Figure 3.2e) and 0.75 mm (FF1 and FOF1) (Figure 3.2f). FF3 and FOF3 were aligned without pre-displacement (Figure 3.2d), and saw-cut samples (FF4 and FOF4) were obtained (Figure 3.2c). All samples were then assembled with two plugs that connect to the pore fluid system of the flow-through apparatus. A heat-shrink tubing jackets the sample to isolate the pore fluid system from the confining pressure fluid (silicone oil), and a thin metal sheet placed between the fracture gap and the jacket was introduced to minimize any risk of jacket punching at elevated confining pressure conditions.

A flow-through apparatus comprising a hydrostatic pressure vessel was used in this study (Milsch et al., 2008b). The specimen assembly was mounted in the vessel and connected to the pore fluid system, which comprises an upstream and a downstream syringe pump (ISCO 260D). The hydrostatic confining pressure is generated with silicone oil using another syringe pump (ISCO 65D). During a flow-through experiment, the downstream pump was maintained in constant pressure mode, with the upstream pump providing a constant fluid flow rate. The flow direction

during a test is from the bottom to the top of the sample. The differential pore pressure between the sample ends is monitored by a differential pressure transducer (IPD 40, ICS Schneider Messtechnik) with a range of 0 - 0.6 MPa and an accuracy of < 0.2%.

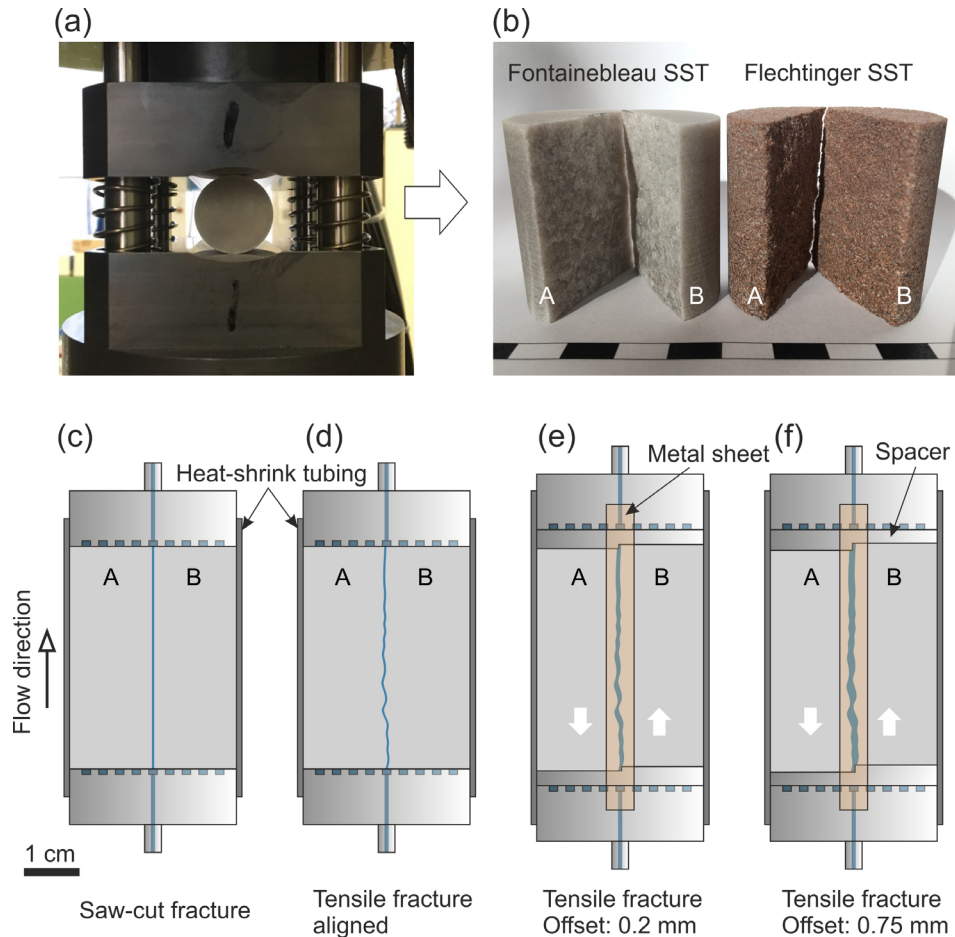


**Figure 3.2** Preparation of the fractured samples. (a) Tensile fracture generated by a Brazilian test setup; (b) representative fractured Fontainebleau sandstone (white) and Flechtinger sandstone (red) cores; schematic illustrations of the assembled specimens, with (c) aligned saw-cut sample core, (d) aligned tensile fracture, (e) mismatched tensile fracture with an offset of 0.2 mm, and (f) mismatched tensile fracture with an offset of 0.75 mm.

### 3.2.2 Experimental procedures

#### 3.2.2.1 Determination of hydraulic aperture

The assembled samples were vacuum-saturated with deionized water before the experiment. After the installation, under an initial confining pressure  $p_c$  of 2 MPa, water was continuously flown

through the entire pore fluid system, keeping the downstream side open to the atmosphere until the system was free of air, as evidenced by the absence of air bubbles in the effluent. The pore pressure  $p_p$  was then increased to 1 MPa and maintained constant throughout the experiment. The confining pressure was further increased to 5 MPa as the starting point of a loading-unloading cycle (5  $\leftrightarrow$  30 MPa for all samples except FF1 (10  $\leftrightarrow$  35 MPa)). During the experiment, the confining pressure was increased or decreased stepwise with a regular interval of 5 MPa, and the sample permeability was measured at each pressure level.

The linear Darcy's law is commonly used to describe fluid flow through porous media (Darcy, 1856),

$$Q = \frac{kA}{\mu L} \Delta P \quad (3.1)$$

where  $Q$  is the flow rate,  $\Delta P$  is the differential pressure over the sample length  $L$ ,  $\mu$  is the dynamic fluid viscosity,  $A$  is the cross-section area of the sample, and  $k$  is its intrinsic permeability. For fluid flow through a single rock fracture, one commonly idealizes the fluid to flow through two smooth, parallel fracture plates. With the assumptions that Darcy's law is valid and that the flow of an incompressible Newtonian fluid is laminar, the so-called "cubic law" is derived by applying the parallel plate model (Zimmerman & Bodvarsson, 1996),

$$Q = \frac{b_h^3 W}{12 \mu L} \Delta P \quad (3.2)$$

where  $W$  is the fracture width (i.e., the sample diameter), and  $b_h$  is the separation distance between the two smooth, adjacent fracture plates. However, in rough fractures, the latter parameter is considered an equivalent aperture, called the hydraulic aperture. Based on the "cubic law", the fracture permeability  $k_f$  can then be expressed as (Witherspoon et al., 1980),

$$k_f = \frac{b_h^2}{12} \quad (3.3)$$

Although the present sandstone samples are fractured porous media, the fracture permeability is orders of magnitude higher than the matrix permeability, which, consequently, is considered to be negligible. In this study, the equivalent hydraulic aperture  $b_h$  was calculated for the principal purpose of comparing its value to the mechanical aperture (i.e., the geometric separation distance between the two fracture surfaces).

#### 3.2.2.2 Determination of mechanical aperture changes

There are several direct and indirect methods of measuring mechanical aperture changes during

loading-unloading operations. Bandis et al. (1983) measured the total vertical deformation of a fractured sample in a uniaxial compression device, where the fracture is placed perpendicular to the normal stress. By subtracting the corresponding deformation of the solid rock without a fracture (obtained from separate measurements on intact samples), fracture aperture deformation was determined. Raven and Gale (1985) performed a direct measurement of the axial deformation of a circular fracture in a cylindrical sample core with three linear variable differential transformers (LVDT) evenly distributed around the sample and oriented in parallel to the longitudinal axis. Vogler et al. (2016) measured the volume changes of the confining pressure fluid during loading-unloading cycles. An additional test on an intact sample was conducted as a reference to calibrate the effects of compression of the rubber jacket and the confining pressure fluid. In addition, Hofmann et al. (2016) measured the axial and lateral strain of a sample, where a single fracture was in parallel to the sample axis, by using two axial extensometers and one circumferential chain extensometer in a triaxial experimental setup. Fracture aperture deformation was indirectly determined by subtracting the elastic axial strain from the total lateral strain.

In this study, the pore pressure was maintained constant at 1 MPa throughout the experiment, and the total volume changes  $\Delta V$  of the pore fluid were monitored with the downstream pump during the loading-unloading cycles. The mechanical aperture changes  $\Delta b_m$  can then be expressed as,

$$\Delta b_m = \frac{\Delta V - \Delta V_{\text{pore}}}{WL} \quad (3.4)$$

where  $\Delta V_{\text{pore}}$  is the corresponding pore volume change of the rock matrix. For Flechtinger sandstone samples,  $\Delta V_{\text{pore}}$  was obtained from previous loading and unloading cycles on intact samples of the same rock at hydrostatic stress conditions (Hassanzadegan et al., 2012; Hassanzadegan et al., 2013). The only calibration parameter here is the sample bulk volume due to the difference in sample sizes. For Fontainebleau sandstone samples, due to the low matrix permeability ( $\sim 1 \times 10^{-18} \text{ m}^2$ ), the low porosity ( $\sim 2.5\%$ ), and the short experimental duration of each loading/unloading interval (5 MPa; about 4 min),  $\Delta V_{\text{pore}}$  for this rock type is assumed negligible.

The total volume changes during initial loading can be attributed to both fracture and pore volume changes and may also result from an adjustment of the specimen assembly, e.g., the closure of small gaps between individual assembly parts. Therefore, in the following, only those results are compared that were obtained at confining pressures between 5 and 30 MPa. In addition to directly measuring mechanical aperture changes, a complementary analysis was performed using the fracture surface topographies obtained from white light interferometry (Section 3.2.3).

### 3.2.3 Fracture surface topography

#### 3.2.3.1 Fracture surface measurements and roughness determination

The methods applied to measure the topography of solid surfaces, including contacting and non-contacting methods, evolved with technological progress and a concurrent increase in efficiency: from early studies using profilometry (Bandis et al., 1983), image analysis of polished cross-sections perpendicular to the fracture (Hakami & Larsson, 1996), laser scanning (Neuville et al., 2012; Singh et al., 2015), photogrammetric scans (Vogler et al., 2016; Vogler et al., 2018), X-ray computed microtomography ( $\mu$ CT) (Renard et al., 2009; Diaz et al., 2017), to white light interferometry (Renard et al., 2012; Zou et al., 2019). In this study, the fracture surface topographies of samples FF2, FF3, FF4, FOF2, FOF3, and FOF4 were measured before the experiments by using white light interferometry (Keyence VR 3000). The resolution of the horizontal x-y coordinates is 23.518  $\mu\text{m}$ , and the vertical resolution is 1.0  $\mu\text{m}$ , which yields approximately two million data points for each surface.

Numerous parameters have been defined to characterize surface roughness (Li & Zhang, 2015), such as the joint roughness coefficient (JRC) (Barton, 1973), which is an empirical parameter obtained by comparing fracture profiles to standards, developed further with the introduction of statistical parameters (Tse & Cruden, 1979). In this study, we apply statistical expressions to directly analyze the scanned 3-D surface data, i.e., the peak asperity height  $R_p$ , the average roughness  $R_m$ , and the root-mean-square roughness  $R_{rms}$ ,

$$R_p = \max|z_i - z_a| \quad (3.5)$$

$$R_m = \frac{1}{n} \sum_{i=1}^n |z_i - z_a| \quad (3.6)$$

$$R_{rms} = \sqrt{\frac{1}{n} \sum_{i=1}^n (z_i - z_a)^2} \quad (3.7)$$

where  $z_i$  is the height of the  $i$ th point and  $z_a$  is the mean height of the elevation plane, which is discretized by  $n$  points. The global statistical parameters provide a direct comparison between samples, helping to distinguish the different surface topographies quantitatively.

In addition, rock interfaces (e.g., faults, natural fractures, and artificial fractures) are commonly classified as self-affine structures over a large range of length scales (Candela et al., 2012), which are used to numerically generate fractures for simulations (Schmittbuhl et al., 2008; Lang et al., 2015; Lang et al., 2016). In such simulations, it is assumed that the fracture surface remains invariant under the transformation,

$$\Delta x \rightarrow \lambda \Delta x, \Delta y \rightarrow \lambda \Delta y, \Delta z \rightarrow \lambda^H \Delta z \quad (3.8)$$

where  $\lambda$  is the wavelength, and  $H$  is the Hurst exponent (Persson et al., 2004; Schmittbuhl et al., 2004), indicating a self-affine behavior if  $H$  is between 0~1.  $H$  can be estimated based on the 1-D Fourier power spectrum,

$$C(q) \propto q^{-1-2H} \quad (3.9)$$

where  $q = 2\pi / \lambda$  is the wavevector varying between  $2\pi / l$  and  $2\pi / a$ , and  $l$  is the observed length, and  $a$  is the smallest wavelength, i.e., 23.518  $\mu\text{m}$ . In this study, the 1-D power spectrum of the profile  $z(x, y_0)$  along the sample length is analyzed, where  $x$  indicates the direction parallel to the displacement. The intrinsic spatial correlation behavior of the surface fluctuations along the displacement can thus be derived.

### 3.2.3.2 Mechanical aperture calculations

Since the fracture surfaces are not identical between samples, it is difficult to quantitatively analyze whether the permeability changes are related to parameter differences (i.e., the displacements) or the intrinsic properties of the fracture surfaces. Thus, further numerical investigations were performed based on the surface topography measurements to obtain correlations between the mechanical aperture and surface roughness, surface displacement, as well as contact area ratio. Mechanical aperture can be determined by measuring the upper and the lower fracture walls relative to a reference plane (Hakami & Larsson, 1996) or by measuring the separation distances oriented perpendicular to the local trend of the fracture walls (Mourzenko et al., 1995; Ge, 1997). Both methods yield very similar results (Konzuk & Kueper, 2004). In this study, the former definition of the mechanical aperture was used by applying a best-fitting plane. The mean mechanical aperture  $b_m$  can then be expressed as,

$$b_m = \frac{1}{A_f} \int_{A_f} \Delta z(x, y) dA \quad (3.10)$$

where  $A_f = W(L-\delta)$  is the nominal fracture area of the adjacent fracture surfaces, with  $\delta$  being the displacement along the sample length, and  $\Delta z(x, y)$  is the height difference between the adjacent points on the upper and the lower fracture surfaces.

For the saw-cut samples FF4 and FOF4, the two surfaces of the halves were used for the calculation. For tensile fractures, the initial matching of the aligned halves is difficult since the data obtained for the adjacent fracture surfaces cannot be exactly related, the datum plane of each scan may not be identical, and the initial contact area is hard to estimate. To simplify the dynamic

adjustment (e.g., movement or rotation) of two surface topographies, duplicate fracture surfaces were used (i.e., the surfaces A and B are identical to one set of the fracture surface data). Therefore, the fracture aperture at aligned conditions, theoretically, is equal to zero when applying this method. In practice, due to the loss of some grains on the fracture surfaces after separation, the two opposite surfaces do not perfectly match. Furthermore, the tensile fractures generated by the Brazilian test method may display a slightly concave surface geometry resulting from damage transfer during splitting since the fracture edges are subject to compression and the maximum tensile stress and strain occur about 5 mm away from the load contact (Li & Wong, 2013). Consequently, the tensile fractures display a slightly larger contact area along the fracture edges compared to the interior of the fracture surfaces. However, this feature was found to be more obvious in Flechtinger sandstone than in Fontainebleau sandstone (see Section 3.3.4 and Figure 3.11).

The procedure of fracture displacement is illustrated in Figure 3.3a, where the lower surface A is fixed, and the upper surface B is allowed to move along the sample length corresponding to specimen B of the true sample. The contact area is maintained at a minimum but  $>3$  contact points, and any rotation due to the surface adjustment is omitted. In this way, one obtains the correlation between the initial mechanical aperture and the displacement of each fracture surface.

Fracture deformation resulting from normal stresses has been extensively studied by applying purely elastic, elasto-plastic, and interpenetration contact models (Li et al., 2015; Kling et al., 2018; Zou et al., 2019). The interpenetration model is a rather simple analytical model yielding fairly good agreement with the results of fluid flow measurements (Watanabe et al., 2008; Nemoto et al., 2009). In this model, the two fracture surfaces are displaced relative to each other, where the overlapping parts of the asperities ( $\Delta z_i < 0$ ) are removed, and their distance is taken as zero (i.e., contacting asperities). Kling et al. (2018) compared the three models and found that the interpenetration model yields the largest contact area. It should be noted that this model is incapable of accounting for loading-unloading cycles that comprise both elastic and irreversible deformation. This study aims to analyze how the geometrical parameters affect aperture closure to better understand the corresponding experimental results. The interpenetration model was applied in all surface analyses, and only geometrical variations and fracture deformation were considered. An example of the aperture distribution and the contact areas for a fracture with an offset is shown in Figure 3.3b. The contact area ratio is expressed as the ratio of the contact area,  $A_c$  to the nominal fracture surface area,

$$R_c = \frac{A_c}{W(L-\delta)} \quad (3.11)$$



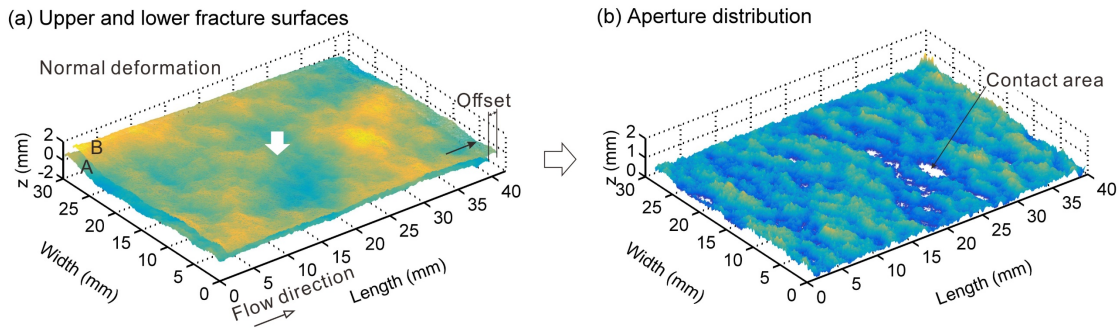


**Figure 3.3** Schematic illustration of fracture aperture determination using the representative example of sample FOF2. (a) The upper fracture surface is displaced along the sample length relative to the lower surface. (b) A fracture aperture distribution with an offset of 1.1759 mm (50 steps of displacement) is shown as an example. The contact area is determined for the deformed state of the fracture surfaces resulting from the applied normal stress.

### 3.2.4 Determination of fracture morphology using X-ray $\mu$ CT scans

To investigate the microstructural changes of the fracture before and after the experiments, the assembled samples were scanned by using an X-ray  $\mu$ CT scanner (GE Phoenix nanotom m 180) at atmospheric conditions. All scans were performed with dried but jacketed sample cores using the same scanning parameters (i.e., timing 500 ms, voltage: 120 kV, current: 90  $\mu$ A, and same sample position relative to the X-ray source and detector) to obtain comparable results. A total of 1080 two-dimensional slices with a voxel size of 20.63  $\mu$ m were obtained for each scan and were then used to reconstruct the three-dimensional models. The fracture void spaces  $V_{f-ct}$  were detected and extracted from the corresponding models, and the respective mean mechanical apertures  $b_{m-ct}$  were derived from,

$$b_{m-ct} = \frac{V_{f-ct}}{A_{f-ct}} \quad (3.12)$$

where  $A_{f-ct}$  is the area of the projection of the 3-D fracture void, which is oriented in parallel to the nominal fracture plane. In addition, the extracted 3-D fracture void was projected onto the nominal fracture plane from which the contact areas  $A_{c-ct}$  were further derived (Figure 3.11). The contact area ratio  $R_{c-ct}$  was then calculated from,

$$R_{c-ct} = \frac{A_{c-ct}}{A_{f-ct}} \quad (3.12)$$

Note that due to the voxel size limit of the reconstructed CT models (voxel sizes in xyz-directions: 20.63  $\mu$ m), fracture apertures smaller than the voxel size could not be accurately

detected. Thus, the fracture aperture might be underestimated in contrast to the contact area ratio, which may be overestimated with this method. Also, the results are numerical products that potentially are not fully equivalent to the true physical parameters. The comparison of the aperture data provides an overall understanding of how the fracture permanently deforms when subjected to normal stress. Not least, the  $\mu$ CT scans were performed at zero-stress and dry conditions. Thus, the fracture apertures at experimental in situ conditions may also show discrepancies with the measured ones.

### 3.3 Results

#### 3.3.1 Hydraulic and mechanical aperture changes during loading-unloading cycles

The evolution of hydraulic apertures (calculated with Eq. 3.2) of Flechtinger and Fontainebleau sandstones resulting from the loading-unloading cycles is displayed in Figure 3.4. One notices that the initial hydraulic apertures of the mismatched tensile fractures are significantly larger than those of both the aligned and the saw-cut fractures for both rock types. The lowest sample permeabilities (calculated with Eq. 3.1) of FF3 (aligned) and FOF4 (saw-cut) at stressed conditions are approximately  $4 \times 10^{-16} \text{ m}^2$  and  $2 \times 10^{-16} \text{ m}^2$ , respectively and thus still two orders of magnitude larger than the corresponding matrix permeability ( $\sim 1 \times 10^{-18} \text{ m}^2$ ), indicating that the introduced fractures are the dominant flow paths even for the smallest fracture apertures and that all fractures are far from being completely closed. Further, it is found that the initial hydraulic aperture increases with an increase of the fracture wall offset. However, the increment of the offset does not proportionally relate to the increment of the initial hydraulic aperture, as distinctly shown in Figure 3.4b, where the samples FOF1 and FOF2 with offsets of 0.75 mm and 0.2 mm, respectively, have an almost identical initial hydraulic aperture. For the two saw-cut samples, it showed that the hydraulic aperture of FF4 is about one order of magnitude larger than that of FOF4, which mainly should be the result of differences in fracture surface roughness as related to the intrinsic rock microstructure, e.g., grain size distribution and porosity (Section 3.2.1).

Hydraulic aperture decreased with increasing confining pressure during loading for all samples. Most experiments display a hysteretic behavior during the stress cycle in a way that the respective aperture is larger during loading than during unloading at the same stress level, except for sample FOF1, whose hydraulic aperture was slightly enhanced after unloading. It is noticed further that for most samples, except for FF2 and FOF3, the hydraulic aperture decrease tends to converge, where a further stress increase results in progressively less reduction in hydraulic aperture. Finally,

irreversible hydraulic aperture changes after the loading-unloading cycles are larger in Flechtinger sandstone samples in comparison to the corresponding Fontainebleau sandstone samples with the same respective offset.

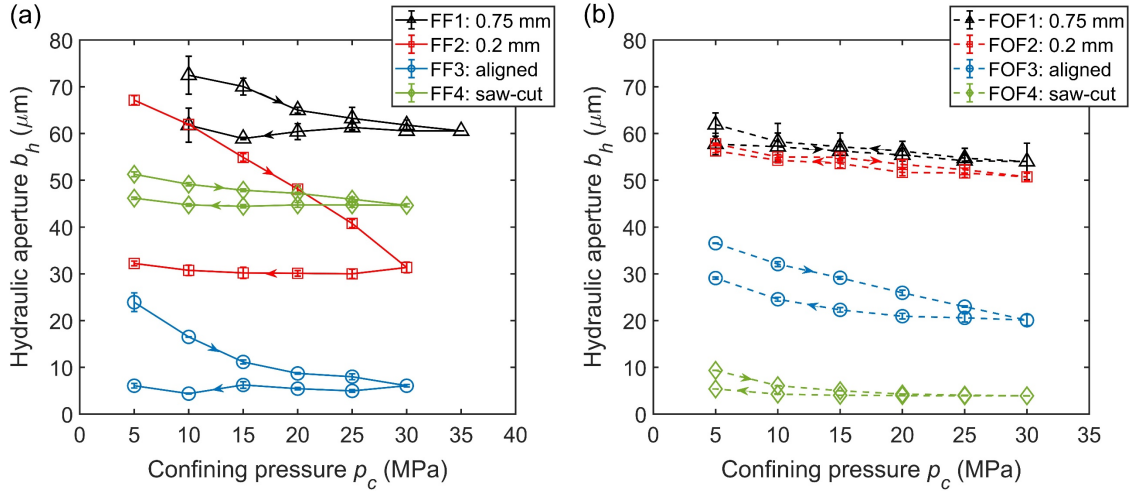


**Figure 3.4** Hydraulic aperture  $b_h$  as a function of confining pressure for (a) Flechtinger sandstone samples and (b) Fontainebleau sandstone samples.

The drained compression tests for determining the variations in mean mechanical aperture started from  $p_c=5$  MPa or  $p_c=10$  MPa (FF1). Therefore, the mechanical aperture changes between ambient pressure and  $p_c=5$  MPa were not measured. Hence, changes in mean mechanical aperture were obtained relative to the respective starting point. The correlation between the mean mechanical aperture changes (calculated with Eq. 3.4) and the confining pressure, as illustrated in Figure 3.5, indicates that these aperture variations are significantly larger than the corresponding hydraulic ones (Figure 3.4). Similarly, the mean mechanical apertures of all samples decreased with increasing confining pressure and also clearly depict the formerly observed hysteretic behavior during loading and unloading. Irreversible partial closure of the fracture after the respective loading-unloading cycle occurred in all samples, most pronounced in FF2, except in FOF4. Excluding FF1, which is not directly comparable since the confining pressure range is  $10 \leftrightarrow 35$  MPa, the total variations in the mean mechanical aperture of the mismatched fractures are significantly larger than those of the aligned fractures in both rock types. Again, the amount of irreversible fracture closure in the saw-cut sample FF4 is significantly larger than that in FOF4. It is further noticed that even for the same fracture setting (i.e., tensile or saw-cut, identical fracture wall offset), the deformation of the fractures in the two rock types differs significantly. Not least, this emphasizes the dominant role of both the rock's mechanical properties as well as the fracture's surface roughness in the deformational response of a fracture to changes in stress.

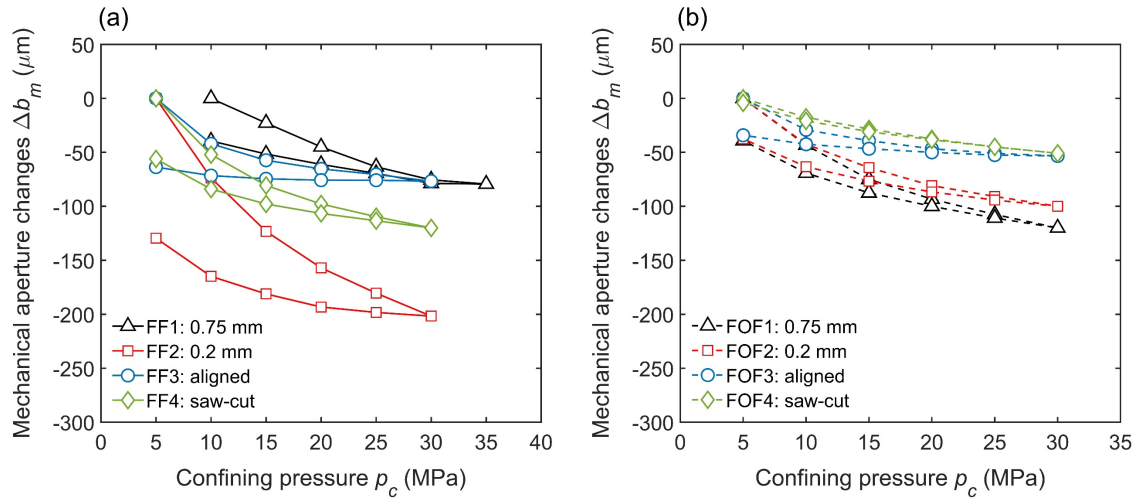


**Figure 3.5** Mechanical aperture changes  $\Delta b_m$  as a function of confining pressure for (a) Flechtinger sandstone samples and (b) Fontainebleau sandstone samples.

### 3.3.2 Surface roughness

3-D views of the scanned fracture surfaces and the corresponding central profiles along the specimen for samples FOF4 and FF4 (saw-cut fractures) as well as FOF2, FOF3, FF2, and FF3 (tensile fractures) are shown in Figure 3.6. The statistical parameters of the fracture surface roughness, as calculated with Eqs. 3.5-3.7, are listed in Table 3.2. It should be noted that these parameters are scale-dependent and related to the length scales of the measured data (i.e., the separation distance between two adjacent points in the raw surface data). However, all surfaces were measured at the same scale and with the same resolution (i.e., 23.518  $\mu\text{m}$  on the x-y plane and 1  $\mu\text{m}$  in the vertical direction). This resolution proved appropriate to observe most of the microstructural features (Figure 3.1) and also permits a direct comparison between samples.

The scanned surface data quantify the roughness of the different fracture types. Saw-cut fractures of both rock types are much smoother than all tensile fracture surfaces.  $R_m$  and  $R_{rms}$  of FOF4 and FF4 are almost one order of magnitude smaller in comparison to the corresponding values of the tensile fractures. However, the fracture surface of FOF4 is significantly smoother than the FF4 surface, which is also directly visible in Figures 3.6a and b. Again, for saw-cut samples, this implies a significant effect of the respective rock microstructure (e.g., grain size distribution and porosity) on the fracture's surface topography. For tensile fractures, surface roughness varies slightly between samples within one order of magnitude.

The 1-D power spectra of the central profiles of the fractures are presented in Figure 3.7. It is noticed that unlike for many igneous rocks such as granite, where the Hurst exponent  $H$  was found to be approximately 0.8 (e.g., Boffa & Allain, 1998; Schmittbuhl et al., 2008), suggesting that the fracture surfaces obey a universal invariance over a larger scale, the present fractures in sandstones likely have two main scaling regimes (Table 3.2). These two main scaling regimes display a larger slope at the smaller wavelengths and a smaller slope at the larger wavelengths. For tensile fractures, the Hurst exponent (Eq. 3.9, derived from the slopes in Figure 3.7) takes a value of  $H_1 = 0.54 \pm 0.04$ , distinctly smaller than  $H_2 = 3.34 \pm 0.21$ .  $H_1$  shows a good agreement with previous studies on sandstone samples ( $H \approx 0.5$  for a wavelength larger than the cut-off wavelength, i.e., the grain size) (Boffa & Allain, 1998; Ponson et al., 2007), which indicates that fractures in tight sandstones are not self-affine on all scales but that a self-similarity may only be valid within a certain range, again, different from igneous rocks. Moreover, the crossover wavelength can be well characterized by an intersection wavelength  $\lambda^*$  between about 300 ~ 400  $\mu\text{m}$ , which is about twice the average grain size and roughly equal to the largest grain size (Figure 3.1). At characteristic length scales below  $\lambda^*$ , the fracture surface roughness is not self-affine.

Particularly for saw-cut fractures, a tendency of the power spectrum to flatten out (i.e., the roll-off region) is observed as the wavelength increases above a certain wavelength  $\lambda^* = 420 \sim 430$   $\mu\text{m}$ , which corresponds to the largest grain size. Since power is proportional to the roughness amplitude, one consequence of this is that the fracture surfaces are independent of the observational length  $l$  for  $l \gg \lambda^*$  (Persson et al., 2004).

**Table 3.2** Statistical surface roughness parameters of selected samples.

Parameters	FF2	FF3	FF4	FOF2	FOF3	FOF4
$R_p$ (mm)	0.810	1.155	0.388	0.935	0.685	0.167
$R_m$ (mm)	0.194	0.251	0.034	0.214	0.152	0.011
$R_{rms}$ (mm)	0.238	0.317	0.044	0.267	0.191	0.015
$H_1$ (-)	0.56	0.58	-0.08	0.50	0.55	-0.24
$H_2$ (-)	3.55	3.49	3.37	3.13	3.14	2.86

$H_1$  and  $H_2$  represent the Hurst exponents for small and large wavevectors, respectively (Figure 3.7). In the regimes of  $H_2 > 1$ , the spectra do not follow a self-affine-like power law, which implies that the surface cannot be classified as fractal. A negative  $H_1$  in saw-cut fractures indicates a roll-off wavevector region.

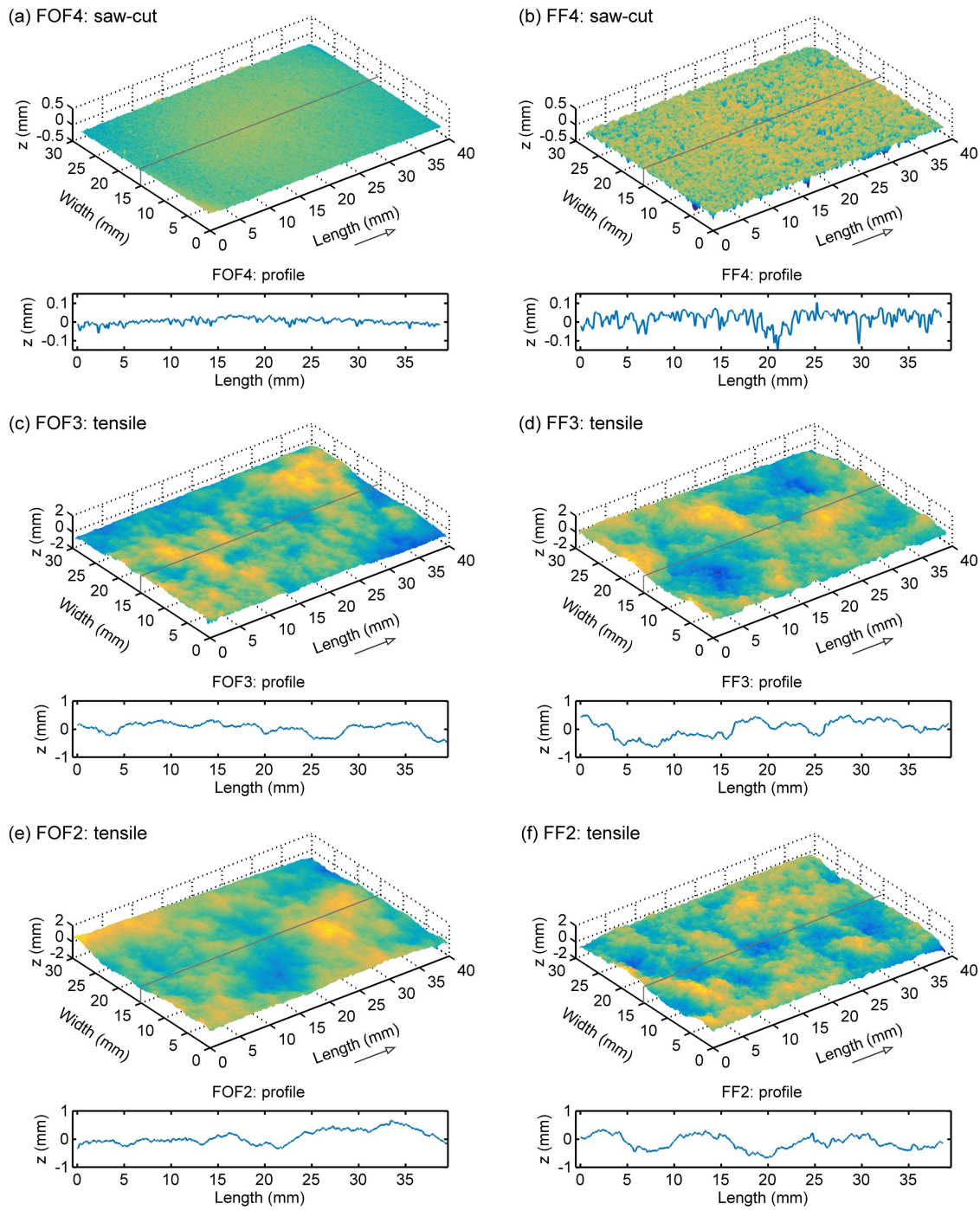


**Figure 3.6** 3-D views of the fracture surfaces of the scanned specimens and their corresponding central profiles along the sample length. The arrows indicate the flow direction in the experiments. (a) FOF4 saw-cut smooth fracture surface; (b) FF4 saw-cut rough fracture surface; (c) FOF3 tensile Fontainebleau fracture surface; (d) FF3 tensile Flechtinger fracture surface; (e) FOF2 tensile Fontainebleau fracture surface; (f) FF2 tensile Flechtinger fracture surface.

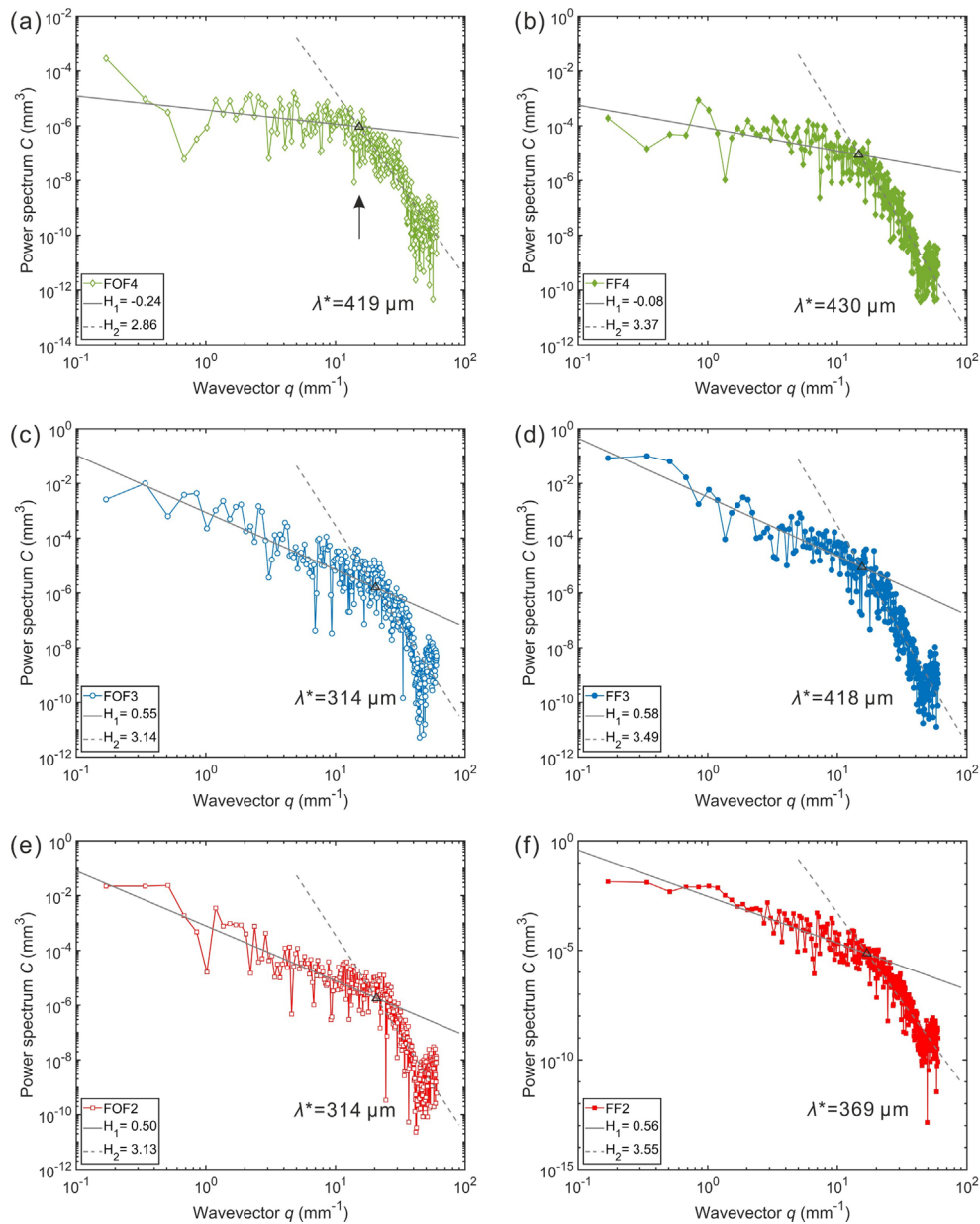


**Figure 3.7** 1-D surface roughness power spectra of the central profiles in the direction parallel to the displacement of fracture surfaces in (a) FOF4, (b) FF4, (c) FOF3, (d) FF3, (e) FOF2, and (f) FF2 (Figure 3.6), where  $H_1$  and  $H_2$  represent the Hurst exponents for small and large wavevectors, respectively, and  $\lambda^*$  indicates the crossover (black triangles) of the two regimes.

### 3.3.3 Numerical fracture apertures

The initial mean mechanical aperture (calculated with Eq. 3.10) between the two adjacent fracture surfaces of the selected samples was derived as a function of the fracture wall offset, as shown in Figure 3.8a. The mean mechanical aperture of all tensile fractures, initially, drastically increases



with increasing offset and then progressively tends to converge, where a further increase of the displacement yields only small aperture fluctuations. Thus, the trend can be roughly classified into three regimes. This is consistent with experimental observations regarding the shear dilation of fractures (Chen et al., 2000). In a theoretical study, Plouraboué et al. (1995) concluded that a rigid mechanical aperture with ongoing horizontal displacement is supposed to scale as  $b_m \propto Z\delta^H$  if the fracture surfaces are self-affine and invariant over a larger scale (e.g.,  $H=0.83$  for a granite fracture investigated in the cited study). Here,  $Z$  is a correction term that is inversely proportional to the displacement  $\delta$ . The present results indicate that the fracture aperture variations cannot be described by a simple power law (Figure 3.8b). In addition, the self-affinity is only valid when the wavelength  $> \lambda^*$ . For  $\delta < \lambda^*$ , this may not strictly apply, in contrast to Plouraboué et al. (1995). Furthermore, it was found that the fracture aperture remains approximately constant when further displacing the surface beyond one-tenth of the sample size.

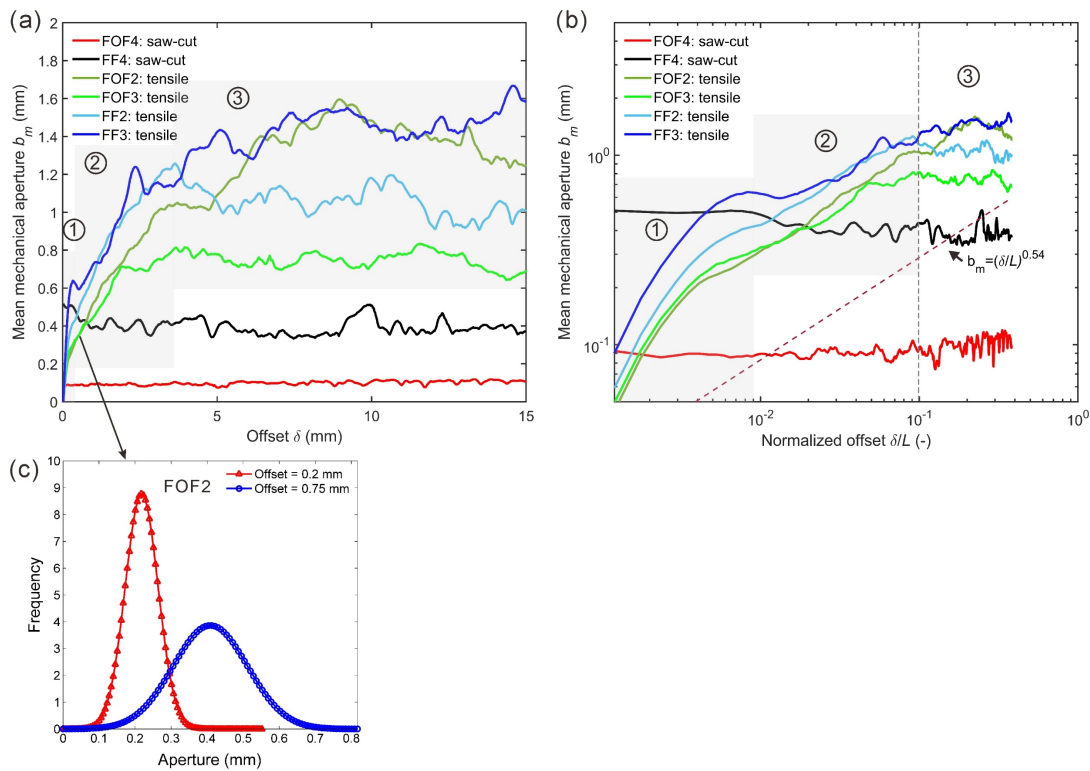


**Figure 3.8** (a) Evolution of the initial mean mechanical aperture with increasing offset of the two adjacent fracture surfaces along the sample length. (b) log-log plot of the initial mean mechanical aperture with normalized offset  $\delta/L$ . The dotted line indicates a simple power law,  $b_m=(\delta/L)^H$ , where  $H=0.54$  corresponds to the present sandstones (Figure 3.7). (c) Representative aperture distributions of sample FOF2 with offsets of 0.2 mm and 0.75 mm, respectively.



The respective convergence aperture values of each rock sample are directly related to the individual fracture's surface roughness. In contrast, for the saw-cut fractures FF4 and FOF4, the initial mechanical apertures show to be more or less independent of the offset, resulting from the existence of a roll-off wavelength (Section 3.3.2), which is consistent with the mathematical analyses of Plouraboué et al. (1995). Here, the initial mechanical aperture is only determined by the surface roughness, which is related to the intrinsic microstructure of the rock matrix. Accordingly, the average  $b_m$  of FF4 and FOF4 during shearing from 0 to 4 mm (i.e., one-tenth of the sample length), as calculated based on the surface models, are 0.42 mm and 0.09 mm, respectively. In addition, the mean  $b_m$  of FF2 and FOF2, which were calculated with a pre-offset of 0.2 mm, equivalent to the true experimental setting, are 0.4086 mm and 0.2584 mm, respectively. Figure 3.8c shows a comparative (numerical) example of the variations in aperture distribution of sample FOF2 for two different offsets (i.e., 0.2 mm and 0.75 mm).

By applying the interpenetration model to the fracture surfaces (Section 3.2.3), one further obtains the evolution of the mean mechanical aperture as a function of the contact area ratio (Eq. 3.11), as shown in Figure 3.9. The initial apertures of the aligned saw-cut fractures in FF4 and FOF4 are 0.517 mm and 0.0868 mm, respectively. For tensile fractures, Figure 3.9b demonstrates that a decrease of the mean mechanical aperture leads to a nonlinear increase in contact area ratio. It is inferred that the residual mechanical aperture and thus the maximum aperture closure value are proportional to the initial mechanical aperture, which well explains the differences in fracture aperture changes observed in the experiments (Figure 3.5).

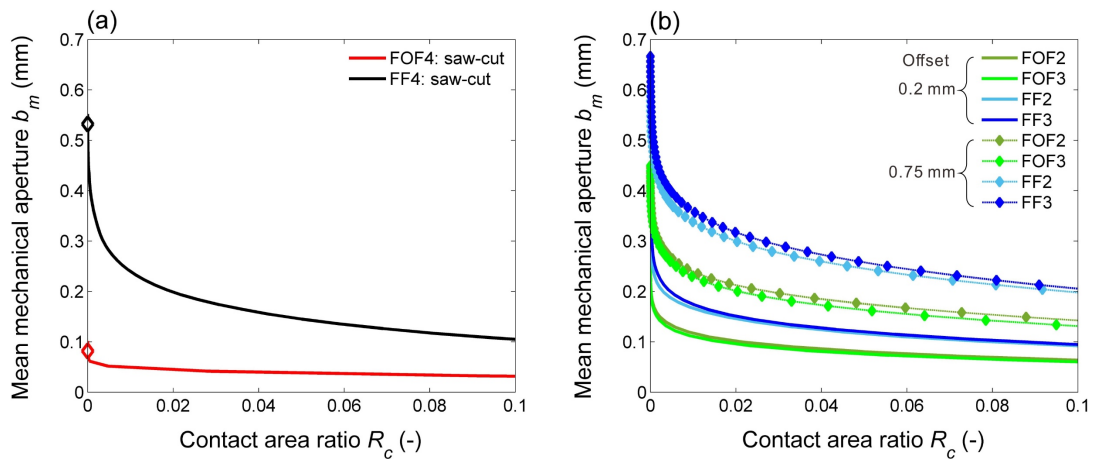


**Figure 3.9** Variations of the mean mechanical aperture  $b_m$  (Eq. 3.10) with increasing contact area ratio  $R_c$  (Eq. 3.11) for (a) saw-cut fractures in FF4 and FOF4 and (b) tensile fractures in FF2, FF3, FOF2, and FOF3.

### **3.3.4 Evolution of fracture aperture and contact area ratio based on X-ray $\mu$ CT**

The initial and final fracture apertures were determined based on the 3-D reconstructed  $\mu$ CT models shown in Figure 3.10. As an exception, the samples FF4 and FOF4 were only scanned before the experiment. It is noticed that all tensile fractures show a substantial change after the experiments, where the contact area has drastically increased. For the aligned tensile fractures FF3 and FOF3, the aperture uniformly decreased so that the residual voids, as detected in the models, appear disconnected after the experiment. Although the initial (unstressed) mechanical aperture can be determined by the CT scans, there is a remaining observational gap between zero-stress conditions and the experimental effective starting stress of 4 MPa. Therefore, only the initial and final mechanical apertures at atmospheric conditions are compared.

The respective contact area ratio before and after the experiment was derived from the projections of the extracted fracture voids (Figure 3.11). The  $\mu$ CT-derived contact areas show a good agreement with the observed damage areas in the fracture surfaces after the experiments, particularly for the displaced Flechtinger samples (Figure C2). The contact areas in the mismatched tensile fractures, representing the permanent damage zones, either enlarged from pre-existing asperities in contact or occurred as new contacts. The contacts are mostly isolated, but some asperities have merged, resulting in a larger contact area. This is particularly observed in Flechtinger sandstone and the Fontainebleau sample with the largest offset (FOF1). In addition, the extension of the contact area is oriented perpendicular to the direction of the shear displacement, which is consistent with previous observations (Auradou et al., 2005; Nemoto et al., 2009). Due to resolution limitations, a similar analysis of the aligned and the saw-cut fractures was difficult to perform.

The mean mechanical apertures and contact area ratios of the samples before and after the experiments based on the  $\mu$ CT models and the fracture projections are listed in Table 3.3. For both rock types, an increase in the fracture wall offset significantly increases both the initial and final apertures and decreases the final contact area ratio. Generally, the mismatched Flechtinger sandstone samples show a larger contact area ratio than the corresponding Fontainebleau sandstone samples. However, a quantitative comparison between samples may lead to misinterpretation due to the differences in surface roughness (Table 3.2). Finally, when comparing the derived initial and final mechanical apertures and the measured initial and final hydraulic apertures, both at a given offset and between offsets, it shows that the variability of the mechanical apertures is significantly larger than that of the hydraulic apertures. A direct comparison and validation of mechanical apertures derived from surface topography calculations and  $\mu$ CT models are difficult, as shown in Table 3.4. This is because of the assumptions of a grid-body and a minimum contact area in surface

analyses and the resolution differences between the methods.

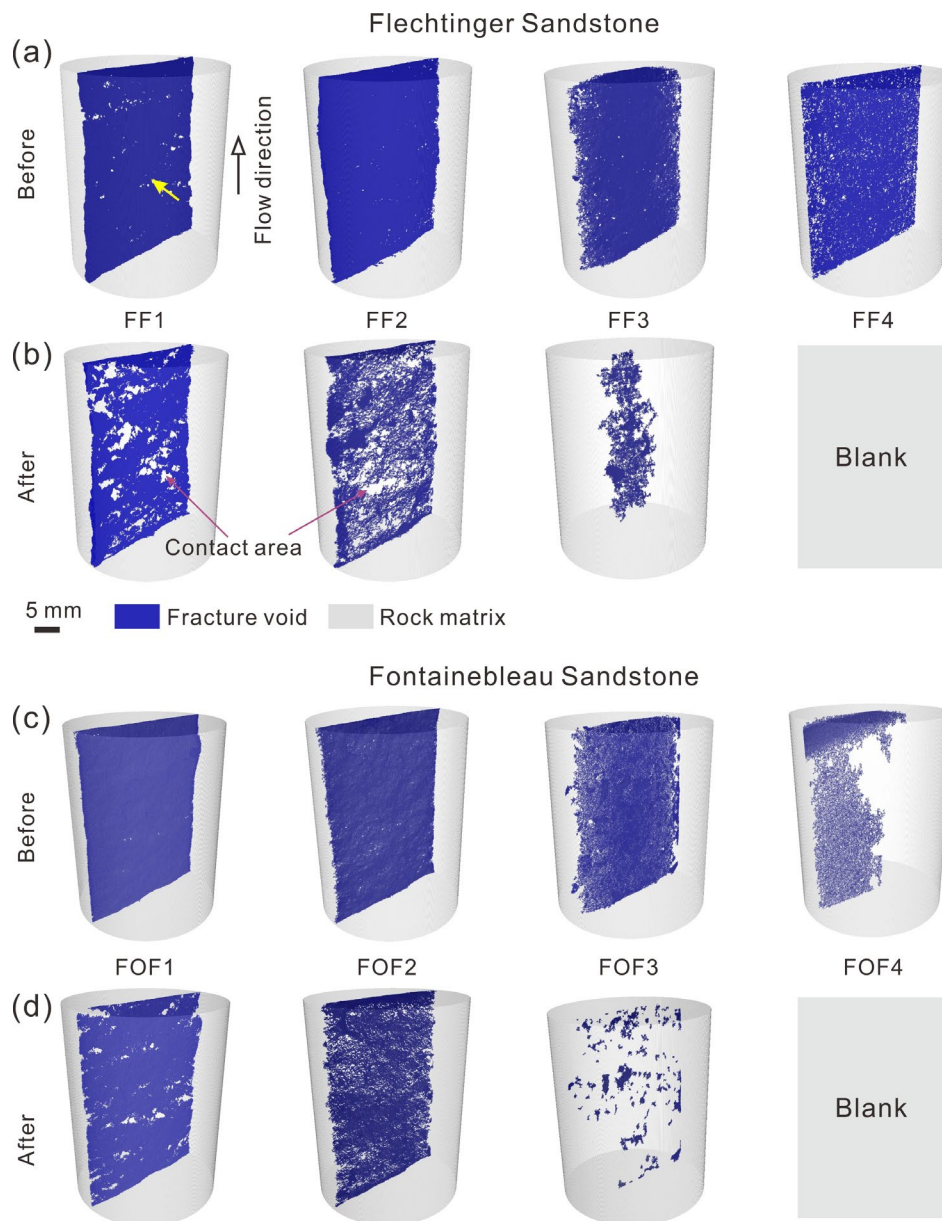


**Figure 3.10** 3-D reconstructed models of the assembled dry rock samples of Flechtinger sandstones (a) before and (b) after the experiments as well as Fontainebleau sandstones (c) before and (d) after the experiments, respectively. The images were obtained from X-ray  $\mu$ CT scans at atmospheric conditions. The fracture void spaces (in blue) of each sample were extracted and the pore spaces in the rock matrix (porosity: 8.1% for Flechtinger samples and 2.5% for Fontainebleau samples) were considered to be negligible. The areas in the fractures shown in the same color as for the matrix indicate the contacting asperities, where the fracture void space is considered to be zero. The yellow arrow indicates the line of sight perpendicular to the fracture projections displayed in Figure 3.11.

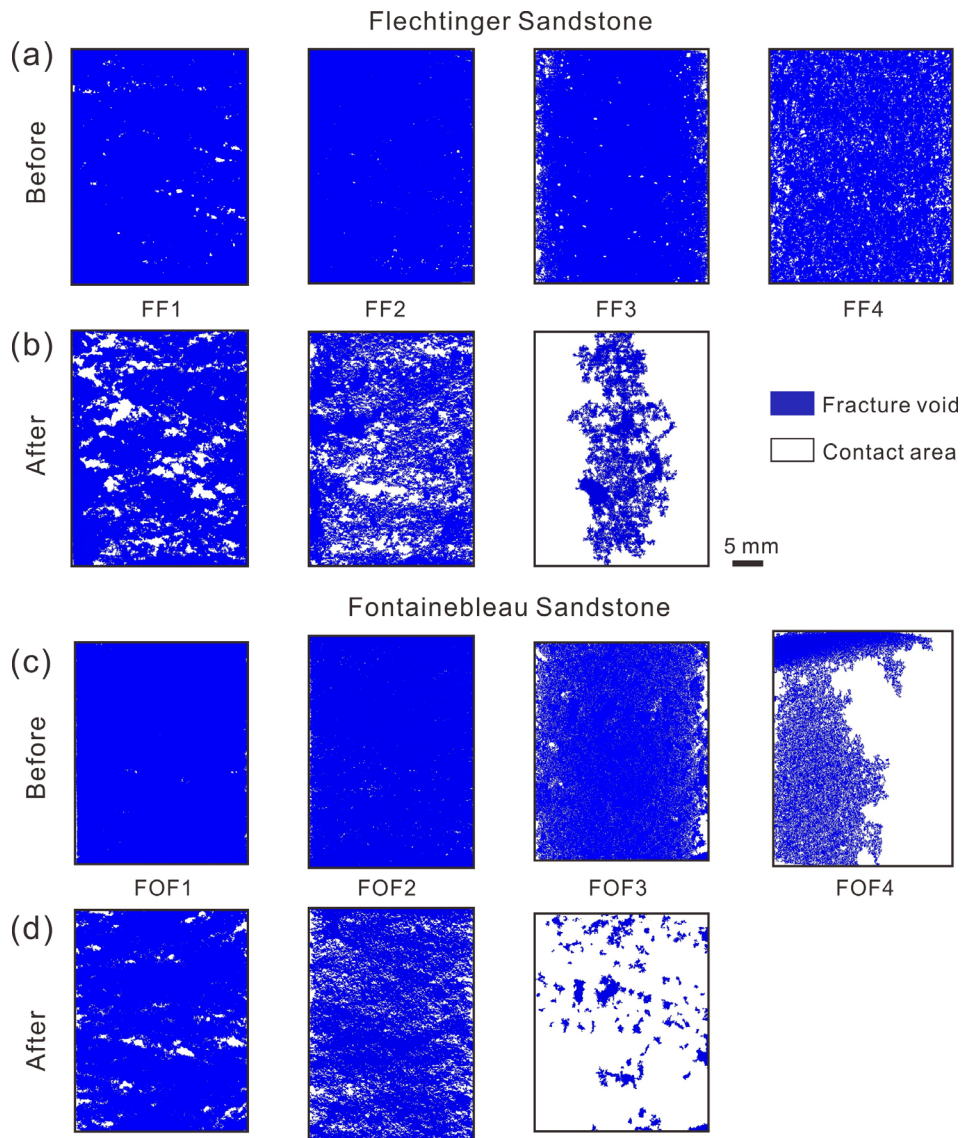


**Figure 3.11** 2-D projections of the extracted fracture void space from the  $\mu$ CT models shown in Figure 3.10. Flechtinger sandstones (a) before and (b) after the experiments as well as Fontainebleau sandstones (c) before and (d) after the experiments, respectively.

**Table 3.3** Evolution of mechanical aperture and contact area ratio determined by analyzing the 3-D X-ray  $\mu$ CT models.

Sample	Offset (mm)	$b_{m-ct}$ ( $\mu$ m)		$\Delta b_{m-ct} / b_{m-ct}$ (%)	$R_{c-ct}$ (%)		$b_h$ ( $\mu$ m)		$p_e$ (MPa)
		Before	After		Before	After	Initial	Final	
FF1	0.75	508.2	279.1	45.08	0.99	11.43	72.5	61.8	9
FF2	0.2	352.9	107.6	69.51	0.36	25.11	67.1	32.2	4
FF3	Aligned	160.8	24.7	84.64	3.89	73.77	23.9	6.1	4
FF4	Saw-cut	119.6	/	/	9.69	/	51.3	46.2	4
FOF1	0.75	365.4	186.7	48.91	0.75	3.67	57.7	61.9	4
FOF2	0.2	185.5	99.2	46.52	0.88	15.54	57.8	56.3	4
FOF3	Aligned	89.3	15.3	82.87	11.33	88.26	36.5	29.1	4
FOF4	Saw-cut	23.5	/	/	61.75	/	9.4	5.4	4

The mechanical aperture  $b_{m-ct}$  and the contact area ratio  $R_{c-ct}$  are obtained based on Eqs. 3.12 and 3.13, respectively.

**Table 3.4** Comparison of initial mechanical apertures obtained from surface topographies (Section 3.3.3) and  $\mu$ CT models (Table 3.3).

Methods	FF2 ( $\delta$ : 0.2 mm)	FOF2 ( $\delta$ : 0.2 mm)	FF4 (saw-cut)	FOF4 (saw-cut)
Surface data $b_m$ ( $\mu$ m)	408.6	258.4	517.0	86.8
$\mu$ CT models $b_{m-ct}$ ( $\mu$ m)	352.9	185.5	119.6	23.5

## 3.4 Discussion

### 3.4.1 Correlation between hydraulic aperture and mechanical aperture

For all experiments, the measured hydraulic apertures and the mechanical apertures derived by the drained compression tests (Section 3.3.1) and the  $\mu$ CT scans (Section 3.3.3) showed significant differences. Figure 3.12 shows the correlation between the changes of the hydraulic and mechanical apertures at effective stresses in the range between 4 and 29 MPa in comparison to a previous study on an aligned and a mismatched granodiorite fracture (Hofmann et al., 2016). It is noticed that the changes of the mechanical and the hydraulic apertures of the aligned fractures are in better agreement compared to the other samples as these data are closer to the " $\Delta b_h = \Delta b_m$  line". In addition, there is no significant difference between the sandstone samples used in this study and

the granodiorite rock reported in the literature (Hofmann et al., 2016), even though their mechanical properties are significantly different. Considering a simple linear correlation  $\Delta b_h = S\Delta b_m$  during loading (where  $S$  is a slope) for all mismatched fractures (including saw-cut fractures, which also represent a kind of mismatch at the microscale),  $S_{\text{mis}} < S_{\text{ali}} < 1$  indicates that the variations in mechanical aperture are significantly larger than those of the hydraulic apertures, which is also consistent with previous studies on granitic fractures (Durham & Bonner, 1994; Chen et al., 2000; Hofmann et al., 2016; Vogler et al., 2016). Moreover, in comparison to  $R_{\text{c-ct}}$  after the experiments (Table 3.3), it is found that  $S \propto R_{\text{c-ct}}$ , implying that the contact area ratio controls the slopes of this linear correlation. Furthermore, the range of mechanical aperture changes under stress is proportional to their initial apertures.

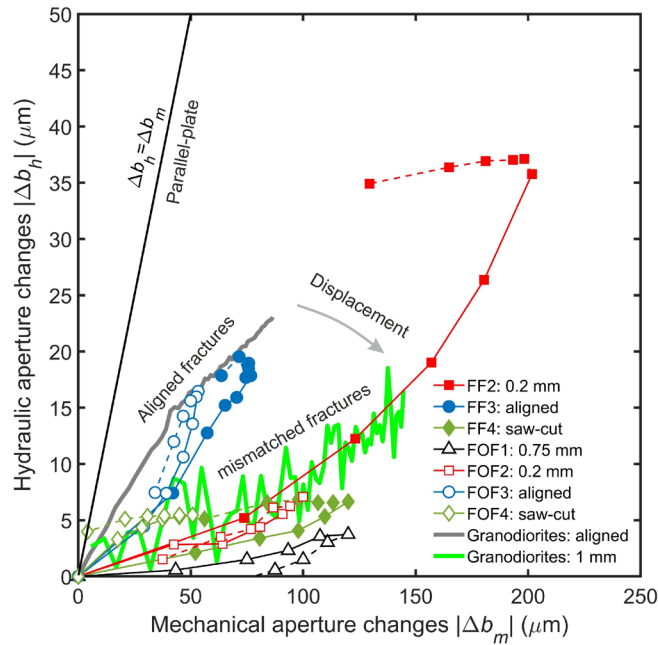


**Figure 3.12** Changes of hydraulic aperture  $|\Delta b_h|$  as a function of mechanical aperture changes  $|\Delta b_m|$  at different effective stresses as calculated from a comparison with the starting values at effective stress of 4 MPa (loading in solid lines and unloading in dotted lines). Results for an aligned granodiorite fracture and a similar fracture with an offset of 1 mm at effective stresses in the same range (i.e., between 4 and 29 MPa) were taken from Hofmann et al. (2016), where confining pressure was continuously varied during the measurements (bold lines), in contrast to the present study where confining pressure was changed stepwise in intervals of 5 MPa (filled and open dots).

The main reason for this discrepancy is the assumption of the smooth parallel-plate model "cubic law" for the calculation of the hydraulic aperture (Witherspoon et al., 1980). Fracture surfaces are in contact at the propping asperities, which are local features rather than being

expanded over a larger area (Figure 3.11). Fracture surfaces are rough rather than ideally smooth, and hence the fluid flow is tortuous within channels defined by the asperities. Therefore, a reduction of the mechanical aperture induced by stress variations does not have an equivalent effect on the flow channels. However, the aperture of an aligned fracture between the opposing fracture surfaces is likely more uniform, and fluid flow may be only affected by the surface tortuosity rather than by flow channels.

This behavior likely results from the differences in normal fracture stiffness (Figure 3.13). The respective stiffness is almost linearly correlated to confining or effective pressure (Raven & Gale, 1985) and the slope of the correlation decreases with increasing fracture wall offset. When compared to the contact area ratio (Table 3.3), the stiffness of the specific rock type shows the same sample order (e.g.,  $R_{c-ct}$ : FOF3>FOF4>FOF2>FOF1 and slope of the stiffness-pressure curve: FOF3>FOF4>FOF2>FOF1). Consequently, the fracture stiffness is mainly determined by the contact area ratio and the mechanical properties (e.g., Young's modulus) of the asperities that bear the normal stress. This affects the correlation between  $\Delta b_h$  and  $\Delta b_m$  significantly.

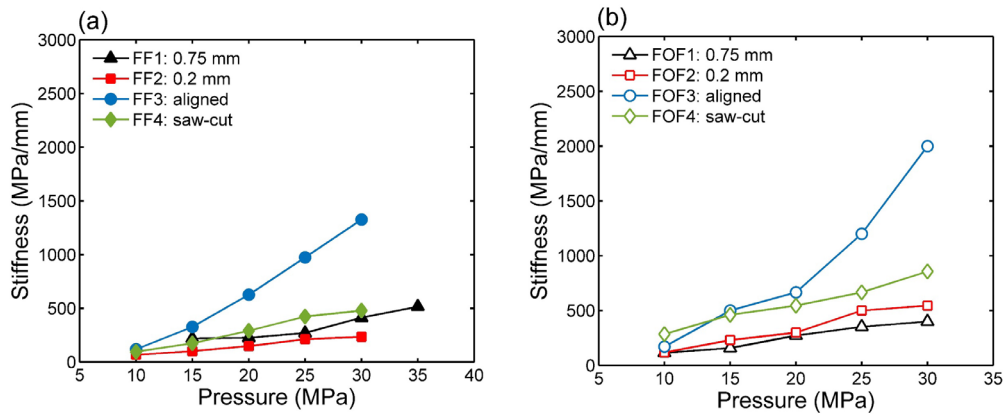


**Figure 3.13** Normal stiffness of the fractures for (a) Flechtinger sandstone samples and (b) Fontainebleau sandstone samples as a function of confining pressure.

A conceptual model is proposed to describe the correlation between hydraulic and mechanical aperture changes under normal stress (Figure 3.14), where the ideal parallel-plate model is presented as a comparison. An aligned rough fracture yields a large contact area ratio and a small initial aperture due to the matching geometry of the fracture surfaces. The flow is mainly affected by the surface tortuosity, and thus the correlation slightly deviates from the ideal case. However, fracture dilation occurs when the surfaces are displaced (Figure 3.8a), leading to a larger initial aperture and a smaller contact area ratio (Table 3.3). Thus, mechanical aperture changes increase under stress. Depending on the strength of the contact asperities to withstand high normal stresses,



hydraulic aperture changes much less upon loading. Therefore, the displaced self-propping fractures should possess rather sustainable hydraulic properties under normal stress. The quantitative effects of surface roughness and offset on fracture aperture will be discussed in Section 3.4.2.

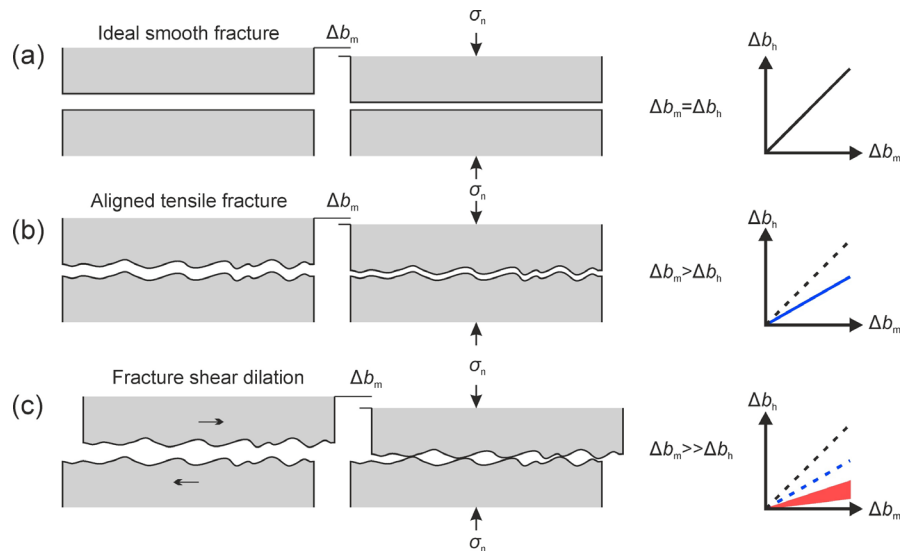


**Figure 3.14** Conceptual model of fracture closure for different fracture types: (a) ideal smooth fracture; (b) aligned rough fracture; (c) displaced rough fracture. The respective correlations between hydraulic and mechanical apertures are depicted on the right.

Previous theoretical and experimental studies on fluid flow in deformable fractures indicate that the hydraulic aperture can be significantly smaller than the mechanical aperture, and a threshold may be reached below which a further reduction in mechanical aperture does not affect the hydraulic aperture (Raven & Gale, 1985; Renshaw, 1995). Most existing correlations between hydraulic and mechanical apertures include either the standard deviation of the aperture (Zimmerman et al., 1991; Renshaw, 1995), the joint roughness coefficient (JRC) (Barton et al., 1985), or the contact asperity ratio (Walsh, 1981). However, recent experimental investigations imply that a stress-dependent anisotropic flow occurs in tensile fractures with displacement (Auradou et al., 2005). The permeability (i.e., the hydraulic aperture) in the direction parallel to the displacement can be three orders of magnitude smaller than that in the direction perpendicular to the displacement, at stresses up to 70 MPa (Nemoto et al. (2009), as also supported by numerical studies (Thompson & Brown, 1991; Méheust & Schmittbuhl, 2001; Matsuki et al., 2006; Lang et al., 2018). Zimmerman et al. (1992) conclude that the permeability of a fracture not only depends on the size of the contact area but also on the shape of the propping asperities. The direct observations on contact asperities show that a preferential orientation of the contact area (i.e.,



perpendicular to the shear displacement) is induced when the adjacent fracture walls are offset. However, this is less obvious as the displacement is increased (Figure 3.11). In summary, without considering the aforementioned effects, the prediction of hydraulic aperture solely based on the average surface roughness, the mean aperture, or the contact area ratio would result in large uncertainties compared to the measured value, especially for fractures with a shear displacement.

### 3.4.2 Fracture roughness and displacement-related fracture aperture

The fracture apertures with displacement are likely determined by the scale-dependent surface roughness. For saw-cut fractures, where a roll-off region occurs, fracture aperture remains invariant when the offset  $\delta$  is larger than  $\lambda^*$  (Figure 3.7a and b), consistent with the numerical analysis of the measured surface data (Figure 3.8a). For tensile fractures, a drastic increase of fracture aperture occurs during the initiation of displacement until about 300~400  $\mu\text{m}$  (regime (1) in Figure 3.8a), which is equal to the crossover wavelength  $\lambda^*$  of these fractures (Section 3.3.2). This behavior is probably controlled by the intrinsic roughness at the grain scale (mostly intergranular fracturing, Figure C1). Moreover, a further increase in displacement  $\delta > \lambda^*$  yields slightly less increase in aperture (regime (2) in Figure 3.8a), and a tendency of the mean aperture to converge is observed in regime (3). The former may be related to the self-affine invariance of the surface. The latter regime (convergence), however, considering a larger fracture size (e.g., dm to m, rather than cm as in this study), may not exist unless a roll-off region occurs at some wavelength scale.

This scale-dependence issue commonly exists in laboratory studies due to the sample size limitations (Hofmann et al., 2016; Vogler et al., 2016; Crawford et al., 2017). However, for hydraulic fracturing induced fractures, which are in the scope of this study, and unlike faults, these are commonly not displaced by large amounts. A small offset may already sufficiently enhance the fracture transmissivity, and thus larger displacements are not necessary for this purpose. In addition, Therefore, laboratory studies on core samples may provide a well-founded lower bound for fracture permeability.

### 3.4.3 Aperture changes with effective stress

The initial contact area, the fracture surface roughness, and the strength of the asperities that are in contact are commonly considered as the factors that mainly determine the deformation of the fracture when subjected to normal stress variations (Bandis et al., 1983; Kling et al., 2018; Zou et al., 2019). Figure 3.15 shows the variation ranges of the hydraulic and mechanical apertures for all

samples. Flechtinger samples yield consistently larger changes in comparison to the corresponding Fontainebleau samples at the same stress conditions. This likely results from the differences in the mechanical properties of the asperities because the initial contact area ratios and the initial fracture apertures of the different samples with the same offset are in about the same range (Table 3.3), although the fracture roughness varies slightly between samples (Table 3.2). Moreover, when the fracture walls are offset, both rock types maintain relatively high hydraulic aperture values compared to the aligned samples due to shear dilation. The trend of dilatancy likely follows the same behavior as obtained from the numerical calculations in Figure 3.8a, where a drastic mechanical aperture increase occurs initially upon a one-two grain size offset, and any further displacement then has progressively less effect. With ongoing brittle asperity failure during loading, the contact area ratio increases. The  $\mu$ CT results clearly demonstrate that the contact area ratios of the mismatched Flechtinger samples are significantly larger than those of the corresponding Fontainebleau samples after the experiments (Table 3.3), which indicates that more permanent damage has occurred in the Flechtinger samples (Figure C2). However, an increase in fracture wall displacement leads to a noticeable reduction of the final contact area ratio in both rocks by increasing the mismatch of the adjacent fracture surfaces. The mechanical damage of the contact asperities only occurs locally unless the adjacent fracture walls are aligned (see cross-section images of the sample ends after the experiments in Figures C3 and C4). It is noticed that the larger the initial mean aperture, the larger is the final aperture (Table 3.3). The smallest contact area ratio of 3.7% (FOF1) was sufficient to keep the fracture open at effective stresses up to 29 MPa. Overall, the contact area is determined, firstly, by the mismatch of the fracture walls and, secondly, by the strength of the asperities. Therefore, a stronger rock (i.e., Fontainebleau sandstone in the present case) displays a significantly smaller contact area ratio than a comparatively softer rock.

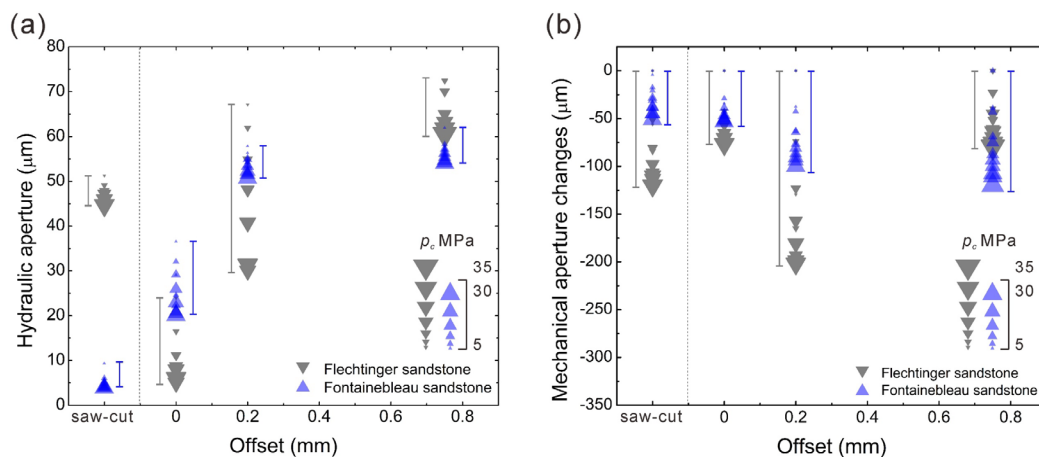


**Figure 3.15** Hydraulic aperture (a) and mechanical aperture changes (b) at the corresponding confining pressure as a function of the respective fracture wall offset.

### 3.4.4 Implications

Unlike randomly open fractures in granitic rocks, fractures generated in sedimentary formations might be largely affected by their intrinsic structure (e.g., bedding, anisotropy) that developed over geological time scales. The fracture surface roughness may be significantly different depending on the rock's individual microstructure. By analyzing the fracture surface roughness of an analogue rock, one may estimate the maximum self-propping potential upon fracture wall displacement based on the fracture surface information. By conducting laboratory flow-through experiments at varying normal stress, one can further estimate the sustainability of fracture permeability, which can be used as first-hand information to decide whether or not to use proppants in the target reservoir. For example, for a fracture surface roughness with a clear roll-off wavelength (Section 3.4.2), a shear displacement larger than this value would consequently have a rather limited effect on mechanical aperture. If the corresponding hydraulic aperture remains significantly small, in this case, proppants would be indispensable since self-propping of the fracture would not be sufficient to allow for substantial fluid flow. This circumstance may occur in anisotropic formations with well-oriented bedding layers and fractures generated along the bedding planes.

In the long term, self-propping fractures undergo a fundamental change in surface roughness by the destruction of asperities induced either by plastic deformation or pressure solution. The fracture surface is thus permanently reshaped in a way to ultimately be flat. Hydraulic stimulation treatments in such pre-existing fractures would be less efficient in comparison to freshly generated ones. Under these circumstances, again, introducing proppants into the fracture would be very helpful. It is worth noting that the contact asperities have a preferential orientation that generally is perpendicular to the displacement (Durham & Bonner, 1994; Méheust & Schmittbuhl, 2001; Nemoto et al., 2009), which is more pronounced when the offset between the adjacent fracture surfaces is small (Section 3.3.4). Therefore, an increase in the displacement would not only increase the aperture but also decrease the flow anisotropy within the fracture.

### 3.5 Conclusions

In the present study, stress-dependent hydraulic and mechanical fracture-aperture changes of displaced tensile fractures, aligned tensile fractures, and saw-cut fractures of two sandstones (i.e., Flechtinger and Fontainebleau) were experimentally investigated at cyclic confining pressures between 5 and 30 MPa. Fracture surface topographies were determined by white light interferometry and the spatial fracture configurations, including information on the contact

asperities, were analyzed with X-ray microtomography.

It was found that a relative fracture-wall displacement can significantly enhance fracture aperture both hydraulically and mechanically, but the enhancement depends on the fracture surface roughness. For saw-cut fractures, where a roll-off wavelength exists for the present sample size, the fracture surfaces remain scale-independent above this wavelength, where any increment of offset would not change the aperture. For tensile fractures, these are likely self-affine with a Hurst exponent of  $0.54 \pm 0.04$  over a larger scale, and thus, fracture aperture is scale-dependent and is consequently increasing with an increase in offset unless a roll-off wavelength occurs. A comparison between the mechanical and hydraulic apertures showed that the mechanical apertures varied significantly more than the corresponding hydraulic apertures for all samples, as is also illustrated in the proposed conceptual model.

The contact area ratio (after a loading-unloading cycle) is inversely correlated with the displacement, resulting from, firstly, the surface roughness and, secondly, the strength of the asperities that are in contact. The contact areas, generally, are oriented in a preferential direction perpendicular to the displacement causing an anisotropy of fluid flow. This anisotropy is more pronounced for small fracture wall offsets.

This study demonstrates the effects of surface roughness, fracture wall offset, and mechanical rock properties on hydraulic and mechanical aperture variations. These factors do not operate independently but act coupled. Rough fractures, an induced fracture wall offset, and relatively strong fracture asperities are essential to keep a fracture sufficiently conductive for fluid flow at stressed conditions. As shown with this study, the self-propping potential of sedimentary rocks can be investigated using analogue rock materials of contrasting mechanical properties to obtain information on how to better design hydraulic stimulation treatments of reservoir formations.

This study should stimulate a number of follow-up investigations with different focuses. Real-time in situ X-ray CT measurements permit monitoring of fracture closure with increasing stress and the evolution of mechanical aperture. Repeat measurements on samples with identically introduced fractures will disclose to what degree possible differences in surface microstructure affect the outcome of the present experiments for the different fracture types. Not least, a more detailed method comparison (i.e., between surface scanning,  $\mu$ CT, and numerical approaches) to derive the mechanical aperture fields and the corresponding contact area ratios will prove valuable for method evaluation and improved relationships between hydraulic and mechanical apertures.

# Chapter 4

## **Mechano-chemical effects on fracture aperture evolution: intermittent flow**

**F**ractures efficiently affect fluid flow in geological formations and thereby determine mass and energy transport in reservoirs. Their response to mechanical and thermal changes, as well as fluid-rock interactions, is of paramount importance. A two-stage flow-through experiment was conducted on a Fontainebleau core containing one macroscopic tensile fracture. In the first short-term stage, the effects of pressure and temperature cycles on the mechanical and hydraulic aperture were investigated. The purpose of the subsequent intermittent-flow long-term (140 days) stage was to constrain the evolution of the geometrical and hydraulic fracture properties resulting from pressure solution. Deionized water was used as the pore fluid, and permeability, as well as the effluent Si concentrations, were systematically measured. Overall, the hydraulic aperture was significantly less affected by pressure, temperature, and time than the mechanical aperture. During the long-term part of the experiment at 140 °C, the effluent Si concentrations likely reached a chemical equilibrium state within less than 8 days of stagnant flow and exceeded the corresponding hydrostatic quartz solubility at this temperature. This implies that the pressure solution was active at the contacting fracture asperities, both at 140 °C and after cooling to 33 °C. The higher temperature yielded a higher dissolution rate and, consequently, faster attainment of chemical equilibrium within the contact fluid. X-ray  $\mu$ CT observations evidenced a noticeable increase in fracture contact area ratio, which, in combination with theoretical considerations, implies a significant decrease in mechanical aperture. In contrast, the sample permeability virtually did not vary. In conclusion, pressure solution-induced fracture aperture changes are affected by the degree of time-dependent variations in pore fluid composition. In contrast to the present case of a quasi-closed system with mostly stagnant flow, in an open system with continuous once-through fluid flow, the activity of the pressure solution may be amplified due to the persistent fluid-chemical nonequilibrium state, thus possibly enhancing aperture and fracture permeability changes.

## **4.1 Introduction**

The long-term fluid and mass transport in fractured rock masses with low matrix permeability under crustal conditions are of significant importance, e.g., for the accumulation of mineral or ore deposits and deep geothermal energy utilization. Studies show that water-saturated quartz sands undergo substantial time-dependent compaction at constant pressure compared to dry aggregates (Schutjens, 1991). In addition, elevated temperatures significantly affect the compaction process of propped fractures (Polak et al., 2003; Yasuhara et al., 2006). The mechanism behind these phenomena is considered to be pressure-induced mineral dissolution. These combined effects are typical in hydrothermal, as well as in enhanced geothermal systems (EGS) when injecting or circulating fluids into or within the host rock. This, in turn, determines the sustainability and lifespan of these reservoirs, not least for resource exploitation and energetic use.

Stress-induced mineral dissolution has previously been studied in unconsolidated aggregates (e.g., quartz grains) under diagenetic conditions (Weyl, 1959; De Boer, 1977a; b; Robin, 1978; Niemeijer et al., 2002; Van Noort et al., 2008a) and in rock fractures (e.g., novaculite and granite) under hydrothermal conditions (Polak et al., 2004; Yasuhara et al., 2004; Yasuhara et al., 2006; Yasuhara et al., 2015). Previous studies provided insight into the mechanism of pressure-induced dissolution, which incorporates three processes: minerals in propping asperities (in fractures, or described as grain-to-grain contacts in aggregates) dissolve inside the contact areas, after which the dissolved minerals diffuse from the inside of the contacts to their peripheries through a thin water film between the adjacent asperities, and ultimately deposit on the free pore walls (Tada et al., 1987; Yasuhara & Elsworth, 2008). This process consequently drives the irreversible and time-dependent porosity reduction in grain aggregates and/or permanent fracture closure. In essence, the compaction of aggregates and the fracture closure result from the same mechanism. Pressure solution is described by a rate-limiting process. Therefore, the progress is determined by the slowest of the three processes above (De Boer, 1977a; Yasuhara & Elsworth, 2008). In addition to the stress-induced mineral dissolution, the solid phases on the free grain or fracture surfaces can also dissolve into the solvent, which is called free-face dissolution, yielding the retreat of these surfaces (Yasuhara et al., 2006; Lu et al., 2018). The two dissolution processes have opposite effects on the geometric alteration of the fracture's void space, thus overall determining the evolution of fracture permeability.

Previous studies have focused on compaction of a fracture associated with pressure solution in an open system with water circulation (Polak et al., 2003; Polak et al., 2004; Yasuhara et al., 2006), but most of these studies lack precise fluid chemical analyses. In an open system with water

circulation, equilibrium in rock-fluid (i.e., water) interactions is not reached as a result of the continuous fluid exchange. Therefore, the reaction between the rock and the fluids can continuously proceed (Polak et al., 2003; Yasuhara et al., 2006). In contrast, in a closed system without water circulation in the void space, a chemical equilibrium may be achieved with time, and the diffusion of the solute may be inhibited due to the progressive reduction of the concentration gradients. Therefore, a question can be raised, i.e., will the rate-limiting process of pressure solution reach some relative equilibrium, and does this consequently affect the progress of fracture closure?

Elias and Hajash (1992) investigated stress-induced quartz solubility using quartz aggregates in a closed system. Fluid samples were taken three times per week at 150 °C in irregular time intervals. The silica concentrations of the effluents were nonlinearly proportional to the applied pressure. Porosity continuously decreased at 150 °C but remained constant at 23 °C. It was concluded that both temperature and pressure played important roles in this process. Another study performed by Yasuhara et al. (2015) presents a long-term observation of the permeability evolution in Berea sandstone, containing a single saw-cut fracture, over about 1000 days. Effluent sampling and permeability measurements were intermittently conducted at regular time intervals of 5 or 10 days. There was almost no permeability reduction in the sample at 90 °C, while the permeability decreased by about one order of magnitude at 20 °C at the end of the experiment. The Si concentrations of the effluents decreased with time. This experiment cannot unequivocally prove that the permeability reduction was induced exclusively by pressure solution, for the following reasons: firstly, saw-cut fractures may lead to a large contact area, and the stress distribution on the bridging asperities may not be sufficient for pressure solution; secondly, the applied confining pressure of 7.5 MPa may be insufficient for reaching the minimum activation energy of pressure solution; and finally, the fracture volume is unknown. Even though the initial pore volume was about 7 ml, each sample volume of 7 ml can significantly dilute the fluid within the fracture, because, as the matrix permeability is significantly smaller than the fracture permeability, the fluid mainly flows through the fracture, rather than through the rock matrix.

Three main factors should be seriously considered in the experimental procedure of investigations into pressure solution creep: small contact area ratios and sufficient effective stresses are needed; the volume of each effluent sample should be equal to the fracture volume, and brittle damages or plastic deformations of the fracture due to mechanical compaction need to be precluded. This study presents a long-term experiment with intermittent flow-through permeability measurements, in conjunction with a chemical effluent analysis. Additionally, the rock sample was microstructurally investigated with a  $\mu$ CT scanner before and after the experiment to quantitatively analyze the induced fracture aperture variations.

## 4.2 Sample material and experimental methods

### 4.2.1 Sample preparation and experimental apparatus

Fontainebleau sandstone was used for this investigation, which is a monomineralic rock with more than 99.5 wt % of quartz. It has a low matrix permeability on the order of  $10^{-18}$  m<sup>2</sup> and low porosity of ~2.5%. A cylindrical sample with a diameter of 30 mm and a length of 40 mm was split by a Brazilian test setup into two halves. A single tensile fracture in the center of the rock sample was thus generated. Due to the geometry of the two halves, the fracture may immediately close under pressure when its two surfaces are aligned. Moreover, the matched fracture surfaces lead to a large contact area, and the stresses on the bridging asperities may be insufficient to induce pressure solution, even under a high confining pressure. Therefore, the two halves were shifted by 750  $\mu$ m along the principal axis using two spacers placed at the two ends of the sample (Figure 4.1a). This pre-displaced fracture is different from a shear fracture induced by shear movement under normal stress due to the absence of a gouge. Fracture aperture, in this case, is mainly self-propped by the contacting asperities associated with the fracture's surface roughness. Figure 4.1a shows the assembled sample, where a heat-shrink tubing (Figure 4.1b) restrains the two halves and isolates the confining pressure from the pore pressure medium when the assembly is in the pressure vessel. Representative propping asperities, fracture walls, and the fracture aperture are clearly visible in the magnified image taken by a micro-camera (Figure 4.1c).

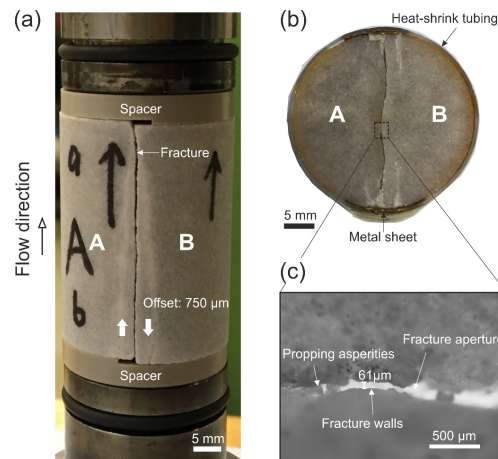


**Figure 4.1** (a) The cylindrical rock sample contains a single tensile fracture along its principal axis. (b) The assembled sample (view after the experiment) is constrained by heat-shrink tubing, and a metal sheet is placed between the fracture edges and the heat-shrink tubing to prevent the latter from punching under confining pressure. (c) A magnified image shows a representative microstructure of the fracture aperture (after the experiment), wherein propping asperities keep the fracture open, and the free fracture walls are directed toward the void space.



Figure 4.2 shows a sketch of the experimental apparatus used (Milsch et al., 2008b). The assembled sample is mounted in a hydrostatic pressure vessel, where the confining pressure is produced by a syringe pump (ISCO 65D, Teledyne, Lincoln, USA) using silicone oil. The oil within the pressure vessel can be heated with an electrical resistance heater connected to a temperature controller. The sample bottom is connected to an upstream pump (ISCO 260D, Teledyne, Lincoln, USA), and its upper end is connected to either a similar downstream pump or an adjustable relief valve. The downstream pump is used for maintaining a precise constant pore pressure during the permeability measurements. With the relief valve, the effluents can be sampled at a predefined and constant fluid pressure. A spiral capillary between the relief valve and the sample is placed in cold water ( $\sim 20\text{ }^{\circ}\text{C}$ ) and serves to cool the fluid during sampling. Water flows through the rock sample from the bottom to the top at a constant flow rate when sample permeability is measured. A differential pressure transducer (IPD 40, ICS Schneider Messtechnik, Hohen Neuendorf, Germany; 0–0.6 MPa range) is placed between the upstream and downstream ends of the sample to monitor pressure difference during the permeability measurements.

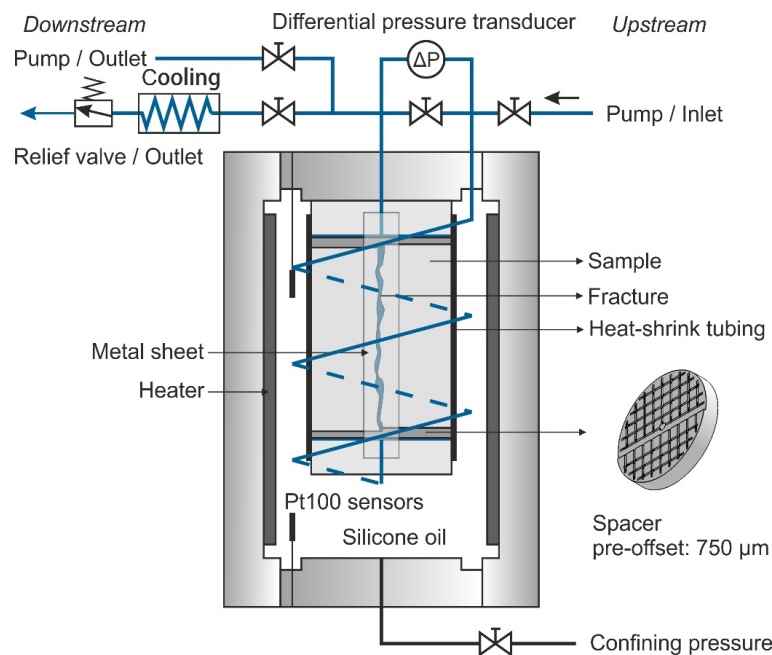


**Figure 4.2** Schematic illustration of the experimental apparatus used for the flow-through experiment. The assembled sample is mounted in a hydrostatic confining pressure vessel and isolated by heat-shrink tubing. The lower and upper sample ends are connected to syringe pumps (ISCO 260D), and a relief valve placed in parallel at the downstream side is used for effluent sampling.

**4.2.2 Experimental procedures**

Before the experiment, the sample was vacuum-saturated with deionized water. When applying confining pressure,  $p_c$ , to the rock sample for the first time, the contacting asperities will be subject to high-stress concentrations, yielding brittle damage and possibly some plastic deformation. The fracture aperture reduction resulting from this mechanical process is not related to any chemical reaction between the rock minerals and the fluid. On the other hand, a temperature increase may cause the volumetric expansion of the rock matrix and lead to geometrical changes of the aperture. Applying non-hydrostatic thermodynamics to pressure solution and free-face dissolution requires the assumption that all solid deformations are elastic and reversible (Engelder, 1982).

Therefore, in this study, three loading-unloading confining pressure cycles between 5 MPa and 30 MPa were performed. The pore pressure,  $p_p$ , was kept constant at 1 MPa throughout the experiment. The temperature,  $T$ , was then varied stepwise between room temperature and 140 °C. Permeability was measured at each constant  $P$  and  $T$  condition. After these initial pressure and temperature variations, constant pressure and temperature were applied for the long-term experiment of 137 days.

Table 4.1 shows the details of the experimental procedures, where the experiment follows the sequence of mechanical, thermal, and chemical operations. Permeability was measured after the fluid flow was halted for time intervals of 8 or 16 days at constant  $P$  and  $T$  conditions. The effluent was sampled before each permeability measurement.

**Table 4.1** Experimental conditions (pressures, temperatures, and the duration) of each stage.

No.	Operation	Duration (Days)	$p_c$ (MPa)	$p_p$ (MPa)	Temperature $T$ (°C)
1	Mechanical	Short-term	5↔10↔15↔20 ↔25↔30 <sup>a</sup>	1	26
2	Thermal	Short-term	10	1	26↔60↔95↔140 <sup>b</sup>
3		0–4	30	1	33→59→86→112→140 <sup>c</sup>
4	Chemical	4–117	30	1	140
5		117–133	10	1	140
6		133–141	10	1	33

<sup>a</sup> Confining pressure was varied stepwise in a cycle between 5 and 30 MPa and was further varied twice continuously in a cycle between 10 and 30 MPa. <sup>b</sup> Temperature was cycled stepwise between room temperature and 140 °C. <sup>c</sup> Temperature was increased stepwise to 140 °C and was then maintained constant for the long-term observations.

### **4.2.3 Sampling and chemical fluid analysis**

Deionized water was used as the permeant throughout the experiment. During the long-term intermittent flow-through experiment (after the mechanical and thermal operations), the flow was stopped for intervals of 8 or 16 days. The fluid within the fracture aperture may gradually reach an elevated element concentration due to fluid-rock interactions. The fluid volume in direct contact with the solid phases within the fracture void space should be approximately equal to the aperture volume. However, the rock sample from end to end was not completely isolated from the pore fluid system. The fluid volume within the apparatus's pore fluid system was significantly larger than the aperture volume. Consequently, the comparatively large volume of the effluent taken for one sample will result in the dilution and mixing of the actual fluid within the fracture, leading to incorrect results of element concentration. On the other hand, one cannot precisely determine the volume within the relief valve and the capillaries at the downstream side. As such, a sample with an improper volume correction may also cause erroneous results.

To better detect and sample the fluid originating from the fracture itself instead of from any other part of the pore fluid system, 20 continuous effluent subsamples were taken from the outlet capillary (i.e., the relief valve in Figure 4.2) at a constant flow rate of 0.5 ml/min, having a volume of about 0.5 ml each. A permeability measurement was subsequently conducted. Therefore, the pore fluid system, including the fracture, was completely flushed with deionized water, causing a reset of the pore fluid composition.

The subsamples were then diluted ten times, and the silica (Si) element concentration was immediately measured by a photometer (Filterphotometer photoLab WTW-S12, Xylem Analytics, Weilheim, Germany) at a wavelength of 665 nm in a measurable range of 0.1–5 mg/l Si. In addition, two series of subsamples were analyzed with an inductively coupled plasma-optical emission spectrometer (5110 ICP-OES, Agilent, Santa Clara, CA, USA).

Silica may exist as soluble silica, as colloids, or as suspended particles in water. It may also be monomeric or polymeric, depending on the aqueous conditions. The test method of the photometer is based on the blue reduced silicomolybdate complex, and this method can only measure the molybdate-reactive silica (i.e., mainly dissolved silicates, monomeric silica, and silicic acid) in water. Highly polymerized or colloidal silica does not react with the molybdate reagent and consequently cannot be detected. Therefore, the results derived with a photometer may underestimate the actual Si concentration when high amounts of polymers exist. However, and in contrast, ICP-OES can determine the total silica concentration of all silica types in water (Aureli et al., 2020).

#### 4.2.4 Determination of fracture aperture

The downstream side of the pore fluid system was switched from the relief valve to the downstream pump after effluent sampling (Figure 4.2). Permeability was subsequently measured at a constant flow rate,  $Q$ , higher than that used during the sampling procedure. The differential pressure,  $\Delta p$ , between the sample ends, was monitored with a differential pressure transducer. With the assumptions that Darcy's law is valid and that the flow of the incompressible Newtonian fluid in the fracture is laminar, by applying the parallel plate model and the related so-called "cubic law", hydraulic aperture,  $b_h$ , can be expressed as (Witherspoon et al., 1980; Zimmerman & Bodvarsson, 1996),

$$b_h = \sqrt[3]{\frac{12\mu LQ}{W\Delta p}} \quad (4.1)$$

where  $\mu$ ,  $W$  and  $L$  are fluid viscosity, fracture width (sample diameter), and sample length, respectively.

After each permeability measurement, all valves were closed except for the inlet-valve of the downstream pump to minimize the pore fluid volume. The downstream pump was needed to maintain a constant pore pressure (1 MPa) within the sample. Additionally, during purely mechanical stage 1 (Table 4.1), the total fluid volume changes,  $\Delta V$ , in the pore fluid system were monitored during the loading-unloading cycles using the downstream pump. The mechanical aperture changes were subsequently calculated from,

$$\Delta b_m = \frac{\Delta V - \Delta V_p}{WL} \quad (4.2)$$

where  $\Delta V_p$  is the corresponding pore volume change of the rock matrix, which can be theoretically estimated based on linear isotropic poroelasticity (Carroll & Katsube, 1983),

$$\Delta V_p = V_b \left( \frac{1}{K_b} - \frac{1}{K_s} \right) \Delta p_e \quad (4.3)$$

where  $\Delta p_e$  is the effective pressure change,  $V_b$  is the sample bulk volume, and  $K_b = 34$  GPa is the static bulk modulus of a Fontainebleau sandstone with a porosity of 2.5%, estimated based on (Arns et al., 2002) and assumed constant in the pressure range between 5 and 30 MPa. The crack porosity of a Fontainebleau sandstone with a porosity of 4%, closed at an applied initial stress of 5 MPa, is only 0.01% (David et al., 2013), which thus can be neglected in the present calculations. Finally,  $K_s$  is the solid bulk modulus of the quartz grains, generally taken as 37 GPa (Sulem & Ouffroukh, 2006).

#### **4.2.5 X-ray micro computed tomography ( $\mu$ CT)**

The microstructure of the assembled but dry sample was observed with an X-ray  $\mu$ CT scanner (GE Phoenix nanotom m 180) before and after the experiment, under atmospheric conditions. To ensure the comparability of the data, the same measurement settings (i.e., timing: 500 ms, voltage: 120 kV, current: 90  $\mu$ A) were used, and a total of 1080 slices were taken at a resolution of 20.63  $\mu$ m. Three-dimensional (3-D) models of the rock sample were then reconstructed based on all of these slices. The fracture void space was finally extracted from the 3-D model and analyzed. Due to the low matrix permeability and the low porosity of the sample, the matrix pore space was not investigated further.

### **4.3 Results**

#### **4.3.1 Effects of pressure and temperature on fracture aperture**

The hydraulic aperture decreased from 57  $\mu$ m to 54  $\mu$ m when the confining pressure was increased from 5 MPa to 30 MPa at room temperature. Unloading stepwise to 5 MPa led to a slight increase of the hydraulic aperture to 62  $\mu$ m. This could result from the migration of some brittle particles within the fracture during unloading. The subsequent two loading-unloading cycles showed that the hydraulic aperture was ultimately constant, being 58  $\mu$ m and 54  $\mu$ m at confining pressures of 10 MPa and 30 MPa, respectively (Figure 4.3a).

In contrast, Figure 4.3b shows that the mechanical aperture varies significantly more as the confining pressure changes. The first loading-unloading cycle, between 5 MPa and 30 MPa, caused an irreversible aperture reduction of about 40  $\mu$ m. The following two cycles, between 10 MPa and 30 MPa, showed progressively less irreversible fracture closure, which indicates that the mechanical deformation tends to become purely elastic. One can infer that these initial loading-unloading operations have settled and stabilized the fracture so that any further irreversible changes of fracture aperture can be considered to be fully attributable to other processes, e.g., fluid-rock interactions.

During the subsequent thermal operation stage (Figure 4.4), the temperature cycle between room temperature and 140  $^{\circ}$ C, at a constant confining pressure of 10 MPa, caused a fully reversible hydraulic aperture variation between 58  $\mu$ m (at room temperature) and 41  $\mu$ m (at 140  $^{\circ}$ C). Therefore, temperature variation has a very limited effect on irreversible fracture closure, at least for short periods of time.

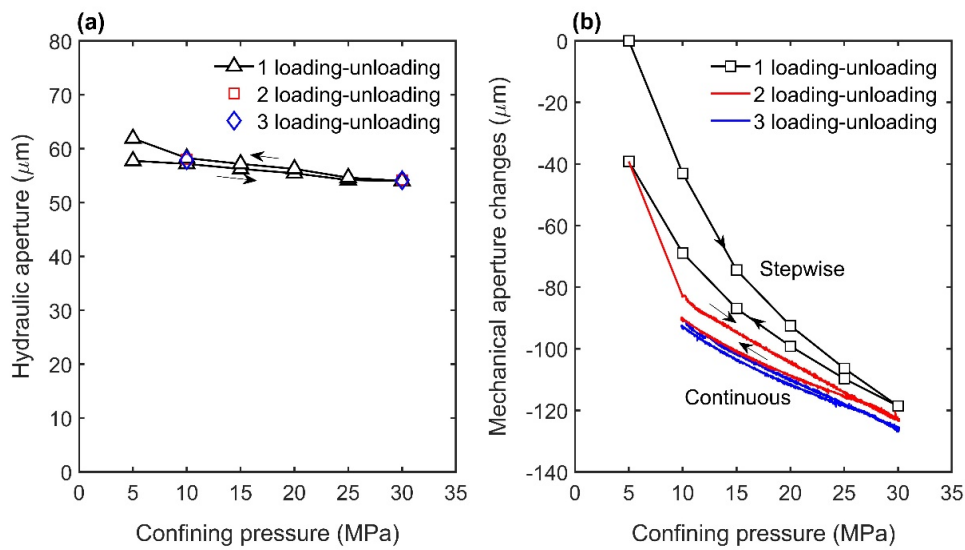


**Figure 4.3** (a) Hydraulic fracture aperture and (b) mechanical fracture aperture changes as a function of confining pressure at a constant pore pressure of 1 MPa. The first loading–unloading cycle between 5 and 30 MPa was performed stepwise in 5-MPa intervals, and the latter two cycles between 10 and 30 MPa were conducted continuously. Permeability was measured at each respective constant pressure level.

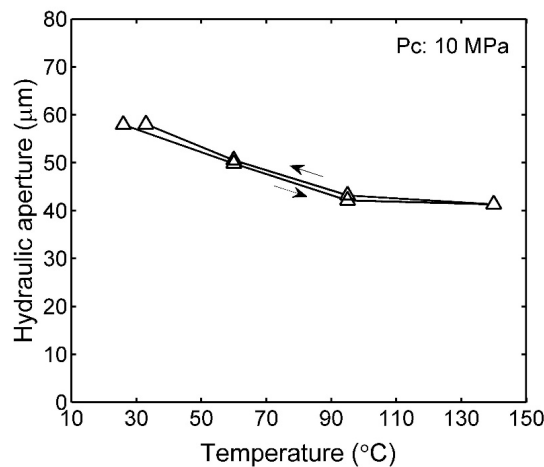


**Figure 4.4** Hydraulic fracture aperture as a function of temperature at constant pore pressure (1 MPa) and confining pressure (10 MPa).

#### 4.3.2 Time-dependent evolution of fracture aperture

After these two sample pre-treatments, it is clear that any further brittle damage and possible plastic deformation have been eliminated for the P-T space of investigation. The confining pressure was subsequently increased to 30 MPa, and the temperature was then increased stepwise from 33  $^{\circ}\text{C}$  to

140 °C. After reaching constant P and T conditions, the hydraulic aperture at the start of the long-term operation was  $\sim 37 \mu\text{m}$  (Figure 4.5).

Figure 4.5 shows the resulting hydraulic aperture evolution over time. The variation of the hydraulic aperture was observed to be negligible ( $a_h: 37 \mu\text{m} \pm 1 \mu\text{m}$ ) throughout the experiment. When, in the end, the temperature was decreased to 33 °C, the hydraulic aperture recovered fully reversibly, to  $59 \mu\text{m}$  at a 10 MPa confining pressure, when compared to Figure 4.4.

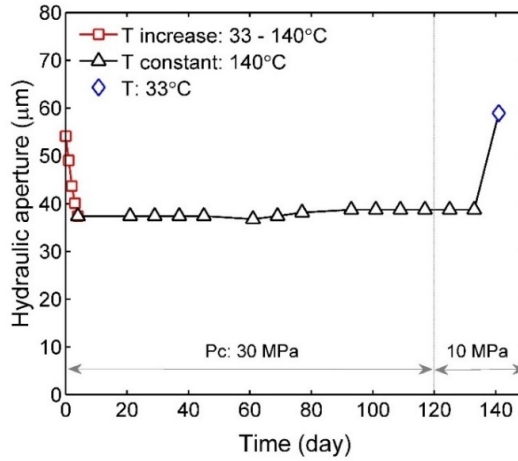


**Figure 4.5** Evolution of hydraulic fracture aperture under different confining pressure and temperature conditions as a function of time during the long-term flow-through experiment (black triangles).

### 4.3.3 Evolution of effluent Si concentration

A significant amount of dissolved solid substance was observed in the sampled fluids. Figure 4.6 shows representative Si concentration profiles along the fracture void space and parts of the pore fluid system under different  $P$  and  $T$  conditions after time intervals of 8 or 16 days. As can be seen in Figure 4.6a, the first effluent measurement taken after the flow was stopped for 16 days clearly reveals that the peak Si concentration is reached in the sixth subsample. Therefore, one can infer that the sixth subsample is the one that best characterizes the fluid directly within the fracture. As such, during subsequent effluent sampling, all (20) subsamples were collected, but only the fifth, sixth and seventh subsamples, as well as some other selected subsamples, were analyzed. This procedure proved sufficient to determine the highest fluid concentration after each time interval of stagnant flow. Therefore, Figures 4.6b–d show less than 20 individual measurements (black squares).

The Si concentration in the injection fluid is about  $3.7 \times 10^{-6}$  mol/l as measured by the photometer, and about  $4.4 \times 10^{-6}$  mol/l as determined by ICP-OES. Therefore, this injection fluid contains monomeric (soluble) silica almost exclusively, and of negligible concentration, i.e., two orders of magnitude lower than the typical effluent Si concentration. Therefore, the Si-enrichment of the fluid evidently resulted from a reaction between the rock and the fluid.

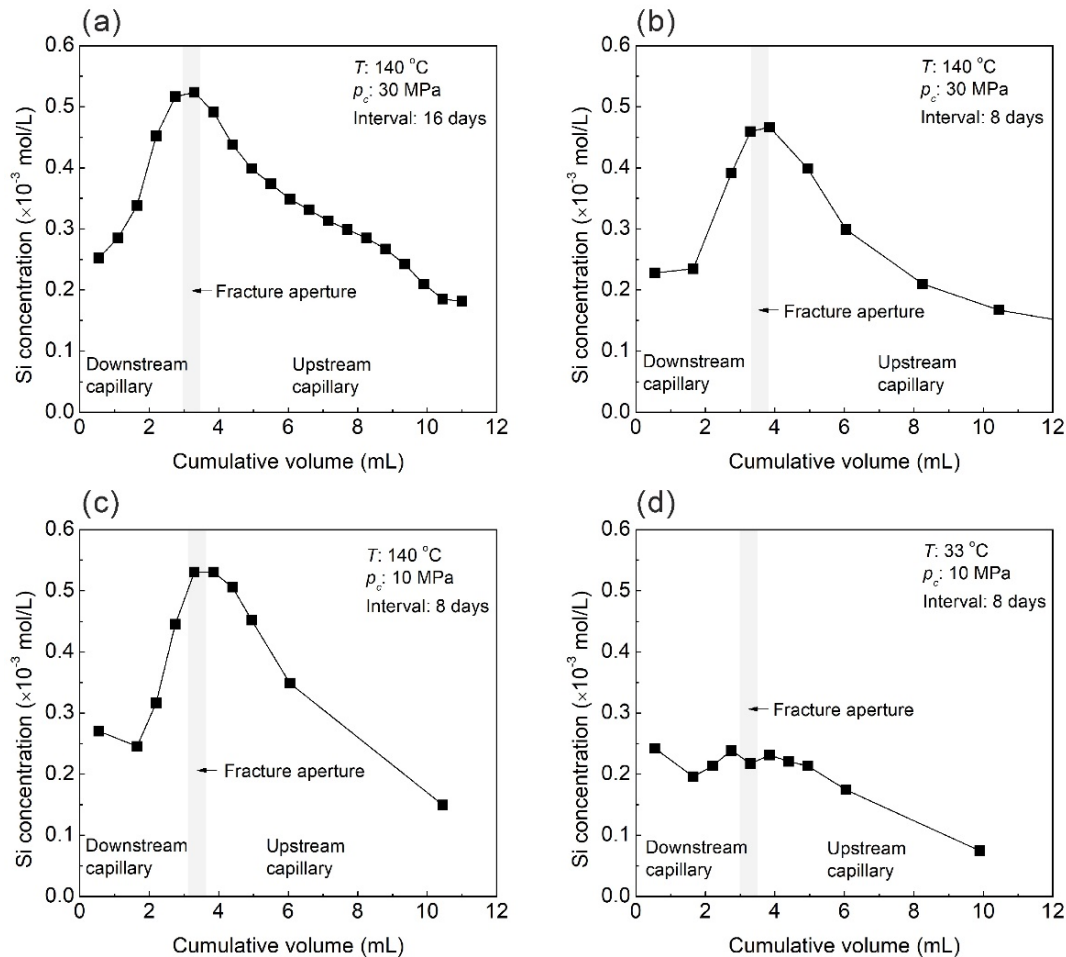


**Figure 4.6** Si concentrations (as measured by a photometer) in the subsamples obtained from the relief valve as a function of cumulative volume. The gray stripe indicates the Si concentration in the fluid from the fracture void, and all the other dots are the Si concentrations in the fluids from the downstream and upstream capillaries, respectively. The fluids were sampled: (a) at 140 °C and a  $p_c$  of 30 MPa after 16 days, (b) at 140 °C and a  $p_c$  of 30 MPa after 8 days, (c) at 140 °C and a  $p_c$  of 10 MPa after 8 days, and (d) at 33 °C at a  $p_c$  of 10 MPa after 8 days of stagnant flow, respectively.

A pronounced peak silica concentration was found in all effluents from the experimental stages at 140 °C (Figures 4.6a–c), but not in the effluent from the final stage at 33 °C (Figure 4.6d). The concentration profiles illustrate that the dissolved silica migrates from the fracture void space to



the upstream and downstream capillaries as a result of diffusion. There are no significant differences in peak Si concentration or profile shape between the samples after a 16-day interval (Figure 4.6a) or an 8-day interval (Figure 4.6b) of stagnant flow under the same  $P$  and  $T$  condition ( $p_c = 30$  MPa and  $T = 140$  °C). A comparison of the two 8-day interval profiles, at 140 °C and a 10-MPa or 30-MPa confining pressure (Figure 4.6b and c), essentially yields the same result. In contrast, after decreasing the temperature from 140 °C to 33 °C at  $p_c = 10$  MPa, the effluent Si concentration profile looks different after an 8-day interval of stagnant flow (Figure 4.6d). There is no obvious concentration peak, and the Si concentration within the fracture decreased to about  $0.24 \times 10^{-3}$  mol/l. Overall, this indicates that the Si concentration in the fracture reaches some upper limit in less than 8 days, and that the latter is clearly temperature-dependent but not significantly confining pressure-dependent.

Figure 4.7 shows the overall peak Si concentrations (i.e., the succession of Si concentrations in the fluid within the fracture void space after time intervals of 8 days or 16 days) as a function of time. As mentioned before, the maximum Si concentration attained is always significantly higher than that of the injection fluid from the upstream pump ( $\sim 4 \times 10^{-6}$  mol/l). Hence, a reaction between the rock and the fluid within the fracture is obvious at all conditions. When comparing all photometer analyses (squares), one notices that the maximum Si concentrations do not show significant variations with time at 140 °C, and they only decreased as the temperature was lowered to 33 °C.

Two additional series of effluent measurements were conducted by ICP-OES. The resulting peak concentrations were  $9.64 \times 10^{-3}$  mol/l after a 16-day interval and  $8.04 \times 10^{-3}$  mol/l after an 8-day interval (Figure 4.7), and thus significantly higher than the concentrations measured using the photometer.

It is noticeable that the concentrations measured by ICP-OES are more than an order of magnitude higher than those analyzed using the photometer. This is related to the differences in Si detection between the two methods measuring total and monomeric silica content, respectively. The dissolved silica within the fracture may reach equilibrium at 140 °C well within the time intervals applied. When the effluent is sampled after passing the cooled spiral capillary (Figure 4.2), the temperature of the effluent is close to room temperature, likely causing the silica to supersaturate. The sampling of all 20 subsamples took about 20 min at a flow rate of 0.5 ml/min, and preparation of the concentration measurements with the photometer took about two hours each time. When the silica concentration exceeds the solubility of silica at room temperature, silica polymers may form before the analyses due to polymerization of the dissolved monomeric silica. It should be noted that the polymerization is time-dependent. Thus, a dilution of the effluents with

deionized water by a factor of 10 may decrease the concentration of the remaining monomeric silica within the effluents to below the solubility limit ( $1.2 \times 10^{-4}$  mol/l) at room temperature, halting the polymerization process. Hence, the monomeric silica concentrations (peak) detected by this method are higher than the solubility.

However, the procedure of sampling and that of the concentration measurements was the same for all effluents throughout the experiment, and a peak Si concentration was also observed in the ICP-OES measurements of total silica. Therefore, the observed monomeric silica characteristics reflect silica dissolution and diffusion processes within and outside of the fracture void space.

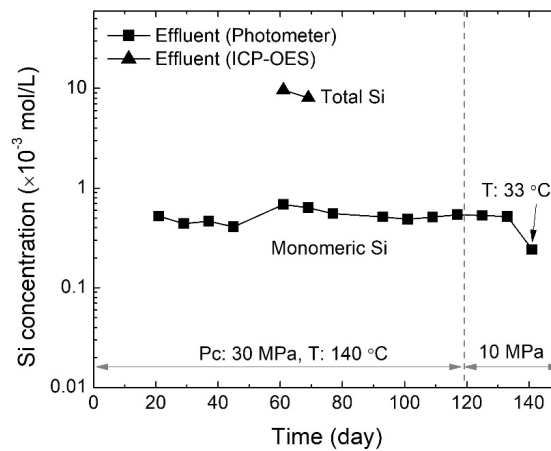


**Figure 4.7** Evolution of maximum Si concentration of each series of effluent subsamples as a function of time and under different confining pressure and temperature conditions.

#### 4.3.4 Microstructure variations

Figure 4.8 shows two reconstructed  $\mu$ CT 3-D models of the fractured sample and two corresponding cross-sectional images at the same respective location, before and after the experiment. The fracture void space underwent an obvious change during the overall experiment: the total fracture volume,  $V_f$ , decreased from  $0.403 \text{ cm}^3$  to  $0.204 \text{ cm}^3$ , and the contact area significantly increased. However, one cannot distinguish between the relative effects of mechanical compression during the initial loading-unloading stage 1 and the pressure solution-induced fracture closure during stages 4 and 5 (Table 4.1). Based on analysis of the extracted fracture void space (i.e., the blue area in Figure 4.8a), one can derive the contact area ratio,  $R_c$ , i.e., the ratio of the total contact area (in white) and the geometric fracture area ( $WL$ ), yielding a value of 3.67% after the experiment. It should be noted that the calculated fracture volume and the contact area ratio are digital products that depend on the resolution of the model and thus may not fully correspond to

the respective true properties of the sample. Furthermore, the X-ray  $\mu$ CT scans were conducted under atmospheric conditions, affecting both  $V_f$  and  $R_c$  parameters. However, at least semi-quantitatively, the observed relative changes in these parameters evidence the geometric evolution of the fracture, and their values can be used for additional analyses.

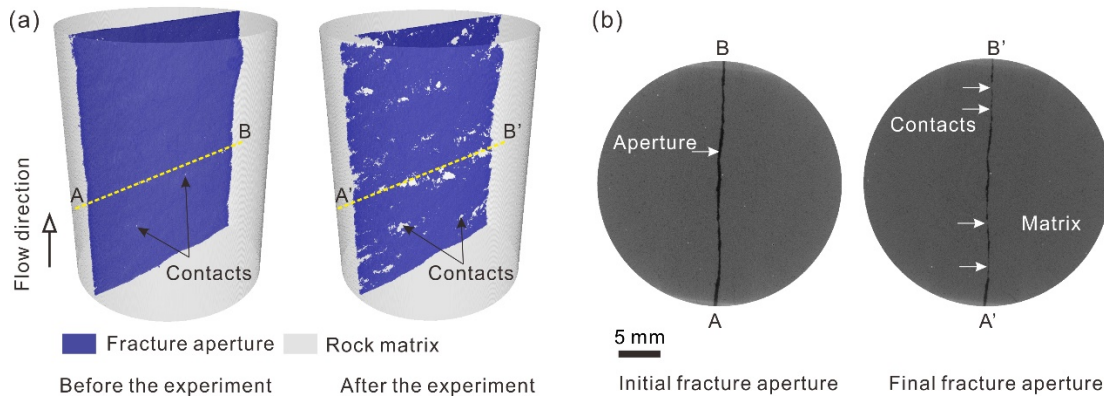


**Figure 4.8** (a) Three-dimensional models of the fractured sample core before (left) and after (right) the flow-through experiment as obtained from the X-ray  $\mu$ CT scans. The fracture void (in blue) was extracted from the reconstructed 3-D models. (b) Images of the cross-sections AB and A'B', with their locations in the core shown in (a), taken perpendicular to the long sample axis before (left) and after (right) the flow-through experiment.

## 4.4 Discussion

### 4.4.1 Mechanical and thermal effects on fracture aperture

Previous studies of rock cores containing a single fracture have shown that a geometric mismatch of the two fracture faces significantly enhances the samples' permeability by increasing the hydraulic aperture in comparison to the well-matched fractures (Durham & Bonner, 1994; Vogler et al., 2016; Crawford et al., 2017). Moreover, the mechanical aperture changes of a sample with a fracture wall offset were more significant than the corresponding hydraulic aperture changes observed when changes in stress or pressure were applied (Vogler et al., 2016). This is because the permanent damage of the fracture's surfaces is not widespread and only occurs at some isolated local contacts (Durham & Bonner, 1994). For example, the true contact area, bearing the normal stress, is roughly 3.67% of the total geometric area of the fracture plane in the present sample (Section 4.3.4). The fluid flows predominantly through the void channels defined by the distribution of the true contacts. When the pressure variations led to the purely elastic deformation

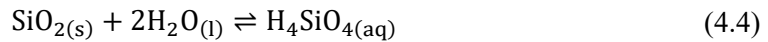
of the contacting asperities, this coincided with the reversible changes of both the mechanical and hydraulic apertures after several loading-unloading cycles (Figure 4.3), indicating that any irreversible mechanical compaction has vanished.

In previous studies, elevated temperatures were shown to affect the rock compaction process via either the increased rate of fluid-rock interactions (Elias & Hajash, 1992; Polak et al., 2003; Yasuhara et al., 2006) or the thermally induced overclosure resulting from solid-phase expansion (Rutqvist, 2015). In contrast, in the present study, temperature variations led to fully reversible aperture changes, indicating that the thermal expansion and contraction of the rock's fracture-matrix assemblage was entirely elastic, at least for short time periods of temperature exposure.

#### 4.4.2 Chemical effects on fracture aperture in the long term

##### 4.4.2.1 Quartz solubility

The reaction (dissolution or precipitation) of quartz in aqueous solutions can be expressed as,



The solubility of quartz under different temperature and hydrostatic pressure conditions can be directly calculated based on an empirical equation derived by Fournier and Potter II (1982), which is shown in Figure 4.9 (black line). As described previously, pressure solution is operative at grain contact boundaries as a result of the chemical potential differences,  $\Delta\mu$ , between the non-hydrostatically stressed boundaries and the stress-free sites and can be expressed as (Paterson, 1973),

$$\Delta\mu = \sigma_{\text{eff}}V_m + \Delta f - U_s \quad (4.5)$$

where  $\sigma_{\text{eff}} = (p_c - p_p)/R_c$  is the normal effective stress on the contacts,  $V_m$  is the molar volume of quartz,  $\Delta f$  is the Helmholtz free energy difference, including the plastic dislocation energy and the elastic strain energy, and  $U_s$  is the surface energy term. The normal stress effect on the chemical potential difference dominates in comparison to the other terms (Renard et al., 1999). Accordingly, the contributions of  $\Delta f$  and  $U_s$  were often omitted from previous studies (Yasuhara et al., 2003; Yasuhara et al., 2004; Lu et al., 2018; Ogata et al., 2018). The equilibrium constant  $K_{\text{eq}} = \gamma^\sigma C_{\text{Si}}^\sigma$  under stressed conditions is correlated with the equilibrium constant  $K_0$  under stress-free conditions, where  $\gamma^\sigma$  is the activity coefficient of quartz, assumed to be 1 in a dilute pressure-free fluid, and  $C_{\text{Si}}^\sigma$  is the quartz solubility under elevated stress within the contact boundary. This former constant can then be expressed as (Paterson, 1973; Renard et al., 1999),

$$\gamma^\sigma C_{Si}^\sigma = K_0 \exp\left(\frac{\Delta\mu}{RT}\right) \quad (4.6)$$

Here, again, it is assumed that the molar Helmholtz free energy and the surface energy terms are negligible in comparison to the normal stress effect (Renard et al., 1999). Further,  $R$  is the gas constant, and  $T$  is the absolute temperature in [K].  $K_0$  depends almost exclusively on temperature and can be directly estimated from  $\log K_0 = 1.881 - 0.002028T - 1560/T$  (Rimstidt & Barnes, 1980). By finally introducing Eq. 4.5 into Eq. 4.6, one can determine the solubility of quartz at the grain contact boundaries at different temperatures. Assuming that the contact area ratio  $R_c$  is in the range of 3.67% to ~10%, as derived from the 3-D  $\mu$ CT models (Section 4.3.4). For a confining pressure of either 10 MPa or 30 MPa, one obtains the two concentration fields displayed in Figure 4.9, which indicate the approximate solubility range of quartz in the water film between the grain contacts at different temperatures.

It is noticeable that the measured total silica concentration is significantly higher than the solubility of quartz at hydrostatic pressure and 140 °C, indicating the activity of pressure solution. The reactive (monomeric) silica concentration is about one order of magnitude smaller than the total silica concentration. A comparison with the hydrostatic solubility line indicates that the fluid is likely undersaturated with respect to monomeric silica at the 140 °C stages but still oversaturated at the 33 °C stage. Possibly, as the fluid was cooled during sampling, precipitation was triggered in the oversaturated Si-rich fluid at 140 °C, and consequently, polymeric and/or colloidal silica may have formed, which could have triggered the oversaturated monomeric silica becoming undersaturated. As the likelihood of precipitation should directly be related to the differential temperature during sampling, monomeric silica may exist metastably at the final 33 °C stage, and consequently, the measured monomeric silica concentration was noticeably higher than the hydrostatic quartz solubility at this temperature.

Pressure solution is a rate-limited process (Paterson, 1973; De Boer et al., 1977) and is controlled by the slowest of the three reaction steps (Gratier et al., 2013). In the present study, the progress of the pressure solution should be linked to, first and foremost, the degree of saturation of the fluid within the water film at 140 °C, which likely is attained rapidly (Section 4.3.3). The rates of Si diffusion into the free pore fluid, and that of possible Si precipitation therein, then control the kinetics of pressure solution. Diffusion was obvious for all experimental stages at 140 °C, but was significantly less pronounced for the 33 °C stage (Figure 4.6). However, as the monomeric silica concentration at 33 °C was higher than the corresponding hydrostatic quartz solubility at this temperature, this indicates that pressure solution was active during all stages of the long-term part of the experiment even under low temperature and pressure conditions. Overall, and in agreement with previous studies, it can be concluded that pressure solution is enhanced by temperature (Elias

& Hajash, 1992) and that any effect of temperature on this process is greater than that of pressure or stress (Yasuhara et al., 2015).

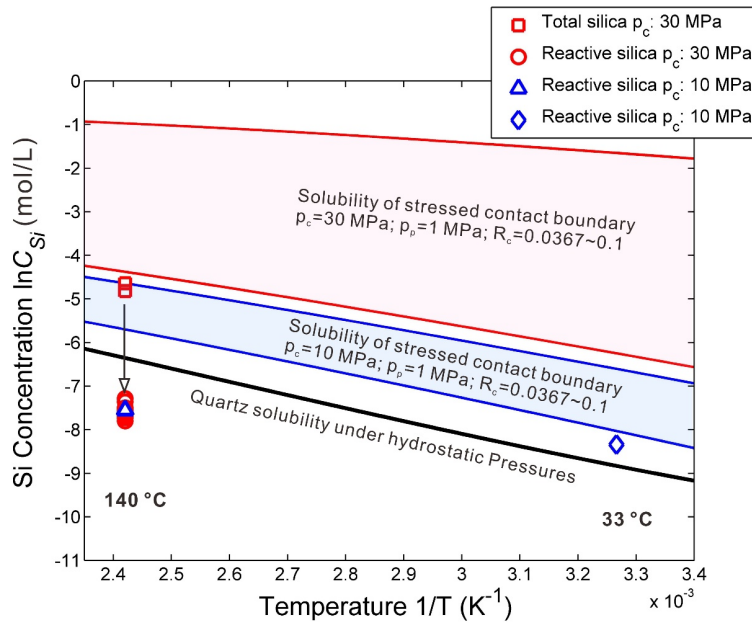


**Figure 4.9** Si concentration as a function of inverse temperature  $1/T$  ( $K^{-1}$ ). The dots indicate the respective measured Si concentrations under the corresponding P and T conditions (see chemical data in S2). The solubility of quartz in water at a hydrostatic pressure of 1 MPa (black line) is taken from Fournier and Potter II (1982).

#### 4.4.2.2 Pressure solution-induced deformation

To distinguish the effects of free face dissolution and pressure solution on the silica concentration of the effluents, it is assumed that the quartz dissolution has reached equilibrium after the respective time intervals of stagnant flow. The measured amount of Si in the effluent then consists of two components, i.e., dissolved silica, either from the free fracture walls or from the contacting asperities. Since the pressure solution rate is significantly higher than the normal dissolution rate of quartz (De Boer, 1977b), the Si concentration in the pore fluid mainly increases due to the diffusion of dissolved silica from the stressed asperities into the pore fluid, which, in turn, may also decelerate the dissolution of quartz on the free fracture walls.

The rate of mechanical fracture aperture variations,  $db_m/dt$ , can be related to the pressure solution rate,  $\dot{m}_{str}(t)$ , of the stressed asperities (yielding fracture closure) and the free face dissolution rate,  $\dot{m}_{fre}(t)$ , of the fracture walls (enlarging the fracture void space),

$$\frac{db_m}{dt} = -\frac{\dot{m}_{str}(t)}{WLR_c\rho} + \frac{\dot{m}_{fre}(t)}{WL(1-R_c)\rho} \quad (4.7)$$

where  $\rho$  is quartz density. Here, the total silica concentration, as measured by ICP-OES, is used to estimate the dissolved mass resulting from pressure-induced quartz dissolution and free face dissolution. The amount of free face dissolution was calculated based on the theoretical quartz solubility (Fournier & Potter II, 1982). Due to the diffusion of the dissolved silica from the fracture toward the upstream and downstream pore fluid system, the entire enclosed fluid volume needs to be accounted for, which can be defined by the observed concentration profiles after the respective time intervals of stagnant flow (Figure 4.6),

$$\Delta b_m = -\frac{\sum_{i=1}^n V_s W_m (C_{total}^i - C_{Si}^i)}{WLR_c\rho} + \frac{\sum_{i=1}^n V_s W_m C_{Si}^i}{WL(1-R_c)\rho} \quad (4.8)$$

where  $V_s$  is the subsample volume,  $W_m$  is the molar weight of quartz, and  $n$  is the total number of the subsamples, taking  $n = 20$  for the calculation.  $C_{total}^i$  and  $C_{Si}^i$  are the total silica concentration in the effluent and the silica concentration of the  $i^{th}$  subsample attributed to free face dissolution, respectively. The ICP-OES data of day 69 at 140 °C was used for the calculation. Although there is some lack of data in this suite of subsamples, it is assumed that the ICP-OES results and the amount of dissolved silica from the free fracture walls follow the same trend as the monomeric silica concentration. Assuming that the contact area ratio is constant throughout the experiment, for a contact area ratio,  $R_c$ , in the range of 3.67% to 20% (Section 4.3.4), this yields  $\Delta b_m \approx -16.49$   $\mu\text{m}$  to  $-2.85$   $\mu\text{m}$  after the respective time interval at 140 °C. Every sampling procedure resets the fluid concentration in the fracture and restarts this process. Therefore, the total mechanical aperture change during the long-term experiment (13 individual sampling events) is  $-214.3$   $\mu\text{m}$  to  $-37.0$   $\mu\text{m}$ , wherein the calculation result is sensitively dependent on the assumed contact area ratio. The final contact area ratio was obtained numerically based on the  $\mu\text{CT}$  models, which may be prone to uncertainty in representing the true contact area ratio due to resolution limitations and the analytical conditions (i.e., room temperature and atmospheric pressure). However, it was observed that the fracture aperture exhibited almost purely elastic deformation after three loading-unloading cycles (Figure 4.3), which implies that the contact area ratio is proportional to the normal stress (Kling et al., 2018). Therefore, one can infer that the actual contact area ratio is greater than 3.67% under stressed conditions within the pressure vessel.

Based on the changes in fracture volume from 0.403  $\text{cm}^3$  to 0.204  $\text{cm}^3$ , as derived from the  $\mu\text{CT}$  models (Section 4.3.4), one can estimate the corresponding changes of the mechanical aperture,  $b_m$ ,

$$b_m = \frac{V_f}{WL} \quad (4.9)$$

As a result, the mechanical aperture decreased from 335.8  $\mu\text{m}$  to 170.0  $\mu\text{m}$  (i.e.,  $\Delta b_m = 165.8 \mu\text{m}$ ), which is consistent with the magnitude of irreversible fracture closure measured during stage 1 (Figure 4.3b). On the other hand, well-connected fracture voids were observed in the 3-D model after the long-term experiment (Figure 4.8a), which allow the fluid to flow through. Free face dissolution and pressure solution creep are two competing processes, whereby the dominant one will control whether the fracture will, overall, tend to open or close. Obviously, during the intermittently conducted long-term experiment, the so-induced geometrical changes of the fracture void space were insufficient to significantly affect the hydraulic aperture, as this property was shown to remain almost constant (Figure 4.5).

#### **4.4.3 Effects of stress corrosion-induced subcritical cracking**

When water and tensile stresses are present in the rock material, stress corrosion-induced subcritical cracking can also contribute to fracture deformation (Atkinson, 1980; Waza et al., 1980; Yasuhara & Elsworth, 2008). Resulting from the applied normal stress, concentrated tensile stresses may occur at the periphery of the contacting asperities perpendicular to the contact area. Hence, subcritical cracking may induce the time-dependent deformation or progressive failure of the asperities, which could lead to fracture closure (Yasuhara & Elsworth, 2008). Particularly under hydrothermal conditions, the crack growth velocity increases with increasing temperature (Nara et al., 2010).

Both pressure solution and subcritical cracking result in very similar geometric responses from the fracture, but these result from completely different mechanisms. Pressure solution mainly leads to an increase in the contact area, accompanied by a decrease in the normal stress on the fracture plane. In contrast, subcritical cracking is directly controlled by the stress and chemical processes operating at the crack tips. Consequently, this may yield the rupturing of the contacting asperities promoting the closure of the fracture. Obviously, this latter process would have a rather limited effect on the effluent concentration. However, in the present study, a significantly enhanced amount of Si, as well as Si oversaturation, were observed in the effluent at 140 °C and 33 °C, respectively (Figure 4.9). This indicates that pressure solution was active during the entire experiment. Moreover, the average fracture closure rate throughout the 137 days for which the experiment was conducted at 140 °C, as calculated from the chemical effluent data and the estimated contact area ratio (Section 4.4.2.2), is in the range of  $3.1 \times 10^{-12} \text{ m/s} \sim 1.8 \times 10^{-11} \text{ m/s}$ . This range is orders of magnitude lower than the subcritical cracking-induced fracture closure rate ( $> 10^{-8} \text{ m/s}$  at 150 °C) estimated for a fractured novaculite sample theoretically investigated



previously (Yasuhara & Elsworth, 2008). Therefore, although one cannot fully neglect any effect of subcritical cracking on fracture closure, under the present experimental conditions, pressure solution overall likely dominated in fracture deformation.

However, both mechanisms may likely operate in parallel. When pressure solution is inactive or very slow (e.g., under low stress and/or low-temperature conditions), subcritical cracking will govern fracture deformation. In contrast, when pressure solution dominates, the progressive increase of the fracture contact area will additionally inhibit subcritical cracking by reducing the normal fracture stress. In summary, one can infer that subcritical cracking may occur at an early stage in the process, whereat mechanical effects dominate over chemical ones (Yasuhara & Elsworth, 2008). In the long term, however, pressure solution determines the rate at which fracture aperture will change.

#### **4.4.4 Implications**

Based on the above considerations, it is implied that pressure solution is more significant than other effects in the deformation of fractures, particularly for long-term exposure under high-temperature conditions, as found in enhanced geothermal or unconventional reservoir systems. Accordingly, the fracture aperture is more susceptible to changes when coupled hydro-thermo-mechano-chemical processes operate under such conditions (Yasuhara et al., 2006; Yasuhara et al., 2011). The present fluid chemistry data indicate that the Si concentration in the pore fluid can significantly affect the progress of pressure solution. This implies that any alteration of the chemical fluid-rock equilibrium, e.g., by injection of undersaturated fluids, might accelerate this process, leading to an enhanced closure of the fracture. Moreover, cold water injection or hot water production may reduce temperature locally, and this would change the concentration of the dissolved silica, accelerating polymerization and precipitation, which finally impacts fracture permeability. Despite simplifications in terms of mineralogy, fluid composition, and experimental duration, the results of this study demonstrate the importance of temperature and fluid elemental concentration in the evolution of fracture aperture.

#### **4.5 Conclusions**

The purpose of this experimental study was to constrain the mechanical, thermal, and long-term chemical feedbacks of pressure, temperature, and fluid-rock interactions on the hydraulic and mechanical aperture of a single macroscopic tensile fracture in a pure quartz sandstone core. Fracture aperture changes resulting from mechanical compaction comprised both the irreversible and reversible (i.e., elastic) portions. The hydraulic aperture was less variable than the mechanical

aperture due to a manually pre-induced mismatch of the two fracture surfaces with an offset of 750  $\mu\text{m}$ . Furthermore, hydraulic aperture changes, as a result of temperature cycling, were shown to be fully reversible and thus thermoelastic.

After any brittle and/or plastic deformation of the fracture had vanished, a long-term intermittent flow-through experiment comprising systematic effluent Si concentration analyses was conducted. Quartz dissolution was active under the effective pressure (9 MPa and 29 MPa) and temperature (33 °C and 140 °C). The Si concentration of the pore fluid increased substantially toward a maximum within a short period of time (i.e., in less than 8 days), indicating chemical equilibrium. Differences in the time intervals of stagnant flow (i.e., 8 days or 16 days) did not seem to affect the respective maximum effluent concentration significantly. Furthermore, macroscopic silica diffusion from the fracture into the upstream and downstream pore fluid system was clearly observed. Silica dissolution predominantly resulted from pressure solution at the contacting fracture asperities. The total Si concentration in the effluent, attributed to the fracture void, was significantly higher than the quartz solubility under the same  $P$  and  $T$  conditions, and precipitation may have occurred therein. The progressive increase in Si concentration within the fracture should feed back into the pressure solution process, thus decelerating pressure solution creep. However, based on microstructural observations via  $\mu\text{CT}$  scanning, the theoretically estimated changes in mechanical aperture were found to be substantial. In contrast, the measured hydraulic aperture was shown to remain more or less constant during the 140 days of the long-term part of the experiment.

Noticeably, it was found that elevated temperatures significantly accelerate the dissolution process and result in higher pore fluid Si concentrations. This implies that fractures in deep geological structures and reservoirs will be more susceptible to pressure solution-induced effects, regarding geometric aperture changes and related variations of hydraulic fracture properties, than shallow ones at lower temperatures. However, the present experiment was conducted in a quasi-closed pore fluid system, with flow only occurring during sampling and subsequent permeability measurements taken for short periods of time. As such, the question of whether a fracture will remain open, ultimately close, or approach some constant aperture in an open system with continuous fluid flow, e.g., in a geological reservoir used to extract geothermal energy, should be the focus of a related future study. Moreover, further efforts are required to undertake the direct measurement of fracture deformations, in addition to the hydraulic measurements. Details of time-dependent fracture closure, in conjunction with fluid chemical analyses, will improve our understanding of these coupled mechano-chemical processes.

# Chapter 5

## **Evolution of fracture aperture induced by fluid-rock interactions: continuous flow**

**P**ressure solution is an important mechanism in the long-term deformation of fractured rock masses, but the kinetics and the conditions for a cessation of this process are poorly understood. A continuous long-term flow-through experiment on a Fontainebleau sample containing a single rough fracture was conducted at 60 °C to constrain the different effects of changes in effective pressure and fluid chemistry on the deformation process. Sequential measurements of effluent Si concentration evidenced that pressure solution was active throughout the experiment at all effective pressures applied (1, 17, and 29 MPa). Consequently, hydraulic fracture aperture, as derived from permeability measurements, decreased by 50 % within the 120 days of the experiment. Microstructural investigations revealed the existence of grain-to-grain contact boundaries with a rough structure that may contain disconnected fluid inclusions at experimental conditions. It is implied that the predominant factor controlling the rate of pressure solution changes from the normal stress drop to the diffusion limit as the overall contact area of fracture asperities increases. For the diffusion regime, the mass transfer coefficient is inversely correlated with effective stress. The notion of a "critical stress", below which pressure solution would cease, should be considered as the criterion, where cessation will not occur until other processes, e.g., precipitation-induced contact boundary healing, become predominant.

## 5.1 Introduction

Pressure solution creep is well-known and a dominant mechanism in the time-dependent deformation and compaction of wet porous rocks and fractures associated with porosity reduction and fracture closure, respectively (Weyl, 1959; Paterson, 1973; Yasuhara et al., 2006). Numerous experimental, analytical, and numerical studies have previously been carried out to understand the processes underlying pressure solution (Raj, 1982; Rutter, 1983; Tada et al., 1987; Taron & Elsworth, 2010). Generally, pressure solution is a rate-limiting process involving three sub-processes operating sequentially, i.e., dissolution of a stressed solid phase into the water film between the contact boundaries, diffusion of the dissolved matter from the interface towards the rock's void space through the water film, and precipitation of this matter onto the walls of the void space exposed to the pore fluid (Rutter, 1976; De Boer, 1977a; De Boer et al., 1977; Gratier & Irigm, 1986). The driving force of this process is the chemical potential gradient between the stressed solid-phase contacts (i.e., the dissolution zone) and the relatively less stressed and water-filled spaces.

For a pressure-solution process with finite effective stresses, zero porosity or full fracture closure will ultimately be achieved (Gratier et al., 2013), which is, of course, in contrast to reality as observed in nature. To retard pressure solution at some final stage yielding non-zero porosity or fracture aperture, the notion of a "critical stress" is introduced in previous studies. For example, Stephenson et al. (1992) proposed some minimum stress needed to break the molecular bonds of the matter within the contact interfaces activating grain interpenetration, which, as further elaborated by Revil (1999; 2001), leads to a temperature-dependent critical stress concept with  $\sigma_1^{crit} = E_A(1 - T/T_A)/4V_m$ , where  $E_A$  (kJ/mol) and  $T_A$  (K) are the molar heat and temperature of fusion of the given mineral, and  $V_m$  (m<sup>3</sup>/mol) and  $T$  (K) are its molar volume and present temperature, respectively. This notion was followed by (e.g., Yasuhara et al., 2003; Yasuhara et al., 2004; Lu et al., 2018), who introduced this critical stress concept into a thermodynamic model (i.e., driving force = effective stress -  $\sigma_1^{crit}$ ). The critical stress is considered as the minimum energy barrier for mineral dissolution activity, where the stress-induced mineral dissolution will cease when the effective stress on the grain contacts is equivalent to  $\sigma_1^{crit}$ . This model obviously needs to assume a thin film structure within the contact boundary. Similarly, Taron and Elsworth (2010) investigated the original expression of this critical stress (see Stephenson et al., 1992), which resulted in three additional parameters, i.e., the burial constant, the number of contacts per grain, and the initial porosity.

Neretnieks (2014) argued that the "critical stress" is inappropriate since stress-induced crystal

dissolution would occur even at the smallest stress difference between the stressed and the unstressed surfaces, which should be a spontaneous process under non-hydrostatic stress conditions. Other studies (e.g., Urai et al., 1986; Spiers et al., 1990; Renard et al., 2000; Niemeijer et al., 2002) do not follow this reasoning. Instead, Van Noort et al. (2008b) proposed a model that considers an island-channel type structure of the contact boundary. A criterion for the balance between the chemical potential gradient driving contact boundary dissolution and surface energy driven contact boundary healing due to neck growth was established, yielding a critical stress  $\sigma_2^{crit} = 2\alpha \sqrt{(E\gamma_{sl}(\cos(\theta/2) - \cos(\theta_{eq}/2)))}/\delta$ , below which healing dominates, causing the cessation of pressure solution. Here,  $\alpha$  (-) is the fraction of the actual contact area within a nominal contact ( $0 < \alpha < 1$ ),  $E$  (MPa) is Young's modulus,  $\gamma_{sl}$  (J/m<sup>2</sup>) is the solid-liquid interfacial energy,  $\delta$  (m) is the mean thickness of the water film within the contact zone,  $\theta$  and  $\theta_{eq}$  (°) are the dihedral angle at the contact conjunction and its equilibrium dihedral angle, respectively. The application of both models results in fairly good agreement with the outcome of the few documented experiments (e.g., Yasuhara et al., 2011; Ogata et al., 2018; Van den Ende et al., 2019) while none of them has been truly tested rigorously, particularly with regard to the cessation of pressure solution, which remains poorly constrained.

To further the scientific discussion mentioned above, it is essential to characterize the stress-dependent evolution of the boundary between contacting grains and the diffusive properties of this interface. However, the diffusion-related parameters (e.g., the diffusion coefficient and the water film thickness) are difficult to be accurately defined. It is argued that the contact interface may be present as (1) a strongly adsorbed water film in a flat grain-to-grain contact boundary with a thickness at the nanometer scale (Rutter, 1983; Renard & Ortoleva, 1997; Gratier et al., 2009) or (2) a dynamic island-channel structure (e.g., Lehner, 1995; De Meer et al., 2005; Van Noort et al., 2008b) with a thin water film containing free fluid within contacting grain boundaries (Gratz, 1991; Renard et al., 1999), possibly with a mean thickness of tens of nanometers to micrometers (Gratier et al., 2013). Moreover, the diffusion coefficient  $D$  (m<sup>2</sup>/s) of the constrained water is estimated to be one to two orders of magnitude smaller than that of free water (Renard et al., 1999; Revil, 2001) in contrast to earlier estimations stating five orders of magnitude (Rutter, 1976). An overall direct measurement of  $D\delta C$ , where  $C$  is the solubility of the diffusing species within the grain boundary fluid, of a halite-glass contact indicated an inverse correlation with effective stress (De Meer et al., 2002). Finally, knowledge of the diffusion-pathway length and its evolution is also of key interest since the load-bearing stress on the contacts will decrease as the pathway length increases, eventually controlling the overall kinetics. Consequently, understanding the contact boundary evolution concurrent with the variations in its diffusive properties is crucial for a better mechanistic

understanding of pressure solution and so induced creep.

In this contribution, a long-term continuous flow-through experiment on a macro-fractured quartz sandstone was performed at three different effective stresses (1, 17, and 29 MPa) and a temperature of 60 °C. The direct measurement of the critical stress, at which compaction would cease, is not possible within laboratory time scales. Hence, only a qualitative evaluation can be provided with this study on whether the pressure-solution cessation depends on a stress threshold or other reactions that play as opposing effects (e.g., healing). In this regard, the structural evolution of the contacting grain boundaries and the development of mass transport therein were investigated. Both deionized water and a defined silica solution were used as the permeating fluids to investigate the effects of solution chemistry on diffusion. Continuous Si concentration measurements of the fluids were performed to evaluate the activity of pressure solution directly. Surface topography scanning, X-ray micro computed tomography ( $\mu$ CT), and scanning electron microscopy (SEM) were applied to investigate the increase in asperity contact area and the concurrent fracture aperture changes as derived from permeability measurements.

## **5.2 Experimental methodology**

### **5.2.1 Sample preparation and experimental setup**

The cylindrical core sample for the flow-through experiment had 30 mm in diameter and 40 mm in length and was drilled from a Fontainebleau sandstone block, quarried near Fontainebleau, France. Fontainebleau sandstone was selected because it is a mineralogically pure natural porous medium composed of > 99.5 wt% quartz having a dense texture (porosity ~2.3 %) and a low matrix permeability on the order of  $10^{-18}$  m<sup>2</sup> as determined with a gas permeameter. Using a Brazilian test setup, the sample was split into two halves along its axis. The displacement-controlled loading rate during splitting was set to  $2 \times 10^{-6}$  m/s to minimize edge damage (Figure E1). To prevent the fracture from immediate closure upon pressurization, a 200  $\mu$ m displacement between the two halves was introduced manually and locked using two PEEK spacers (Figure 5.1a). The specimen assembly was then mounted in the pressure vessel.

The continuous flow-through experiment was conducted with a flow-through apparatus (Figure 5.1b), where the flow rate and pore pressure were controlled by operating the upstream pump in constant-flow rate mode against a relief valve located downstream. The relief valve also served for sampling the effluent in defined time intervals. A downstream pump was set in parallel to precisely stabilize the pore pressure during the permeability measurements, which was necessary

as these required high flow rates.

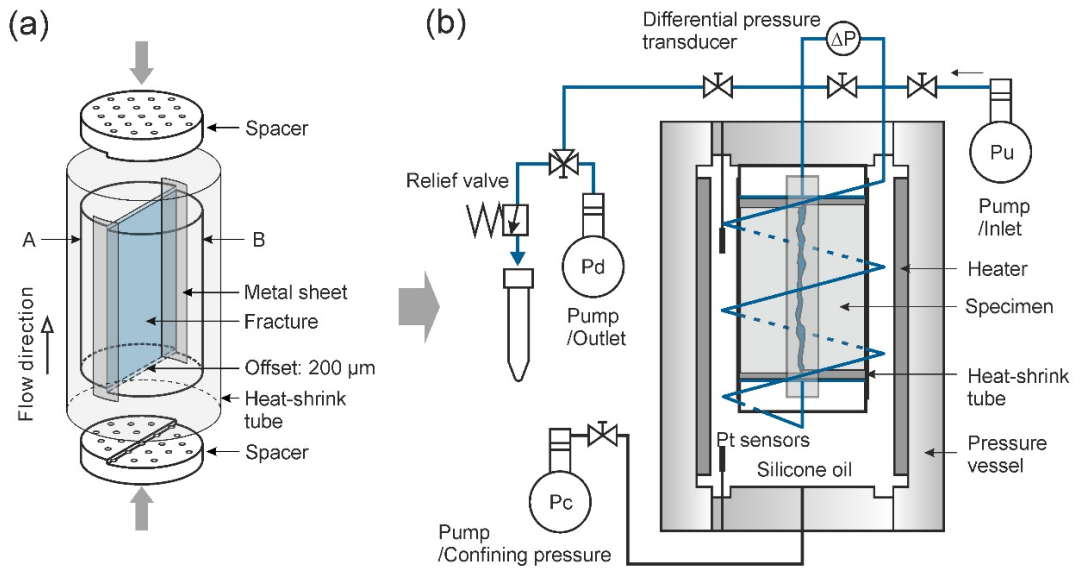


**Figure 5.1** Schematic illustration of the experimental setup: (a) the assembled specimen halves were jacketed by a heat-shrink tubing to isolate the pore fluid system from the silicone oil in the pressure vessel. Two metal sheets along the fracture edges were used to prevent the heat-shrink tubing from punching at elevated confining pressure. (b) Hydrostatic confining pressure is applied using an oil medium pressure vessel connected to a syringe pump (ISCO 65D). The isolated pore fluid system consists of an upstream and a downstream pump (ISCO 260D), the latter set in parallel with a relief valve. A pressure transducer (IPD 40, ICS Schneider Messtechnik) is implemented for precise measurements of the upstream and downstream pressure difference at an accuracy of  $1.2 \times 10^{-3}$  MPa and a differential pressure range of up to 0.6 MPa. An electrical resistance heater located in the pressure vessel is used for heating the sample, where two Pt100 sensors enable temperature monitoring. All wetted parts of the pore fluid system are made of Hastelloy C-276 to exclude any formation of corrosion products during a long-term flow-through experiment.

## 5.2.2 Experimental procedures

The experimental stages of this study and their respective procedures are shown in Figure 5.2. During the pre-loading stage conducted in an autoclave and thus not in the flow-through apparatus (i.e., stage-I), the yet dry specimen assembly was pressurized four times up to 20 MPa to minimize irreversible deformation at later stages. The assembly was then vacuum-dried at 60 °C, saturated with deionized water, and subsequently mounted in the pressure vessel of the flow-through apparatus. The flow rate throughout the experiment was held constant at 0.1 ml/min, as was the downstream pressure  $p_p$  set to 1 MPa. The experiment started at a confining pressure  $p_c$  of 2 MPa

(stage-II), which increased to 18 MPa for stage-III. During stage-III, the deionized water as injected so far was replaced by a silica solution of defined composition (Section 5.2.3). The fluid exchange was conducted by emptying and refilling the entire pore fluid system several times with the target fluid. During stage-IV, the injected solution was again replaced by deionized water, maintaining confining pressure at 18 MPa. The purpose of this fluid exchange sequence was to investigate the potential influence of fluid chemistry on the rate of fracture closure driven by pressure solution. Subsequently, an unloading-reloading cycle was performed (stage-V). Here, the confining pressure was decreased to 2 MPa and kept constant for 28 hours. After reloading, the confining pressure was held constant at 18 MPa for 188 hours (stage-VI) and subsequently at 30 MPa for 239 hours (stage-VII). Afterwards, the experiment was terminated by complete unloading.

To observe a noticeable decrease in fracture permeability within a reasonable experimental time frame, the temperature was elevated to 60 °C. Performing this kind of experiment at even higher temperatures would also have been possible (e.g., Niemeijer et al., 2002; Van Noort et al., 2008a; Gratier et al., 2009). However, time-dependent fracture permeability variations are attributed to the pressure-solution creep (the fracture closure) and free-face dissolution (the enlargement of the fracture aperture), which play opposing effects. The higher the temperature, the higher would be the contribution from free-face dissolution to the total measured effluent concentration. In contrast, in case the former can be neglected, the chemical fluid analysis directly reflects the dissolution processes at the asperity contacts related to pressure solution.

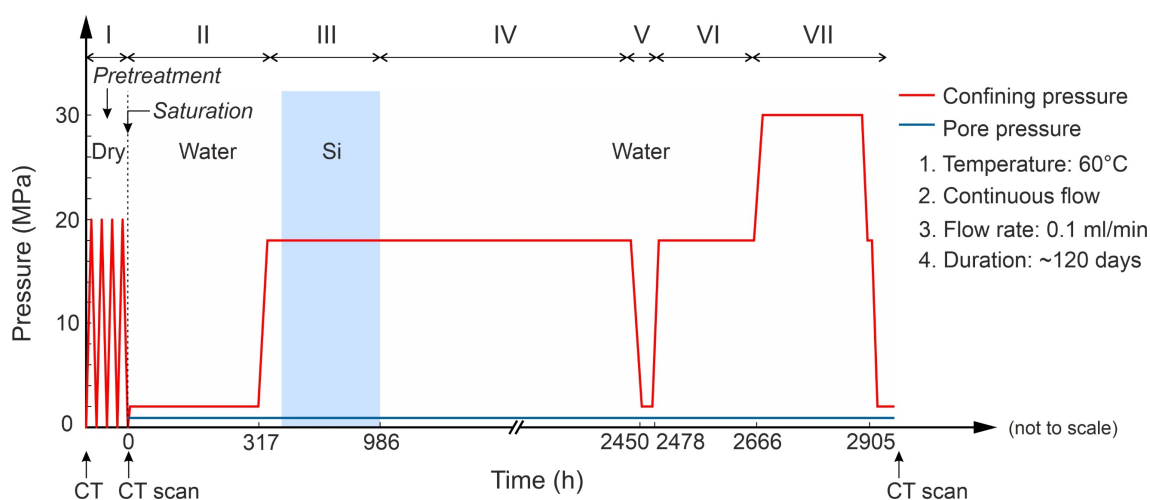


**Figure 5.2** Schematic of the experimental procedures, conditions, and stages of the entire experiment.

The effluent with a volume of 3 ml was sampled from the relief valve at a constant flow rate of 0.1 ml/min once every 24 hours. In stage-V, one fluid sample was collected right after unloading



and another one after 28 hours at the same stress condition. The collected fluid samples, including those of deionized water and the prepared silica solution from the upstream syringe pump, were analyzed by inductively coupled plasma optical emission spectrometry (ICP-OES) with an analyzed element wavelength of 251.611 nm.

Permeability was always measured after effluent sampling. To push the differential pore pressure into the measuring range of the differential pressure transducer, the flow rate was increased to 2–4 ml/min during permeability testing. One permeability measurement took approximately 2–4 mins and was performed three times per week. Afterwards, the flow rate was instantaneously restored to 0.1 ml/min, accompanied by switching the outlet port from the downstream pump to the relief valve. From measured sample permeability, hydraulic aperture  $b_h$  was calculated by applying the "cubic law" (Witherspoon et al., 1980),

$$b_h = \sqrt[3]{\frac{12\mu L Q_v}{W\Delta P}} \quad (5.1)$$

where  $\mu$  (Pa/s) is the dynamic fluid viscosity,  $W$  and  $L$  (m) are the width and length of the fracture,  $\Delta P$  (Pa) is the differential pressure between the upstream and downstream sides of the sample, and  $Q_v$  ( $\text{m}^3/\text{s}$ ) is the flow rate at vessel temperature. Given the temperature difference between the vessel and the upstream syringe pump,  $Q_v$  was calculated from the measured flow rate  $Q_p$  in the syringe pump as  $Q_v = Q_p \rho_p / \rho_v$ , where  $\rho_p$  and  $\rho_v$  ( $\text{kg}/\text{m}^3$ ) are the fluid densities at room temperature (25 °C) and vessel temperature (60 °C), respectively. In addition to hydraulic aperture, mechanical aperture changes during loading or unloading steps were also determined by measuring the volume changes of the pore fluid at drained conditions and stagnant flow (**Appendix D**).

### 5.2.3 Preparation of the silica solution

Deionized water was exclusively used as the permeating fluid except for stage-III. The silica solution prepared for stage-III was close to saturation with a Si concentration of  $\sim 2.60 \times 10^{-4}$  mol/l and a pH value of  $\sim 6.89$ , additionally containing  $\sim 3.65 \times 10^{-3}$  mol/l NaCl indirectly originating from the initial Si standard solution. The Si standard solution with 1000 mg/l of Si and 0.5 mol/l of NaOH was diluted with deionized water and neutralized with HCl. This Si-rich solution was prepared in relation to the solubility of quartz at 60 °C (i.e.,  $3.03 \times 10^{-4}$  mol/l) and neutral pH conditions (Fournier & Potter II, 1982) with the purpose to investigate a change in pressure solution rate during the experiment. The increase in pore fluid salinity may change the concentration gradient between the contact interfaces and the pore fluids affecting the overall pressure solution process.

### **5.2.4 Microstructural observations**

To quantitatively characterize the evolution of fracture surface topography and fracture aperture resulting from mechanical compaction and pressure solution creep, a series of microstructural investigations were performed, including 3-D surface profilometry, X-ray micro computed tomography ( $\mu$ CT), and scanning electron microscopy (SEM). The surface topographies of the two specimen halves were measured before stage-I and after the completion of the experiment using white light interferometry (Keyence VR-3200). The resolutions on the horizontal plane and the vertical z-axis were 23.518  $\mu\text{m}$  and 0.01  $\mu\text{m}$ , respectively. Several reference points were marked on the fracture surface to ensure that each scan had an identical observation area. The two scans of each specimen half, i.e., before and after the experiment, were adjusted based on the same reference plane, and the changes in surface topography were subsequently evaluated by a point-by-point subtraction of the two surface-scan datasets.

The evolution of the contact area ratio with time is closely related to the evolution of the pressure solution process. To characterize the contact area growth and the concurrent mechanical aperture changes, three X-ray  $\mu$ CT scans were conducted at different experimental stages (Figure 5.2). To obtain comparable results, all scans were performed with a dried but jacketed sample core at atmospheric conditions using the same scanning parameters (i.e., timing: 750 ms; voltage: 120 kV; current: 90  $\mu\text{A}$ ; voxel size: 20.63  $\mu\text{m}$ ), yielding a total of 1080 two-dimensional slices. The 3-D CT models of the sample were then generated by using all of the 1080 slices of each scan. The first and the second scan were conducted before and after the pre-loading stage (stage-I), respectively. Hence, the initial, mechanically induced aperture closure can be quantified. In addition, the initial contact area ratio before the onset of pressure solution can be determined. Ultimately, the sample core was scanned again after the completion of the experiment to observe the final microstructure of the fracture. Finally, the sample halves were taken apart after the experiment, and the fracture surfaces were carbon-coated for high magnification SEM imaging of fracture surface features.

## **5.3 Experimental results**

### **5.3.1 Evolution of fracture permeability**

The hydraulic aperture was subjected to a progressive reduction throughout the flow-through experiment, as shown in Figure 5.3. In stage-II (4 - 317 hours), the hydraulic aperture decreased from 60.7 to 55.6  $\mu\text{m}$  at the Terzaghi effective pressure (i.e.,  $p_c - p_p$ ) of 1 MPa. Then, the confining pressure was increased to 18 MPa, implying that the effective stress was increased to 17 MPa. This

effective stress increase had an immediate (i.e., elastic) effect on the hydraulic aperture, which underwent a decrease by 3.4  $\mu\text{m}$  from 55.6 to 52.2  $\mu\text{m}$ . During the following 42 hours, the hydraulic aperture continuously decreased and converged to 48.6  $\mu\text{m}$ . At 412 hours, the deionized water in the sample void space was exchanged with the silica solution (Section 5.2.3) as the injection fluid (stage-III). This fluid exchange did not affect the hydraulic aperture during the following 189 hours. From 601 hours onwards, the hydraulic aperture started to decrease and converged to about 41  $\mu\text{m}$  at 986 hours. At this moment, the silica solution was exchanged for deionized water, which caused the hydraulic aperture to remarkably decrease (stage-IV). After undergoing a continuous decrease to  $25 \pm 1 \mu\text{m}$ , the hydraulic aperture remained approximately constant after 2089 hours. In stage-V, where confining pressure was decreased from 18 MPa to 2 MPa, the hydraulic aperture instantaneously increased to approximately 33  $\mu\text{m}$ . In stage-VI, effective pressure was restored to 17 MPa to complete an unloading-reloading cycle. As a result, the hydraulic aperture returned to 25  $\mu\text{m}$ . In the final stage-VII, a further increase in effective pressure to 29 MPa was applied, which caused the hydraulic aperture to decrease by less than 1  $\mu\text{m}$  with no significant change afterwards. After approximately 2900 hours (i.e., 120 days), the experiment was completed by unloading to 17 MPa and further to 1 MPa effective pressure yielding a final hydraulic aperture of 29.8  $\mu\text{m}$ . The total irreversible reduction in hydraulic fracture aperture thus cumulated to 30.9  $\mu\text{m}$  or approximately 50 % with respect to the initial aperture.

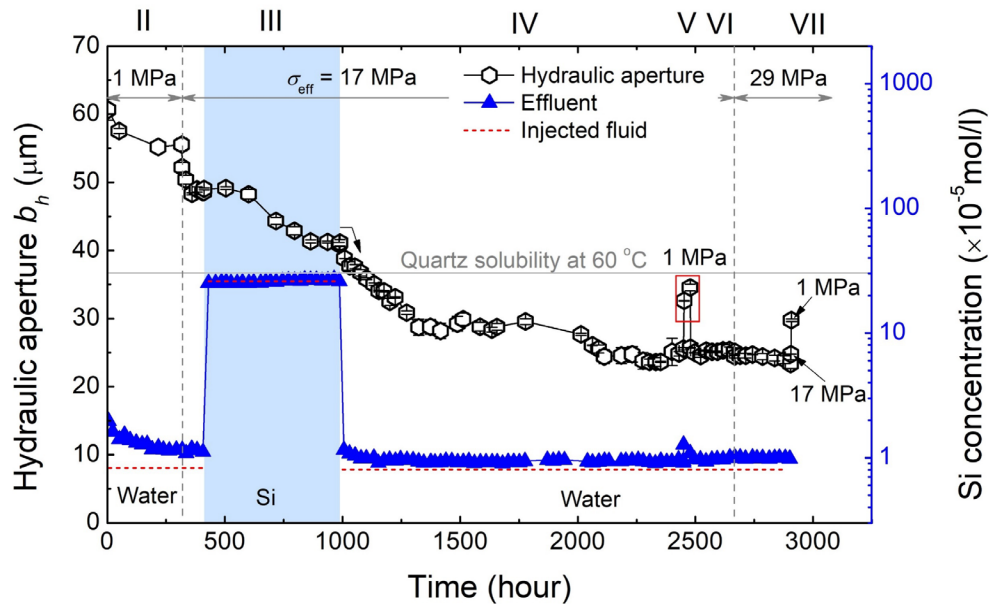


**Figure 5.3** Evolution of hydraulic aperture (hexagons) and effluent Si concentration (triangles) at varying conditions of effective stress ( $\sigma_{\text{eff}} = 1, 17,$  and  $29 \text{ MPa}$ ). The Si concentration in the injected fluid is shown in addition (red dashed line). During the stage highlighted in light blue, a silica solution with  $\sim 2.60 \times 10^{-4} \text{ mol/l}$  of Si was used as the permeating fluid.

### 5.3.2 Evolution of effluent Si concentration

The effluent was enriched in Si compared to the injected fluid concentrations throughout the experiment, irrespective of how the effective pressure and fluid chemistry conditions were varied (Figure 5.4). Matter (i.e., quartz) that is dissolved into the pore fluid and transported through the rock fracture generally emanates from two locations: (a) from the free fracture walls and (b) from the contacting asperities. The dissolution rate constant  $k_+$  of quartz can be calculated using the Arrhenius equation,

$$k_+ = A \exp(-E_{\text{act}}/RT) \quad (5.2)$$

where  $A \approx 1.59 \text{ mol/m}^2 \text{ s}$  is the frequency factor,  $E_{\text{act}} \approx 72 \text{ kJ/mol}$  is the activation energy of quartz (Rimstidt & Barnes, 1980),  $R$  is the gas constant, and  $T = 333 \text{ K}$  is the absolute experimental temperature. Furthermore, the dissolution rate of quartz dissolving from the free fracture walls  $\dot{m}_{\text{fre}}$  is given by,

$$\dot{m}_{\text{fre}} = c_{\text{fre}}^{\text{Si}} Q_v = 2WL f_r f_i (1 - R_c) k_+ \quad (5.3)$$

where  $c_{\text{fre}}^{\text{Si}}$  is the portion of Si concentration in the fluid that is related to free-face dissolution during fluid flow at a constant flow rate  $Q_v$  and  $f_r$  is the fracture surface roughness factor, which is the ratio between the rough fracture surface area and the geometric fracture surface plane  $WL$ . It is determined from the surface scan data (Figure E3), yielding a factor of about 1.14 for both specimen surfaces.  $f_i$  is the average grain boundary roughness factor, which can be estimated from  $f_i = S_{\text{BET}} d \rho_d / 6$  (Tester et al., 1994), where  $\rho_d = 2.65 \times 10^3 \text{ kg/m}^3$  is the quartz density and  $S_{\text{BET}} = 0.021 \text{ m}^2/\text{g}$  is the specific surface area of the rock-forming quartz grains, measured by krypton adsorption based on the Brunauer-Emmett-Teller (BET) theory. Here, an average grain diameter  $d = 2 \times 10^{-4} \text{ m}$  (estimated from thin section image analysis; Figure E2) is assumed, yielding  $f_i = 1.86$ . Accordingly, for a contact area ratio  $R_c$  in the range between 0.1 and 0.4,  $c_{\text{fre}}^{\text{Si}}$  will range from  $1.48 \times 10^{-8}$  to  $2.21 \times 10^{-8} \text{ mol/l}$ , which is three orders of magnitude lower than the measured concentration differences between the inlet and outlet fluids (Figure 5.4) and can, consequently, be neglected for the entire experiment. The surface retreat of the free fracture walls due to free-face dissolution thus is negligible at the present temperature (60 °C), and the effluent concentration difference can be considered to be entirely attributable to pressure solution that occurs on the contacting asperities.

Pressure solution thus was active from the beginning of the experiment even though the effective pressure in stage-II was as low as 1 MPa (Figure 5.4a). During this stage, the low contact area ratio amplified the macroscopic effective stress yielding high normal contact stresses on the

asperities. As a result of a local stress decrease as the contact area increased with time, the sampled effluent Si concentration continuously decreased. During the subsequent stage-III, the effective pressure was increased from 1 to 17 MPa. However, despite the significantly higher normal contact stress, no immediate effect on the effluent Si concentration was observed, both for deionized water and silica solution as the pore fluid (Figure 5.4a and b). After about 650 hours, the effluent Si concentration started to increase (Figure 5.4b). During stage-IV, the pore fluid change to deionized water caused the effluent Si concentration to gradually decrease and ultimately converge to approximately  $9.4 \times 10^{-6}$  mol/l for the remainder of this stage (Figure 5.4c). Subsequently (stage-V), as the effective pressure was decreased to 1 MPa, the effluent Si concentration showed a pronounced peak with about  $1.3 \times 10^{-5}$  mol/l and then decreased to  $1.1 \times 10^{-5}$  mol/l within the next 28 hours. During stage-VI, the effective pressure was restored to 17 MPa, and the effluent Si concentration returned to the level observed at the end of stage-IV. Finally (stage-VII), the effective pressure was increased to 29 MPa for 239 hours with no significant change in measured Si concentration until the end of the experiment.

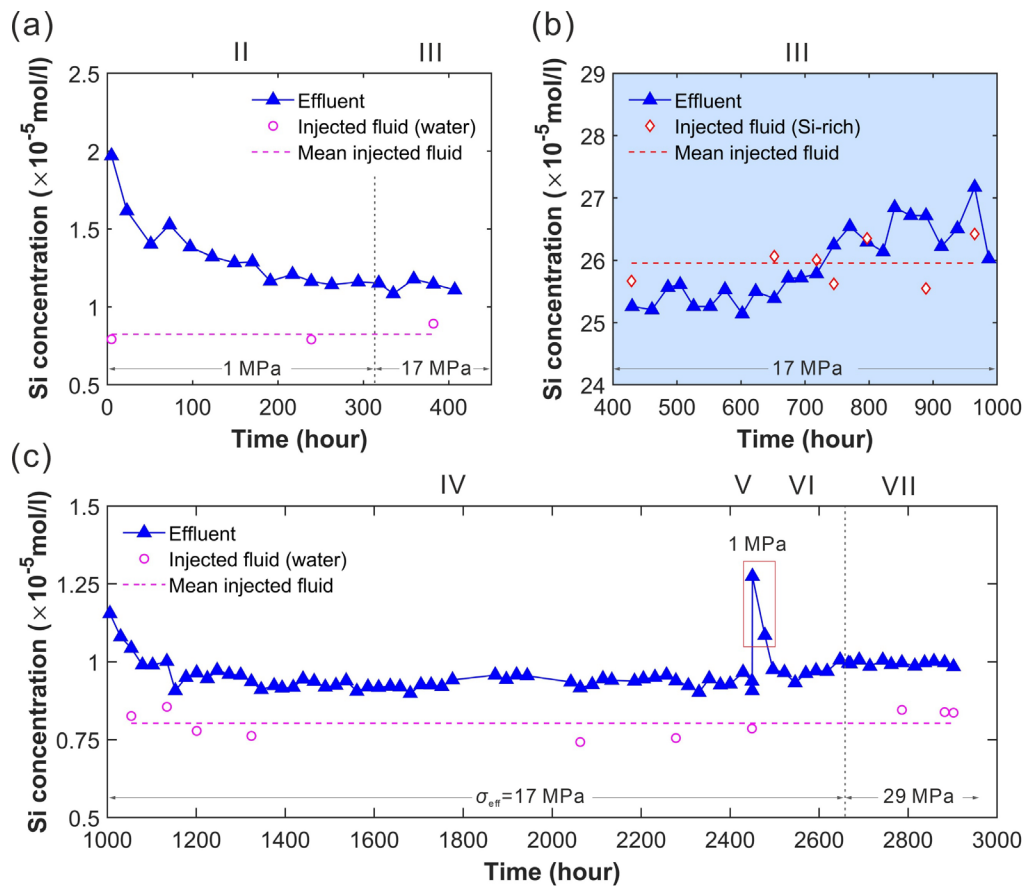


**Figure 5.4** Evolution of the Si concentrations of the injected fluids (deionized water in pink circles and the silica solution in red diamonds) and the effluents (blue triangles) during different experimental stages: (a) stage-II and partially stage-III; (b) stage-III; (c) stages-IV through VII.

### 5.3.3 Surface topography analysis

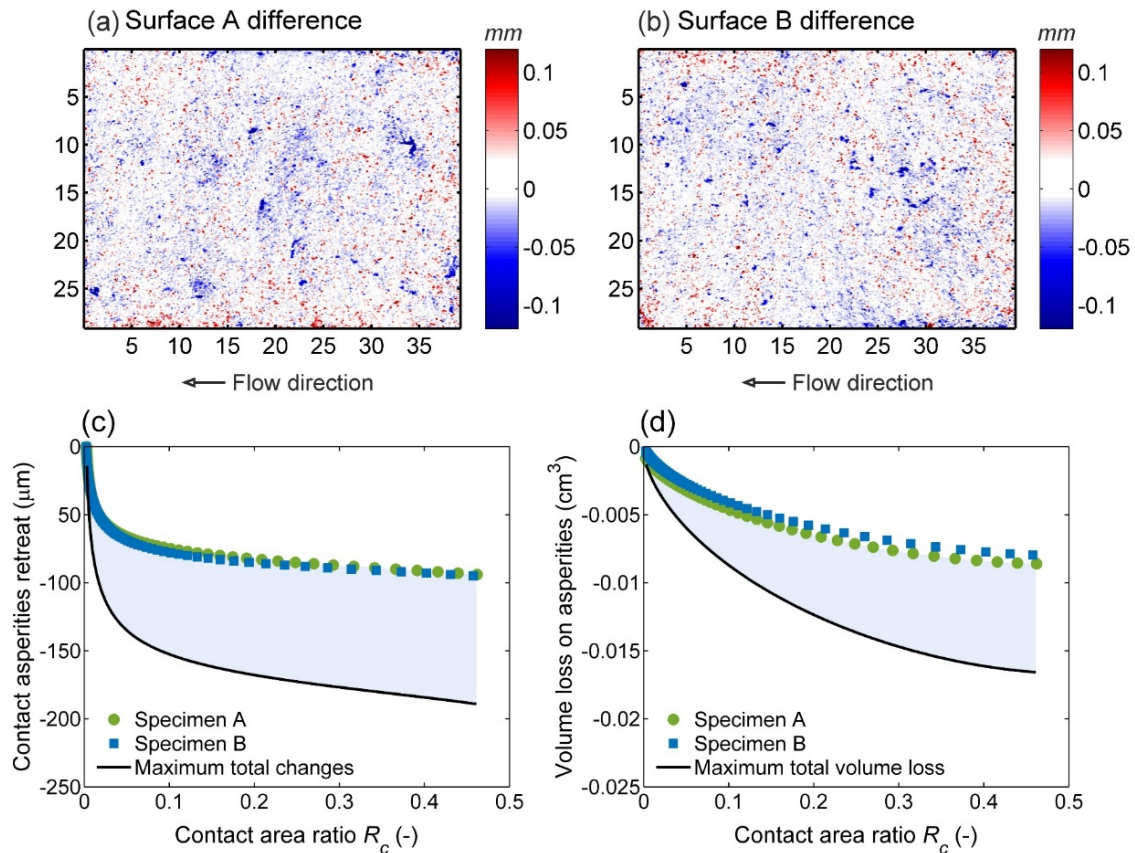


**Figure 5.5** Height differences of (a) fracture surface A and (b) fracture surface B were calculated by subtracting the respective initial surface data set from the final one. The numbers on the axis indicate sample dimensions in mm. A height reduction (in blue) or a height increase (in red) of the solid volume indicates geometric topography changes of the fracture surfaces. (c) The retreat of contact asperities and (d) volume loss on asperities of specimen A (circles) and specimen B (squares) as a function of contact area ratio. The maximum contact area ratio was derived by comparing the initial and the final surface topography of each fracture half (i.e., the totality of blue area divided by  $WL$  in (a) and in (b), respectively), yielding a value of about 0.46 in both cases. The evolution of the contact area ratio was determined by progressively adding the increase in the asperity contact area to the initial topography. The approximate maximum fracture aperture change (solid black line) resulting from the asperity retreat on both fracture surfaces A and B was calculated by additivity, assuming that the distribution of the height differences is identical on both surfaces. The area colored in light blue in (c) or, equivalently, in (d) indicates the uncertainty in fracture aperture change and volume loss if this assumption were incorrect.

The distribution of the fracture surface height differences (Figure 5.5a and b) were determined by a point-by-point subtraction of the surface topographies before and after the experiment (Figure

E3). The comparison of the height distribution indicates that most height changes occur in the range of  $\pm 100 \mu\text{m}$  (Figure E4). A surface height increase is mostly noticed further away from the asperities. A surface height decrease at asperity contacts results in a net reduction in fracture aperture yielding fracture closure. By simply summing the retreat of contact asperities, the range of the mechanical aperture closure as a function of the contact area ratio was presented in Figure 5.5c. The contact area growth is nonlinearly correlated to vertical displacement, which may amount to as much as  $180 \mu\text{m}$ . Similarly (Figure 5.5d), the total decrease in fracture volume of the two fracture surfaces as related to the asperities is estimated to approach a maximum of  $1.6 \times 10^{-2} \text{ cm}^3$ .

### 5.3.4 $\mu\text{CT}$ -based image analysis

Fracture voids (Figure 5.6a) were extracted from each  $\mu\text{CT}$  model and subsequently projected onto the selected datum plane to obtain the 2-D projections (Figure 5.6b). The contact areas  $A_c$  at the three experimental stages were identified and colored in yellow, which clearly indicates the serial changes resulting from mechanical compaction during the pre-loading stage (stage-I) and pressure solution at later stages, respectively. To quantitatively characterize the variations in fracture aperture, the mean mechanical aperture  $b_m$ , the number of isolated contacts  $n$ , the contact area ratio  $R_c$ , the mean pathway length of all isolated contacts  $l$ , and the averaged equivalent radius  $r$  were calculated based on the  $\mu\text{CT}$  models (Table 5.1).

**Table 5.1** Statistical summary of the  $\mu\text{CT}$  data.

Parameters	$b_m$ ( $\mu\text{m}$ )	$n$ (-)	$R_c$ (-)	$l$ ( $\mu\text{m}$ )	$r$ ( $\mu\text{m}$ )
Before the pre-loading stage	240.5	659	0.42 %	74.5	40.4
After the pre-loading stage	169.4	5252	4.12 %	79.5	45.1
After the entire experiment	139.1	4210	12.38 %	152.6	87.2

The mean mechanical aperture,  $b_m = V_B / WL$ , is calculated based on the corresponding volume,  $V_B$  of the fracture void space at different stages as obtained from the  $\mu\text{CT}$  models (Figure 5.6a);  $n$ : number of isolated contacts, statistically derived from the area indicated in yellow in Figure 5.6b;  $R_c = A_c / WL$ : contact area ratio;  $l = \sum(\text{width} + \text{length}) / 2n$ : mean pathway lengths of all isolated contacts (Figure E5);  $r = \sqrt{R_c WL / n\pi}$ : averaged equivalent radius, calculated by assuming circular contacts.

Mechanical compaction (stage-I) has rather limited effects on the average contact area (see  $l$  and  $r$  before and after the pre-loading stage in Table 5.1), resulting mainly in new contact points (i.e., enlarging  $R_c$  by increasing  $n$ ) rather than enlarging the area of the existing contact asperities. The loading-unloading process during this stage rearranged the fracture contacts and minimized



further mechanical deformation at later stages. After the experiment, pressure solution had resulted in an increase in total contact area accompanied by an enlargement of the mean pathway length of contacts, thereby causing longer diffusion paths. In addition,  $n$  decreased from 5252 to 4210 during the experiment indicating that contact area growths do not necessarily occur independently but that some of the contacts in close vicinity may have merged (Renard et al., 2012).

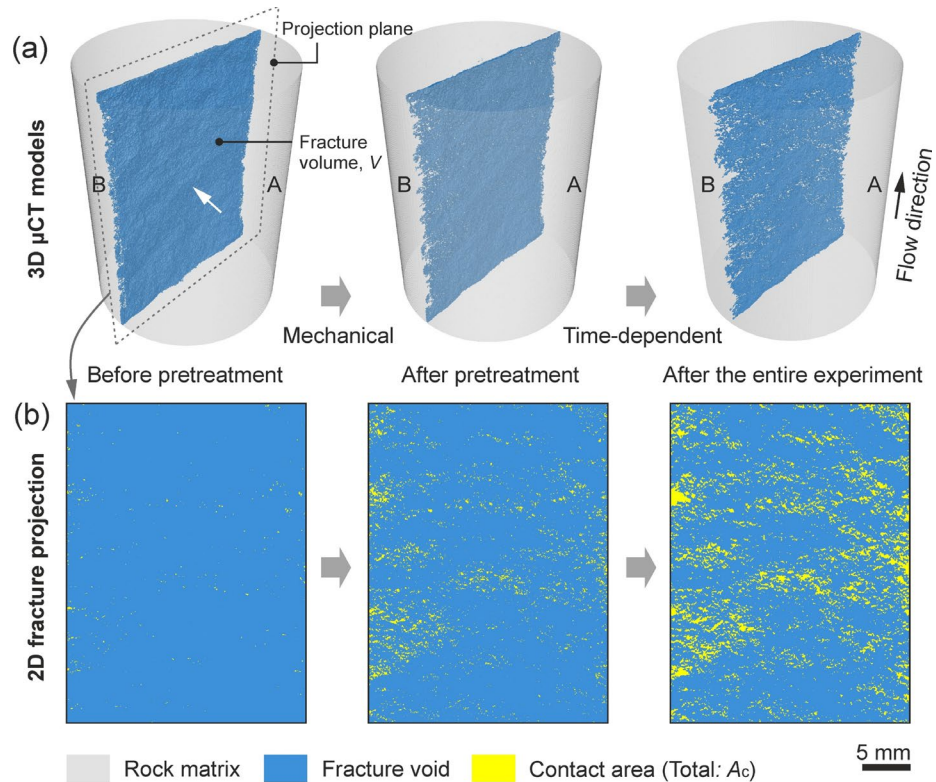


**Figure 5.6** (a) X-ray  $\mu$ CT-based 3-D perspective models obtained at different experimental stages: before the pre-loading stage, after the pre-loading stage, and after the entire experiment, respectively. (b) 2-D projections of the extracted fracture with the fracture voids (blue) and the contact areas (yellow) for the same three stages. The white arrows in (a) indicate the orientations of the projections. It should be noted that the fracture configurations are digital products that are based on resolution and image analysis and that were obtained at atmospheric conditions providing a qualitative idea of the evolution of fracture aperture at experimental in situ conditions.

### 5.3.5 SEM analysis

SEM imaging was performed to take a closer look at the final microstructure of the exposed asperity contact surfaces after separation of the two fracture halves. Two distinct types of contacts were identified, which are pervasive in both specimens: (a) nominally flat or undulating contacts with some internal roughness at the micrometer scale (Figure 5.7a and b) and (b) truly rough contacts with signs of micro-fracturing or grain crushing (Figure 5.7c and d). All contacts are more



or less circular in shape, and their size is in the range of tens of micrometers, whereas none of them shows an ideally flat geometry.

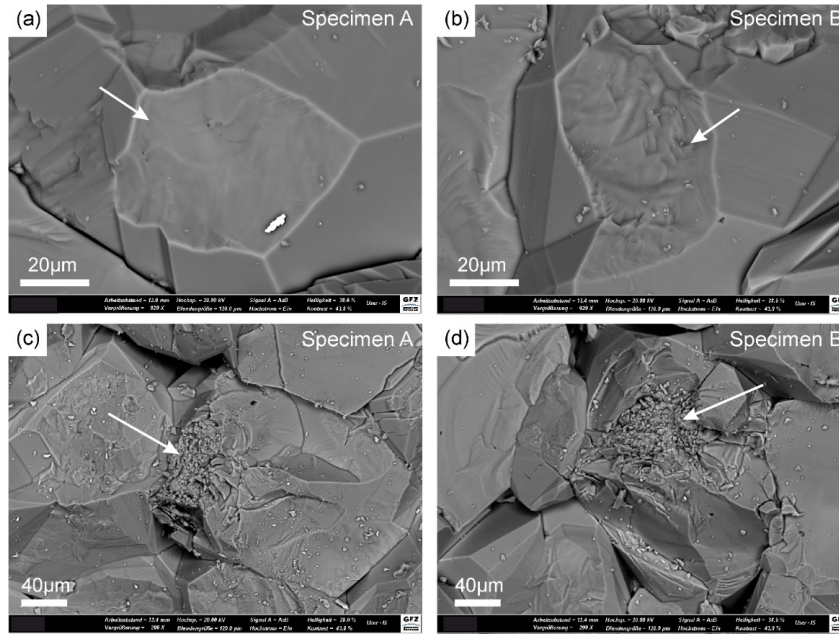


**Figure 5.7** Backscattered electron (BSE) micrographs of contact asperities (arrows) after the experiment. Nominally flat or undulating contact asperities with micrometer-scale intra-granular roughness, (a) specimen A and (b) specimen B. Rough asperities displaying features of microfracturing or crushing within the former contact boundary, (c) specimen A and (d) specimen B.

## 5.4 Discussion

### 5.4.1 Determination of the contact boundary and water film thickness

The transient peak concentration  $c_{\text{out}}^1 = 1.27 \times 10^{-5}$  mol/l (stage-V in Figure 5.4c) after unloading from 17 to 1 MPa comprises three components, (a) the partial release of water from the formerly stressed contacts due to the opening of the fracture, (b) the diffusion of Si from the remaining contacts to the void space, and (c) the additional dissolution on the increased reaction surface area. The last component (c) is negligible since the dissolution on the free-fracture walls is orders of magnitude lower than the measured peak concentration difference (see Section 5.3.2). Even considering the entire fracture surface area (i.e.,  $2WLf_i$ ), the free-face dissolution is impossible to achieve such a transient increase. If one assumes that the measured effluent concentration  $c_{\text{out}}^2 = 1.08 \times 10^{-5}$  mol/l after 28 hours at 1 MPa effective pressure is the result of Si diffusion from the remaining contacts, one can establish a mass balance according to,

$$V_s(c_{\text{out}}^1 - \bar{c}_{\text{in}}) = V_{\text{con}}c_{\text{con}}^{\text{Si}} + (V_s - V_{\text{con}})(c_{\text{out}}^2 - \bar{c}_{\text{in}}) \quad (5.4)$$

where the left term represents the measured peak concentration (mol) consisting of the two components (a) and (b) mentioned above. Further,  $V_s$  is the volume of the effluent sample (3 ml),  $V_{\text{con}} = f_r WL \Delta R_c \delta$  is the released water volume constrained in the contact zone,  $\delta$  is the mean thickness of the water film,  $c_{\text{con}}^{\text{Si}}$  is its mean concentration at effective stress of 17 MPa, and  $\bar{c}_{\text{in}} = 8.02 \times 10^{-6}$  mol/l is the mean injected Si concentration (dash line in Figure 5.4a and c). Rearranging Eq. 5.4 yields,

$$c_{\text{con}}^{\text{Si}} = (c_{\text{out}}^1 - c_{\text{out}}^2) \frac{V_s}{f_r WL \Delta R_c \delta} + c_{\text{out}}^2 - \bar{c}_{\text{in}} \quad (5.5)$$

where  $f_r = 1.14$  is the fracture surface roughness factor (Figure E3). The maximum  $R_c$  derived by comparing the differences in surface topography is about 0.46 (Section 5.3.3), and the final  $R_c$  at atmospheric conditions is approximately 0.12 (Section 5.3.4). Accordingly, given a reasonable contact area ratio change  $\Delta R_c$  in the range of 0.1~0.4 after unloading from 17 to 1 MPa, a correlation between  $c_{\text{con}}^{\text{Si}}$  and the mean thickness  $\delta$  of the contact boundary at an effective pressure of 17 MPa can be derived as shown in Figure 5.8. Gratier et al. (2009) estimated that the mean thickness of the water film between an indenter and a quartz crystal is in the range of 2~10 nm. Renard and Ortoleva (1997) introduce a theoretical model, combining electrical double layer theory with that of osmotic pressure, where the water film thickness is inversely correlated with the normal stress and varies within the nanometer range. For the present experiment, when applying a flat contact model and assuming a water film thickness of 5 nm, this yields unreasonably high water film Si concentrations (i.e., >2 mol/l). On the other hand, a flat contact boundary with a thickness at the micrometer scale is unable to transmit any normal stress between solids. Thus, isolated fluid inclusions should exist within the nominal contacts to trap the Si-rich fluid, as structurally has been observed in halite (Urai et al., 1986; Hickman & Evans, 1992). Likewise, the contact boundaries are mostly rough structures (Figure 5.7), which also has been observed by Van Noort et al. (2008a) in granular quartz aggregates and by Gratier et al. (2009) in indenter experiments with quartz crystals, however, both at temperatures higher than 300 °C.

The solubility of quartz  $C_{\text{eq}}^\sigma$  at an effective pressure of 17 MPa can be calculated according to (Renard et al., 1999),

$$\gamma^\sigma C_{\text{eq}}^\sigma = K_0(T, p_0) \exp\left(\frac{\Delta\mu}{RT}\right) \quad (5.6)$$

where  $\Delta\mu = V_m(p_c - p_p) / \alpha R_c$  is the chemical potential difference assuming that the molar Helmholtz free energy and the surface energy term are negligible. Further,  $R$  is the gas constant,  $\gamma^\sigma$  is the activity coefficient of quartz assumed to be equal to 1 in a dilute pressure-free state, and  $K_0$  is the equilibrium constant, which can be estimated by  $\log K_0 = 1.881 - 2.028 \times 10^{-3} T - 1560/T$  (Rimstidt &

Barnes, 1980). With the nominal  $R_c$  in the range of 0.1~0.4 and assuming a constant  $\alpha = 0.3$  (Van Noort et al., 2008b), the solubility  $C_{eq}^\sigma$  of stressed quartz in the contact boundary is in the range of  $1.1 \times 10^{-3} \sim 3.5 \times 10^{-2}$  mol/l. Assuming that the isolated fluid within the contacts is saturated ( $c_{con}^{Si} = C_{eq}^\sigma$ ), where pressure solution is limited by diffusion, and that the contacts are fully open after unloading ( $\Delta R_c \approx R_c$ ), the mean contact boundary thickness  $\delta$  can be calculated by combining Eqs. 5.5 and 5.6 yielding a range of 1.19~9.46  $\mu\text{m}$ . Since the contacts may merge during growth (Section 5.3.4), forming a constrained fluid-filled pocket, the volume of Si-rich fluid therein may also contribute to the measured peak concentration  $c_{out}^1$  yielding an overestimation of the calculated  $\delta$  value. If pressure solution is limited by dissolution, where the solubility within the contacts is not reached, the constraint water content within the contact boundaries should be larger than the estimated one,  $V_{con} = f_r WL \Delta R_c \delta$  ( $\delta = 1.19 \sim 9.46 \mu\text{m}$ ) to obey the measured peak Si concentration.

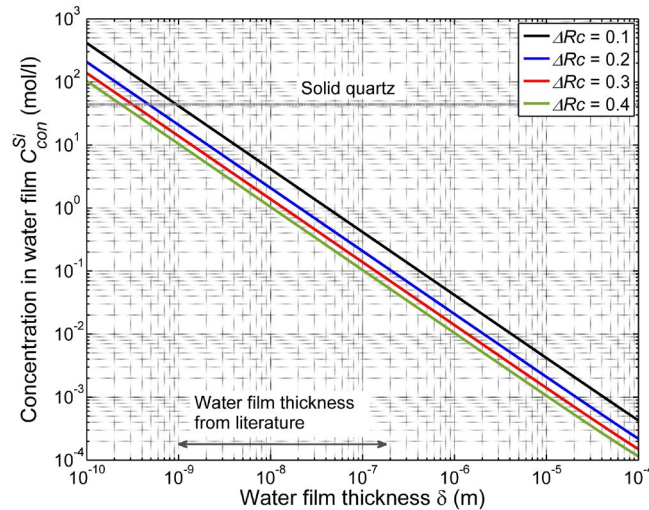


**Figure 5.8** Concentration of the water film constrained in the contact boundaries as a function of the mean water film thickness  $\delta$  and in relation to the change in contact area ratio  $\Delta R_c$  (Eq. 5.5). The correlations were derived from the directly measured Si concentrations during stage-V, i.e., of the effluent  $c_{out}^1$  after unloading from 17 to 1 MPa and  $c_{out}^2$  after 28 hours at 1 MPa effective pressure, respectively. The range of water film thickness is taken from (Renard & Ortoleva, 1997; De Meer et al., 2005; Gratier et al., 2009).

#### 5.4.2 Effects of contact-boundary morphology on mass transfer and aperture closure

Previous investigations on pressure solution in quartz aggregates at 150 °C showed that the strain rate and the Si concentration vary proportionally with effective stress (Elias & Hajash, 1992; Dewers & Hajash, 1995). In this study, a stress increase did not result in an increase in effluent

concentration over time periods of hundreds of hours (Figure 5.4a stage-III, from 1 to 17 MPa and Figure 5.4c stage-VII, from 17 to 29 MPa) and a noticeable aperture closure only occurred after the loading in stage-III rather than in stage-VII. Nevertheless, it was shown (Elias & Hajash, 1992) that the porosity of quartz aggregates remains constant at room temperature but decreases continuously at 150 °C despite identical stress conditions. A possible explanation for the contrasting behavior in the present case may, apart from temperature, relate to the existence of fluid inclusions within the asperity contacts. The Si-enriched fluid within the grain-to-grain interface, as produced by stress-induced dissolution, may migrate towards the pores within the contact preferentially. If this were true, there would be no immediate effect on the effluent concentration until a substantial overall concentration gradient between the contacts and the macroscopic fracture void space is established. This could likewise explain the trend of effluent Si concentration during stage-III between 400 and 650 hours (Figure 5.4b), where a sudden increase in Si concentration would restrict the mass transfer towards the free void space until an equilibrium of the fluid concentrations within the contacts and the fracture is reached.

The evolution of the contact area, overall, controls the entire fracture closure process by affecting both the normal stress on the asperities and the mean diffusion pathway within the contact boundary. The mean mechanical aperture was shown to nonlinearly decrease as the contact area ratio increases (Figure 5.5c). The aperture closure rate is largest at an early stage when the contact area ratio is small (Table 5.1). During stage-I, closure occurs by mechanical compaction as pressure solution is inactive due to the absence of water (Schutjens, 1991). Afterwards (stage-II through stage-VII), at wet conditions, the contact area ratio continuously increases by a factor of three concurrently with an enlargement of the mean diffusion pathway by a factor of about two (Section 5.3.4), yielding a significantly lowered aperture closure rate as observed towards the end of the present experiment.

### **5.4.3 Stress-dependent diffusion**

Assuming a flat water film, the mass transfer coefficient  $D\delta$  has been shown to range from  $10^{-21}$ – $10^{-19}$  m<sup>3</sup>/s (Rutter, 1976; Gratier & Irigm, 1986). In addition, Dysthe et al. (2002) concluded that  $D\delta$  is inversely related to stress. However, in the present case, the contact boundaries showed to develop rough structures during pressure solution. An apparent  $D\delta$  can now be considered, i.e., the mean diffusion coefficient of the rough contact boundary times the mean water film thickness. As was shown before, the measured effluent concentration  $c_{\text{out}}^{\sigma_1} \approx 9.35 \times 10^{-6}$  mol/l (i.e., the converging concentration at  $\sigma_1 = 17$  MPa) is smaller than  $c_{\text{out}}^{\sigma_2} = c_{\text{out}}^2 \approx 1.08 \times 10^{-5}$  mol/l at  $\sigma_2 = 1$  MPa (Figure 5.4c). Therefore, a diffusion-limited process needs to be assumed, and there must be changes in the

pathway of contacts and/or of  $D\delta$  to cause the observed variations in diffusion. Considering an average Si concentration in the water film within the contacts, i.e., assuming that the fluid within inclusions is saturated with respect to the solubility of the actual contacts, the diffusion flux rate  $\dot{m}_{\text{diff}}^\sigma$  can be calculated (Taron & Elsworth, 2010), further assuming contact areas of circular shape,

$$\dot{m}_{\text{diff}}^\sigma = (c_{\text{out}}^\sigma - \bar{c}_{\text{in}})Q_v = \sum_{i=1}^n 8D\delta(C_{\text{eq}}^\sigma - c_{\text{pore}}) \frac{2A_c^i}{l_i} \quad (5.7)$$

where  $c_{\text{out}}^\sigma$  is the effluent concentration at the respective effective pressure ( $\sigma_1 = 17$  MPa;  $\sigma_2 = 1$  MPa) and  $c_{\text{pore}} \approx \bar{c}_{\text{in}}$  is the pore fluid concentration. Further,  $A_c^i = R_c WL/n$  and  $l_i \approx 2r_i = 2(A_c^i/\pi)^{1/2}$  are the mean contact area and the mean pathway length of the contacts, respectively. In order to simplify the calculation, it is assumed that  $n$  remains constant. By combining Eqs. 5.6 and 5.7, one can estimate the changes of  $D\delta$  at an effective pressure of 17 MPa with respect to 1 MPa, yielding,

$$\frac{c_{\text{out}}^{\sigma_1} - \bar{c}_{\text{in}}}{c_{\text{out}}^{\sigma_2} - \bar{c}_{\text{in}}} = \frac{D_1 \delta_1}{D_2 \delta_2} \sqrt{\frac{R_c}{R_c - \Delta R_c}} \frac{K_0 \exp\left(\frac{\sigma_1 V_m}{\alpha R_c RT}\right) - \bar{c}_{\text{in}}}{K_0 \exp\left(\frac{\sigma_2 V_m}{\alpha (R_c - \Delta R_c) RT}\right) - \bar{c}_{\text{in}}} \quad (5.8)$$

where  $R_c$  is the contact area ratio at 17 MPa (0.1~0.4), and  $\Delta R_c$  is the change in the contact area ratio after unloading from 17 to 1 MPa. Figure 5.9 shows the ratio  $D_1 \delta_1 / D_2 \delta_2$  as a function of  $\Delta R_c$ , where  $\Delta R_c < (16/17) R_c$  in all cases as  $C_{\text{eq}}^{\sigma_2} < C_{\text{eq}}^{\sigma_1}$ . Hence, the apparent  $D\delta$  likely varies inversely with pressure or, more generally, with stress within the limits of the assumptions stated above.

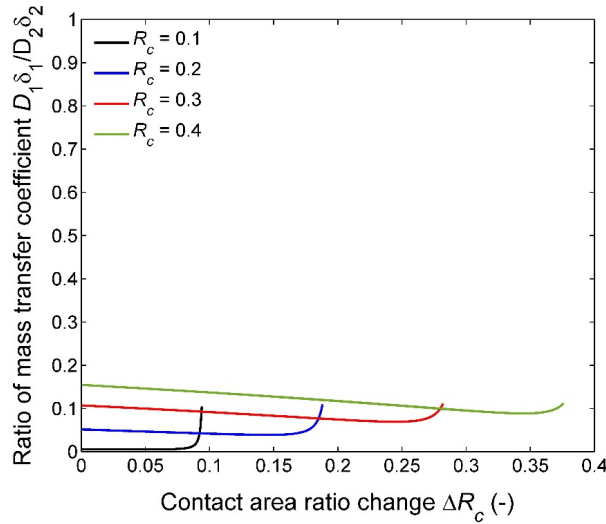


**Figure 5.9** The ratio of the apparent mass transfer coefficients  $D_1 \delta_1$  (at an effective pressure of 17 MPa) and  $D_2 \delta_2$  (at an effective pressure of 1 MPa) as a function of the contact area ratio change  $\Delta R_c$  during unloading from 17 to 1 MPa and in relation to the contact area ratio  $R_c$  range estimated for the present experiment.

#### **5.4.4 Equilibrium of pressure solution-induced compaction**

As was shown in Figure 5.3 and Figure 5.4, the hydraulic aperture and the effluent Si concentration tend to converge towards a constant value at constant effective pressure irrespective of its magnitude, i.e.,  $\sigma_{\text{eff}} = 1, 17, \text{ and } 29 \text{ MPa}$  in the present case. The decrease in both properties reflects an approach towards a chemo-mechanical equilibrium. Furthermore, the surface topography measurements confirm that the normal stress on the asperities will decrease as they expand their contact areas. As stated in Section 5.1, at present, there are two hypotheses regarding this compaction equilibrium related to pressure solution.

Both hypotheses consider pressure solution as a stress-controlled process, where stress migration across expanding contacts leads to the cessation of the former. The difference between the two hypotheses is that, in the first one,  $\sigma_1^{\text{crit}}$  is considered as an energy barrier. Therefore, in some previous studies, this term was used in a thermodynamic framework so that the driving force = effective stress  $- \sigma_1^{\text{crit}}$  (e.g., Yasuhara et al., 2003; Taron & Elsworth, 2010; Lu et al., 2018; Ogata et al., 2018). In contrast,  $\sigma_2^{\text{crit}}$  is considered as the criterion that pressure solution will not cease until some other counteracting process (e.g., healing resulting from neck growth within contacts) becomes predominant (Van Noort et al., 2008b). The present data now permits a qualitative analysis of the two hypotheses.

$\sigma_1^{\text{crit}}$  is temperature-dependent, yielding 77.7 MPa for quartz at 60 °C (Section 5.1). Since pressure solution proceeded at 1 MPa effective pressure during stage-II and stage-V, the normal contact stress is required to always exceed 77.7 MPa during contact area growth. This is likely inconsistent with the estimation that the approximate maximum stress on the contacts during stage-V is 33.3 MPa, as calculated with  $R_c = 0.1$  and  $\alpha = 0.3$ . Furthermore, a previous experimental study performed using a novaculite sample with an aligned tensile fracture at an effective pressure of 1.38 MPa (Yasuhara et al., 2006) evidenced substantial aperture closure accompanied by Si transfer into the pore fluid at 20 °C and thus the activity of pressure solution. In the former investigation, the contact area ratio resulting from the carefully matched fracture surfaces likely was significantly larger than in the present case yielding an even smaller average contact stress. Both studies thus imply that a minimum energy barrier may be inexistent.

$\sigma_2^{\text{crit}}$  depends on the structure of the contact boundary, i.e., the parameters  $\alpha$  and  $\delta$ . As was shown before, the contact boundary is a dynamic and rough structure as pressure solution proceeds, as was also observed by Van Noort et al. (2008a); and Gratier et al. (2009). Two characteristic contact types were identified (Section 5.3.5), i.e., (1) nominally flat or undulating contact boundaries displaying some internal roughness and (2) strikingly rough contacts containing micro-

fractures. This indicates that  $\alpha$  may show large variations ( $0 < \alpha < 1$ ) as contacts might flatten at long-term constant stress or roughen as stress is increased above some threshold. In addition, as  $D\delta$  is stress-dependent,  $\delta$  might also be inversely related to stress (Renard & Ortoleva, 1997). The equilibrium of pressure solution in this regard is unstable as the onset of healing will further enlarge the actual contact area reducing the contact stress. The reactivation of pressure solution may thus require stress to become enhanced.

However, the notion of  $\sigma_2^{crit}$  is based on the concept of an island-channel structure, where the solid-to-solid contact islands are distributed within the nominal contact zone (Van Noort et al., 2008b). The driving force for healing is the surface energy difference between solid-solid and solid-liquid interfaces in the true contact junctions. The fluid within the channels is essentially connected to the fracture void space and does not support any non-hydrostatic stress. The present experimental results support the existence of fluid inclusions within the contacts (Section 5.4.1). However, it is impossible to confirm the existence of a water film within the actual contact islands from these results. Dissolution may occur across a rough grain-to-grain contact that contains a fluid phase that could be discontinuous, either inside the actual contact island or on the island margins (Raj, 1982). As a result of the serial diffusion process (actual contacts  $\rightarrow$  inclusions  $\rightarrow$  fracture void space), as discussed in Section 5.4.2, the fluid inclusions may supersaturate as dissolved matter from the actual contacts diffuses in and, consequently, precipitation might occur. Accordingly, this would accelerate neck growth accompanied by surface energy-driven contact boundary healing causing the cessation of pressure solution.

## 5.5 Conclusions

A long-term (120 days) flow-through experiment on pressure solution creep in a fractured pure quartz sandstone (Fontainebleau) of low matrix permeability was performed at 60 °C, varying effective pressure (1, 17, and 29 MPa) and injection fluid chemistry (deionized water and silica solution). The purpose of the parameter changes was to constrain (1) the conditions yielding an acceleration or deceleration of fracture closure and (2) the concurrent changes in effluent Si concentration.

It showed that pressure solution was active throughout the experiment. At an early stage, pressure solution is dominated by stress migration across expanding contacts. Later on, pressure solution is more and more controlled by diffusion. Surface topography measurements evidenced that the overall contact area is continuously growing. Contact area expansion causes a stress

redistribution over the fracture surface, impacting the diffusion process due to a length increase of the diffusion paths. In combination with a measurement of Si concentration in the fluid released from the contacts after unloading, SEM imaging implied that the contact boundaries are not as flat as was previously assumed. Instead, the rough contacts, as were observed, may contain fluid inclusions that control the kinetics of pressure solution by affecting the contact stress and an ongoing serial diffusion process. In the latter, the mass transfer coefficient of the contact boundaries is inversely correlated with effective stress.

This study suggests that pressure solution, most likely, is a spontaneous process that occurs at minimum non-hydrostatic stress resulting from chemical potential differences but not requiring the notion of a "critical stress". Furthermore, there is strong support for the hypothesis that the cessation of pressure solution is a dynamic process that will only occur when other processes (e.g., precipitation-induced contact boundary healing) become predominant.



# Chapter 6

## General conclusions, implications and suggestions

### 6.1 Summary and remarks

This thesis presents a systematic experimental study on the transport properties of both porous and fractured sandstones. Emphasis is placed on how fluid-rock interactions govern the evolution of rock mass permeability under hydrothermal conditions. After a brief background introduction to fluid flow through porous media and rock fractures, three main scientific questions that the thesis tries to answer within the framework of geothermal reservoir utilization are outlined in Chapter 1. These questions are (1) how clay (i.e., illite) particles mechanistically can induce a rock permeability decline associated with cyclic temperature and fluid salinity variations; (2) what the correlation between the stress-dependent fracture permeability and the factors fracture surface roughness, fracture wall offset, and mechanical matrix properties is; and (3) how the rock fracture aperture and its hydraulic conductivity evolve over a longer period of time due to fluid-rock interactions. The following Chapters 2-5 then aim to answer these questions. The main conclusions drawn from these experimental studies can be summarized as follows:

- 1) The mechanisms of an irreversible permeability reduction of illite-bearing sandstones induced by increasing temperature and decreasing pore fluid salinity ( $\text{Na}^+$ ) operated rather independently and were identified as thermo-mechanical pore throat closure and illite particle migration, respectively. Initially, illite particles are tightly attached to the pore walls in Flechtinger sandstones due to their morphology and, most importantly, as  $\text{K}^+$  and divalent cations, e.g.,  $\text{Ca}^{2+}$ ,  $\text{Mg}^{2+}$  are present at the exchangeable sites, enhancing the charged particles' stability. Thus, initial sample permeability was not affected by low pore fluid salinity, and illite particles are unfavorable to be mobilized at these conditions. However, illite will be sensitive to mobilization when a cation exchange of  $\text{Na}^+$  has occurred, and the pore salinity subsequently is reduced (Chapter 2). This behavior was

found at both room temperature and 145 °C. The major contribution of this study is to distinguish different mechanisms of permeability decline with respect to temperature and fluid salinity changes.

- 2) Hydro-mechanical investigations on self-propping fractures demonstrate that a relative fracture wall offset can significantly increase fracture aperture and hydraulic conductivity, but the degree of increase strongly depends on the fracture surface roughness. Fracture surfaces in nature are always found to be self-affine over a larger scale, and, consequently, an incremental fracture wall offset likely leads to an increase in fracture aperture. However, for some fracture types, e.g., saw-cut fractures and fractures along bedding layers in natural sedimentary rocks, surface roughness remains scale-independent as long as the fracture area is larger than a roll-off wavelength, and thus, any further displacement does not affect fracture aperture significantly.

Additionally, direct observations of fracture configurations by  $\mu$ CT show that the contact area ratio after stress loading-unloading inversely correlates with the fracture offset, depending on the respective surface roughness and the strength of the contact asperities. It is apparent that under stressed conditions, a rock fracture with a higher mechanical strength yields a sustainable permeability and experiences less contact asperity damage. Moreover, it was also found that the contact asperities mainly occur isolated and tend to be preferentially oriented perpendicular to the fracture wall displacement, which may induce flow anisotropy.

- 3) A further main contribution of this thesis is to experimentally characterize the long-term evolution of fracture aperture under hydrothermal conditions. Pressure solution remains active in stressed fractured samples (i.e., pure quartz Fontainebleau sandstone). There is evidence that the Si concentration of the pore fluid can become larger than the hydrostatic quartz solubility at the same temperature during stagnant flow (Chapter 4) and that the measured Si dissolution rate is faster than the corresponding quartz free face dissolution rate during continuous flow (Chapter 5). Therefore, pressure solution plays a paramount role in the long-term evolution of fracture aperture and hydraulic conductivity at the conditions applied in this study.

It was further demonstrated that the pore fluid Si concentration could have a remarkable effect on the process of pressure solution. The cumulative Si content in the pore fluid, either transported from stressed interfaces or introduced artificially by inlet flow, can retard mass diffusion, causing a slowdown of fracture closure. In contrast, reducing the pore fluid Si concentration will accelerate the process by disturbing the chemical equilibrium as a

result of the so enlarged concentration gradient between non-hydrostatically stressed and hydrostatically stressed locations. Furthermore, the existence of grain-to-grain contact boundaries with a rough inner structure was evidenced, which may contain discontinuous fluid inclusions. Thus, the slowdown of fracture closure, as induced by fluid-rock interactions (i.e., pressure solution in this case), is governed by a reduction of the non-hydrostatic stress on the asperities due to a contact area growth and solute accumulation within the contact interfaces.

## **6.2 Implications for natural rock systems and engineering applications**

For any geo-resources (oil/gas/heat) exploitation from certain reservoirs, the fluid transport properties of the reservoir rocks are of primary importance. Formation permeability decline/damage is a high risk in reservoir utilization and needs to be avoided. This study provides insights into permeability variations under hydrothermal conditions, which may help to minimize potential risks. Furthermore, the fundamental studies on the deformation behavior of fractured pure quartz sandstone will also improve the current knowledge of early diagenesis.

### **6.2.1 Seasonal heat storage in aquifers**

Heat storage in sandstone aquifers used for district heating is a way to balance energy demands and resources in different seasons. The heat from sources such as waste incineration or solar power needs to be stored/extracted by pumping fluids into/from aquifers. The efficiency depends on the aquifer permeability, and a permeability decline may increase the costs and even cause the project to fail. Therefore, rock permeability changes related to temperature and fluid salinity changes are crucial.

It is noticed that fluid-illite interactions within the pore space of Flechtinger sandstone can significantly affect its permeability by orders of magnitude regardless of the temperature conditions. Temperature increase alone also negatively affects permeability, operating with a different mechanism (i.e., thermo-mechanical). This implies that such Lower Permian (Upper Rotliegend) sedimentary rocks may be inappropriate for heat storage. However, if sandstone permeability remains relatively high (on the order of mD) after a temperature increase, the aquifer formation permeability can be sustainable when not reducing fluid salinity. In contrast, previous studies on Berea sandstone containing kaolinite clay particles showed a different behavior. Temperature increase and fluid salinity reduction act coupled in kaolinite particle migration and the concurrent

permeability decline (Schembre & Kovscek, 2005; Rosenbrand & Kjøller, 2014; Rosenbrand et al., 2015b). Elevating temperature already causes particle migration, and thus, any further fluid salinity reduction at some elevated temperature does not affect permeability further. Schembre and Kovscek (2005) analyzed the threshold conditions of temperature and fluid salinity at which kaolinite particles start to release.

These discrepancies emphasize that a single rock property obtained for a certain sample containing one clay type cannot be simply extended to other samples containing different clays. The intrinsic properties (e.g., cations at the exchangeable sites) and the morphologies that the specific clay presents in the pore space (e.g., coating, lining, and attaching) need to be elaborately investigated. Furthermore, for a potential reservoir of any geothermal application, the thermochemical properties of the formation need to be carefully taken into account.

### **6.2.2 Permeability of deep geothermal reservoirs**

Fracture networks are always the predominant pathways for fluid flow in deep geothermal reservoirs. They are either pre-existing or artificially generated. In general, reservoir stimulation is needed to enhance its productivity for economic utilization (e.g., Blöcher et al., 2016; Hofmann et al., 2019; Zang et al., 2020).

Hydraulic fracturing in a tight sedimentary formation to enhance its conductivity for fluid flow requires a preceding understanding of the target formation. Generally, natural fracture surface roughness is self-affine over a larger scale (Schmittbuhl et al., 1995), where fracture wall displacement is proportional to fracture aperture. However, here it was also found that saw-cut fractures remain scale-independent as long as the fracture area is larger than a roll-off wavelength. This case may occur when fractures propagate along the bedding or certain smooth layers formed over geological time scales. Fracture aperture would remain unchanged when further increasing the offset of these "smooth" fractures. Under these circumstances, introducing proppants into the fracture would be necessary. Based on the experimental results, it was found that knowing the fracture surface roughness, the fracture wall offset, and the mechanical matrix properties of analogue rock materials is important for evaluating fracture transport properties and their sustainability under stressed conditions and for designing hydraulic stimulation treatments of reservoir formations.

In addition, the long-term experiments indicate that the propping asperities undergo retreat and expansion due to pressure solution (Chapter 5), which may cause both smoothening of the fracture surface and permeability reduction. After a long-term fracture deformation, any further hydraulic stimulation might be less efficient to enhance the hydraulic conductivity compared to the previous

ones, unless sufficient displacement is generated or proppants are injected.

### **6.2.3 Long-term sustainability of fractures in the Earth's upper crust**

The present fundamental studies on fractured pure quartz sandstone deformation imply that the contact boundary, where pressure solution occurs, presents a rough structure that likely contains fluid inclusions rather than an adsorbed thin fluid film. Furthermore, it was found that the creep mechanisms operate in such a way that a fundamental transition from stress migration across contacts (i.e., when the contacts are still small) to a diffusion related process (i.e., when the contacts are sufficiently large) occurs at present (moderate) temperature (Chapter 5). This is in contrast to previous studies on quartz aggregates at 400 - 600 °C under effective pressures of 50 - 150 MPa (Niemeijer et al., 2002) and at 300 - 600 °C under effective pressures of 35 - 100 MPa (Van Noort et al., 2008a), where pressure solution is suggested as a dissolution (interface kinetics of quartz) controlled process. This might be because diffusion at such (high) temperatures is faster than dissolution due to the fact that the activation energy of diffusion (Nakashima, 1995) is smaller than that of dissolution for quartz (Rimstidt & Barnes, 1980) at these conditions. This interpretation might be partially supported by Elias and Hajash (1992), who found that long-term, persistent, time-dependent compaction of quartz aggregates was maintained under all effective pressures of 17.2 – 69 MPa at 150 °C rather than under 69 MPa at 23 °C.

It is noticed that, in addition to the temperature influence, the isolated fluid inclusions within contacts also significantly affect the sequential diffusion process. Although the dissolution rate still remains slow, the mass diffusion from the nominal contact boundary to the macroscopically connected pores is a more complicated process in this case.

Overall, the observations imply that generated fractures will likely be sustainable at shallow depth, where the temperature is relatively low. However, fractures at deeper crustal conditions (temperatures > ~300 °C, high effective stresses) may experience persistent deformation and permeability reduction. This is not only detrimental for the utilization of deep reservoirs but will impact natural fluid flow.

## **6.3 Suggestions for further research**

This study improves the current knowledge of the fluid transport properties of clay-bearing sandstones and rock fractures. It is evident that 1) the clay phases play an important role in rock permeability evolution when changing temperature and fluid salinity, and 2) rock fracture

deformation with time is a process attributed to the interplay of stress changes and fluid-rock interactions. However, there are still a number of questions that remain to be answered, and some extensive research needs to be carried out. Suggestions for further work include some theoretical and practical aspects as follows:

- 1) Permeability of illite-bearing sandstones decreases upon temperature increase and fluid salinity reduction (NaCl). An important question for engineering purposes is whether one can recover permeability by (i) increasing fluid salinity, (ii) injecting solutions enriched by divalent cations, or (iii) altering fluid flow dynamics.
- 2) For time-dependent fracture closure, it was found that the evolution of contact boundaries plays a critical role during pressure solution, affecting not only the contact stress variations but also the diffusive properties of the dissolved matter within the contact interfaces. Therefore, an in-depth investigation of contact boundary evolution under stressed conditions is important for a better understanding of pressure solution (De Meer et al., 2002; Dysthe et al., 2002; Dysthe et al., 2003; De Meer et al., 2005). The contact boundary characteristics and the pressure solution process need to be further elaborated on a single grain-to-grain contact scale. Indentation experiments (e.g., Gratier et al., 2009; Gratier et al., 2014) combined with fluid flow and fluid element analyses may be a suitable and efficient method to perform such investigations.
- 3) This study demonstrated the inexistence of a temperature-dependent threshold energy (i.e., previously used in thermodynamic models), below which pressure solution would cease. Therefore, a modified theory is required to describe the retardation and/or cessation of pressure solution and fracture aperture closure. In addition, other mechanisms such as mineral precipitation, stress corrosion, and surface energy-driven neck growth would need to be considered in further studies.
- 4) It was noticed that the pore fluid chemistry has remarkable effects on the pressure solution and thus fracture deformation processes. However, natural geofluids are much more complex compared to deionized water and the Si-enriched solution as used in the present studies (Chapters 4 and 5) (Milsch et al., 2008a). For example, the Lower Permian (Rotliegend) reservoir rock at the mentioned Groß Schönebeck site is saturated with a highly saline Ca-Na-Cl type formation fluid ( $\approx 265\text{g/l}$ ) (Regenspurg et al., 2015). Therefore, it is necessary to investigate how rock reacts with natural geofluids. In geothermal applications, thermal fluids may become oversaturated due to fluid circulation or a temperature decrease during operation. This process may cause mineral precipitation in rock pores or fracture void spaces and, consequently, a permeability decline (e.g.,

Hilgers & Tenthorey, 2004; Prajapati et al., 2018; Wetzel et al., 2020; Tranter et al., 2021). In addition to the effects of pressure solution, studies of mineral precipitate-related permeability changes are also important, for example: where does the precipitation preferentially occur, and how do mineral precipitates affect rock permeability?

- 5) In addition to measuring a fracture's hydraulic conductivity, as described in the present work, real-time measurements of fracture deformation will provide direct information about fracture evolution, which is indispensable in further studies.
- 6) The present experiments were conducted under hydrostatic pressure conditions. Performing flow-through experiments under true triaxial conditions may also be considered to gain more details on the anisotropic fluid transport properties of rock fractures.
- 7) For the long-term investigations of fracture closure, the present studies were conducted only with pure quartz (Fontainebleau) sandstone to simplify the reactions between pore fluid and rock matrix. Evidently, the mineralogical composition of natural rock systems is much more complex, where other minerals may accelerate or decelerate the pressure solution process, which needs to be considered in further studies.
- 8) Time-dependent fracture permeability variation after shearing or during shearing is also a critical point requiring more investigations. Unlike the ideally prepared pre-displaced fractures under hydrostatic pressures in the present study, shearing fractures under stressed conditions will yield dilatancy and/or asperity damage, which may lead to differences in permeability evolution. These types of fractures are more realistic for natural conditions. For example, natural earthquakes or hydraulic stimulations can generate new fractures or shear pre-existing ones. How these fractures evolve over time is not only important for the understanding of earthquakes (fault reactivation) but also for the evaluation of reservoir efficiency.

## Appendices

### Appendix A: Calculation of the particle interaction energy by DLVO theory (Chapter 2)

According to DLVO theory, the total interaction free energy between two (solid) phases in an aqueous solution can be calculated by combining the London-van der Waals attraction  $V_{\text{vdW}}$  and the commonly repulsive, electrical double layer (EDL) interaction  $V_{\text{EDL}}$  (Leite et al., 2012). In addition, the extended Born potential  $V_{\text{BR}}$  is a short-range ( $< 0.5$  nm) molecular interaction resulting from the overlap of electron clouds. Therefore, its magnitude is negligible compared to  $V_{\text{vdW}}$  and  $V_{\text{EDL}}$  for particle separations larger than 0.5 nm (Khilar & Fogler, 1987). In the following, all other possible interactions (e.g., Tchistiakov, 2000) are neglected, and the total interaction free energy thus is expressed as,

$$V_{\text{total}} = V_{\text{EDL}} + V_{\text{vdW}} + V_{\text{BR}} \quad (\text{A1})$$

Considering a sphere-plate geometry, the van der Waals interaction free energy at a separation distance  $d$  is defined as (Gregory, 1981; Bergström, 1997),

$$V_{\text{vdW}}^{i,i}(d) = -\frac{A_{131}r_p}{6d} \quad (\text{A2a})$$

for illite particle to illite plate interactions and

$$V_{\text{vdW}}^{q,i}(d) = -\frac{A_{132}r_p}{6d} \quad (\text{A2b})$$

for illite particle to quartz plate interactions, respectively, where  $r_p$  is the particle radius. Based on the SEM observations (Figure 2.2), an average particle radius of 1.2  $\mu\text{m}$  is assumed. The Hamaker constant  $A$  characterizes the interaction between clay minerals (subscript 1) and the grain walls (subscript 2) separated by an aqueous fluid (subscript 3) (Israelachvili, 2011),

$$A_{131} = \frac{3k_{\text{B}}T}{4} \left( \frac{\epsilon_1 - \epsilon_3}{\epsilon_1 + \epsilon_3} \right)^2 + \frac{3h\nu_e}{16\sqrt{2}} \frac{(n_1^2 - n_3^2)^2}{(n_1^2 + n_3^2)^{\frac{3}{2}}} \quad (\text{A3a})$$



$$A_{132} = \frac{3k_B T}{4} \left( \frac{\varepsilon_1 - \varepsilon_3}{\varepsilon_1 + \varepsilon_3} \right) \left( \frac{\varepsilon_2 - \varepsilon_3}{\varepsilon_2 + \varepsilon_3} \right) + \frac{3h\nu_e}{8\sqrt{2}} \frac{(n_1^2 - n_3^2)(n_2^2 - n_3^2)}{(n_1^2 + n_3^2)^{\frac{1}{2}}(n_2^2 + n_3^2)^{\frac{1}{2}} \left[ (n_1^2 + n_3^2)^{\frac{1}{2}} + (n_2^2 + n_3^2)^{\frac{1}{2}} \right]} \quad (\text{A3b})$$

where  $k_B = 1.381 \times 10^{-23}$  J/K is the Boltzmann constant,  $T$  is the absolute temperature, and  $h = 6.626 \times 10^{-34}$  Js is the Planck constant.  $\varepsilon_1$ ,  $\varepsilon_2$ , and  $\varepsilon_3$  are the dielectric permittivities,  $n_1$ ,  $n_2$ , and  $n_3$  are the refractive indexes, and the subscripts 1, 2, and 3 denote clay, quartz, and NaCl solution, respectively.  $\nu_e = 3 \times 10^{15}$  s<sup>-1</sup> is the main electronic absorption frequency (Israelachvili, 2011). The dielectric permittivity of illite  $\varepsilon_1$  is taken from Josh and Clennell (2015). The dielectric permittivity of quartz  $\varepsilon_2$  is independent of temperature in the range between 20 °C and 175 °C, according to Stuart (1955). Finally, the temperature and salinity-dependent dielectric permittivity of a NaCl solution  $\varepsilon_3$  is given, e.g., by Marshall (2008) and Maribo-Mogensen et al. (2013). A constant refractive index  $n_1 = 1.59$  is assumed (Friedrich et al., 2008), and the temperature-dependent indices  $n_2$  and  $n_3$  are taken from Leviton and Frey (2006) and Aly and Esmail (1993), respectively.

According to Gouy-Chapman theory (Butt et al., 2006), the net surface charge density  $\sigma_{\text{illite}}$  defines the surface potential  $\Psi_1$  of illite as expressed by the Grahame equation (Grahame, 1947),

$$\Psi_1 = \frac{2k_B T}{ze} \ln \left( \frac{\sigma_{\text{illite}}}{\sqrt{8N_A c \varepsilon_0 \varepsilon_r k_B T}} + \sqrt{\frac{\sigma_{\text{illite}}^2}{8N_A c \varepsilon_0 \varepsilon_r k_B T} + 1} \right) \quad (\text{A4})$$

where  $c$  is the cation concentration in the solution,  $z$  is the valence of the respective cation,  $e$  is the elementary charge, and  $N_A$  is the Avogadro constant.  $\varepsilon_0 = 8.854 \times 10^{12}$  C<sup>2</sup>/Nm<sup>2</sup> is the vacuum permittivity, and  $\varepsilon_r$  is the relative permittivity of the solvent given by Maribo-Mogensen et al. (2013). The counter-ions that extend from a negatively charged surface into the aqueous solution result in a diffuse EDL. The thickness of this EDL is known as the Debye screening length  $\kappa^{-1}$ , which is expressed as,

$$\kappa^{-1} = \sqrt{\frac{\varepsilon_0 \varepsilon_r k_B T}{N_A c e^2 z^2}} \quad (\text{A5})$$

Assuming a constant surface charge density where the surface charges are uniformly distributed on the illite crystals, the surface potentials of two illite phases are equal. Consequently, the interaction free energy of the EDL for the illite particle to illite plate system is (Gregory, 1975)

$$V_{\text{EDL}}^{i,i}(d) = 64\pi r_p k_B T N_A c z^2 \kappa^{-2} \tanh^2 \left( \frac{ze\Psi_1}{4k_B T} \right) e^{-\kappa d} \quad (\text{A6a})$$

Similarly, for the illite particle to quartz plate system, the interaction free energy is

$$V_{\text{EDL}}^{q,i}(d) = 64\pi r_p k_B T N_A c z^2 \kappa^{-2} \tanh \left( \frac{ze\Psi_1}{4k_B T} \right) \tanh \left( \frac{ze\Psi_2}{4k_B T} \right) e^{-\kappa d} \quad (\text{A6b})$$

where the surface potential of quartz  $\Psi_2$ , approximated by the zeta potential, is temperature-dependent (Ramachandran & Somasundaran, 1986; Schembre & Kovsky, 2005; Rodríguez & Araujo, 2006) and decreases as temperature increases.

Finally, the extended Born potential is expressed as (Ruckenstein & Prieve, 1976),

$$V_{\text{BR}}(d) = \frac{A\sigma_c^6}{7560} \left[ \frac{8r_p+d}{(2r_p+d)^7} + \frac{6r_p-d}{d^7} \right] \quad (\text{A7})$$

where the collision diameter  $\sigma_c = 0.5$  nm is assumed to be constant (Elimelech et al., 2013).

**Appendix B: Experimental data of the permeability measurements (Chapter 2)**

**Table B1 Sample FS1.**

No.	Stage	Temperature (°C)	Permeability (mD)	Max flow rate (ml/min)	Fluid	Total time (h)	Flow direction
1		25	5.016	2	H <sub>2</sub> O	2	Bottom to top
2		40	3.407	2	H <sub>2</sub> O	8	-
3		58	0.636	1	H <sub>2</sub> O	27	-
4		76	0.254	0.3	H <sub>2</sub> O	35	-
5	1	79	0.184	0.25	H <sub>2</sub> O	98	-
6		96	0.155	0.2	H <sub>2</sub> O	103	-
7		117	0.143	0.2	H <sub>2</sub> O	108	-
8		119	0.158	0.2	H <sub>2</sub> O	123	-
9		140	0.197	0.4	H <sub>2</sub> O	127	-
10		121	0.209	0.3	H <sub>2</sub> O	132	-
11		118	0.217	0.3	H <sub>2</sub> O	146	-
12		97	0.205	0.3	H <sub>2</sub> O	152	-
13	2	81	0.193	0.25	H <sub>2</sub> O	155	-
14		80	0.191	0.25	H <sub>2</sub> O	156	-
15		61	0.175	0.1	H <sub>2</sub> O	173	-
16		43	0.158	0.05	H <sub>2</sub> O	197	-
17		60	0.168	0.1	H <sub>2</sub> O	202	-
18		78	0.168	0.2	H <sub>2</sub> O	222	-
19	3	95	0.182	0.2	H <sub>2</sub> O	248	-
20		118	0.212	0.3	H <sub>2</sub> O	270	-
21		141	0.212	0.4	H <sub>2</sub> O	274	-
22		141	0.222	0.5	H <sub>2</sub> O	296	-
23		120	0.229	0.4	H <sub>2</sub> O	321	-
24		96	0.223	0.3	H <sub>2</sub> O	342	-
25	4	80	0.222	0.3	H <sub>2</sub> O	367	-
26		61	0.190	0.15	H <sub>2</sub> O	391	-
27		43	0.183	0.1	H <sub>2</sub> O	412	-
28		43	0.151	0.05	H <sub>2</sub> O	606	-
29		43	0.144	0.05	H <sub>2</sub> O	804	Top to bottom
30	5	43	0.145	0.05	H <sub>2</sub> O	846	-
31		43	0.144	0.05	H <sub>2</sub> O	1281	-

Notes: Stages 1-4 indicate the respective temperature increase or decrease; during Stage 5 the flow direction was reversed.

**Table B2 Sample FS3.**

No.	Stage	Temperature (°C)	Permeability (mD)	Max flow rate (ml/min)	Fluid	Total volume (ml)	Flow time (h)	Cumulative flow time (h)	Total time (h)	Flow direction
1		25	25.229	2	H <sub>2</sub> O	176	3.17	3.17	4	Bottom to top
2		25	22.777	2	H <sub>2</sub> O	380	3	6.17	22	-
3	1	25	21.258	1	H <sub>2</sub> O	594	3.63	9.8	50	-
4		25	17.007	1	H <sub>2</sub> O	794	3.33	13.13	74	-
5		25	16.673	1	H <sub>2</sub> O	836	0.68	13.81	284	-
6		25	16.673	1	H <sub>2</sub> O	1082	4.1	17.91	290	-
7		25	16.673	1	H <sub>2</sub> O	1101	0.32	18.23	525	-
8		25	19.013	1	2.0 M Na	1116	0.25	18.48	552	-
9		41	12.148	1	2.0 M Na	1126.5	0.17	18.65	622	-
10	2	61	7.493	1	2.0 M Na	1133.5	0.12	18.77	625	-
11		81	3.970	1	2.0 M Na	1139.5	0.1	18.87	642	-
12		98	2.216	1	2.0 M Na	1144.5	0.08	18.95	645	-
13		121	1.150	1	2.0 M Na	1148.5	0.07	19.02	649	-
14		145	0.606	1	2.0 M Na	1154.5	0.1	19.12	666	-
15		145	0.621	1	2.0 M Na	1158.5	0.07	19.19	693	-
16	3	145	0.598	1	1.0 M Na	1170.5	0.2	19.39	713	-
17		145	0.524	1	0.5 M Na	1193.5	0.38	19.77	715	-
18		145	0.020	0.03	H <sub>2</sub> O	1195.74	1.3	21.07	720	-
19		121	0.024	0.03	H <sub>2</sub> O	1200.42	2.67	23.74	747	-
20		99	0.025	0.03	H <sub>2</sub> O	1207.225	3.8	27.54	789	-
21	4	81	0.026	0.03	H <sub>2</sub> O	1212.98	3.2	30.74	813	-
22		61	0.029	0.03	H <sub>2</sub> O	1218.418	3	33.74	836	-
23		41	0.036	0.03	H <sub>2</sub> O	1223.446	2.8	36.54	860	-
24		29	0.035	0.02	H <sub>2</sub> O	1252.074	23.8	60.34	1049	-

Notes: Stage 1: flow-through experiment with a large volume of deionized water; Stage 2: fluid exchange and temperature increase from 25 to 145 °C; Stage 3: salinity decrease from 2 M NaCl to deionized water at 145 °C; Stage 4: temperature decrease from 145 °C to room temperature.

**Table B3 Sample FS4.**

No.	Stage	Temperature (°C)	Permeability (mD)	Max flow rate (ml/min)	Fluid	Total volume (ml)	Flow time (h)	Cumulative flow time (h)	Total time (h)	Flow direction
1		27	24.295	2	H <sub>2</sub> O	14.45	0.2	0.2	1	Bottom to top
2	1	27	24.295	2	H <sub>2</sub> O	19.45	0.08	0.28	69	-
3		27	22.982	1	H <sub>2</sub> O	24.45	0.08	0.37	117	-
4		27	22.982	1	H <sub>2</sub> O	26.95	0.05	0.42	141	-
5		27	21.803	1	H <sub>2</sub> O	31.95	0.08	0.5	262	-
6		27	22.817	1	2.0 M Na	44.95	0.27	0.77	263	-
7		42	19.177	1	2.0 M Na	49.95	0.08	0.85	268.5	-
8	2	62	10.218	1	2.0 M Na	57.45	0.13	0.97	284.5	-
9		81	4.502	1	2.0 M Na	60.95	0.06	1.03	292.5	-
10		100	2.532	1	2.0 M Na	63.95	0.05	1.08	308.5	-
11		122	0.651	1	2.0 M Na	66.95	0.05	1.13	332.5	-
12		145	0.445	0.5	2.0 M Na	69.95	0.1	1.23	340	-
13		122	0.468	0.5	2.0 M Na	72.35	0.08	1.32	405	-
14		100	0.475	0.5	2.0 M Na	75.35	0.1	1.42	412	-
15		81	0.502	0.5	2.0 M Na	78.75	0.1	1.52	429	-
16	3	62	0.526	0.4	2.0 M Na	82.55	0.16	1.67	436.5	-
17		42	0.561	0.3	2.0 M Na	84.45	0.1	1.77	452.5	-
18		29	0.565	0.2	2.0 M Na	86.45	0.17	1.94	475.3	-
19		28	0.542	0.2	1.0 M Na	93.75	0.61	2.55	477.3	-
20		28	0.519	0.2	0.5 M Na	103.5	0.81	3.36	479	-
21	4	28	0.009	0.002	H <sub>2</sub> O	114.13	22	25.36	502	-
22		28	0.010	0.003	H <sub>2</sub> O	119.204	26	51.36	528	-
23		27	0.009	0.005	H <sub>2</sub> O	137.219	44	95.36	957	-

Notes: Stage 1: flow-through experiment with a small volume of deionized water; Stage 2: fluid exchange and temperature increase from 25 to 145 °C; Stage 3: temperature decrease from 145 °C to room temperature; Stage 4: salinity decrease from 2 M NaCl to deionized water at room temperature. FS4 underwent additional procedures beyond Stage 4 which are excluded from the present study.

### Appendix C: Images of the fracture microstructures (Chapter 3)

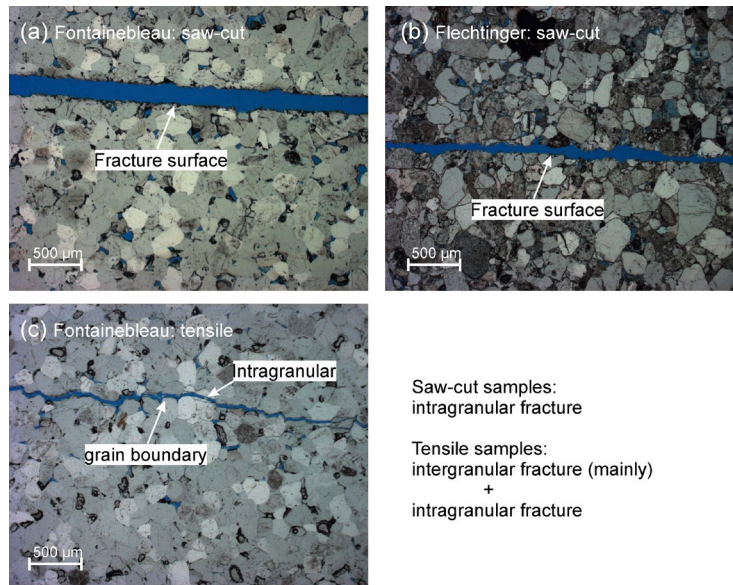


**Figure C1** Thin section images of fractures in (a) saw-cut Fontainebleau sandstone, (b) saw-cut Flechtinger sandstone, and (c) tensile fractured Fontainebleau sandstone. These representative fracture features were taken on other samples of the same respective rock type. The tensile fractures in Flechtinger sandstone are mainly intergranular (see Figure C3) due to its relatively low strength and weak cementation (Zang et al., 1996).

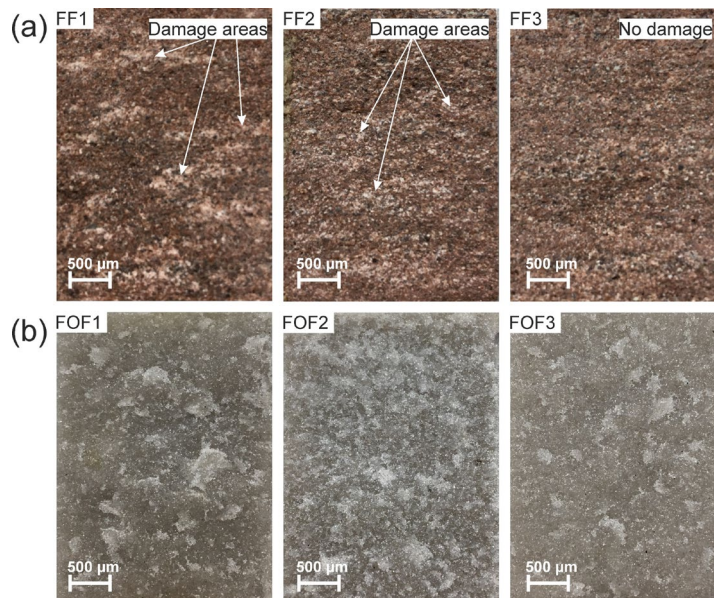


**Figure C2** Images of fracture surfaces after the experiments. (a) Flechtinger samples and (b) Fontainebleau samples. Areas of microdamage can be identified in the displaced Flechtinger samples but show to be highly localized.

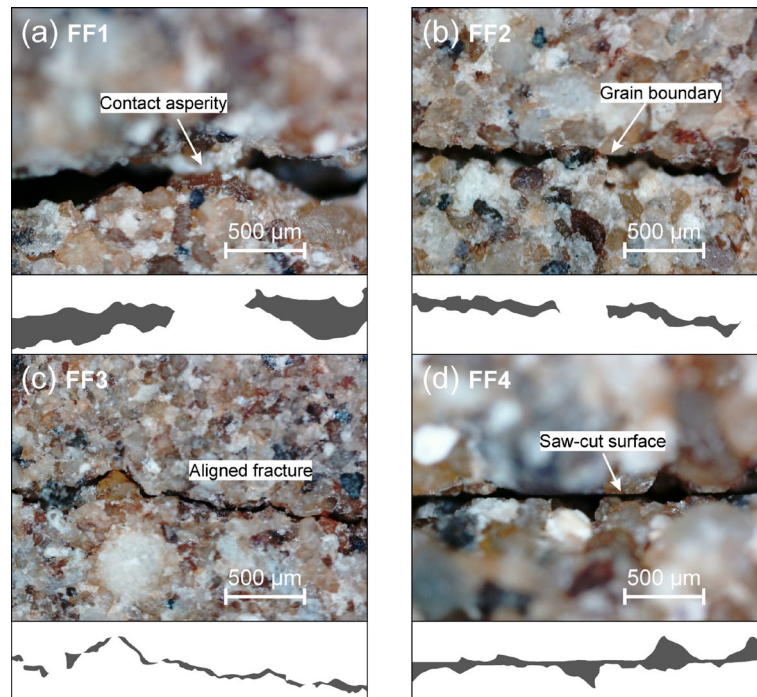


**Figure C3** Images and sketches of the fracture void space taken on the Flechtinger sandstone sample ends after the experiments at dry and unconfined but jacketed conditions. (a)-(d) Samples FF1 through FF4.

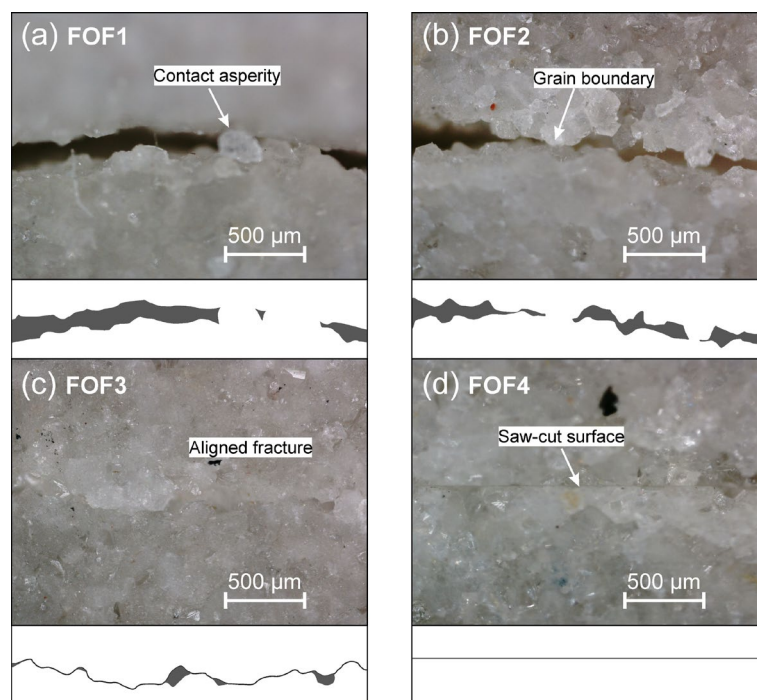


**Figure C4** Images and sketches of the fracture void space taken on the Fontainebleau sandstone sample ends after the experiments at dry and unconfined but jacketed conditions. (a)-(d) Samples FOF1 through FOF4.

## Appendix D: Changes of mechanical aperture during the loading-unloading sequences (Chapter 5)

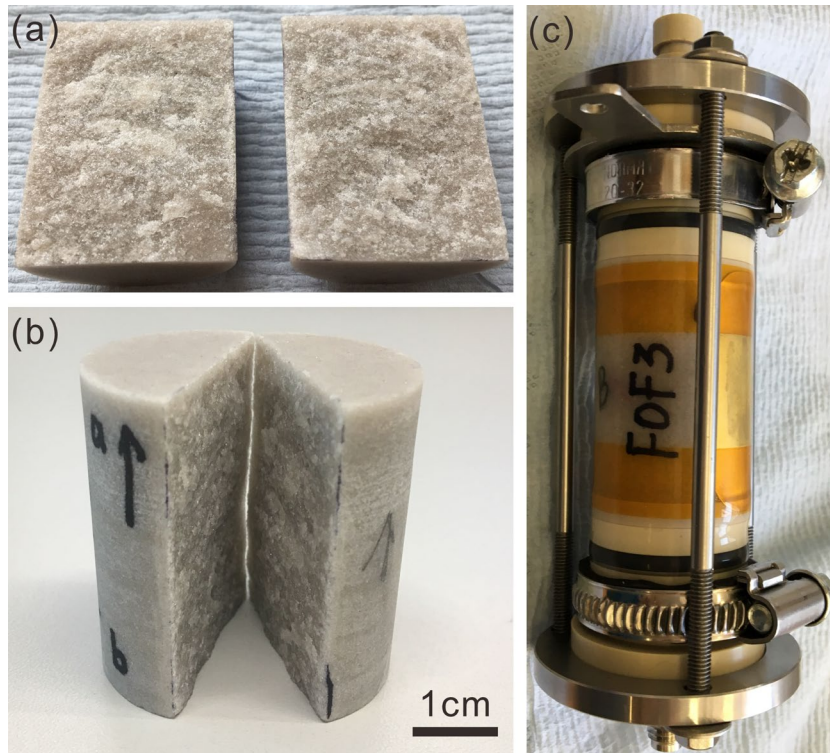
The volume changes of the fracture void space in the course of the loading/unloading steps can be determined by measuring the volume increment/decrement of the pore fluid extracted from (or injected into) the sample at constant pore pressure. During the changes of confining pressure, the pore pressure was maintained constant at 1 MPa. The total pore volume change  $\Delta V$  was monitored by this drained compression test. The variation of the mean mechanical aperture can be determined by  $\Delta b_m = (\Delta V - \Delta V_{\text{pore}}) / WL$ , where  $W$  and  $L$  are the width and the length of the fracture, respectively. The change of the pore volume within the rock matrix,  $\Delta V_{\text{pore}}$ , can be neglected due to the extremely low permeability of the matrix (on the order of  $10^{-18} \text{ m}^2$ ), the low porosity of the sample ( $\sim 2.3\%$ ), and the short experimental duration of the loading/unloading process (about 4 min). Therefore, it can be assumed that measuring  $\Delta V$  only yields correct results for both compaction (-) and opening (+) of the fracture.

The fracture is subjected to sufficient irreversible deformation since the loading path from 2 to 18 MPa yields a significant difference in mechanical aperture changes (Table C1. Nos.1 and 3). Further loading-unloading stages between 2~18 and 18~30 MPa seem to have no significant effect on the mechanical aperture, indicating a fully reversible behavior. The resolution of volume changes is  $1 \text{ mm}^3$  (i.e., a minimum change of  $0.83 \text{ }\mu\text{m}$  in the overall aperture), which likely is insufficient to observe aperture changes during the time period between stages V and VII.

**Table C1** Mean mechanical aperture changes during loading-unloading stages determined by drained compression experiments.

No.	Stage	$p_c$ (MPa)	$p_p$ (MPa)	$\Delta V$ (ml)	$\Delta b_m$ ( $\mu\text{m}$ )
1	post-II	2 – 18	1	-0.130	-108.33
2	pre-V	18 – 2	1	0.071	59.17
3	post-V	2 – 18	1	-0.077	-64.17
4	VII	18 – 30	1	-0.019	-15.83
5	post-VII	30 – 18	1	0.019	15.83
6	post-VII	18 – 2	1	0.077	64.17



**Appendix E: Supplementary materials (Chapter 5)**

**Figure E1** Photographs of the rock sample used for the experiment. (a) Artificial tensile fracture generated with a Brazilian test setup at a loading displacement rate of  $2 \times 10^{-6}$  m/s to minimize the risk of edge damage; (b) the two halves of the sample core; (c) assembly of the fractured sample with a relative offset of 200  $\mu\text{m}$  along its length, jacketed by a heat-shrink tube and additional sealing parts. The sample is 3 cm in diameter and 4 cm in length.

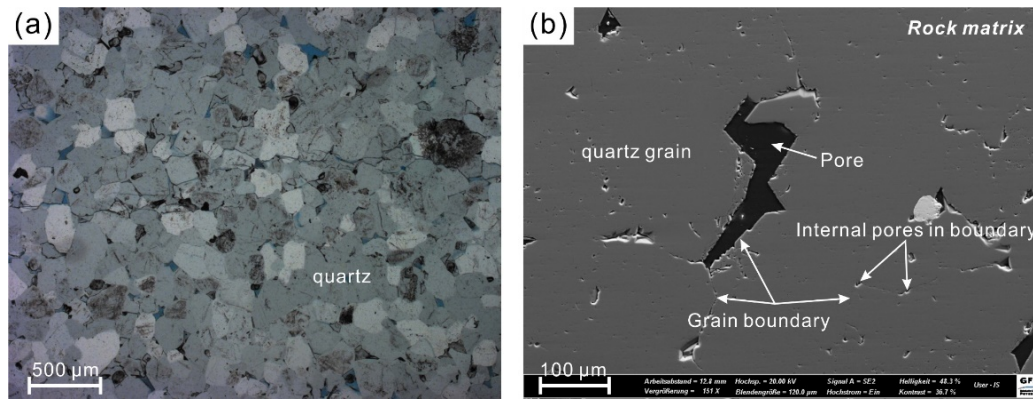


**Figure E2** Microstructure of the rock matrix. (a) Optical microscopy image of a polished thin section with an average diameter of the quartz grains estimated to be 200  $\mu\text{m}$ ; (b) SEM micrograph of a thin section evidencing a well-consolidated rock matrix.

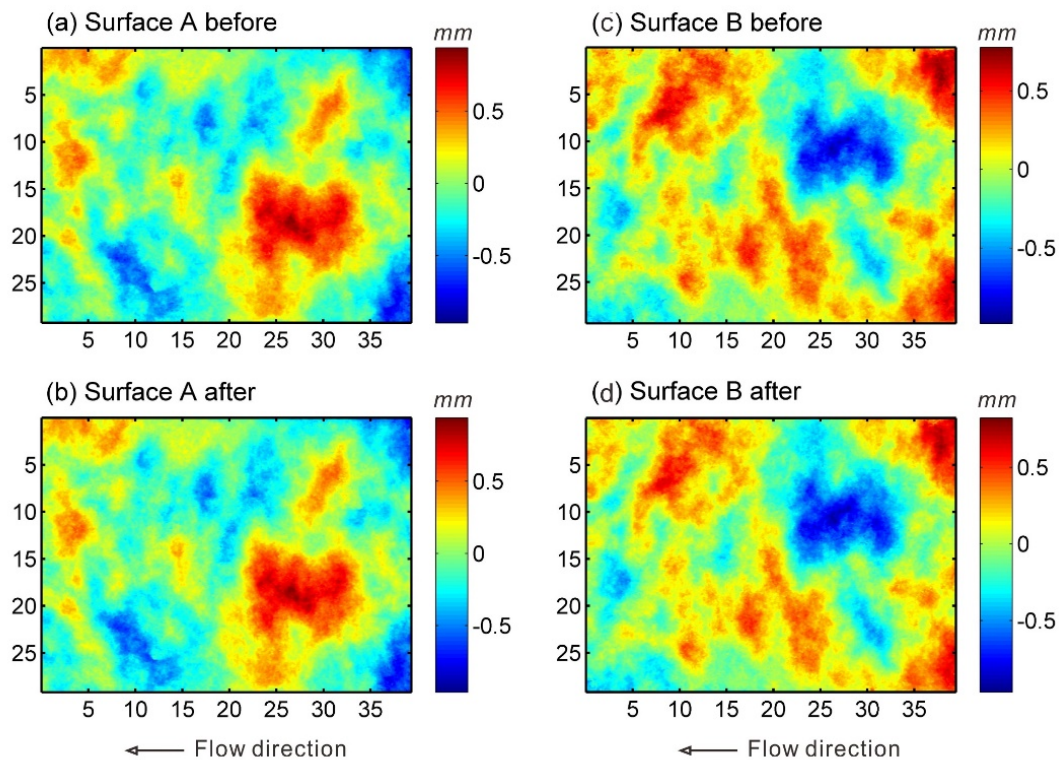


**Figure E3** Topography of the fracture surfaces measured by white light interferometry. (a) and (b) Specimen A, (c) and (d) specimen B before and after the flow-through experiment, respectively. The fracture surface roughness factor  $f_r$ , expressed by the ratio between the rough fracture surface area and the geometric fracture surface plane, is derived by the models yielding a value of 1.14.

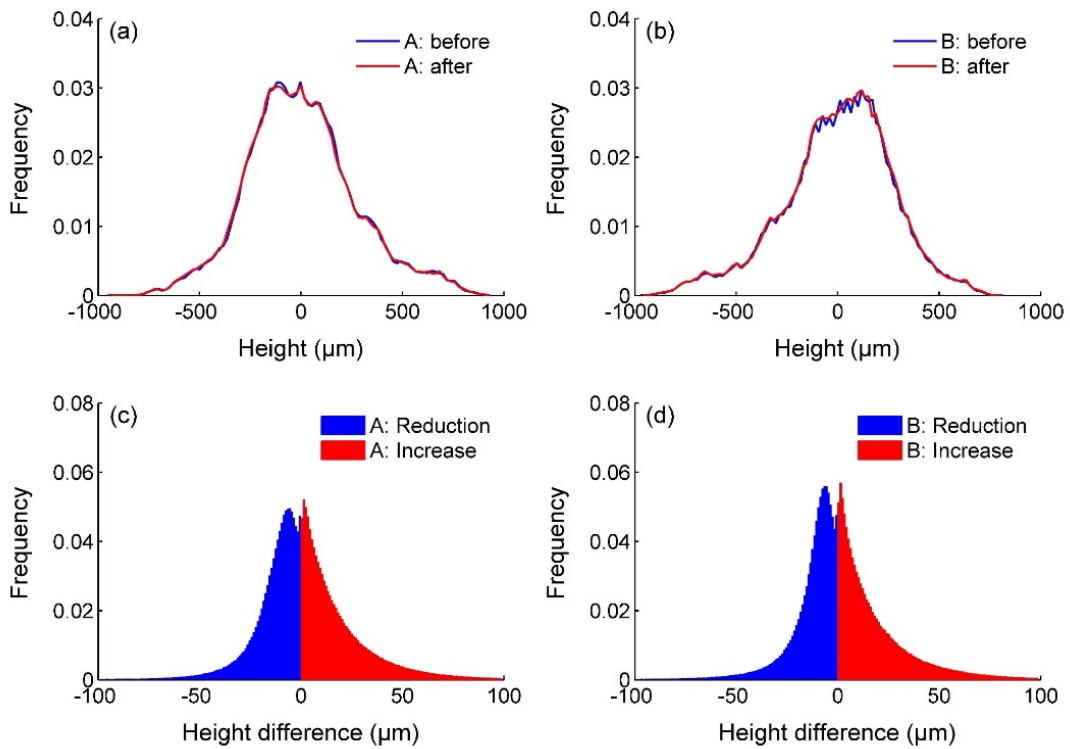


**Figure E4** Histograms of fracture surface roughness of (a) specimen A and (b) specimen B before and after the experiment. Distribution of height differences of (c) surface A and (d) surface B derived by comparing the initial and final roughness of the fracture surfaces.

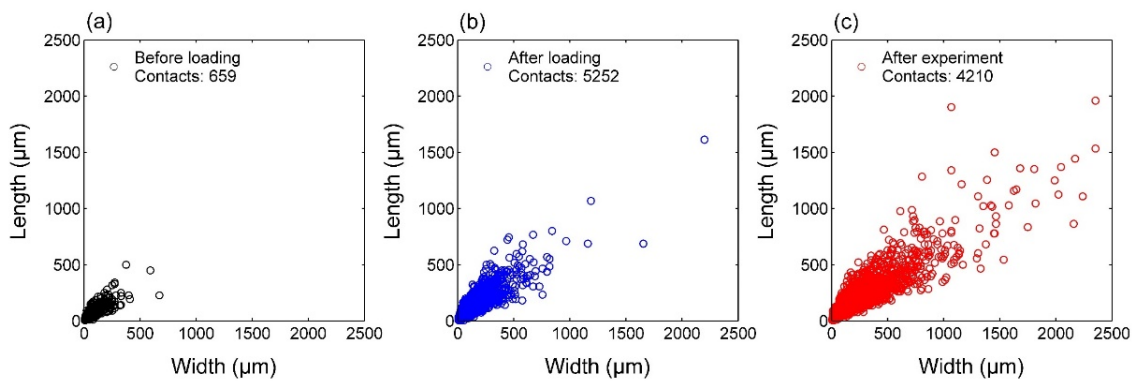


**Figure E5** Length and width of each isolated contact area obtained from the 2D projections of fracture apertures measured by X-ray  $\mu$ CT scans (Figure 5.6b) at different stages: (a) before the preloading stage; (b) after the preloading stage; (c) after the entire experiment.

## References

- Aben, F., Doan, M. L., Gratier, J. P., & Renard, F. (2017). Experimental postseismic recovery of fractured rocks assisted by calcite sealing. *Geophysical Research Letters*, *44*(14), 7228-7238. <https://doi.org/10.1002/2017gl073965>
- Al-Ani, T., & Sarapää, O. (2008). *Clay and clay mineralogy: Physical-chemical properties and industrial uses*. Finland: Geological Survey of Finland.
- Aly, K. M., & Esmail, E. (1993). Refractive index of salt water: effect of temperature. *Optical Materials*, *2*(3), 195-199. [https://doi.org/10.1016/0925-3467\(93\)90013-Q](https://doi.org/10.1016/0925-3467(93)90013-Q)
- Anderson, R. L., Ratcliffe, I., Greenwell, H. C., Williams, P. A., Cliffe, S., & Coveney, P. V. (2010). Clay swelling - A challenge in the oilfield. *Earth-Science Reviews*, *98*(3-4), 201-216. <https://doi.org/10.1016/j.earscirev.2009.11.003>
- Arns, C. H., Knackstedt, M. A., Pinczewski, W. V., & Garboczi, E. J. (2002). Computation of linear elastic properties from microtomographic images: Methodology and agreement between theory and experiment. *Geophysics*, *67*(5), 1396-1405. <https://doi.org/10.1190/1.1512785>
- Atkinson, B. K. (1980). Stress corrosion and the rate-dependent tensile failure of a fine-grained quartz rock. *Tectonophysics*, *65*(3-4), 281-290.
- Auradou, H., Drazer, G., Hulin, J.-P., & Koplik, J. (2005). Permeability anisotropy induced by the shear displacement of rough fracture walls. *Water Resources Research*, *41*(9), W09423. <https://doi.org/10.1029/2005WR003938>
- Aureli, F., Ciprotti, M., D'Amato, M., do Nascimento da Silva, E., Nisi, S., Passeri, D., et al. (2020). Determination of total silicon and SiO<sub>2</sub> particles using an ICP-MS based analytical platform for toxicokinetic studies of synthetic amorphous silica. *Nanomaterials*, *10*(5), 888. <https://doi.org/10.3390/nano10050888>
- Azari, M., & Leimkuhler, J. M. (1990). Formation permeability damage induced by completion brines. *Journal of Petroleum Technology*, *42*(04), 486-492. <https://doi.org/10.2118/17149-PA>
- Bandis, S. C., Lumsden, A. C., & Barton, N. R. (1983). Fundamentals of rock joint deformation. *International Journal of Rock Mechanics and Mining Sciences*, *20*(6), 249-268. [https://doi.org/10.1016/0148-9062\(83\)90595-8](https://doi.org/10.1016/0148-9062(83)90595-8)
- Baptist, O. C., & Sweeney, S. (1954). The effect of clays on the permeability of reservoir sands to waters of different saline contents. *Clays and Clay Minerals*, *3*(1), 505-515.
- Barton, N. (1973). Review of a new shear-strength criterion for rock joints. *Engineering geology*, *7*(4), 287-332. [https://doi.org/10.1016/0013-7952\(73\)90013-6](https://doi.org/10.1016/0013-7952(73)90013-6)
- Barton, N., Bandis, S., & Bakhtar, K. (1985). Strength, deformation and conductivity coupling of rock joints. *International Journal of Rock Mechanics and Mining Sciences*, *22*(3), 121-140. [https://doi.org/10.1016/0148-9062\(85\)93227-9](https://doi.org/10.1016/0148-9062(85)93227-9)
- Baud, P., Wong, T.-f., & Zhu, W. (2014). Effects of porosity and crack density on the compressive strength of rocks. *International Journal of Rock Mechanics and Mining Sciences*, *67*, 202-211. <https://doi.org/10.1016/j.ijrmms.2013.08.031>

- Baudracco, J., & Aoubouazza, M. (1995). Permeability variations in Berea and Vosges sandstone submitted to cyclic temperature percolation of saline fluids. *Geothermics*, 24(5-6), 661-677. [https://doi.org/10.1016/0375-6505\(95\)00027-5](https://doi.org/10.1016/0375-6505(95)00027-5)
- Bedrikovetsky, P. (2008). Upscaling of stochastic micro model for suspension transport in porous media. *Transport in Porous Media*, 75(3), 335-369. <https://doi.org/10.1007/s11242-008-9228-6>
- Bedrikovetsky, P., Siqueira, F. D., Furtado, C. A., & Souza, A. L. S. (2011). Modified particle detachment model for colloidal transport in porous media. *Transport in Porous Media*, 86(2), 353-383. <https://doi.org/10.1007/s11242-010-9626-4>
- Bedrikovetsky, P., Zeinijahromi, A., Siqueira, F. D., Furtado, C. A., & de Souza, A. L. S. (2012). Particle detachment under velocity alternation during suspension transport in porous media. *Transport in Porous Media*, 91(1), 173-197. <https://doi.org/10.1007/s11242-011-9839-1>
- Bergström, L. (1997). Hamaker constants of inorganic materials. *Advances in Colloid and Interface Science*, 70, 125-169. [https://doi.org/10.1016/S0001-8686\(97\)00003-1](https://doi.org/10.1016/S0001-8686(97)00003-1)
- Bhattacharjee, S., Elimelech, M., & Borkovec, M. (1998). DLVO interaction between colloidal particles: beyond Derjaguin's approximation. *Croatica Chemica Acta*, 71(4), 883-903.
- Blöcher, G., Reinsch, T., Henniges, J., Milsch, H., Regenspurg, S., Kummerow, J., et al. (2016). Hydraulic history and current state of the deep geothermal reservoir Groß Schönebeck. *Geothermics*, 63, 27-43. <https://doi.org/10.1016/j.geothermics.2015.07.008>
- Blöcher, G., Zimmermann, G., & Milsch, H. (2009). Impact of poroelastic response of sandstones on geothermal power production. *Pure and Applied Geophysics*, 166(5-7), 1107-1123. <https://doi.org/10.1007/s00024-009-0475-4>
- Boffa, J., & Allain, C. (1998). Experimental analysis of fracture rugosity in granular and compact rocks. *The European Physical Journal Applied Physics*, 2(3), 281-289. <https://doi.org/10.1051/epjap:1998194>
- Brown, G. O. (2002). Henry Darcy and the making of a law. *Water Resources Research*, 38(7), (11-11)-(11-12). <https://doi.org/10.1029/2001WR000727>
- Brown, S. R., & Scholz, C. H. (1985). Closure of random elastic surfaces in contact. *Journal of Geophysical Research*, 90(B7), 5531-5545. <https://doi.org/10.1029/JB090iB07p05531>
- Butt, H. J., Graf, K., & Kappl, M. (2006). *Physics and chemistry of interfaces*. Weinheim: John Wiley & Sons. <https://doi.org/10.1002/3527602313>
- Candela, T., Renard, F., Klinger, Y., Mair, K., Schmittbuhl, J., & Brodsky, E. E. (2012). Roughness of fault surfaces over nine decades of length scales. *Journal of Geophysical Research: Solid Earth*, 117(B8), B08409. <https://doi.org/10.1029/2011JB009041>
- Carroll, M. M., & Katsube, N. (1983). The role of Terzaghi effective stress in linearly elastic deformation. *Journal of Energy Resources Technology*, 105(4), 509-511. <https://doi.org/10.1115/1.3230964>
- Casse, F. J., & Ramey, H. J. (1979). The effect of temperature and confining pressure on single-phase flow in consolidated rocks. *Journal of Petroleum Technology*, 31(08), 1051-1059. <https://doi.org/10.2118/5877-PA>
- Cebell, W. A., & Chilingarian, G. V. (1972). Some data on compressibility and density anomalies in halloysite, hectorite, and illite clays. *AAPG Bulletin*, 56(4), 796-802. <https://doi.org/10.1306/819A4086-16C5-11D7-8645000102C1865D>
- Chen, Z., Narayan, S. P., Yang, Z., & Rahman, S. S. (2000). An experimental investigation of hydraulic behaviour of fractures and joints in granitic rock. *International Journal of Rock Mechanics and Mining Sciences*, 37(7), 1061-1071. <https://doi.org/10.1016/S1365->

1609(00)00039-3

- Civan, F. (2015). *Reservoir formation damage*: Gulf Professional Publishing.
- Cooper, J. R. (2008). *Release on the IAPWS formulation 2008 for the viscosity of ordinary water substance*. Berlin, Germany: IAPWS R12-08.
- Cosgrove, J. (1995). The expression of hydraulic fracturing in rocks and sediments. *Geological Society, London, Special Publications*, 92(1), 187-196. <https://doi.org/10.1144/GSL.SP.1995.092.01.10>
- Crawford, B. R., Tsenn, M. C., Homburg, J. M., Stehle, R. C., Freysteinson, J. A., & Reese, W. C. (2017). Incorporating scale-dependent fracture stiffness for improved reservoir performance prediction. *Rock Mechanics and Rock Engineering*, 50(12), 3349-3359. <https://doi.org/10.1007/s00603-017-1314-z>
- Darcy, H. (1856). *Les fontaines publique de la ville de Dijon*. Paris: Dalmont.
- David, E., C. , Fortin, J., Schubnel, A., Guéguen, Y., & Zimmerman, R. W. (2013). Laboratory measurements of low- and high-frequency elastic moduli in Fontainebleau sandstone. *Geophysics*, 78(5), D369-D379. <https://doi.org/10.1190/Geo2013-0070.1>
- De Boer, R. (1977a). On the thermodynamics of pressure solution-interaction between chemical and mechanical forces. *Geochimica et Cosmochimica Acta*, 41(2), 249-256. [https://doi.org/10.1016/0016-7037\(77\)90232-0](https://doi.org/10.1016/0016-7037(77)90232-0)
- De Boer, R. (1977b). Pressure solution: theory and experiments. *Tectonophysics*, 39(1-3), 287-301. [https://doi.org/10.1016/0040-1951\(77\)90101-9](https://doi.org/10.1016/0040-1951(77)90101-9)
- De Boer, R., Nagtegaal, P., & Duyvis, E. (1977). Pressure solution experiments on quartz sand. *Geochimica et Cosmochimica Acta*, 41(2), 257-264. [https://doi.org/10.1016/0016-7037\(77\)90233-2](https://doi.org/10.1016/0016-7037(77)90233-2)
- De Meer, S., Spiers, C. J., & Nakashima, S. (2005). Structure and diffusive properties of fluid-filled grain boundaries: An in-situ study using infrared (micro) spectroscopy. *Earth and Planetary Science Letters*, 232(3-4), 403-414. <https://doi.org/10.1016/j.epsl.2004.12.030>
- De Meer, S., Spiers, C. J., Peach, C. J., & Watanabe, T. (2002). Diffusive properties of fluid-filled grain boundaries measured electrically during active pressure solution. *Earth and Planetary Science Letters*, 200(1-2), 147-157. [https://doi.org/10.1016/S0012-821X\(02\)00585-X](https://doi.org/10.1016/S0012-821X(02)00585-X)
- Deraguin, B., & Landau, L. (1941). Theory of the stability of strongly charged lyophobic sols and of the adhesion of strongly charged particles in solution of electrolytes. *Acta Physicochim: USSR*, 14, 633-662.
- Desbois, G., Urai, J. L., Hemes, S., Schröppel, B., Schwarz, J.-O., Mac, M., & Weiel, D. (2016). Multi-scale analysis of porosity in diagenetically altered reservoir sandstone from the Permian Rotliegend (Germany). *Journal of Petroleum Science and Engineering*, 140, 128-148. <https://doi.org/10.1016/j.petrol.2016.01.019>
- Dewers, T., & Hajash, A. (1995). Rate laws for water-assisted compaction and stress-induced water-rock interaction in sandstones. *Journal of Geophysical Research*, 100(B7), 13093-13112. <https://doi.org/10.1029/95JB00912>
- Dezayes, C., Genter, A., & Valley, B. (2010). Structure of the low permeable naturally fractured geothermal reservoir at Soultz. *Comptes Rendus Geoscience*, 342(7-8), 517-530.
- Diaz, M., Kim, K. Y., Yeom, S., Zhuang, L., Park, S., & Min, K. B. (2017). Surface roughness characterization of open and closed rock joints in deep cores using X-ray computed tomography. *International Journal of Rock Mechanics and Mining Sciences*, 98, 10-19. <https://doi.org/10.1016/j.ijrmms.2017.07.001>



- Durham, W. B., & Bonner, B. P. (1994). Self-propping and fluid flow in slightly offset joints at high effective pressures. *Journal of Geophysical Research*, 99(B5), 9391-9399. <https://doi.org/10.1029/94jb00242>
- Dysthe, D., Renard, F., Porcheron, F., & Rousseau, B. (2002). Fluid in mineral interfaces—molecular simulations of structure and diffusion. *Geophysical Research Letters*, 29(7), 13-11-13-14. <https://doi.org/10.1029/2001GL013208>
- Dysthe, D. K., Renard, F., Feder, J., Jamtveit, B., Meakin, P., & Jossang, T. (2003). High-resolution measurements of pressure solution creep. *Physical Review E*, 68(1), 011603. <https://doi.org/10.1103/PhysRevE.68.011603>
- Elias, B. P., & Hajash, J. A. (1992). Changes in quartz solubility and porosity due to effective stress: An experimental investigation of pressure solution. *Geology*, 20(5), 451-454. [https://doi.org/10.1130/0091-7613\(1992\)020<0451:CIQSAP>2.3.CO;2](https://doi.org/10.1130/0091-7613(1992)020<0451:CIQSAP>2.3.CO;2)
- Elimelech, M., Gregory, J., & Jia, X. (2013). *Particle deposition and aggregation: measurement, modelling and simulation*: Oxford England: Butterworth-Heinemann.
- Engelder, T. (1982). A natural example of the simultaneous operation of free-face dissolution and pressure solution. *Geochimica et Cosmochimica Acta*, 46(1), 69-74. [https://doi.org/10.1016/0016-7037\(82\)90291-5](https://doi.org/10.1016/0016-7037(82)90291-5)
- Fang, Y., Elsworth, D., Ishibashi, T., & Zhang, F. (2018). Permeability evolution and frictional stability of fabricated fractures with specified roughness. *Journal of Geophysical Research: Solid Earth*, 123(11), 9355-9375. <https://doi.org/10.1029/2018jb016215>
- Fischer, C., Dunkl, I., von Eynatten, H., Wijbrans, J. R., & Gaupp, R. (2012). Products and timing of diagenetic processes in Upper Rotliegend sandstones from Bebertal (North German Basin, Parchim Formation, Flechtingen High, Germany). *Geological Magazine*, 149(5), 827-840. <https://doi.org/10.1017/S0016756811001087>
- Fournier, R. O., & Potter II, R. W. (1982). An equation correlating the solubility of quartz in water from 25 to 900 C at pressures up to 10,000 bars. *Geochimica et Cosmochimica Acta*, 46(10), 1969-1973. [https://doi.org/10.1016/0016-7037\(82\)90135-1](https://doi.org/10.1016/0016-7037(82)90135-1)
- Friedrich, F., Steudel, A., & Weidler, P. G. (2008). Change of the refractive index of illite particles by reduction of the Fe content of the octahedral sheet. *Clays and Clay Minerals*, 56(5), 505-510. <https://doi.org/10.1346/CCMN.2008.0560503>
- Gabriel, G., & Inamdar, G. (1983). An experimental investigation of fines migration in porous media. *Paper presented at SPE Annual Technical Conference and Exhibition*, Society of Petroleum Engineers, San Francisco, CA, USA.
- García-García, S., Jonsson, M., & Wold, S. (2006). Temperature effect on the stability of bentonite colloids in water. *Journal of Colloid and Interface Science*, 298(2), 694-705. <https://doi.org/10.1016/j.jcis.2006.01.018>
- Ge, S. (1997). A governing equation for fluid flow in rough fractures. *Water Resources Research*, 33(1), 53-61. <https://doi.org/10.1029/96WR02588>
- Genter, A., & Traineau, H. (1996). Analysis of macroscopic fractures in granite in the HDR geothermal well EPS-1, Soultz-sous-Forêts, France. *J. Volcanol Geoth, Res.*, 72(1-2), 121-141.
- Gobran, B. D., Brigham, W. E., & Ramey Jr., H. J. (1987). Absolute permeability as a function of confining pressure, pore pressure, and temperature. *SPE Formation Evaluation*, 2(01), 77-84.
- Gräf, V., Jamek, M., Rohatsch, A., & Tschegg, E. (2013). Effects of thermal-heating cycle treatment on thermal expansion behavior of different building stones. *International Journal of Rock Mechanics and Mining Sciences*, 64, 228-235.

- <https://doi.org/10.1016/j.ijrmms.2013.08.007>
- Grahame, D. C. (1947). The electrical double layer and the theory of electrocapillarity. *Chemical Reviews*, 41(3), 441-501. <https://doi.org/10.1021/cr60130a002>
- Gratier, J.-P., Dysthe, D. K., & Renard, F. (2013). The role of pressure solution creep in the ductility of the earth's upper crust, in *Advances in Geophysics*. pp. 47-179, Elsevier. <https://doi.org/10.1016/B978-0-12-380940-7.00002-0>
- Gratier, J.-P., Renard, F., & Labaume, P. (1999). How pressure solution creep and fracturing processes interact in the upper crust to make it behave in both a brittle and viscous manner. *Journal of Structural Geology*, 21(8-9), 1189-1197. [https://doi.org/10.1016/S0191-8141\(99\)00035-8](https://doi.org/10.1016/S0191-8141(99)00035-8)
- Gratier, J., & Irigm, R. G. (1986). Experimental pressure solution-deposition on quartz grains: the crucial effect of the nature of the fluid. *Journal of Structural Geology*, 8(8), 845-856. [https://doi.org/10.1016/0191-8141\(86\)90030-1](https://doi.org/10.1016/0191-8141(86)90030-1)
- Gratier, J. P., Guiguet, R., Renard, F., Jenatton, L., & Bernard, D. (2009). A pressure solution creep law for quartz from indentation experiments. *Journal of Geophysical Research*, 114(B3), B03403. <https://doi.org/10.1029/2008JB005652>
- Gratier, J. P., Renard, F., & Vial, B. (2014). Postseismic pressure solution creep: Evidence and time-dependent change from dynamic indenting experiments. *Journal of Geophysical Research: Solid Earth*, 119(4), 2764-2779. <https://doi.org/10.1002/2013JB010768>
- Gratz, A. J. (1991). Solution-transfer compaction of quartzites: Progress toward a rate law. *Geology*, 19(9), 901-904. [https://doi.org/10.1130/0091-7613\(1991\)019<0901:Stcoqp>2.3.Co;2](https://doi.org/10.1130/0091-7613(1991)019<0901:Stcoqp>2.3.Co;2)
- Gray, D. H. (1966). Formation damage in sandstones caused by clay dispersion and migration. *Clays and Clay Minerals*, 14(1), 355-366. <https://doi.org/10.1346/ccmn.1966.0140131>
- Gregory, J. (1975). Interaction of unequal double layers at constant charge. *Journal of Colloid and Interface Science*, 51(1), 44-51. [https://doi.org/10.1016/0021-9797\(75\)90081-8](https://doi.org/10.1016/0021-9797(75)90081-8)
- Gregory, J. (1981). Approximate expressions for retarded van der Waals interaction. *Journal of Colloid and Interface Science*, 83(1), 138-145. [https://doi.org/10.1016/0021-9797\(81\)90018-7](https://doi.org/10.1016/0021-9797(81)90018-7)
- Guildner, L. A., Johnson, D. P., & Jones, F. E. (1976). Vapor pressure of water at its triple point. *Journal of Research of the National Bureau of Standards - A. Physics and Chemistry*, 80A(3), 505-521. <https://doi.org/10.6028/jres.080A.054>
- Habibi, A., Ahmadi, M., Pourafshary, P., & Al-Wahaibi, Y. (2012). Reduction of fines migration by nanofluids injection: an experimental study. *SPE Journal*, 18(02), 309-318.
- Hakami, E., & Larsson, E. (1996). Aperture measurements and flow experiments on a single natural fracture. *International Journal of Rock Mechanics and Mining Sciences*, 33(4), 395-404. [https://doi.org/10.1016/0148-9062\(95\)00070-4](https://doi.org/10.1016/0148-9062(95)00070-4)
- Hassanzadegan, A., Blöcher, G., Milsch, H., Urpi, L., & Zimmermann, G. (2013). The effects of temperature and pressure on the porosity evolution of flechtinger sandstone. *Rock Mechanics and Rock Engineering*, 47(2), 421-434. <https://doi.org/10.1007/s00603-013-0401-z>
- Hassanzadegan, A., Blöcher, G., Zimmermann, G., & Milsch, H. (2012). Thermoporoeleastic properties of Flechtinger sandstone. *International Journal of Rock Mechanics and Mining Sciences*, 49, 94-104. <https://doi.org/10.1016/j.ijrmms.2011.11.002>
- Hickman, S. H., & Evans, B. (1992). Growth of grain contacts in halite by solution-transfer: Implications for diagenesis, lithification, and strength recovery, in *International Geophysics*. pp. 253-280, Elsevier. [https://doi.org/10.1016/S0074-6142\(08\)62825-9](https://doi.org/10.1016/S0074-6142(08)62825-9)



- Hilgers, C., & Tenthorey, E. (2004). Fracture sealing of quartzite under a temperature gradient: experimental results. *Terra Nova*, 16(4), 173-178. <https://doi.org/10.1111/j.1365-3121.2004.00545.x>
- Himes, R., Vinson, E., & Simon, D. (1989). Clay stabilization in low-permeability formations. *Paper presented at SPE Production Operations Symposium*, Society of Petroleum Engineers, Oklahoma, USA.
- Hofmann, H., Blocher, G., Milsch, H., Babadagli, T., & Zimmermann, G. (2016). Transmissivity of aligned and displaced tensile fractures in granitic rocks during cyclic loading. *International Journal of Rock Mechanics and Mining Sciences*, 87, 69-84. <https://doi.org/10.1016/j.ijrmms.2016.05.011>
- Hofmann, H., Zimmermann, G., Farkas, M., Huenges, E., Zang, A., Leonhardt, M., et al. (2019). First field application of cyclic soft stimulation at the Pohang Enhanced Geothermal System site in Korea. *Geophysical Journal International*, 217(2), 926-949. <https://doi.org/10.1093/gji/ggz058>
- Huang, B., & Liu, J. (2017). Experimental investigation of the effect of bedding planes on hydraulic fracturing under true triaxial stress. *Rock Mechanics and Rock Engineering*, 50(10), 2627-2643. <https://doi.org/10.1007/s00603-017-1261-8>
- Huenges, E. (2010). *Geothermal energy systems: exploration, development, and utilization*. Weinheim: Wiley-VCH.
- Israelachvili, J. N. (2011). *Intermolecular and surface forces*. Amsterdam, The Netherlands: Elsevier. <https://doi.org/10.1016/C2009-0-21560-1>
- Jing, X. D. (1990). The effect of clay, pressure and temperature on the electrical and hydraulic properties of real and synthetic rocks, (Doctoral dissertation). London, UK: Imperial College London (University of London).
- Joseph, K., H. Ezzat, K., & Robert J., C. (1981). Tables of the dynamic and kinematic viscosity of aqueous NaCl solutions in the temperature range 20-150 °C and the pressure range 0.1-35 MPa. *American Institute of Physics and the American Chemical Society*, 10(1), 71-87. <https://doi.org/10.1063/1.555641>
- Josh, M., & Clennell, B. (2015). Broadband electrical properties of clays and shales: Comparative investigations of remolded and preserved samples. *Geophysics*, 80(2), D129-D143. <https://doi.org/10.1190/geo2013-0458.1>
- Juanes, R., Spiteri, E. J., Orr, F. M., & Blunt, M. J. (2006). Impact of relative permeability hysteresis on geological CO<sub>2</sub> storage. *Water Resources Research*, 42(12), W12418. <https://doi.org/10.1029/2005WR004806>
- Kahr, G., & Madsen, F. T. (1995). Determination of the cation exchange capacity and the surface area of bentonite, illite and kaolinite by methylene blue adsorption. *Applied Clay Science*, 9(5), 327-336. [https://doi.org/10.1016/0169-1317\(94\)00028-O](https://doi.org/10.1016/0169-1317(94)00028-O)
- Khilar, K. C., & Fogler, H. S. (1983). Water sensitivity of sandstones. *Society of Petroleum Engineers Journal*, 23(01), 55-64. <https://doi.org/10.2118/10103-PA>
- Khilar, K. C., & Fogler, H. S. (1984). The existence of a critical salt concentration for particle release. *Journal of Colloid and Interface Science*, 101(1), 214-224. [https://doi.org/10.1016/0021-9797\(84\)90021-3](https://doi.org/10.1016/0021-9797(84)90021-3)
- Khilar, K. C., & Fogler, H. S. (1987). Colloidally induced fines migration in porous media. *Reviews in Chemical Engineering*, 4(1-2), 41-108. <https://doi.org/10.1515/REVCE.1987.4.1-2.41>
- Kia, S., Fogler, H. S., & Reed, M. (1987). Effect of salt composition on clay release in Berea sandstones. *Paper presented at SPE International Symposium on Oilfield Chemistry*, Society

- of Petroleum Engineers, San Antonio, Texas, USA. <https://doi.org/10.2118/15318-PA>
- Kling, T., Huo, D., Schwarz, J. O., Enzmann, F., Benson, S., & Blum, P. (2016). Simulating stress-dependent fluid flow in a fractured core sample using real-time X-ray CT data. *Solid Earth*, 7(4), 1109-1124. <https://doi.org/10.5194/se-7-1109-2016>
- Kling, T., Vogler, D., Pastewka, L., Amann, F., & Blum, P. (2018). Numerical simulations and validation of contact mechanics in a granodiorite fracture. *Rock Mechanics and Rock Engineering*, 51(9), 2805-2824. <https://doi.org/10.1007/s00603-018-1498-x>
- Kluge, C., Blöcher, G., Barnhoorn, A., Schmittbuhl, J., & Bruhn, D. (2021). Permeability evolution during shear zone initiation in low-porosity rocks. *Rock Mechanics and Rock Engineering*. <https://doi.org/10.1007/s00603-020-02356-0>
- Konzuk, J. S., & Kueper, B. H. (2004). Evaluation of cubic law based models describing single-phase flow through a rough-walled fracture. *Water Resources Research*, 40(2), W02402. <https://doi.org/10.1029/2003WR002356>
- Kranzz, R., Frankel, A., Engelder, T., & Scholz, C. (1979). The permeability of whole and jointed Barre granite. *International Journal of Rock Mechanics and Mining Sciences*, 16(4), 225-234. [https://doi.org/10.1016/0148-9062\(79\)91197-5](https://doi.org/10.1016/0148-9062(79)91197-5)
- Kushnir, A. R., Heap, M. J., & Baud, P. (2018). Assessing the role of fractures on the permeability of the Permo-Triassic sandstones at the Soultz-sous-Forêts (France) geothermal site. *Geothermics*, 74, 181-189. <https://doi.org/10.1016/j.geothermics.2018.03.009>
- Kwon, O., Herbert, B. E., & Kronenberg, A. K. (2004a). Permeability of illite-bearing shale: 2. Influence of fluid chemistry on flow and functionally connected pores. *Journal of Geophysical Research*, 109, B10206. <https://doi.org/10.1029/2004JB003055>
- Kwon, O., Kronenberg, A. K., Gangi, A. F., Johnson, B., & Herbert, B. E. (2004b). Permeability of illite-bearing shale: 1. Anisotropy and effects of clay content and loading. *Journal of Geophysical Research*, 109, B10205. <https://doi.org/10.1029/2004jb003052>
- Lang, P. S., Paluszny, A., Nejati, M., & Zimmerman, R. W. (2018). Relationship between the orientation of maximum permeability and intermediate principal stress in fractured rocks. *Water Resources Research*, 54(11), 8734-8755. <https://doi.org/10.1029/2018wr023189>
- Lang, P. S., Paluszny, A., & Zimmerman, R. W. (2015). Hydraulic sealing due to pressure solution contact zone growth in siliciclastic rock fractures. *Journal of Geophysical Research: Solid Earth*, 120(6), 4080-4101. <https://doi.org/10.1002/2015JB011968>
- Lang, P. S., Paluszny, A., & Zimmerman, R. W. (2016). Evolution of fracture normal stiffness due to pressure dissolution and precipitation. *International Journal of Rock Mechanics and Mining Sciences*, 88, 12-22. <https://doi.org/10.1016/j.ijrmms.2016.06.004>
- Lehner, F. K. (1995). A model for intergranular pressure solution in open systems. *Tectonophysics*, 245(3-4), 153-170. [https://doi.org/10.1016/0040-1951\(94\)00232-X](https://doi.org/10.1016/0040-1951(94)00232-X)
- Leite, F. L., Bueno, C. C., Da Roz, A. L., Ziemath, E. C., & Oliveira, O. N. (2012). Theoretical models for surface forces and adhesion and their measurement using atomic force microscopy. *International Journal of Molecular Sciences*, 13(10), 12773-12856. <https://doi.org/10.3390/ijms131012773>
- Leviton, D. B., & Frey, B. J. (2006). Temperature-dependent absolute refractive index measurements of synthetic fused silica. *Paper presented at Optomechanical Technologies for Astronomy*, International Society for Optics and Photonics, Orlando, Florida, USA. <https://doi.org/10.1117/12.672853>
- Li, B., Zhao, Z., Jiang, Y., & Jing, L. (2015). Contact mechanism of a rock fracture subjected to normal loading and its impact on fast closure behavior during initial stage of fluid flow

- experiment. *International Journal for Numerical and Analytical Methods in Geomechanics*, 39(13), 1431-1449. <https://doi.org/10.1002/nag.2365>
- Li, D., & Wong, L. N. Y. (2013). The Brazilian disc test for rock mechanics applications: review and new insights. *Rock mechanics and rock engineering*, 46(2), 269-287. <https://doi.org/10.1007/s00603-012-0257-7>
- Li, Y. R., & Zhang, Y. B. (2015). Quantitative estimation of joint roughness coefficient using statistical parameters. *International Journal of Rock Mechanics and Mining Sciences*, 77, 27-35. <https://doi.org/10.1016/j.ijrmms.2015.03.016>
- Lu, R., Nagel, T., Shao, H., Kolditz, O., & Shao, H. (2018). Modeling of dissolution-induced permeability evolution of a granite fracture under crustal conditions. *Journal of Geophysical Research: Solid Earth*, 123(7), 5609-5627. <https://doi.org/10.1029/2018JB015702>
- Maribo-Mogensen, B., Kontogeorgis, G. M., & Thomsen, K. (2013). Modeling of dielectric properties of aqueous salt solutions with an equation of state. *The Journal of Physical Chemistry B*, 117(36), 10523-10533. <https://doi.org/10.1021/jp403375t>
- Marshall, W. L. (2008). Dielectric constant of water discovered to be simple function of density over extreme ranges from -35 to +600 °C and to 1200 MPa (12000 Atm.), believed universal. *Nature Precedings*, 1-1. <https://doi.org/10.1038/npre.2008.2472.1>
- Matsuki, K., Chida, Y., Sakaguchi, K., & Glover, P. (2006). Size effect on aperture and permeability of a fracture as estimated in large synthetic fractures. *International Journal of Rock Mechanics and Mining Sciences*, 43(5), 726-755. <https://doi.org/10.1016/j.ijrmms.2005.12.001>
- McDowell-Boyer, L. M., Hunt, J. R., & Sitar, N. (1986). Particle transport through porous media. *Water Resources Research*, 22(13), 1901-1921. <https://doi.org/10.1029/WR022i013p01901>
- McKay, W. I., & Brigham, W. E. (1984). *Effects of temperature on the absolute permeability of consolidated sandstone*. CA, USA: Petroleum Research Institute, Stanford University.
- Méheust, Y., & Schmittbuhl, J. (2001). Geometrical heterogeneities and permeability anisotropy of rough fractures. *Journal of Geophysical Research: Solid Earth*, 106(B2), 2089-2102. <https://doi.org/10.1029/2000JB900306>
- Meng, F., Li, X., Baud, P., & Wong, T. f. (2020). Effective stress law for the permeability and pore volume change of clayey sandstones. *Journal of Geophysical Research: Solid Earth*, e2020JB019765.
- Milsch, H., Hofmann, H., & Blocher, G. (2016). An experimental and numerical evaluation of continuous fracture permeability measurements during effective pressure cycles. *International Journal of Rock Mechanics and Mining Sciences*, 89, 109-115. <https://doi.org/10.1016/j.ijrmms.2016.09.002>
- Milsch, H., Seibt, A., & Spangenberg, E. (2008a). Long-term petrophysical investigations on geothermal reservoir rocks at simulated in situ conditions. *Transport in Porous Media*, 77(1), 59-78. <https://doi.org/10.1007/s11242-008-9261-5>
- Milsch, H., Spangenberg, E., Kulenkampff, J., & Meyhöfer, S. (2008b). A new apparatus for long-term petrophysical investigations on geothermal reservoir rocks at simulated in-situ conditions. *Transport in Porous Media*, 74(1), 73-85. <https://doi.org/10.1007/s11242-007-9186-4>
- Min, K.-B., Rutqvist, J., & Elsworth, D. (2009). Chemically and mechanically mediated influences on the transport and mechanical characteristics of rock fractures. *International Journal of Rock Mechanics and Mining Sciences*, 46(1), 80-89. <https://doi.org/10.1016/j.ijrmms.2008.04.002>
- Mohan, K. K., & Fogler, H. S. (1997). Effect of pH and layer charge on formation damage in

- porous media containing swelling clays. *Langmuir*, 13(10), 2863-2872.  
<https://doi.org/10.1021/la960868w>
- Mohan, K. K., Fogler, H. S., Vaidya, R. N., & Reed, M. G. (1993). Water sensitivity of sandstones containing swelling and non-swelling clays. *Colloids and Surfaces A: Physicochemical and Engineering Aspects*, 73, 237-254. [https://doi.org/10.1016/0927-7757\(93\)80019-B](https://doi.org/10.1016/0927-7757(93)80019-B)
- Moore, D. E., Morrow, C. A., & Byerlee, J. D. (1982). Use of swelling clays to reduce permeability and its potential application to nuclear waste repository sealing. *Geophysical Research Letters*, 9(9), 1009-1012.
- Mourzenko, V. V., Thovert, J.-F., & Adler, P. M. (1995). Permeability of a single fracture; validity of the Reynolds equation. *Journal de Physique II*, 5(3), 465-482.  
<https://doi.org/10.1051/jp2:1995133>
- Mungan, N. (1968). Permeability reduction due to salinity changes. *Journal of Canadian Petroleum Technology*, 7(03), 113-117. <https://doi.org/10.2118/68-03-04>
- Musharova, D., Mohamed, I. M., & Nasr-El-Din, H. A. (2012). Detrimental effect of temperature on fines migration in sandstone formations. *Paper presented at SPE International Symposium and Exhibition on Formation Damage Control*, Society of Petroleum Engineers, Louisiana, USA.
- Nakashima, S. (1995). Diffusivity of ions in pore water as a quantitative basis for rock deformation rate estimates. *Tectonophysics*, 245(3-4), 185-203.  
[https://doi.org/10.1016/0040-1951\(94\)00234-Z](https://doi.org/10.1016/0040-1951(94)00234-Z)
- Nara, Y., Hiroyoshi, N., Yoneda, T., & Kaneko, K. (2010). Effects of relative humidity and temperature on subcritical crack growth in igneous rock. *International Journal of Rock Mechanics and Mining Sciences*, 47(4), 640-646.  
<https://doi.org/10.1016/j.ijrmms.2010.04.009>
- Nemoto, K., Watanabe, N., Hirano, N., & Tsuchiya, N. (2009). Direct measurement of contact area and stress dependence of anisotropic flow through rock fracture with heterogeneous aperture distribution. *Earth and Planetary Science Letters*, 281(1-2), 81-87.  
<https://doi.org/10.1016/j.epsl.2009.02.005>
- Neretnieks, I. (2014). Stress-mediated closing of fractures: Impact of matrix diffusion. *Journal of Geophysical Research: Solid Earth*, 119(5), 4149-4163.  
<https://doi.org/10.1002/2013JB010645>
- Neuville, A., Toussaint, R., & Schmittbuhl, J. (2012). Fracture aperture reconstruction and determination of hydrological properties: a case study at Draix (French Alps). *Hydrological processes*, 26(14), 2095-2105. <https://doi.org/10.1002/hyp.7985>
- Niemeijer, A., Spiers, C., & Bos, B. (2002). Compaction creep of quartz sand at 400–600 °C: Experimental evidence for dissolution-controlled pressure solution. *Earth and Planetary Science Letters*, 195(3-4), 261-275. [https://doi.org/10.1016/S0012-821X\(01\)00593-3](https://doi.org/10.1016/S0012-821X(01)00593-3)
- Ochi, J., & Vernoux, J.-F. (1998). Permeability decrease in sandstone reservoirs by fluid injection: hydrodynamic and chemical effects. *Journal of hydrology*, 208(3-4), 237-248.  
[https://doi.org/10.1016/S0022-1694\(98\)00169-3](https://doi.org/10.1016/S0022-1694(98)00169-3)
- Ogata, S., Yasuhara, H., Kinoshita, N., Cheon, D.-S., & Kishida, K. (2018). Modeling of coupled thermal-hydraulic-mechanical-chemical processes for predicting the evolution in permeability and reactive transport behavior within single rock fractures. *International Journal of Rock Mechanics and Mining Sciences*, 107, 271-281.  
<https://doi.org/10.1016/j.ijrmms.2018.04.015>
- Omar, A. E. (1990). Effect of brine composition and clay content on the permeability damage of

- sandstone cores. *Journal of Petroleum Science and Engineering*, 4(3), 245-256.  
[https://doi.org/10.1016/0920-4105\(90\)90014-T](https://doi.org/10.1016/0920-4105(90)90014-T)
- Paterson, M. (1973). Nonhydrostatic thermodynamics and its geologic applications. *Reviews of Geophysics*, 11(2), 355-389. <https://doi.org/10.1029/RG011i002p00355>
- Pei, L., Blöcher, G., Milsch, H., Deon, F., Zimmermann, G., Rühaak, W., et al. (2016). Thermal strain in a water-saturated limestone under hydrostatic and deviatoric stress states. *Tectonophysics*, 688, 49-64. <https://doi.org/10.1016/j.tecto.2016.09.020>
- Persson, B. N., Albohr, O., Tartaglino, U., Volokitin, A., & Tosatti, E. (2004). On the nature of surface roughness with application to contact mechanics, sealing, rubber friction and adhesion. *Journal of physics: Condensed matter*, 17(1), R1-R62.  
<https://doi.org/10.1088/0953-8984/17/1/R01>
- Plouraboué, F., Kurowski, P., Hulin, J.-P., Roux, S., & Schmittbuhl, J. (1995). Aperture of rough cracks. *Physical review E*, 51(3), 1675. <https://doi.org/10.1103/PhysRevE.51.1675>
- Polak, A., Elsworth, D., Liu, J., & Grader, A. S. (2004). Spontaneous switching of permeability changes in a limestone fracture with net dissolution. *Water Resources Research*, 40, W03502. <https://doi.org/10.1029/2003WR002717>
- Polak, A., Elsworth, D., Yasuhara, H., Grader, A. S., & Halleck, P. M. (2003). Permeability reduction of a natural fracture under net dissolution by hydrothermal fluids. *Geophysical Research Letters*, 30(20), 2020. <https://doi.org/10.1029/2003GL017575>
- Ponson, L., Auradou, H., Pessel, M., Lazarus, V., & Hulin, J.-P. (2007). Failure mechanisms and surface roughness statistics of fractured Fontainebleau sandstone. *Physical Review E*, 76(3), 036108. <https://doi.org/10.1103/PhysRevE.76.036108>
- Potter, J. M., Nur, A., & Dibble Jr., W. E. (1980). *Effect of temperature and solution composition on the permeability of St. Peters sandstone: role of iron (III)*. Stanford, CA, USA: Stanford Rock Physics Project; Dept. of Geology, Stanford University.
- Prajapati, N., Selzer, M., Nestler, B., Busch, B., Hilgers, C., & Ankit, K. (2018). Three-dimensional phase-field investigation of pore space cementation and permeability in quartz sandstone. *Journal of Geophysical Research: Solid Earth*, 123(8), 6378-6396.  
<https://doi.org/10.1029/2018jb015618>
- Rahman, S. S., Rahman, M. M., & Khan, F. A. (1995). Response of low-permeability, illitic sandstone to drilling and completion fluids. *Journal of Petroleum Science and Engineering*, 12(4), 309-322. [https://doi.org/10.1016/0920-4105\(94\)00052-6](https://doi.org/10.1016/0920-4105(94)00052-6)
- Raj, R. (1982). Creep in polycrystalline aggregates by matter transport through a liquid phase. *Journal of Geophysical Research*, 87(B6), 4731-4739.  
<https://doi.org/10.1029/JB087iB06p04731>
- Ramachandran, R., & Somasundaran, P. (1986). Effect of temperature on the interfacial properties of silicates. *Colloids and Surfaces*, 21, 355-369. [https://doi.org/10.1016/0166-6622\(86\)80104-4](https://doi.org/10.1016/0166-6622(86)80104-4)
- Raven, K., & Gale, J. (1985). Water flow in a natural rock fracture as a function of stress and sample size. *International Journal of Rock Mechanics and Mining Sciences*, 22(4), 251-261.  
[https://doi.org/10.1016/0148-9062\(85\)92952-3](https://doi.org/10.1016/0148-9062(85)92952-3)
- Regenspurg, S., Feldbusch, E., Byrne, J., Deon, F., Driba, D. L., Hennings, J., et al. (2015). Mineral precipitation during production of geothermal fluid from a Permian Rotliegend reservoir. *Geothermics*, 54, 122-135. <https://doi.org/10.1016/j.geothermics.2015.01.003>
- Renard, F., Beauprêtre, S., Voisin, C., Zigone, D., Candela, T., Dysthe, D. K., & Gratier, J.-P. (2012). Strength evolution of a reactive frictional interface is controlled by the dynamics of contacts and chemical effects. *Earth and Planetary Science Letters*, 341-344, 20-34.

- <https://doi.org/10.1016/j.epsl.2012.04.048>
- Renard, F., Bernard, D., Desrues, J., & Ougier-Simonin, A. (2009). 3D imaging of fracture propagation using synchrotron X-ray microtomography. *Earth and Planetary Science Letters*, 286(1-2), 285-291. <https://doi.org/10.1016/j.epsl.2009.06.040>
- Renard, F., Gratier, J.-P., & Jamtveit, B. (2000). Kinetics of crack-sealing, intergranular pressure solution, and compaction around active faults. *Journal of Structural Geology*, 22(10), 1395-1407. [https://doi.org/10.1016/S0191-8141\(00\)00064-X](https://doi.org/10.1016/S0191-8141(00)00064-X)
- Renard, F., & Ortoleva, P. (1997). Water films at grain-grain contacts: Debye-Hückel, osmotic model of stress, salinity, and mineralogy dependence. *Geochimica et Cosmochimica Acta*, 61(10), 1963-1970. [https://doi.org/10.1016/S0016-7037\(97\)00036-7](https://doi.org/10.1016/S0016-7037(97)00036-7)
- Renard, F., Park, A., Ortoleva, P., & Gratier, J.-P. (1999). An integrated model for transitional pressure solution in sandstones. *Tectonophysics*, 312(2-4), 97-115. [https://doi.org/10.1016/S0040-1951\(99\)00202-4](https://doi.org/10.1016/S0040-1951(99)00202-4)
- Renshaw, C. E. (1995). On the relationship between mechanical and hydraulic apertures in rough-walled fractures. *Journal of Geophysical Research*, 100(B12), 24629-24636. <https://doi.org/10.1029/95JB02159>
- Revil, A. (1999). Pervasive pressure-solution transfer: A poro-visco-plastic model. *Geophysical Research Letters*, 26(2), 255-258. <https://doi.org/10.1029/1998GL900268>
- Revil, A. (2001). Pervasive pressure solution transfer in a quartz sand. *Journal of Geophysical Research*, 106(B5), 8665-8686. <https://doi.org/10.1029/2000JB900465>
- Rimstidt, J. D., & Barnes, H. (1980). The kinetics of silica-water reactions. *Geochimica et Cosmochimica Acta*, 44(11), 1683-1699. [https://doi.org/10.1016/0016-7037\(80\)90220-3](https://doi.org/10.1016/0016-7037(80)90220-3)
- Robin, P.-Y. F. (1978). Pressure solution at grain-to-grain contacts. *Geochimica et Cosmochimica Acta*, 42(9), 1383-1389. [https://doi.org/10.1016/0016-7037\(78\)90043-1](https://doi.org/10.1016/0016-7037(78)90043-1)
- Rodríguez, K., & Araujo, M. (2006). Temperature and pressure effects on zeta potential values of reservoir minerals. *Journal of Colloid and Interface Science*, 300(2), 788-794. <https://doi.org/10.1016/j.jcis.2006.04.030>
- Rosenbrand, E., Fabricius, I. L., Fisher, Q., & Grattoni, C. (2015a). Permeability in Rotliegend gas sandstones to gas and brine as predicted from NMR, mercury injection and image analysis. *Marine and Petroleum Geology*, 64, 189-202. <https://doi.org/10.1016/j.marpetgeo.2015.02.009>
- Rosenbrand, E., & Kjøller, C. (2014). Effect of temperature on sandstone permeability: Mineral-fluid interaction: Technical University of Denmark, Department of Civil Engineering.
- Rosenbrand, E., Kjøller, C., Riis, J. F., Kets, F., & Fabricius, I. L. (2015b). Different effects of temperature and salinity on permeability reduction by fines migration in Berea sandstone. *Geothermics*, 53, 225-235. <https://doi.org/10.1016/j.geothermics.2014.06.004>
- Ruckenstein, E., & Prieve, D. C. (1976). Adsorption and desorption of particles and their chromatographic separation. *AIChE Journal*, 22(2), 276-283. <https://doi.org/10.1002/aic.690220209>
- Russell, T., Wong, K., Zeinijahromi, A., & Bedrikovetsky, P. (2018). Effects of delayed particle detachment on injectivity decline due to fines migration. *Journal of Hydrology*, 564, 1099-1109. <https://doi.org/10.1016/j.jhydrol.2018.07.067>
- Rutqvist, J. (2015). Fractured rock stress-permeability relationships from in situ data and effects of temperature and chemical-mechanical couplings. *Geofluids*, 15(1-2), 48-66. <https://doi.org/10.1111/gfl.12089>
- Rutter, E. (1976). The kinetics of rock deformation by pressure solution. *Trans. R. Soc. London*,

- A, 283, 203-219. <https://doi.org/10.1098/rsta.1976.0079>
- Rutter, E. (1983). Pressure solution in nature, theory and experiment. *Journal of the Geological Society*, 140(5), 725-740. <https://doi.org/10.1144/gsjgs.140.5.0725>
- Saadi, F. A., Wolf, K.-H., & Kruijdsdijk, C. v. (2017). Characterization of Fontainebleau sandstone: quartz overgrowth and its impact on pore-throat framework. *Journal of Petroleum & Environmental Biotechnology*, 08(03), 1-12. <https://doi.org/10.4172/2157-7463.1000328>
- Sausse, J. (2002). Hydromechanical properties and alteration of natural fracture surfaces in the Soultz granite (Bas-Rhin, France). *Tectonophysics*, 348(1-3), 169-185. [https://doi.org/10.1016/S0040-1951\(01\)00255-4](https://doi.org/10.1016/S0040-1951(01)00255-4)
- Schembre, J., & Kovscek, A. (2005). Mechanism of formation damage at elevated temperature. *Journal of Energy Resources Technology*, 127(3), 171-180. <https://doi.org/10.1115/1.1924398>
- Schembre, J., Tang, G.-Q., & Kovscek, A. (2006). Wettability alteration and oil recovery by water imbibition at elevated temperatures. *Journal of Petroleum Science and Engineering*, 52(1-4), 131-148. <https://doi.org/10.1016/j.petrol.2006.03.017>
- Schepers, A., & Milsch, H. (2013). Relationships between fluid-rock interactions and the electrical conductivity of sandstones. *Journal of Geophysical Research: Solid Earth*, 118(7), 3304-3317. <https://doi.org/10.1002/jgrb.50241>
- Schmittbuhl, J., Renard, F., Gratier, J.-P., & Toussaint, R. (2004). Roughness of stylolites: implications of 3D high resolution topography measurements. *Physical Review Letters*, 93(23), 238501-238504. <https://doi.org/10.1103/PhysRevLett.93.238501>
- Schmittbuhl, J., Schmitt, F., & Scholz, C. (1995). Scaling invariance of crack surfaces. *Journal of Geophysical Research: Solid Earth*, 100(B4), 5953-5973. <https://doi.org/10.1029/94jb02885>
- Schmittbuhl, J., Steyer, A., Jouniaux, L., & Toussaint, R. (2008). Fracture morphology and viscous transport. *International Journal of Rock Mechanics and Mining Sciences*, 45(3), 422-430. <https://doi.org/10.1016/j.ijrmmms.2007.07.007>
- Schneider, C. A., Rasband, W. S., & Eliceiri, K. W. (2012). NIH Image to ImageJ: 25 years of image analysis. *Nature methods*, 9(7), 671-675. <https://doi.org/10.1038/nmeth.2089>
- Schutjens, P. M. (1991). Experimental compaction of quartz sand at low effective stress and temperature conditions. *Journal of the Geological Society*, 148(3), 527-539. <https://doi.org/10.1144/gsjgs.148.3.0527>
- Sharma, M. M., Yortsos, Y. C., & Handy, L. L. (1985). Release and deposition of clays in sandstones. *Paper presented at SPE Oilfield and Geothermal Chemistry Symposium*, Society of Petroleum Engineers, Phoenix, Arizona, USA. <https://doi.org/10.2118/13562-ms>
- Singh, K. K., Singh, D., & Ranjith, P. (2015). Laboratory simulation of flow through single fractured granite. *Rock Mechanics and Rock Engineering*, 48(3), 987-1000. <https://doi.org/10.1007/s00603-014-0630-9>
- Smith, S. J. (1967). Susceptibility of interlayer potassium in illites to exchange, (Doctoral dissertation). Ames, Iowa, USA: Iowa State University of Science and Technology.
- Somerton, W. (1980). Some physical properties of Cerro Prieto cores. *Geothermics*, 9(1-2), 159-168. [https://doi.org/10.1016/0375-6505\(80\)90029-2](https://doi.org/10.1016/0375-6505(80)90029-2)
- Somerton, W. H. (1992). *Thermal properties and temperature-related behavior of rock/fluid systems*. Amsterdam, The Netherlands: Elsevier.
- Somerton, W. H., Janah, A. H., & Ashqar, P. I. (1981). Thermal expansion of fluid saturated rocks under stress. *Paper presented at SPWLA 22nd Annual Logging Symposium*, Society of Petrophysicists and Well-Log Analysts, Mexico City, Mexico.

- Spiers, C., Schutjens, P., Brzesowsky, R., Peach, C., Liezenberg, J., & Zwart, H. (1990). Experimental determination of constitutive parameters governing creep of rocksalt by pressure solution. *Geological Society, London, Special Publications*, 54(1), 215-227. <https://doi.org/10.1144/GSL.SP.1990.054.01.21>
- Stephenson, L., Plumley, W., & Palciauskas, V. (1992). A model for sandstone compaction by grain interpenetration. *J. Sediment. Petrol.*, 62(1), 11-22.
- Stuart, M. R. (1955). Dielectric constant of quartz as a function of frequency and temperature. *Journal of Applied Physics*, 26(12), 1399-1404. <https://doi.org/10.1063/1.1721922>
- Sulem, J., & Ouffroukh, H. (2006). Hydromechanical behaviour of Fontainebleau sandstone. *Rock Mechanics and Rock Engineering*, 39(3), 185-213. <https://doi.org/10.1007/s00603-005-0065-4>
- Sun, Y. Z., Xie, L. Z., He, B., Gao, C., & Wang, J. (2016). Effects of effective stress and temperature on permeability of sandstone from CO<sub>2</sub>-plume geothermal reservoir. *Journal of Rock Mechanics and Geotechnical Engineering*, 8(6), 819-827. <https://doi.org/10.1016/j.jrmge.2016.07.004>
- Sundberg, J., Back, P.-E., Christiansson, R., Hökmark, H., Ländell, M., & Wrafter, J. (2009). Modelling of thermal rock mass properties at the potential sites of a Swedish nuclear waste repository. *International Journal of Rock Mechanics and Mining Sciences*, 46(6), 1042-1054. <https://doi.org/10.1016/j.ijrmms.2009.02.004>
- Tada, R., Maliva, R., & Siever, R. (1987). A new mechanism for pressure solution in porous quartzose sandstone. *Geochimica et Cosmochimica Acta*, 51(9), 2295-2301. [https://doi.org/10.1016/0016-7037\(87\)90282-1](https://doi.org/10.1016/0016-7037(87)90282-1)
- Tanaka, N., Graham, J., & Crilly, T. (1997). Stress-strain behaviour of reconstituted illitic clay at different temperatures. *Engineering Geology*, 47(4), 339-350. [https://doi.org/10.1016/S0013-7952\(96\)00113-5](https://doi.org/10.1016/S0013-7952(96)00113-5)
- Taron, J., & Elsworth, D. (2010). Constraints on compaction rate and equilibrium in the pressure solution creep of quartz aggregates and fractures: Controls of aqueous concentration. *Journal of Geophysical Research*, 115(B7), B07211. <https://doi.org/10.1029/2009jb007118>
- Tchistiakov, A. A. (2000). Colloid chemistry of in-situ clay-induced formation damage. *Paper presented at SPE International Symposium on Formation Damage Control*, Society of Petroleum Engineers, Lafayette, Louisiana, USA. <https://doi.org/10.2118/58747-MS>
- Tester, J. W., Worley, W. G., Robinson, B. A., Grigsby, C. O., & Feerer, J. L. (1994). Correlating quartz dissolution kinetics in pure water from 25 to 625 °C. *Geochimica et Cosmochimica Acta*, 58(11), 2407-2420. [https://doi.org/10.1016/0016-7037\(94\)90020-5](https://doi.org/10.1016/0016-7037(94)90020-5)
- Thompson, M. E., & Brown, S. R. (1991). The effect of anisotropic surface roughness on flow and transport in fractures. *Journal of Geophysical Research: Solid Earth*, 96(B13), 21923-21932. <https://doi.org/10.1029/91jb02252>
- Tranter, M., De Lucia, M., & Kühn, M. (2021). Numerical investigation of barite scaling kinetics in fractures. *Geothermics*, 91, 102027. <https://doi.org/10.1016/j.geothermics.2020.102027>
- Tse, R., & Cruden, D. (1979). Estimating joint roughness coefficients. *International Journal of Rock Mechanics and Mining Sciences*, 16(5), 303-307. [https://doi.org/10.1016/0148-9062\(79\)90241-9](https://doi.org/10.1016/0148-9062(79)90241-9)
- Urai, J. L., Spiers, C. J., Zwart, H. J., & Lister, G. S. (1986). Weakening of rock salt by water during long-term creep. *Nature*, 324(6097), 554-557. <https://doi.org/10.1038/324554a0>
- Vaidya, S., Bailey, S., Pasternack, T., & Kennedy, G. (1973). Compressibility of fifteen minerals to 45 kilobars. *Journal of Geophysical Research*, 78(29), 6893-6898. <https://doi.org/10.1029/JB078i029p06893>



- Van den Ende, M. P., Niemeijer, A., & Spiers, C. (2019). Influence of grain boundary structural evolution on pressure solution creep rates. *Journal of Geophysical Research: Solid Earth*, *124*(10), 10210-10230. <https://doi.org/10.1029/2019JB017500>
- Van Noort, R., Spiers, C. J., & Pennock, G. M. (2008a). Compaction of granular quartz under hydrothermal conditions: Controlling mechanisms and grain boundary processes. *Journal of Geophysical Research*, *113*(B12), B12206. <https://doi.org/10.1029/2008JB005815>
- Van Noort, R., Visser, H. J., & Spiers, C. J. (2008b). Influence of grain boundary structure on dissolution controlled pressure solution and retarding effects of grain boundary healing. *Journal of Geophysical Research*, *113*(B3), B03201. <https://doi.org/10.1029/2007JB005223>
- Verwey, E. J. W. (1947). Theory of the stability of lyophobic colloids. *The Journal of Physical Chemistry*, *51*(3), 631-636. <https://doi.org/10.1021/j150453a001>
- Vogler, D., Amann, F., Bayer, P., & Elsworth, D. (2016). Permeability evolution in natural fractures subject to cyclic loading and gouge formation. *Rock Mechanics and Rock Engineering*, *49*(9), 3463-3479. <https://doi.org/10.1007/s00603-016-1022-0>
- Vogler, D., Settgast, R. R., Annavarapu, C., Madonna, C., Bayer, P., & Amann, F. (2018). Experiments and simulations of fully hydro-mechanically coupled response of rough fractures exposed to high-pressure fluid injection. *Journal of Geophysical Research: Solid Earth*, *123*(2), 1186-1200. <https://doi.org/10.1002/2017JB015057>
- Walsh, J. (1981). Effect of pore pressure and confining pressure on fracture permeability. *International Journal of Rock Mechanics and Mining Sciences*, *18*(5), 429-435. [https://doi.org/10.1016/0148-9062\(81\)90006-1](https://doi.org/10.1016/0148-9062(81)90006-1)
- Washburn, E. W. (1921). The dynamics of capillary flow. *Physical Review*, *17*(3), 273.
- Watanabe, N., Hirano, N., & Tsuchiya, N. (2008). Determination of aperture structure and fluid flow in a rock fracture by high-resolution numerical modeling on the basis of a flow-through experiment under confining pressure. *Water Resources Research*, *44*, W06412. <https://doi.org/10.1029/2006wr005411>
- Waza, T., Kurita, K., & Mizutani, H. (1980). The effect of water on the subcritical crack growth in silicate rocks. *Tectonophysics*, *67*(1-2), 25-34.
- Wei, K. K., Morrow, N. R., & Brower, K. R. (1986). Effect of fluid, confining pressure, and temperature on absolute permeabilities of low-permeability sandstones. *SPE Formation Evaluation*, *1*(04), 413-423.
- Weinbrandt, R., Ramey Jr, H., & Casse, F. (1975). The effect of temperature on relative and absolute permeability of sandstones. *Society of Petroleum Engineers Journal*, *15*(05), 376-384. <https://doi.org/10.2118/4142-PA>
- Wetzel, M., Kempka, T., & Kühn, M. (2020). Hydraulic and mechanical impacts of pore space alterations within a sandstone quantified by a flow velocity-dependent precipitation approach. *Materials*, *13*(14), 3100. <https://doi.org/10.3390/ma13143100>
- Weyl, P. K. (1959). Pressure solution and the force of crystallization: a phenomenological theory. *Journal of Geophysical Research*, *64*(11), 2001-2025. <https://doi.org/10.1029/JZ064i011p02001>
- Wilkinson, M., & Haszeldine, R. S. (2002). Fibrous illite in oilfield sandstones - a nucleation kinetic theory of growth. *Terra Nova*, *14*(1), 56-60. <https://doi.org/10.1046/j.1365-3121.2002.00388.x>
- Wilson, L., Wilson, M. J., Green, J., & Patey, I. (2014). The influence of clay mineralogy on formation damage in North Sea reservoir sandstones: A review with illustrative examples. *Earth-Science Reviews*, *134*, 70-80. <https://doi.org/10.1016/j.earscirev.2014.03.005>

- Witherspoon, P. A., Wang, J. S., Iwai, K., & Gale, J. E. (1980). Validity of cubic law for fluid flow in a deformable rock fracture. *Water Resources Research*, *16*(6), 1016-1024. <https://doi.org/10.1029/WR016i006p01016>
- Wong, T., & Brace, W. F. (1979). Thermal expansion of rocks: some measurements at high pressure. *Tectonophysics*, *57*(2-4), 95-117. [https://doi.org/10.1016/0040-1951\(79\)90143-4](https://doi.org/10.1016/0040-1951(79)90143-4)
- Yasuhara, H., & Elsworth, D. (2008). Compaction of a rock fracture moderated by competing roles of stress corrosion and pressure solution. *Pure and Applied Geophysics*, *165*(7), 1289-1306. <https://doi.org/10.1007/s00024-008-0356-2>
- Yasuhara, H., Elsworth, D., & Polak, A. (2003). A mechanistic model for compaction of granular aggregates moderated by pressure solution. *Journal of Geophysical Research*, *108*(B11), 2530. <https://doi.org/10.1029/2003JB002536>
- Yasuhara, H., Elsworth, D., & Polak, A. (2004). Evolution of permeability in a natural fracture: Significant role of pressure solution. *Journal of Geophysical Research*, *109*(B3), B03204. <https://doi.org/10.1029/2003JB002663>
- Yasuhara, H., Kinoshita, N., Ohfuji, H., Lee, D. S., Nakashima, S., & Kishida, K. (2011). Temporal alteration of fracture permeability in granite under hydrothermal conditions and its interpretation by coupled chemo-mechanical model. *Applied Geochemistry*, *26*(12), 2074-2088. <https://doi.org/10.1016/j.apgeochem.2011.07.005>
- Yasuhara, H., Kinoshita, N., Ohfuji, H., Takahashi, M., Ito, K., & Kishida, K. (2015). Long-term observation of permeability in sedimentary rocks under high-temperature and stress conditions and its interpretation mediated by microstructural investigations. *Water Resources Research*, *51*(7), 5425-5449. <https://doi.org/10.1002/2014WR016427>
- Yasuhara, H., Polak, A., Mitani, Y., Grader, A., Halleck, P., & Elsworth, D. (2006). Evolution of fracture permeability through fluid-rock reaction under hydrothermal conditions. *Earth and Planetary Science Letters*, *244*(1-2), 186-200. <https://doi.org/10.1016/j.epsl.2006.01.046>
- You, Z., Bedrikovetsky, P., Badalyan, A., & Hand, M. (2015). Particle mobilization in porous media: Temperature effects on competing electrostatic and drag forces. *Geophysical Research Letters*, *42*(8), 2852-2860. <https://doi.org/10.1002/2015GL063986>
- You, Z., Yang, Y., Badalyan, A., Bedrikovetsky, P., & Hand, M. (2016). Mathematical modelling of fines migration in geothermal reservoirs. *Geothermics*, *59*, 123-133. <https://doi.org/10.1016/j.geothermics.2015.05.008>
- Yu, M., Hussain, F., Arns, J. Y., Bedrikovetsky, P., Genolet, L., Behr, A., et al. (2018). Imaging analysis of fines migration during water flow with salinity alteration. *Advances in Water Resources*, *121*, 150-161. <https://doi.org/10.1016/j.advwatres.2018.08.006>
- Zambrano, M., Pitts, A. D., Salama, A., Volatili, T., Giorgioni, M., & Tondi, E. (2019). Analysis of fracture roughness control on permeability using SfM and fluid flow simulations: implications for carbonate reservoir characterization. *Geofluids*, *2019*, 1-19. <https://doi.org/10.1155/2019/4132386>
- Zang, A., Stephansson, O., Zimmermann, G., Hofmann, H., Niemz, P., Kim, K. Y., et al. (2020). Concept of fatigue hydraulic fracturing and applications in hard rock predicted from laboratory and in situ experiments. *Paper presented at 54th US Rock Mechanics/Geomechanics Symposium*, American Rock Mechanics Association.
- Zang, A., Wagner, C. F., & Dresen, G. (1996). Acoustic emission, microstructure, and damage model of dry and wet sandstone stressed to failure. *Journal of Geophysical Research: Solid Earth*, *101*(B8), 17507-17521. <https://doi.org/10.1029/96JB01189>
- Zhao, Y., Zhu, G., Zhang, C., Liu, S., Elsworth, D., & Zhang, T. (2018). Pore-scale reconstruction and simulation of non-Darcy flow in synthetic porous rocks. *Journal of*

- 
- Geophysical Research: Solid Earth*, 123(4), 2770-2786.  
<https://doi.org/10.1002/2017jb015296>
- Zhuang, L., Jung, S. G., Diaz, M., Kim, K. Y., Hofmann, H., Min, K.-B., et al. (2020). Laboratory true triaxial hydraulic fracturing of granite under six fluid injection schemes and grain-scale fracture observations. *Rock Mechanics and Rock Engineering*, 53(10), 4329-4344. <https://doi.org/10.1007/s00603-020-02170-8>
- Zimmerman, R. W., & Bodvarsson, G. S. (1996). Hydraulic conductivity of rock fractures. *Transport in Porous Media*, 23(1), 1-30. <https://doi.org/10.1007/BF00145263>
- Zimmerman, R. W., Chen, D.-W., & Cook, N. G. (1992). The effect of contact area on the permeability of fractures. *Journal of Hydrology*, 139(1-4), 79-96. [https://doi.org/10.1016/0022-1694\(92\)90196-3](https://doi.org/10.1016/0022-1694(92)90196-3)
- Zimmerman, R. W., Kumar, S., & Bodvarsson, G. S. (1991). Lubrication theory analysis of the permeability of rough-walled fractures. *International Journal of Rock Mechanics and Mining Sciences*, 28(4), 325-331. [https://doi.org/10.1016/0148-9062\(91\)90597-F](https://doi.org/10.1016/0148-9062(91)90597-F)
- Zimmermann, G., Zang, A., Stephansson, O., Klee, G., & Semiková, H. (2018). Permeability enhancement and fracture development of hydraulic In situ experiments in the Äspö Hard Rock Laboratory, Sweden. *Rock Mechanics and Rock Engineering*, 52(2), 495-515. <https://doi.org/10.1007/s00603-018-1499-9>
- Zou, L., Li, B., Mo, Y., & Cvetkovic, V. (2019). A high-resolution contact analysis of rough-walled crystalline rock fractures subject to normal stress. *Rock Mechanics and Rock Engineering*, 53(5), 2141–2155. <https://doi.org/10.1007/s00603-019-02034-w>

## List of figures

<b>Figure 1.1</b> Schematic diagram of fluid transport through porous media and rock fractures in the subsurface.....	3
<b>Figure 1.2</b> Schematic diagram of (a) a representative pore and pore throat structure with clay mineral coating and (b) charged particles under aqueous conditions, where electrical double layers are established.....	4
<b>Figure 1.3</b> Schematic diagram of asperity contacts in a macroscopic fracture and time-dependent deformation induced by fluid-rock interactions under aqueous fluid conditions.....	5
<b>Figure 1.4</b> Schematic of the scope of this study .....	7
<b>Figure 2.1</b> Schematic sketch of sample preparation for the different microstructural analyses ...	16
<b>Figure 2.2</b> Scanning electron micrographs in BSE and SE modes of the starting material.....	17
<b>Figure 2.3</b> Permeability as a function of temperature for samples FS1, FS3 and FS4 .....	19
<b>Figure 2.4</b> Comparison of the microstructure before and after the flow-through experiments ....	21
<b>Figure 2.5</b> Cumulative porosity as a function of pore diameter measured by MIP .....	22
<b>Figure 2.6</b> Concentrations of Na, K, Ca and Mg oxides in pore-filling illite as measured by electron microprobe analysis (EMPA) on polished thin sections .....	24
<b>Figure 2.7</b> Total interaction free energy between illite particle and illite plate and between illite particle and quartz plate .....	30
<b>Figure 3.1</b> Optical micrographs and grain size distributions of Fontainebleau sandstone and Flechtinger sandstone.....	37
<b>Figure 3.2</b> Preparation of the fractured samples.....	39
<b>Figure 3.3</b> Schematic illustration of fracture aperture determination.....	45
<b>Figure 3.4</b> Hydraulic aperture as a function of confining pressure .....	47
<b>Figure 3.5</b> Mechanical aperture changes as a function of confining pressure.....	48
<b>Figure 3.6</b> 3-D views of the fracture surfaces of the scanned specimens and their corresponding central profiles along the sample length.....	50
<b>Figure 3.7</b> 1-D surface roughness power spectra of the central profiles in the direction parallel to the displacement of fracture surface.....	51
<b>Figure 3.8</b> Evolution of the initial mean mechanical aperture with increasing offset of the two adjacent fracture surfaces along the sample length.....	52
<b>Figure 3.9</b> Variations of the mean mechanical aperture with increasing contact area ratio .....	53
<b>Figure 3.10</b> 3-D reconstructed models of the assembled dry rock samples before and after the experiments .....	55
<b>Figure 3.11</b> 2-D projections of the extracted fracture void space from the $\mu$ CT models .....	56

<b>Figure 3.12</b> Changes of hydraulic aperture as a function of mechanical aperture changes at different effective stresses.....	58
<b>Figure 3.13</b> Normal stiffness of the fractures.....	59
<b>Figure 3.14</b> Conceptual model of fracture closure for different fracture types.....	60
<b>Figure 3.15</b> Hydraulic aperture and mechanical aperture changes at the corresponding confining pressure as a function of the respective fracture wall offset.....	62
<b>Figure 4.1</b> Sample preparation.....	68
<b>Figure 4.2</b> Schematic illustration of the experimental apparatus.....	69
<b>Figure 4.3</b> Hydraulic fracture aperture and mechanical fracture aperture changes as a function of confining pressure.....	74
<b>Figure 4.4</b> Hydraulic fracture aperture as a function of temperature.....	74
<b>Figure 4.5</b> Evolution of hydraulic fracture aperture under different confining pressure and temperature conditions as a function of time.....	75
<b>Figure 4.6</b> Si concentrations (as measured by a photometer) in the subsamples obtained from the relief valve as a function of cumulative volume.....	76
<b>Figure 4.7</b> Evolution of maximum Si concentration as a function of time and under different confining pressure and temperature conditions.....	78
<b>Figure 4.8</b> Three-dimensional models of the fractured sample core before and after the flow-through experiment as obtained from the X-ray $\mu$ CT scans.....	79
<b>Figure 4.9</b> Si concentration as a function of inverse temperature $1/T$ ( $K^{-1}$ ).....	82
<b>Figure 5.1</b> Schematic illustration of the experimental setup.....	91
<b>Figure 5.2</b> Schematic of the experimental procedures, conditions, and stages of the entire experiment.....	92
<b>Figure 5.3</b> Evolution of hydraulic aperture and effluent Si concentration at varying conditions of effective stress.....	95
<b>Figure 5.4</b> Evolution of the Si concentrations of the injected fluids and the effluents.....	97
<b>Figure 5.5</b> Height differences of fracture surface A and B before and after the experiment.....	98
<b>Figure 5.6</b> X-ray $\mu$ CT-based 3-D perspective models obtained at different experimental stages.....	100
<b>Figure 5.7</b> Backscattered electron (BSE) micrographs of contact asperities after the experiment.....	101
<b>Figure 5.8</b> Concentration of the water film constrained in the contact boundaries as a function of the mean water film thickness.....	103
<b>Figure 5.9</b> The ratio of the apparent mass transfer coefficients as a function of the contact area ratio change.....	105
<b>Figure C1</b> Thin section images of fractures.....	122
<b>Figure C2</b> Images of fracture surfaces after the experiments.....	122
<b>Figure C3</b> Images and sketches of the fracture void space taken on the Flechtinger sandstone sample ends.....	123

<b>Figure C4</b> Images and sketches of the fracture void space taken on the Fontainebleau sandstone sample ends .....	123
<b>Figure E1</b> Photographs of the rock sample used for the experiment.....	125
<b>Figure E2</b> Microstructure of the rock matrix of Fontainebleau sandstone .....	126
<b>Figure E3</b> Topography of the fracture surfaces measured by white light interferometry .....	126
<b>Figure E4</b> Histograms of fracture surface roughness .....	127
<b>Figure E5</b> Length and width of each isolated contact area.....	127

---

## List of tables

<b>Table 2.1</b> Mineral composition of Flechtinger sandstone .....	12
<b>Table 2.2</b> Summary of experimental conditions.....	15
<b>Table 2.3</b> Median concentrations of Na, K, Ca, and Mg oxides in pore-filling illite before and after the flow-through experiments .....	23
<b>Table 3.1</b> Basic physical parameters of the two rock types.....	37
<b>Table 3.2</b> Statistical surface roughness parameters of selected samples .....	49
<b>Table 3.3</b> Evolution of mechanical aperture and contact area ratio determined by analyzing the 3-D X-ray $\mu$ CT models .....	57
<b>Table 3.4</b> Comparison of initial mechanical apertures obtained from surface topographies .....	57
<b>Table 4.1</b> Experimental conditions and the duration of each stage .....	70
<b>Table 5.1</b> Statistical summary of the $\mu$ CT data .....	99
<b>Table B1</b> Sample FS1 .....	119
<b>Table B2</b> Sample FS3 .....	120
<b>Table B3</b> Sample FS4.....	121
<b>Table C1</b> Mean mechanical aperture changes during loading-unloading stages determined by drained compression experiments.....	124

## **Curriculum Vitae**

Page 148 contains private data. Hence, it is not part of the online publication.